



Universidade do Minho
Escola de Engenharia

Hadi Baghi

**Shear Strengthening of Reinforced
Concrete Beams with SHCC-FRP Panels**

Hadi Baghi **Shear Strengthening of Reinforced
Concrete Beams with SHCC-FRP Panels**

UMinho | 2015

março de 2015



Universidade do Minho
Escola de Engenharia

Hadi Baghi

**Shear Strengthening of Reinforced
Concrete Beams with SHCC-FRP Panels**

Tese de Doutoramento
Engenharia Civil

Trabalho efectuado sob a orientação do
Professor Doutor Joaquim António Oliveira de Barros

STATEMENT OF INTEGRITY

I hereby declare having conducted my thesis with integrity. I confirm that I have not used plagiarism or any form of falsification of results in the process of the thesis elaboration.

I further declare that I have fully acknowledged the Code of Ethical Conduct of the University of Minho.

University of Minho, _____

Full name: _____

Signature: _____

Acknowledgements

First, I give thanks to God for protection and ability to do work.

The research reported in this thesis has been carried out at the Civil Engineering Department of University of Minho, Portugal, under the supervision of Prof. Joaquim Antonio Oliveira de Barros. This work was funded by project PTDC/ECM/114511/2009 “PrePam: Pre-fabricated thin panels using advanced materials for structural rehabilitation”, is gratefully acknowledged.

I would like to express my sincere gratitude to my advisor Prof. Joaquim Barros for the continuous support of my Ph.D study and research, for his patience, motivation, enthusiasm, and immense knowledge. He provided me continuous support for following my ideas and development of the work presented here. I could not have imagined having a better advisor and mentor for my Ph.D study.

I would also like to thank the technicians of the laboratory of the civil engineering department of University of Minho, engineers Marco, Mateus, Jesus Carlos, Pokee, Carlos Palha, and Helder. I also thank the CiviTest and Casais companies for the contribution on the execution of the beams.

I am also grateful to all my friends that always supported and encouraged me and stayed near me during the development of the present work. I would also to thank Esmaeel for being a great companion, and a special thanks goes to Mohsen for all his friendship and support.

I finish with Iran, where the most basic source of my life energy resides: my family. I have an amazing family, unique in many ways. I am indebted to my father, for his care and love. My father, is the person who established and natured my fundamental learning character, showing me the joy of intellectual pursuit ever since I was a child. I cannot ask for more from my mother as she is simply perfect. I have no suitable word that can fully describe her unflagging love and support throughout my life. Last but not least, my gratitude goes to my brother Hani, I had a great childhood with him.

Abstract

The main purpose of this thesis is to assess the potentialities of Hybrid Composite Plates (HCPs) for the shear strengthening of reinforced concrete (RC) beams. HCP is a thin plate of Strain Hardening Cementitious Composite (SHCC) reinforced with Carbon Fiber Reinforced Polymer (CFRP) laminates applied according to the Near Surface Mounted technique (NSM). Due to the excellent bond conditions between SHCC and CFRP laminates, these reinforcements provide the necessary tensile strength capacity to the HCP, while the high post-cracking tensile deformability and resistance of SHCC avoids the occurrence of premature fracture failure of this cement composite in the stress transfer process between these two materials when the HCP is crossed by a shear crack.

Different HCPs with different CFRP laminates percentage are adopted for the shear strengthening of the beams. Two different processes are investigated to apply the HCPs to the beam's concrete substrate: by using epoxy adhesive; in addition to the epoxy adhesive it is also used mechanical anchors. From the results it was verified that when epoxy adhesive is only used, the shear strengthening contribution of the HCPs is limited by the tensile strength of the concrete substrate of the strengthened beams. Mechanical anchors were therefore used in order to prevent a premature debonding of the HCPs and apply a certain confinement to the concrete in the zone of the beam to be strengthened, resulting favorable effects in terms of shear strengthening.

Experimental programs with intact and damage RC beams are carried out to assess the shear strengthening contribution of HCPs. The results obtained from these tests are also used for determining the predictive performance of the analytical model developed to evaluate the shear resistance of RC beams strengthened with HCPs.

To further explore the potentialities of HCPs for the shear strengthening of RC beams, advanced numerical simulations are performed by using a FEM-based computer program, whose adequate predictive performance is demonstrated by simulating the experimental tests carried out.

Keywords: Hybrid Composite Plate; CFRP laminates; Shear strengthening; Mechanical anchors; Numerical simulation; Finite Element Method.

Sumário

O principal objetivo desta tese é avaliar as potencialidades de um novo tipo de painel compósito híbrido no reforço ao corte de vigas de betão armado (BA). Este fino painel, designado na língua inglesa por *Hybrid Composite Plate* e com a abreviatura HCP, é composto por argamassa reforçada com fibras, a qual após endurecida é reforçada por finas lâminas de polímero reforçado com fibras de carbono (CFRP) aplicadas segundo a técnica “Instalação próxima da superfície” que na bibliografia em Inglês é conhecida por *NearSurfaceMounted* (NSM). Estes laminados de CFRP são instalados em finos entalhes executados no painel e colados com resina epóxi. Esta argamassa apresenta comportamento de endurecimento em tração, designada na língua inglesa por *StrainHardeningCementitious Composite* (SHCC), pelo que após o início da fendilhação da matriz desenvolve capacidade crescente de resistência à tração até nível de extensão relativamente elevado. O elevado desempenho em tração do SHCC permite mobilizar eficazmente a elevada resistência em tração dos laminados de CFRP, pois as microfibras que reforçam o SHCC evitam a ocorrência de rotura precoce por fratura durante o processo de transferência de tensões destes para o meio circundante, situação esta que ocorre quando o HCP é atravessado por fenda de corte que se desenvolve na viga a reforçar.

Diferentes configurações de HCP foram investigadas para o reforço ao corte de vigas de BA, em especial a percentagem e inclinação de laminados de CFRP e o processo de fixar os HCPs às faces laterais da viga a reforçar. No que respeita a este último aspeto, dois métodos foram estudados, um em que o HCP é aplicado recorrendo apenas a adesivo epóxi, e um outro em que para além do adesivo epóxi o painel é fixo recorrendo a ancoragens mecânicas. Os programas de ensaios experimentais evidenciaram a elevada eficácia desta técnica de reforço, principalmente quando os HCP são aplicados com adesivo e ancoragens, pois o nível de reforço garantido pelo HCP aplicado exclusivamente por adesivo está limitado pela resistência à tração do betão do substrato da viga a reforçado, dado ocorrer destacamento precoce do HCP. Este destacamento é evitado recorrendo a ancoragens mecânicas, as quais permitem ainda introduzir algum confinamento no betão da viga a reforçar dado poderem ser aplicadas com uma certa pós-tensão, resultando maior eficácia de reforço ao corte de vigas de BA conseguida com a presente técnica.

Recorrendo a conceitos e formulações existentes no quadro do comportamento e reforço ao corte de vigas de BA, foram desenvolvidas duas novas formulações, cuja capacidade preditiva foi avaliada não somente com os resultados obtidos nos programas experimentais executados, mas também recorrendo a resultados experimentais existentes na bibliografia da especialidade.

No intuito de melhor compreender as potencialidades da técnica de reforço desenvolvida neste trabalho, recorrendo a estudos paramétricos, foi inicialmente avaliada a capacidade preditiva de um modelo constitutivo existente no programa de elementos finitos FEMIX, fazendo a simulação dos ensaios executados experimentalmente. Constatou-se que o modelo constitutivo que modela o amolecimento em tração e em corte do processo de abertura e deslizamento de uma fenda em betão permite simular com elevado rigor quer a resposta deformacional, como o padrão de fendilhação registado nos ensaios experimentais. Utilizando este modelo, foram efetuados estudos paramétricos para evidenciar a influência de parâmetros relevantes na eficácia da técnica de reforço proposta.

Palavras chave: Reforço ao corte, Painel compósito híbrido; laminados de CFRP; argamassa com endurecimento em tração; Formulações analíticas; Análise não linear material (FEM)

Contents

Chapter 1: Introduction	1
Chapter 2: An Overview on the Shear Strengthening of the Reinforced Concrete Beams.....	5
2.1 Introduction.....	5
2.2 Fundamental Concepts of Shear.....	5
2.2.1 Crack development	5
2.2.2 Shear failure modes of concrete beams	8
2.3 Fiber Reinforced Polymer for Shear Strengthening	9
2.3.1 Externally Bonded Reinforcement	11
2.3.2 Near Surface Mounted	18
2.3.3 Embedded Through Section.....	25
2.4 Fiber Reinforced Concrete for Shear Strengthening	32
2.5 Conclusion	39
Chapter 3: Shear Strengthening of Reinforced Concrete Beams with Hybrid Composite Plate	41
3.1 Introduction.....	41
3.2 Contextualization of the Experimental Programs	42
3.3 Series I: Beams of Rectangular Cross Section.....	43
3.3.1 Beams and test setup	43
3.3.2 Material properties	46
3.3.3 Preparation of the beams.....	48
3.3.4 Tests and results	49
3.4 Series II: Beams of T Cross Section	57
3.4.1 Beams and test setup	57
3.4.2 Preparation of the beams.....	61
3.4.3 Tests and results	62
3.5 Series III: Repair of Existing RC beams	73
3.5.1 Beams and test setup	73
3.5.2 Test and results.....	74
3.6 Conclusions.....	79
Chapter 4: Numerical Simulation and Parametric Study.....	81
4.1 Introduction.....	81
4.2 Multi-Directional Fixed Smeared Crack Model	81
4.3 Modeling Beam Shear Strengthened with NSM Technique	87
4.4 Modeling of the Beams of Series I.....	94
4.5 Modeling of the Beams of Series II	99
4.6 Modeling of the Beams of Series III	104
4.7 Parametric Study for Assessing the Potentialities of the Developed Strengthening Technique	106
4.7.1 Influence of strengthening configuration and percentage of CFRP laminates	108
4.7.2 Influence of mechanical anchors	111

4.7.3 Flexural strengthening of the beams.....	112
4.7.4 Influence of SHCC instead of Mortar.....	115
4.7.5 Influence of the torque level applied to the mechanical anchors.....	116
4.8 Conclusions.....	117
Chapter 5: Shear Behavior of SHCC Material	119
5.1 Introduction.....	119
5.2 Review of Mode II Testing Methods	120
5.3 Iosipescu Shear Test.....	122
5.4 Experimental Program.....	123
5.4.1 Development of fixture and specimen.....	123
5.4.2 Test setup and monitoring system	126
5.4.3 Test results and discussion.....	126
5.5 Numerical Simulation.....	129
5.6 Parametric Study.....	131
5.6.1 Influence β parameter defining the first branch of the $\tau_t^{cr} - \gamma_t^{cr}$ diagram	131
5.6.2 Shear retention factor versus softening diagram for modeling the crack shear behavior	132
5.6.3 Plain cementitious material.....	133
5.6.4 Influence of notch tip radius	135
5.7 Conclusion	138
Chapter 6: Analytical Model to Predict Shear Capacity of Reinforced Concrete Beams Strengthened with NSM and HCPs.....	141
6.1 Introduction.....	141
6.2 Truss Model.....	141
6.3 Compression Field Theory (CFT).....	143
6.4 Modified Compression Field Theory (MCFT).....	144
6.4.1 Equilibrium between cracks.....	147
6.4.2 Equilibrium across cracks	149
6.4.3 Solution technique for MCFT.....	153
6.4.4 MCFT vs. Truss Model.....	156
6.5 Simplified Modified Compression Field Theory.....	156
6.5.1 Solution technique for simplified MCFT	161
6.6 ACI Building Code.....	161
6.7 Eurocode.....	162
6.7.1 Concrete members without shear reinforcement.....	162
6.7.2 Concrete members with shear reinforcement.....	163
6.8 Formulation of NSM Technique	163
6.8.1 Nanni approach	163
6.8.2 Bianco approach.....	165
6.9 New Approach to Determine Shear Capacity of RC Beams Strengthened with NSM Technique	170
6.9.1 Nanni simplified MCFT (NSMCFT).....	171

6.9.2 Bianco simplified MCFT (BSMCFT)	171
6.10 Estimate of Shear Capacity of Concrete Beams	172
6.11 Assessment of the Applicability of Analytical Formulations for Predicting the Shear Capacity of RC Beams Strengthened with Hybrid Composite Plate.....	180
6.11.1 Shear resistance of the SHCC plate.....	181
6.11.2 Assessment of the predictive performance of the considered formulations.....	181
6.12 Conclusion	184
Chapter 7: Conclusions and Recommendation for Future Research.....	185
7.1 Experimental research	185
7.2 Numerical research.....	186
7.3 Analytical work	187
7.4 Suggestions for Future Research.....	188
References:.....	191
List of Symbols:.....	197
Annex A: Iosipescu shear test fixture.....	203
Annex B: Modified Compression Field Theory.....	207
Annex C: Simplified Modified Compression Field Theory.....	209
Annex D: Example of NSMCFT and BSMCFT	211

Contents of Figures

Figure 1-1: Hybrid shear strengthening technique for RC beams	2
Figure 2-1: Types of cracks in concrete beams subjected to shear and bending moments (ACI Committee 2011)6	6
Figure 2-2: Components of shear resistance for concrete cracked without shear reinforcement	7
Figure 2-3: Crack in high strength concrete	7
Figure 2-4: Shear failure due to concrete crushing in the web region	8
Figure 2-5: Web shear failure	8
Figure 2-6: Flexural-shear failure	9
Figure 2-7: A comparison among CFRP, GFRP, AFRP, and steel in term of stress strain relationship (Alnatit 2011).....	10
Figure 2-8: Typical wrapping schemes for shear strengthening using FRP sheets or strips (ACI Committee 440 2000).....	11
Figure 2-9: Two-span continuous beams (dimensions in mm) (Khalifa et al. 1999).....	12
Figure 2-10: Test set-up and strengthening schemes (Khalifa et al. 1999)	13
Figure 2-11: T cross section beams (dimensions in mm) (Khalifa and Nanni 2000).....	14
Figure 2-12: Test setup and strengthening schemes (Khalifa and Nanni 2000).....	15
Figure 2-13: (a) longitudinal reinforcement, (b) strengthening scheme (dimensions in cm) (Alzoubi et al. 2007)	16
Figure 2-14: Details of the control beams (dimensions in mm) (Barros and Dias 2003)	17
Figure 2-15: Effect of shear reinforcement and epoxy-bonded FRP sheets on cracking pattern (Mofidi and Chaallal 2011)	18
Figure 2-16: Near Surface Mounted FRP laminate to increase the beam (a) shear capacity, (b) bending capacity	19
Figure 2-17: Cross section of beams: (a) beams without stirrups, and (b) beams with stirrups (dimensions in inches) (De Lorenzis and Nanni 2001).....	20
Figure 2-18: Geometrical details of the RC beams (Rizzo and De Lorenzis 2009).....	21
Figure 2-19: Geometry of the control beam (dimensions in mm) (Dias and Barros 2010)	22
Figure 2-20: Geometry of the reference beam (dimensions in mm) (Barros and Dias 2013).....	24
Figure 2-21: NSM shear strengthening configurations (CFRP laminates at dashed lines) (dimensions in mm) (Barros and Dias 2013)	24

Figure 2-22: Embedded Through-Section (ETS) strengthening technique concept for the shear strengthening of reinforced concrete beams (Barros and Dalfré 2013)	26
Figure 2-23: Details of tested beams: (a) longitudinal view; (b) cross-section with no transverse reinforcement; (c) cross-section with transverse steel stirrups (dimensions in mm) (Chaallal et al. 2011)	27
Figure 2-24: Geometry of the beams (dimensions in mm) (Barros and Dalfré 2013)	29
Figure 2-25: Tested beams: geometry, steel reinforcements applied in all beams (dimensions in mm) (Breveglieri et al. 2014)	30
Figure 2-26: (a) Schematic illustration of uniaxial stress-strain curves for brittle, quasi-brittle, and strain-hardening cementitious materials, (b) Schematic of three deformation stages of a SHCC during a uniaxial tensile test	32
Figure 2-27: Typical dimensions of the tested beams, and reinforcement details of the ductile beams (Maheri et al. 2004)	33
Figure 2-28: Retrofit configurations: (a) one plate bonded on the tensile face, (b) one plate bonded on the tensile face and four plates bonded on the vertical sides, and (c) one plate bonded on the tension face and two plates fully covering the vertical faces (Maheri et al. 2004)	34
Figure 2-29: Beam geometry (dimensions in mm) (Mostosi et al. 2011)	36
Figure 2-30: Load Deflection curves (Esmaeeli et al. 2013a)	37
Figure 2-31: Typical cracks pattern and the failure modes of the beams (Esmaeeli et al. 2013a)	38
Figure 2-32: (a) one example of RC beams, (b) test setup, and (c) repair/strengthening scheme (dimensions in mm) (Ruano et al. 2014)	38
Figure 3-1: A schematic view of HCP (dimensions in mm)	42
Figure 3-2: Geometry and reinforcement arrangement of the concrete beams (dimensions in mm)	44
Figure 3-3: Configurations of the HCPs in beam: (a) SP-4L90-I, and (b) and SP-3L45-I (dimensions in mm) ..	45
Figure 3-4: Monitoring system- position of the: (a) LVDTs, and (b) strain gages in CFRP laminates (dimensions in mm)	46
Figure 3-5: The envelope and the average tensile stress vs. crack opening displacement (COD) obtained in notched specimens (Esmaeeli et al. 2013b)	47
Figure 3-6: (a) Force vs. deflection at the loaded-section, and (b) $\Delta F / F^{NSM-4L90-I}$ vs. deflection at the loaded-section for the beams strengthened with SHCC plates and HCPs	49
Figure 3-7: Crack patterns and failure modes of the C-R-I beam	51

Figure 3-8: Crack patterns and failure modes of the NSM-4L90-I beam.....	52
Figure 3-9: Force vs. strain in monitored laminates in SGs where the maximum strains were registered.....	53
Figure 3-10: Crack patterns and failure modes of the SP-I beam.....	54
Figure 3-11: Crack patterns of the C-R-I (gray color) and SP-I (black color) at failure load.....	54
Figure 3-12: Crack patterns and failure modes of the SP-4L90-I beam.....	55
Figure 3-13: Crack patterns and failure modes of the SP-3L45-I beam.....	56
Figure 3-14: Crack patterns and failure modes of the 7S-R-I beam.....	56
Figure 3-15: Geometry and reinforcement arrangement of the concrete beams (dimensions in mm).....	57
Figure 3-16: Position of the CFRP laminates of the HCPs in: (a) SP-3L45-II beam, (b) SP-5L45-II beam, (c) a section of the strengthened beam with HCP (dimensions in mm).....	59
Figure 3-17: Position of the CFRP laminates and mechanical anchors (a) SP-3L45-B-II, (b) SP-5L45-B-II, (c) position of the bolts inside of the RC beams (dimensions in mm).....	60
Figure 3-18: Monitoring system- position of the: (a) LVDTs, and (b) strain gages in CFRP laminates (dimensions in mm).....	61
Figure 3-19: (a) Force vs. deflection at the loaded-section, (b) $\Delta F / F^{NSM-3L45-II}$ vs. deflection at the loaded-section for the beams strengthened with SHCC/HCPs, and (c) $\Delta F / F^{SP-II}$ vs. deflection at the loaded-section for the beams strengthened with HCPs.....	64
Figure 3-20: Crack patterns and failure modes of the C-R-II beam.....	65
Figure 3-21: Crack patterns and failure modes of the 7S-R-II beam.....	66
Figure 3-22: Crack patterns and failure modes of the NSM-3L45-II beam.....	67
Figure 3-23: The mode of failure of an NSM CFRP laminate subjected to an imposed end slip (Bianco et al. 2010).....	67
Figure 3-24: Force vs. strain in monitored laminates in SGs where the maximum strains were registered.....	68
Figure 3-25: Crack patterns and failure modes of the SP-II beam.....	69
Figure 3-26: Crack patterns and failure modes of the SP-3L45-II beam.....	70
Figure 3-27: Final crack pattern of the SP-3L45-B-II beam.....	71
Figure 3-28: Final crack pattern of the SP-5L45-II beam.....	71
Figure 3-29: Crack patterns and failure modes of the SP-5L45-B-II beam.....	72
Figure 3-30: Geometry of the repaired beams.....	74
Figure 3-31: Load-deflection at loaded section (a) rectangular cross section, and (b) T cross section beams.....	75

Figure 3-32: Final crack pattern of R-SP-3L45-III beam	77
Figure 3-33: Final crack pattern of the SP-5L45-III beam	78
Figure 3-34: Final crack pattern of the R-SP-5L45-III beam	79
Figure 4-1: Crack stress components (Ventura-Gouveia et al. 2008).....	83
Figure 4-2: Tri-linear stress-strain diagram to simulate the fracture mode I crack propagation (Barros et al. 2013)	85
Figure 4-3: Diagrams to simulate the relationship between the crack shear stress and crack shear strain component, and possible shear crack statuses (Barros et al. 2013)	86
Figure 4-4: General information about the beams of the experimental program (dimensions in mm) (Barros et al. 2013).....	88
Figure 4-5: Finite element mesh of the beam 2S-4LI45 (dimensions in mm) (Barros et al. 2013).....	89
Figure 4-6: Uniaxial constitutive model for the steel bars (Barros et al. 2013)	90
Figure 4-7: Comparison between experimental and numerical force vs. deflection at the loaded section relationships	91
Figure 4-8: Crack patterns of the beams (in pink color: crack completely open; in red color: crack in the opening process; in cyan color: crack in the reopening process; in green color: crack in the closing process; in blue color: closed crack).....	93
Figure 4-9: Geometry, mesh and support condition of C-R-I beam (dimensions in mm)	96
Figure 4-10: Comparison between experimental and numerical force vs. deflection at the loaded section relationships	97
Figure 4-11: Crack patterns of the beams.....	98
Figure 4-12: Finite element mesh of the C-R-II beam (dimensions in mm)	100
Figure 4-13: Comparison between experimental and numerical force vs. deflection at the loaded section relationships	102
Figure 4-14: Crack patterns of the beams.....	103
Figure 4-15: Comparison between experimental and numerical force vs. deflection at the loaded section relationships	105
Figure 4-16: Crack patterns of the beams.....	106
Figure 4-17: Strengthening scheme of the specimens (dimensions in mm).....	107

Figure 4-18: Influence of inclination and percentage of the CFRP laminates on the relationship between the force and the deflection at loaded section	109
Figure 4-19: Influence of inclination and percentage of the CFRP laminates on the crack patterns.....	109
Figure 4-20: Influence of through bolts on the relationship between the force and the deflection at loaded section	111
Figure 4-21: Influence of through bolts on the failure of the beams	112
Figure 4-22: Influence of Shear and Flexural strengthening of the RC beams on the relationship between load and deflection	113
Figure 4-23: Influence of Shear and Flexural strengthening of the RC beams on the crack patterns	114
Figure 4-24: Influence of SHCC instead of mortar on the relationship between the force and the deflection at loaded section.....	115
Figure 4-25: Influence of mortar instead of SHCC on the crack patterns at ultimate load of the strengthened beam with mortar plates.....	115
Figure 4-26: Influence of concrete confinement on the relationship between the force and the deflection at loaded section.....	116
Figure 4-27: Influence of the torque level applied on the mechanical bolts on the crack patterns at the ultimate load of the beam with the lowest torque level (SP-5L45-T10).....	117
Figure 5-1: Concept of Iosipescu Shear Test	119
Figure 5-2: Different mode II test setups: (a) Pure shear panel test (Collins and Mitchell 1991); (b) Double-Edge Notched compression (Reinhardt et al. 1997); (c) Axisymmetric shear specimen according to Tada et al. (1985); (d) short beam shear test (ASTM 2000)	121
Figure 5-3: Shear force and moment diagram for Ohno shear beam test.....	121
Figure 5-4: Internal force and bending moment in Iosipescu specimen.....	122
Figure 5-5: Single notch specimen	123
Figure 5-6: Comparison between (a) Ohno shear beam test and (b) Iosipescu shear test (Krishnan et al. 2009).....	123
Figure 5-7: Developed Iosipescu fixtures and specimens (Ho et al. 1993).....	124
Figure 5-8: Developed Iosipescu fixture and specimen at university of Minho	125
Figure 5-9: The position of the LVDT to measure sliding of the shear crack at notched section	126
Figure 5-10: The envelope and average stress vs. crack sliding	127
Figure 5-11: Typical crack patterns Iosipescu specimens tested	127

Figure 5-12: Crack pattern of one specimen at different phase	128
Figure 5-13: Finite element mesh of the Iosipescu specimen	130
Figure 5-14: Comparison between experimental and numerical average shear stress vs. sliding relationship ...	130
Figure 5-15: Crack patterns of the specimens	130
Figure 5-16: Influence of shear retention factor on average shear stress	132
Figure 5-17: Representation of the crack shear stress-crack shear strain diagram for the β equal to 0.1, 0.5 and 0.9	132
Figure 5-18: Influence of using the crack shear softening diagram vs. shear retention factor with $P_1 = 3$	133
Figure 5-19: Influence of using the crack shear softening diagram vs. shear retention factor with $P_1 = 3$ on crack pattern	133
Figure 5-20: A comparison between SHCC and Plain Cementitious Material (PCM) on shear stress	134
Figure 5-21: Influence of PCM instead of SHCC on the crack patterns	134
Figure 5-22: Normalized shear stress variation along pure shear section for different notch tip radius	136
Figure 5-23: Shear stress distribution for different notch tip radius (dark blue: maximum shear stress, and light blue minimum shear stress)	136
Figure 5-24: Influence of notch tip radius on shear stress-sliding relationship.....	136
Figure 5-25: Shear stress distribution and crack pattern of specimens with different radius at different stages (in pink color: crack completely open; in red color: crack in the opening process; in cyan color: crack in the reopening process; in green color: crack in the closing process; in blue color: closed crack).....	137
Figure 6-1: Truss models (Brown et al. 2005)	142
Figure 6-2: Equilibrium conditions for a truss of 45° angle (Collins and Mitchell 1991)	142
Figure 6-3: Mohr's circle for average strain	144
Figure 6-4: (a) test setup used to apply shear and normal stress (Vecchio and Collins 1986), (b) one specimen under loading (ACI-ASCE Committee 445 1999).....	145
Figure 6-5: Comparison principal stress and principal strain (Vecchio and Collins 1986)	145
Figure 6-6: Stress- strain relationship for cracked concrete.....	146
Figure 6-7: Average stress-strain relationship for cracked concrete in tension (Collinset al. 1996).....	147
Figure 6-8: Principal stresses in concrete and variation of tensile stresses in the compressive struts.....	149
Figure 6-9: Force transmission a) across the crack, b) between the cracks (Collins et al. 1996)	150
Figure 6-10: Crack spacing in reinforced concrete (Duthinh and Carino 1996)	151

Figure 6-11: Equations of modified compression field theory	152
Figure 6-12: Parameters influencing crack (Collins and Mitchell 1991, Kuchma et al. 2008)	154
Figure 6-13: Transmission of forces across cracks	157
Figure 6-14: Determination of β and θ values for element without transverse reinforcement (Bentz et al. 2006).....	159
Figure 6-15: Comparison of values for θ given by simple equations with values determined from MCFT for elements with and without transverse reinforcement (Bentz et al. 2006).....	160
Figure 6-16: Comparison of values for β given by simple equations with values determined from MCFT for elements with and without transverse reinforcement (Bentz et al. 2006).....	161
Figure 6-17: Definition of l_{net} , l_b , l_{max} (Nanni et al. 2004).....	165
Figure 6-18: Representation of l_{max} (Nanni et al. 2004).....	165
Figure 6-19: Schematic representation of the Bianco et al. (2014) model	167
Figure 6-20: Ratio between experimental and predicted shear resistance.....	179
Figure 6-21: Predicted non-dimensional failure shear force of the beams, in compression with experimental values.....	180
Figure 6-22: Ratio between experimental and predicted results of the beams strengthened with HCPs	183

Contents of Tables

Table 2-1: Details and results of the continuous RC beams (Khalifa et al. 1999)	14
Table 2-2: Details and results of the T cross section RC beams (Khalifa and Nanni 2000).....	15
Table 2-3: Details and results of the beams (Alzoubi et al. 2007).....	16
Table 2-4: Main results of the tested beams (Barros and Dias 2003).....	17
Table 2-5: Details and results of the tested beams (De Lorenzis and Nanni 2001)	20
Table 2-6: Details and results of the tested beams (Rizzo and De Lorenzis 2009).....	22
Table 2-7: Details and results of the tested beams (Dias and Barros 2010).....	23
Table 2-8: Details and results of the tested beams (Barros and Dias 2013).....	25
Table 2-9: The main results of the experimental program (Chaallal et al. 2011).....	28
Table 2-10: General information and corresponding results of the tested beams (Barros and Dalfre 2013)	30
Table 2-11: General information and corresponding results of the tested beams (Breveglieri et al. 2014)	31
Table 2-12: Mix and material properties of CARDIFRC Mix I and Mix II (Maheri et al. 2004)	33
Table 2-13: Details and main results of the tested beams (Maheri et al. 2004)	35
Table 2-14: Specimens characteristics (Mostosi et al. 2011).....	36
Table 2-15: Shear strengthening schemes and beam's geometry and reinforcement (dimensions in mm) (Esmaeeli et al. 2013a).....	37
Table 2-16: Details and results of the tested beams (Ruano et al. 2014).....	39
Table 3-1: Shear strengthening/reinforcement configurations applied in the L_i beam's shear span of the tested beams.....	45
Table 3-2: SHCC mix procedure (Esmaeeli et al. 2013b)	47
Table 3-3: SHCC mix proportions based on the weight ratio percentage (Esmaeeli et al. 2013b)	47
Table 3-4: Material properties	48
Table 3-5: Relevant results in terms of load and deflection capacity	50
Table 3-6: Shear strengthening/reinforcement in the monitored shear span of the tested beams	58
Table 3-7: Values of the properties of intervening materials.....	61
Table 3-8: Relevant results in terms of load and deflection capacity	63
Table 3-9: Shear strengthening/reinforcement in the monitored shear span of the tested beams	73
Table 3-10: Relevant results in terms of load and deflection capacity	76
Table 4-1: Values of the parameters of the constitutive model for the concrete.....	89

Table 4-2: Values of the parameters of the steel constitutive model (Barros et al. 2013)	90
Table 4-3: Properties of CFRP laminates	91
Table 4-4: Values of the parameters of the constitutive model for the concrete	95
Table 4-5: Values of the parameters of the constitutive model for the SHCC	95
Table 4-6: Values of the parameters of the steel constitutive model	96
Table 4-7: Values of the parameters of the constitutive model for the concrete	99
Table 4-8: Values of the parameters of the constitutive model for the SHCC	99
Table 4-9: Values of the parameters of the steel constitutive model	101
Table 5-1: Values of the properties of SHCC materials.....	125
Table 5-2: Values of the parameters of the SHCC constitutive model.....	129
Table 6-1: Summary of experimental and analytical results.....	175
Table 6-2: Average and Standard Deviation of $F_{exp} / F_{prediction}$ for different approaches	179
Table 6-3: Analytical vs. experimental results of the strengthened and repaired beams with HCPs	182
Table 6-4: Average, Standard Deviation, and coefficient of variation of all the tested beams.....	182
Table 6-5: Average, Standard Deviation, and coefficient of variation of the strengthened beams with HCPs...	183

Chapter 1

Introduction

There is a great need for upgrading Reinforced Concrete (RC) structures all over the world in order to carry higher ultimate loads or to satisfy certain serviceability requirements. One of the strengthening methods that have been applied in the last three decades includes the external bonding of thin steel plates to tensile or shear regions of the RC members using an epoxy adhesive or mechanical anchors. However, there are two major disadvantages of this method: difficulty to manipulate the steel plates at the construction site due to their weight, and also durability debilities associated with a reduction in the bond between steel plates surface and adhesive, or even the susceptibility of the steel plates to corrosion (Abdel-Jaber et al. 2003; Saafan 2006).

Fiber reinforced polymer (FRP) composite materials are regarded as an alternative for externally bonded steel plates, by adopting externally bonded reinforcement (EBR) technique (Abdel-Jaber et al. 2003; Saafan 2006). Numerous research studies have been carried out to evaluate the efficiency of the EBR technique to increase the flexural and shear strength of RC members (Khalifa et al. 1998; Abdel-Jaber et al. 2003). However, this technique has some issues that can compromise its strengthening effectiveness, such as: debonding of the FRP, lack of protection (vandalism and fire), preparation of the surface, and stress concentration caused by anchorage devices when used for avoiding the premature debonding of the FRP.

The Near Surface Mounted (NSM) FRP laminates/rods is another strengthening technique that has been used to increase the shear capacity of RC beams (Nanni et al. 2004, Dias and Barros 2013). In this method, carbon fiber reinforced polymer (CFRP) laminates/rods are embedded into grooves open on the concrete cover using an adhesive. Research has shown that a significant increase in the shear resistance of RC beams is reachable using the NSM CFRP technique (De Lorenzis and Nanni 2001, Dias and Barros 2010, Rezazadeh et al. 2014). However, debonding of the FRP laminates/rods and/or fracture of concrete surrounding these composites are still inevitable, which limit their strengthening potential.

Strain Hardening Cementitious Composite (SHCC) is a class of fiber reinforced cement composites (FRCC) that exhibits ductile behavior under tensile load, with a strain hardening response rather than the tension softening character presented by conventional fiber reinforced cement composites (FRCC) after crack initiation (Li 1998). In recent years, SHCC

has been used for developing new construction systems and for the structural rehabilitation, since this type of materials exhibits ductile shear response, high energy absorption capacity, and stable hysteretic loops even at large drifts (Parra-Montesinos and Wight 2000, Esmaeeli et al. 2015).

In this present work, thin plates of SHCC strengthened with CFRP laminates according to the NSM technique are used to increase the shear capacity of RC beams. This strengthening technique is called Hybrid Composite Plate (HCP). Due to the excellent bond conditions between SHCC and CFRP laminates, these reinforcements provide the necessary tensile strength capacity to the HCP, while the high post-cracking tensile deformability and resistance of SHCC avoids the occurrence of premature fracture failure of this cement composite in the stress transfer process between these two materials when the HCP is crossed by a shear crack. To bond the CFRP laminates into the SHCC plate, slits are opened on the surface of the plate and CFRP laminates are inserted into these slits and bonded to the surrounding SHCC with an appropriate epoxy adhesive. The HCPs are bonded to the lateral faces of the beams using epoxy adhesive, and mechanical anchors can also be used (Figure 1-1). The mechanical anchors are used to prevent a premature debonding of the HCPs due to the relatively low tensile strength of the concrete substrate of the strengthened beams. Furthermore, by installing the mechanical bolts with a certain prestress (controlled by the applied torque) some confinement can be introduced to the concrete in the zone of the beam to be strengthened, resulting favorable effects in terms of shear strengthening.

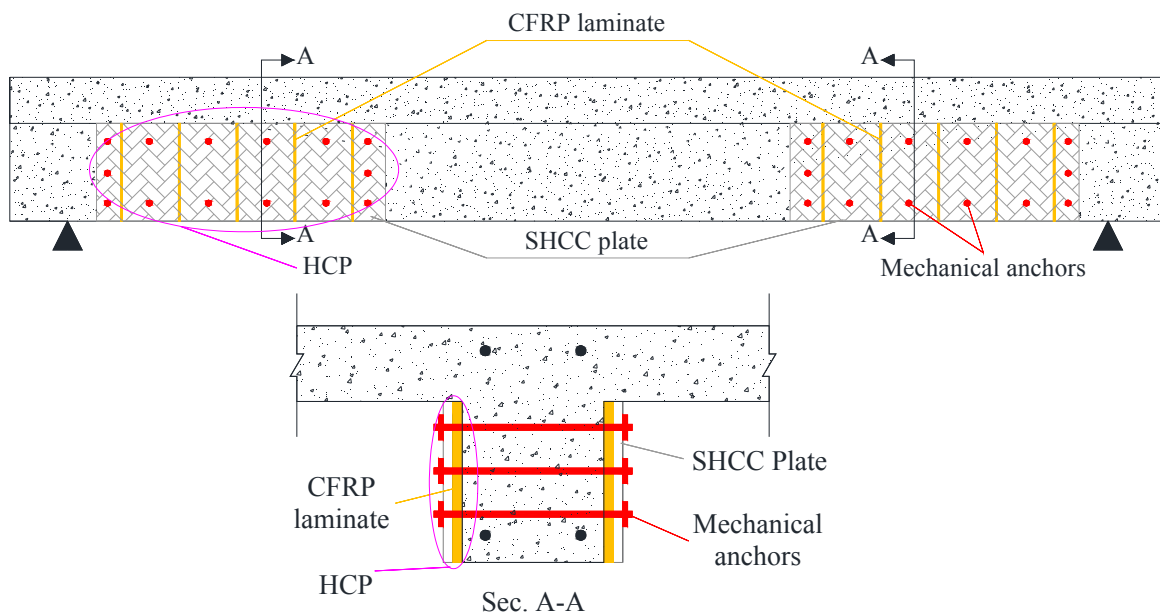


Figure 1-1: Hybrid shear strengthening technique for RC beams

Besides the contribution of the SHCC for the strengthening efficiency of HCPs, the SHCC also assures some protection to the CFRP laminates and adhesive in terms of vandalism, aggressive environmental conditions, and fire.

The thesis is organized in seven chapters including this introduction:

Chapter 2 provides a review of the available literature about the object of this thesis. In this chapter the fundamentals of shear for RC beams, and the different shear strengthening techniques are presented and discussed.

Chapter 3 presents the experimental program carried out to investigate the effectiveness of HCPs for the shear strengthening of RC beams. The experimental program is described in detail, and the obtained results are presented and discussed. The results include the failure modes, and the load-deflection response of the tested beams, as well as the strain field developed in the CFRP laminates during the load process.

In chapter 4, a brief description of the multi-directional fixed smeared crack model used to simulate the experimentally tested beams is given. This model, available in FEMIX computer program, is specially dedicated to simulate RC elements failing in shear, since it includes a constitutive law for the smeared cracks for simulating not only the fracture mode I softening behavior, but also the shear softening. After has been demonstrated that this model is capable of predicting with high accuracy the relevant behavioral aspects of the tested beams, an extensive parametric study is carried out for assessing the influence of some particularities of the adopted shear strengthening systems on their strengthening effectiveness for RC beams.

In Chapter 5, the shear behavior of the SHCC is investigated by Iosipescu shear test method. The experimental program is detailed and the obtained results are presented and discussed. For better understanding the shear behavior of SHCC, numerical simulations and parametric studies are carried out.

In chapter 6, two prominent models that are used to predict the shear capacity of RC beams are presented: Truss Model (TM) and Modified Compression Field Theory (MCFT). Based on the MCFT, a new formulation is proposed to predict the shear capacity of RC beams strengthened with HCPs.

Finally in chapter 7, the relevant achievements of the research activities carried out are presented, and recommendations for future work are provided.

Chapter 2

An Overview on the Shear Strengthening of the Reinforced Concrete Beams

2.1 Introduction

Reinforced Concrete (RC) structures often require repair and strengthening due to alterations on the load or support conditions, deterioration of the materials, or structural damage caused by earthquake or extreme loading events. Externally bonded steel plates, fiber reinforced polymer, and reinforced concrete layers are some of the many techniques presently available. The following study of existing literature will focus on shear strengthening and retrofitting of RC beams. It includes a review of two different materials for strengthening of concrete structures Fiber Reinforced Polymer (FRP) and Fiber Reinforced Concrete (FRC).

2.2 Fundamental Concepts of Shear

Despite of vast efforts to calculate the shear strength of concrete members over the last 100 years, there is no fully accepted physical model that describes shear failure. The reason is that shear is a complex mechanism and it depends on many factors such as dowel effect of the flexural reinforcing bars, internal friction due to interlock of aggregates, and contribution of compressive struts formed during the loading process of a beam failing in shear (Halim et al. 2011).

2.2.1 Crack development

A crack forms in the direction that requires the minimum amount of energy for concrete fracture (Carolin and Täljsten 2005). When a simply support beam is subjected to uniformly distributed load, three types of cracks are identified:

- Flexural cracks: They form in the tensile zone near the mid-span, and have a predominant orientation orthogonal to the axis of the beam, and propagate to the compressive zone of the cross section. These cracks form in the regions that are governed by flexural deformation.

- Flexure-shear cracks: The flexural cracks formed in regions where flexural and shear deformation are both significant.
- Web shear cracks: This type of cracks generally forms near the supports of deep cross section beams with thin webs, in the zones of beam of relatively small bending moments and high shear forces.

Figure 2-1 shows the formation of the type of cracks that can be formed in a beam subjected to uniformly distributed load (ACI Committee 2011).

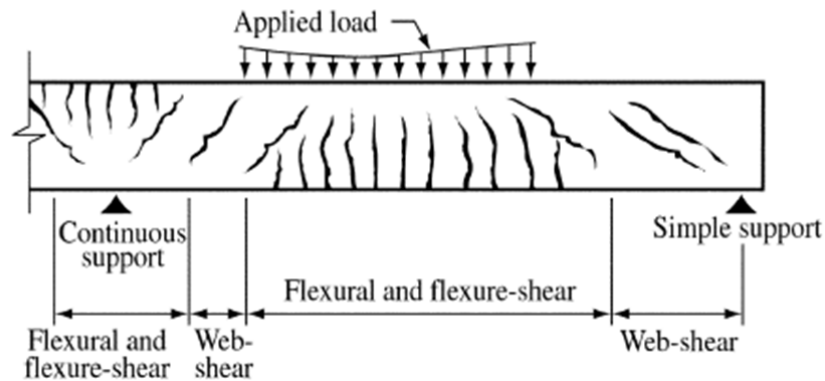


Figure 2-1: Types of cracks in concrete beams subjected to shear and bending moments (ACI Committee 2011)

When a RC beam without shear reinforcement is subjected to shear deformation, the shear is resisted by three main components (Abdel-Jaber et al. 2003) (Figure 2-2):

1. Concrete in compression zone, V_c [20-40%];
2. Internal friction, V_a [35-50%];
3. Dowel effect provided by longitudinal bars, V_d [35-50%];

In an uncracked region of a concrete beam with a shear span (a) to effective depth (d) ratio (a/d , see Figure 2-4) less than 2.5, the shear force is transferred by inclined compressive struts to the supports, and orthogonally to the struts are developed tensile strains that justify the occurrence of inclined cracks in this region. In cracked regions of the member, the behavior of the concrete between cracks is still governed by the continuous mechanics, as well as the behavior of the uncracked concrete in the compression zone. The integration of the shear stresses over the depth of the compression zone gives a shear force component, which is generally considered as the concrete contribution for the shear resistance (ACI-ASCE Committee 445 1999).

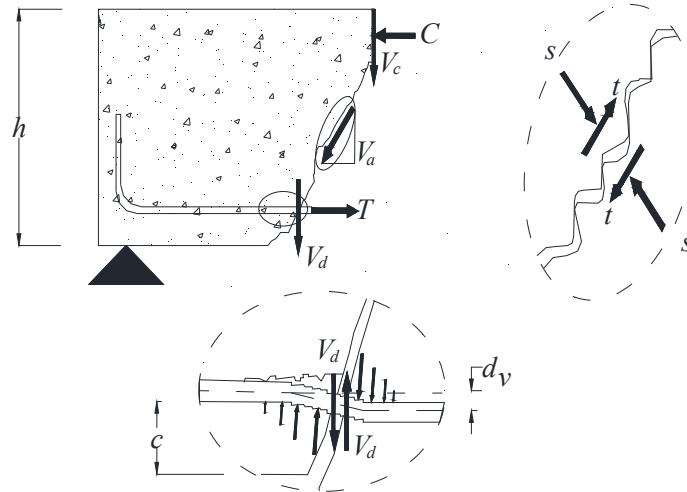


Figure 2-2: Components of shear resistance for concrete cracked without shear reinforcement

Shear transfer mechanism in the crack surface of a concrete beam is due to aggregate interlock effect. The physical explanation for aggregate interlock is that aggregates protruding from the crack surface provide resistance against slip of the both faces of a crack (ACI-ASCE Committee 445 1999). As shown in Figure 2-3, the crack in high-strength concrete ($f'_c \geq 70MPa$) progresses through rather than around aggregates, and this type of crack has a smooth surface with relatively small aggregate interlocking shear resisting mechanism.

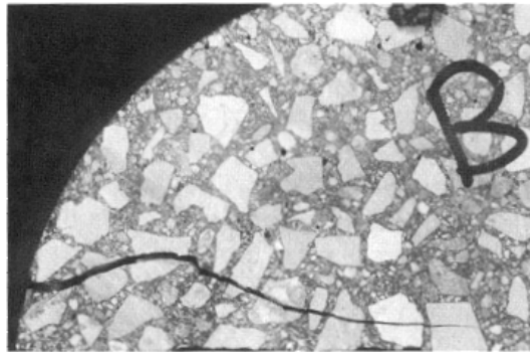


Figure 2-3: Crack in high strength concrete

Dowel effect is not significant in concrete beams without transverse reinforcement, because the shear resisting mechanism due to dowel effect becomes limited by the tensile strength of concrete cover in the zone where the shear crack crosses the longitudinal tensile bars (ACI-ASCE Committee 445 1999). However, in concrete beams with high percentage of longitudinal bars of relatively large diameter, particularly when bars are arranged in more

than one layer, the dowel action may be significant, since this arrangement can form a stiff internal member.

2.2.2 Shear failure modes of concrete beams

Web compressive failure: during the loading process of a RC beam susceptible to shear failure, diagonal compressive struts are formed (Figure 2-4) that can fail by concrete crushing. This type of failure generally occurs in RC beams over reinforced in shear, and is of brittle nature since concrete crushing occurs before yielding of the shear reinforcement.

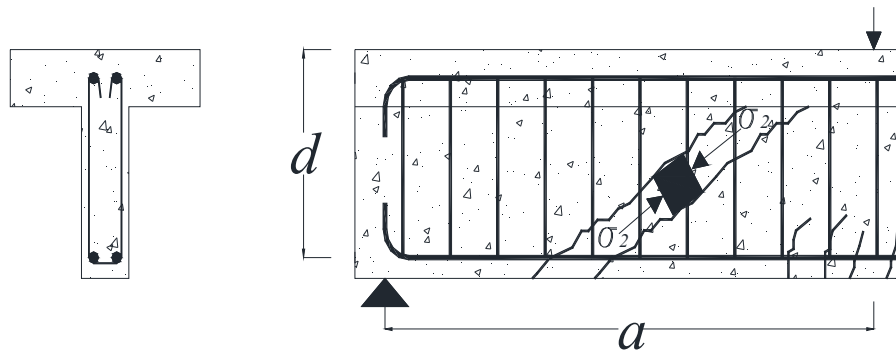


Figure 2-4: Shear failure due to concrete crushing in the web region

Web shear failure: It forms near the support areas of the beam where relatively small bending moments and high shear forces are installed. This type of failure is predominant in RC beams without transverse reinforcement (Figure 2-5). It occurs when the principal tensile stress reaches the concrete tensile strength, and diagonal shear crack is formed. The load at this occurrence coincides with load carrying capacity of the beam. If the beam has transverse reinforcement, the load can increase after the occurrence of web shear cracks due to the resisting contribution of the stirrups crossing this type of cracks (Blanksvärd 2009, ACI Committee 2011).

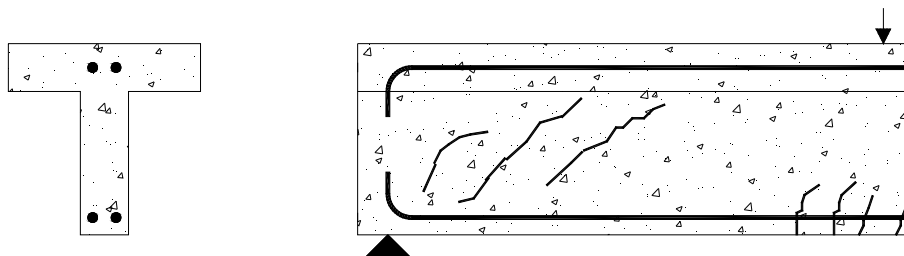


Figure 2-5: Web shear failure

Flexural-shear failure: in this type of failure, cracks form in the tension region of beams, and propagate diagonally toward the compression zone of the concrete member (Figure 2-6). A flexural-shear failure is characterized by the yielding initiation of the longitudinal bars, crossing the crack (Figure 2-2). It is followed by the occurrence of the shear failure, since due to the hardening nature and dowel effect of the longitudinal steel bars, the load continues to increase moderately, and finally the flexural crack degenerates in a critical flexural-shear crack.

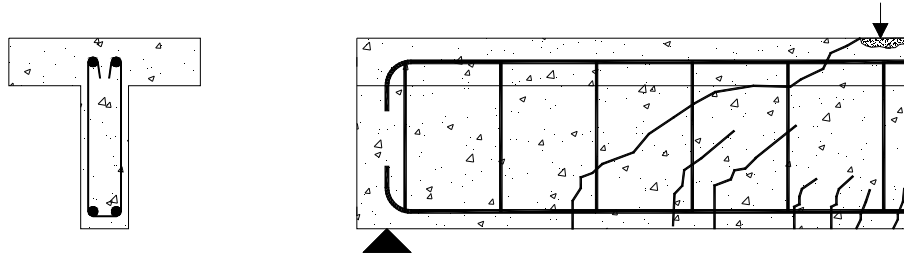


Figure 2-6: Flexural-shear failure

2.3 Fiber Reinforced Polymer for Shear Strengthening

Bonding steel plate to the tension zones of concrete members with adhesive resins was shown to be a workable technique for increasing the shear and flexural strengths of RC beams. Many buildings and bridges have been strengthened by this technique. Because steel plates can corrode, leading to a deterioration of their bond to the concrete substrate, and due to the difficulty of their installation, which requires the use of heavy equipment, researchers have started using FRP materials as an alternative to steel plates (ACI Committee 440 2000). The use of FRP composites for strengthening RC structures was first studied at Swiss Federal Laboratory for Material Testing and Research (EMPA). Since then, many research studies in flexural and shear strengthening of RC structures have been carried out, particularly in USA, Japan, and Europe (ACI Committee 440 2000). FRP composites consist of high strength fibers embedded in a polymer resin. The fibers are the main constituent to carry the load and have a wide range of strength and stiffness. Continuous Glass (GFRP), Aramid (AFRP), and Carbon (CFRP) fibers are common reinforcements used with FRP composites. A comparison among CFRP, GFRP, AFRP, and steel bars in terms of stress-strain relationship is illustrated in Figure 2-7.

Some advantages of FRP reinforcement are as follows (Sena-Cruz 2004):

- Light weight
- Corrosion resistance
- High longitudinal resistance
- Electromagnetic transparency

And some disadvantages of FRP reinforcement are as follows (Alnatit 2011):

- No yielding before rupture
- Abrupt degradation of properties under high temperatures
- Low transverse strength
- Low modulus of elasticity (a part carbon FRP)
- Low durability of glass fibers in a moist environment
- Low durability of some glass and aramid fibers in an alkaline environment

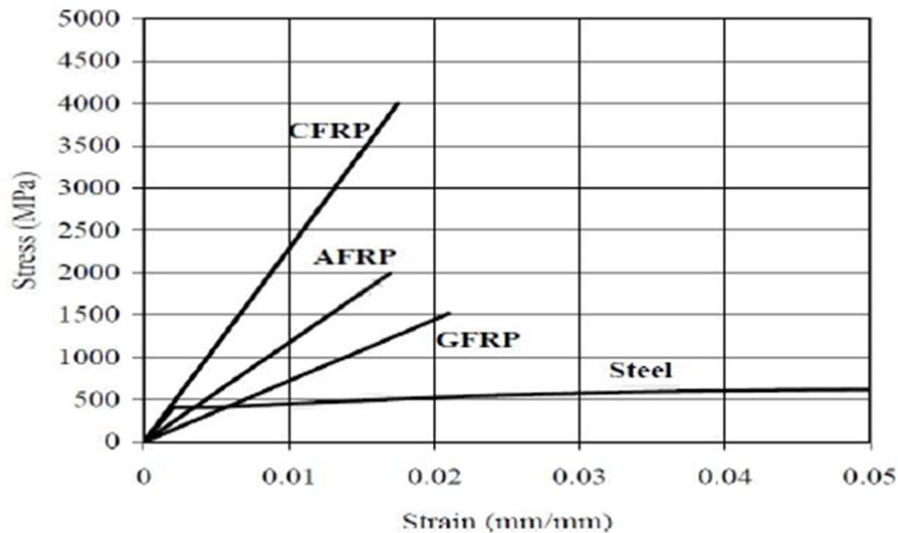


Figure 2-7: A comparison among CFRP, GFRP, AFRP, and steel in term of stress strain relationship (Alnatit 2011)

Recently, application of CFRP have attracted special attention of researchers for shear strengthening of RC structures according to Externally Bonded Reinforcement (EBR), Near Surface Mounted (NSM), and Embedded Through Section (ETS) techniques.

A literature review on the shear strengthening of RC beams with aforementioned techniques is provided in the following sections.

2.3.1 Externally Bonded Reinforcement

Common shear strengthening configurations of this technique include: (a) side bonding, (b) U-wrapping, and (c) fully wrapping (Figure 2-8) (ACI Committee 440 2000).

The following procedures are used in the application of the EBR technique:

1. The cement past is removed by sandblast or emery;
2. The edges of the beams must be rounded in U-wrapping and fully wrapping to prevent stress concentration in the FRP regions at the corners of the beam's cross section;
3. The concrete surface and FRP sheets are cleaned;
4. The surface of concrete and FRP sheets are saturated by an appropriate epoxy adhesive;
5. FRP sheets are fixed to the surface of the concrete beams.

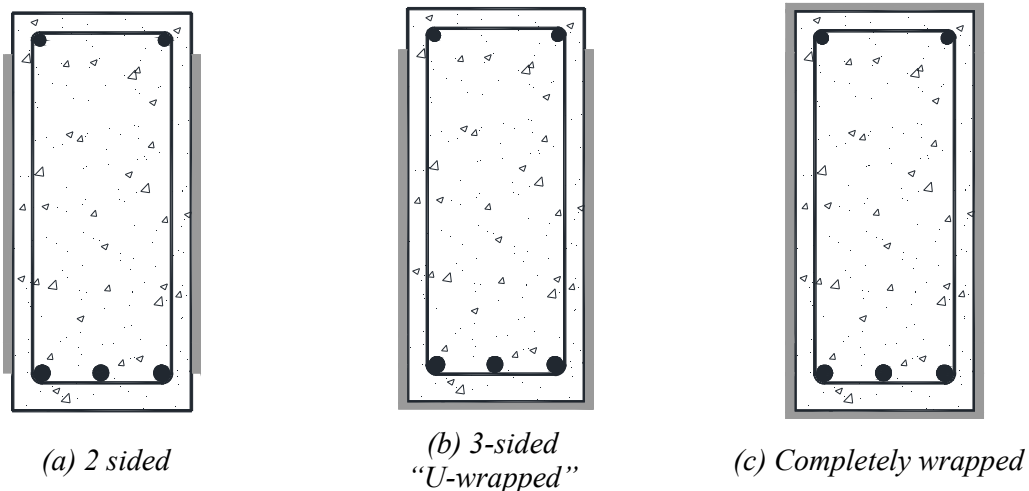


Figure 2-8: Typical wrapping schemes for shear strengthening using FRP sheets or strips (ACI Committee 440 2000)

The curing time of the adhesive, indicated by supplier, must be respected before submitting the strengthened element to the work loading conditions.

Khalifa and his co-workers investigated the performance of two-span continuous RC beams (Figure 2-9 and Figure 2-10) (Khalifa et al. 1999) and T cross section RC beams (Figure 2-11 and Figure 2-12) (Khalifa and Nanni 2000) strengthened in shear with externally bonded carbon fiber reinforced polymer sheets (CFRP). In these experimental programs the shear behavior of the strengthened beams with CFRP sheets were investigated by considering the following variables: CFRP amount (sheet or strip), 90°/0° ply combination, configuration of the CFRP sheets (such as wrapping scheme), and also anchorage of the CFRP sheets.

The two-span continuous RC beams were grouped into three series with different longitudinal and transverse reinforcement, and also different concrete compressive strength. Series CW consisted of two beams of $2\phi 32$ as longitudinal reinforcement in top and bottom zones of the beam. The stirrups in the monitored shear span were designed to occur shear failure in this span. The concrete compressive strength of this series was 27.5 MPa.

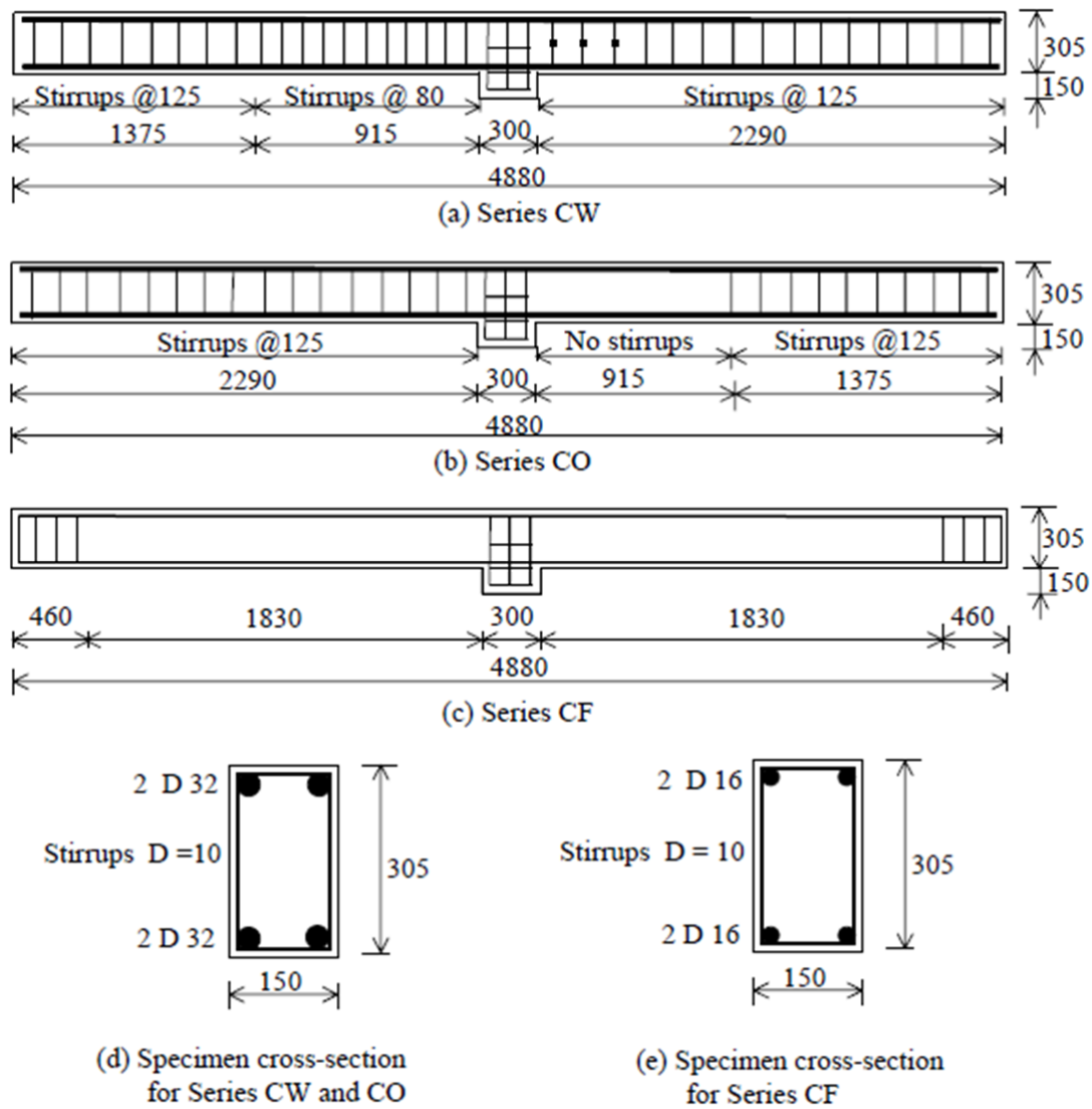


Figure 2-9: Two-span continuous beams (dimensions in mm) (Khalifa et al. 1999)

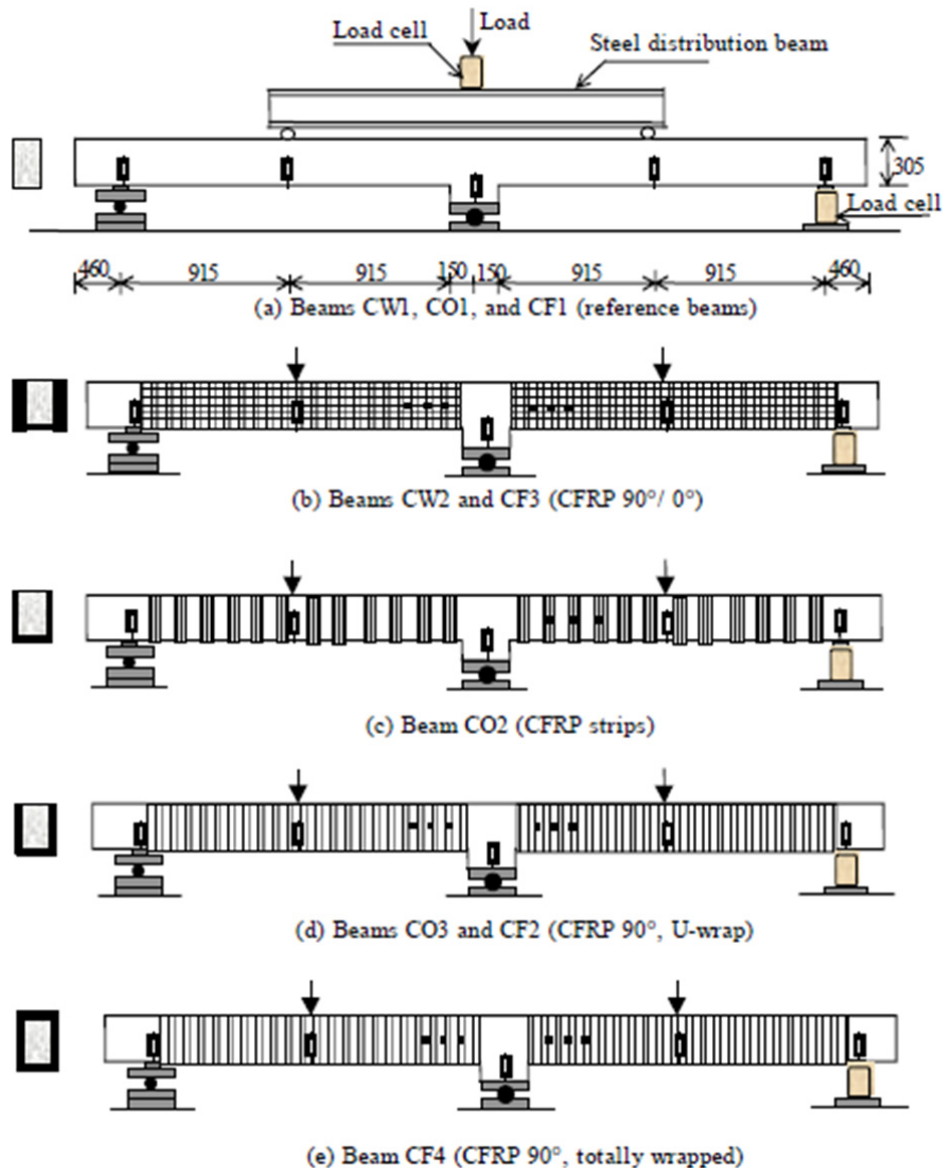
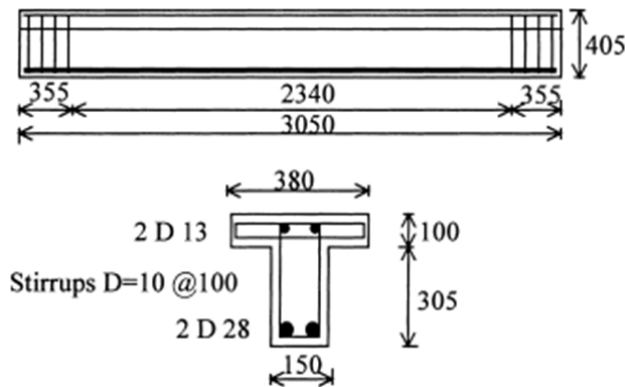


Figure 2-10: Test set-up and strengthening schemes (Khalifa et al. 1999)

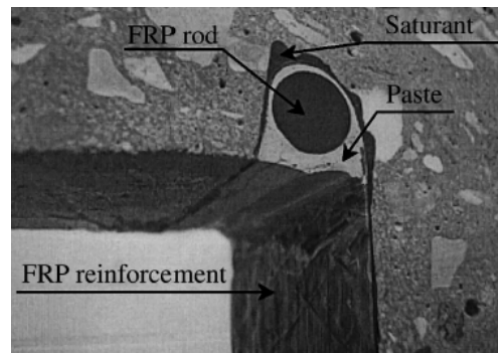
Series CO consisted of three beams with equal longitudinal reinforcement as that of series CW. No steel stirrups were provided in monitored shear span. The concrete compressive strength of this series was 20.5 MPa. And finally series CF consisted of four beams flexurally reinforced with $2\phi 16$ bars at bottom and top zones, with no shear reinforcement. The concrete compressive strength of this series was 50 MPa. Table 2-1 presents the strengthening schemes, ultimate load, and also failure mode of two-span continuous beams.

Table 2-1: Details and results of the continuous RC beams (Khalifa et al. 1999)

Beam designation	Strengthening schemes	Ultimate load (kN)	Failure mode
CW1	-	508	Shear
CW2	The first ply was attached in form of continuous U-wraps (90°), the second ply was bonded to the two sides of the beam (0°)	623	Shear
CO1	-	220	Shear
CO2	Strips in the form of U-wraps	265	CFRP debonding
CO3	Continuous sheets in the form of U-wraps	330	CFRP debonding
CF1	-	268	Shear
CF2	Continuous sheets in the form of U-wraps	337	Flexural
CF3	The first ply was attached in form of continuous U-wraps (90°), the second ply was bonded to the two sides of the beam (0°)	394	Flexural
CF4	Continuous sheets in the form of completely-wraps	400	Flexural



(a) Beams specimens and detailing dimensions



(b) Anchored system used in T cross section beams

Figure 2-11: T cross section beams (dimensions in mm) (Khalifa and Nanni 2000)

The strengthening schemes, ultimate load, and failure mode of the T cross section beams are presented in Table 2-2.

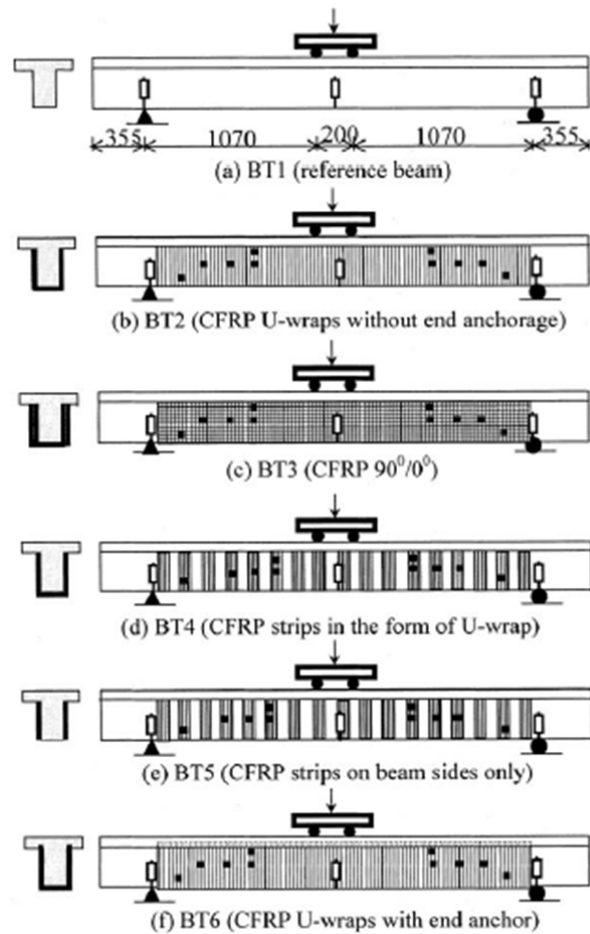


Figure 2-12: Test setup and strengthening schemes (Khalifa and Nanni 2000)

Table 2-2: Details and results of the T cross section RC beams (Khalifa and Nanni 2000)

<i>Beam designation</i>	<i>Strengthening schemes</i>	<i>Ultimate load (kN)</i>	<i>Failure mode</i>
<i>BT1</i>	-	180	Shear
<i>BT2</i>	Continuous sheets in the form of U-wraps	310	CFRP debonding
<i>BT3</i>	Two plies (90°/0°)	314	CFRP debonding
<i>BT4</i>	Strips in the form of U-wraps	324	CFRP debonding
<i>BT5</i>	Strips on the two beam sides only	242	CFRP debonding
<i>BT6</i>	Continuous U-wraps with end anchor	442	Flexural

Based on the results, the authors concluded:

- EBR technique can be used to increase the shear capacity of RC beams in both positive and negative moment regions.

- The proposed anchor system can be very effective in strengthening configurations where bonded/or development length of FRP is critical, i.e. premature debonding of the CFRP has tendency to occur.
- Applying CFRP sheets in U-wrap scheme is more effective than applying CFRP sheets on the beam's lateral sides.
- The contribution of the CFRP was decreased by increasing the percentage of existing steel stirrups.

Shear strengthening of pre-damaged RC beams with CFRP strips was studied by Alzoubi et al. (2007). The experimental program included four rectangular beams (Figure 2-13).

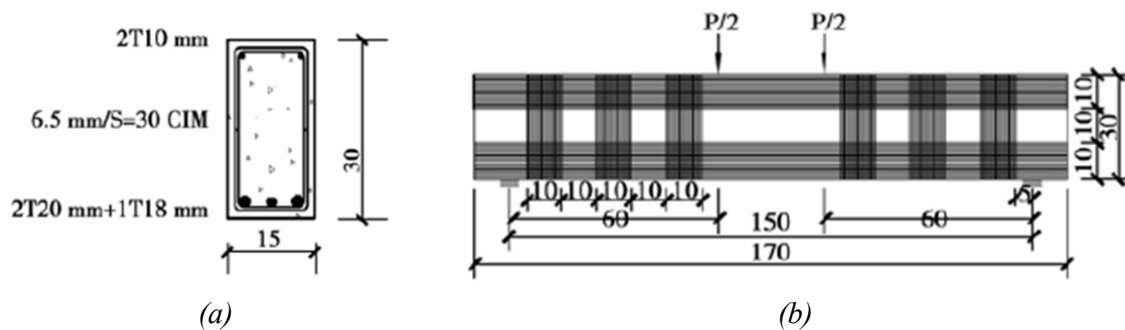


Figure 2-13: (a) longitudinal reinforcement, (b) strengthening scheme (dimensions in cm) (Alzoubi et al. 2007)

B1 was control beam and B2 was a beam without pre-damaged and strengthened with EBR technique to upgrade its shear capacity. Two beams were damaged up to 50% (B3) and 89% (B4) of ultimate load carrying capacity of the control beam (B1), and then fully unloaded. These last two beams were repaired and strengthened with EBR technique. After have been repaired, the beams were loaded up to failure. Table 2-3 represents the details and results of the tested beams. The strengthened and repaired beams failed in shear with debonding of the CFRP strips, which means that the full tensile capacity of the FRP was not mobilized

Table 2-3: Details and results of the beams (Alzoubi et al. 2007)

Beam designation	Percentage of damaged (%)	Ultimate load (kN)	Deflection at ultimate load (mm)	Failure mode
B1	-	155	0.408	Shear
B2	0	235	0.610	Debonding of the CFRP
B3	50	230	0.689	Debonding of the CFRP
B4	89	225	0.695	Debonding of the CFRP

Barros and Dias (2003) investigated the strengthening effectiveness of EBR strips of CFRP sheet (U-wrapped) and laminate strips of CFRP embedded into the slits made on the lateral surface of the concrete beams (NSM technique). Figure 2-14 shows the details of the beams.

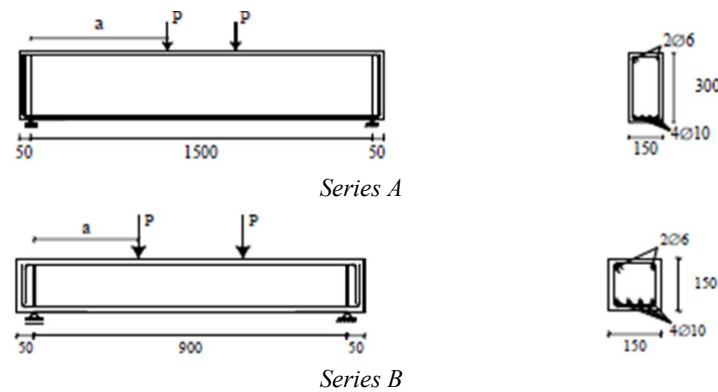


Figure 2-14: Details of the control beams (dimensions in mm) (Barros and Dias 2003)

The details and results of the strengthened beams are presented in Table 2-4.

Table 2-4: Main results of the tested beams (Barros and Dias 2003)

	Concrete Compressive strength (MPa)	Beam designation	Shear reinforcing system	Ultimate load (kN)	Deflection at peak load (mm)
Beams Series A	37.6MPa	VAI0	-	100	2.8
		VAE-30	Stirrups (300mm spacing)	169	16.2
		VAM-19	Strips CFRP sheet (190mm spacing)	122	3.8
		VACV-20	Vertical CFRP Laminate (200mm spacing)	158	12.9
		VACI-30	Inclined CFRP Laminate (300mm spacing)	158	31
Beams Series B	49.5MPa	VB10	-	74	2
		VBE-15	Stirrups (150mm spacing)	121	8.5
		VBM-8	Strips CFRP sheet (80mm spacing)	111	4.4
		VBCV-10	Vertical CFRP Laminate (100mm spacing)	131	6.8
		VBCI-15	Inclined CFRP Laminate (150mm spacing)	120	4.3

The results shown the laminate strips of the CFRP were most effective than strips of the CFRP sheets in terms of load carrying capacity, ductility of the beam, and post peak load carrying capacity. In the post-peak stage of the beams reinforced with laminates of the CFRP a very high residual load carrying capacity was sustained up to a relatively large deflection, which was not happened on the beam reinforced with strips of CFRP sheets.

In a study conducted by Mofidi and Chaallal (2011), conceptual modeling of FRP sheets was studied. The experimental observations have shown that in a RC beam with no or low shear reinforcement, the beam failed along a single shear crack line (Figure 2-15a), while in a RC beam with suitable percentage of transverse reinforcement the shear crack pattern tended to be distributed over a large width (Figure 2-15b). The last condition was also true when a RC

beam was strengthened with CFRP sheets, such was the case of the beam in Figure 2-15c that was reinforced with EBR CFRP sheets. The beam failed with one major shear crack and two surface shear crack (in the concrete cover) that joined the major shear crack in the concrete core. This led to debonding of CFRP sheet attached to a large chunk of concrete. On the other hand, a more distributed crack pattern can accelerate premature debonding of the CFRP sheets (Figure 2-15c).



(a) beam without shear reinforcement



(b) beam with shear reinforcement



(c) beam with shear reinforcement and reinforced with EB FRC sheet

Figure 2-15: Effect of shear reinforcement and epoxy-bonded FRP sheets on cracking pattern (Mofidi and Chaallal 2011)

Based on the results in literature (Mofidi and Chaallal 2011, Barros and Dias 2003, Khalifa et al. 1999), debonding of the FRP is the main disadvantage of the EBR technique that avoids the full exploitation of the strengthening potentialities of these materials. However, proper anchoring can prevent/delay premature debonding, as long as special attention is taken to consider the high stress concentrations developed in the anchored zones in order to avoid premature rupture of the FRP (Coelho et al. 2012).

2.3.2 Near Surface Mounted

In this technique slits are opened on the surface of the RC beams, and laminates/rods are inserted into these slits, and bonded to the concrete substrate by using an appropriate epoxy

adhesive (Figure 2-16). Typically, the CFRP laminates have a cross section of about 1.4 mm thick and 10 to 20 mm width, while FRP rods can have a diameter between 8 to 12 mm.

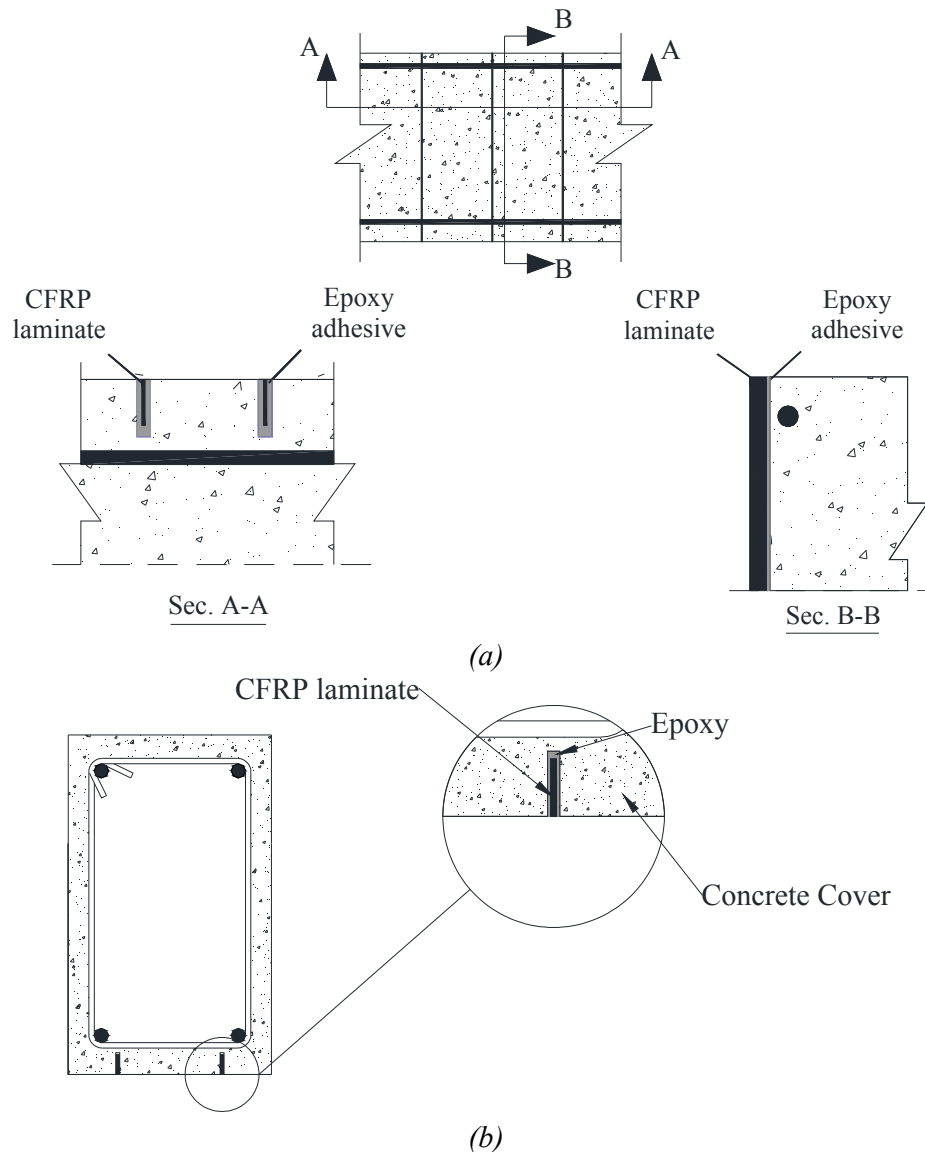


Figure 2-16: Near Surface Mounted FRP laminate to increase the beam (a) shear capacity, (b) bending capacity

The following procedures are used in the application of the NSM technique:

- 1- Slits are opened in the concrete cover using a saw-cut machine;
- 2- The slits and laminates/rods are cleaned by compressed air and appropriate cleaner (acetone for instance), respectively;
- 3- The slits are filled by an appropriate adhesive (epoxy for instance);
- 4- The laminates/rods are inserted into the slits and adhesive in excess is removed.

The adhesive curing time recommended by the supplier should be respected, unless reliable experimental results support other decision.

The first known experiment with NSM in shear strengthening of RC beams was reported by De Lorenzis and Nanni (2001), by using CFRP rods. Figure 2-17 presents the cross section of the eight beams that were tested under four point bending configuration with a shear span ratio (a/d) of 3.

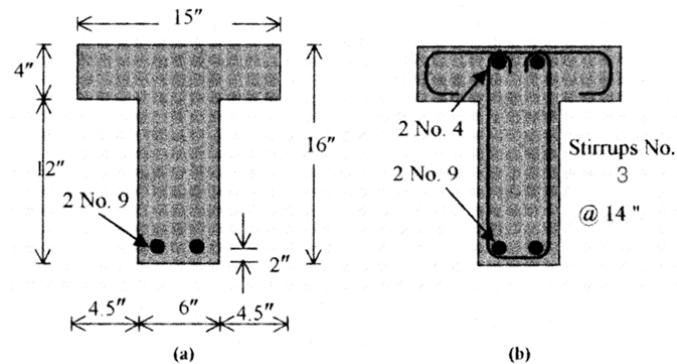


Figure 2-17: Cross section of beams: (a) beams without stirrups, and (b) beams with stirrups (dimensions in inches) (De Lorenzis and Nanni 2001)

Table 2-5 presents details and results of the tested beams.

Table 2-5: Details and results of the tested beams (De Lorenzis and Nanni 2001)

Beam designation	Steel stirrups		NSM FRP rods				Ultimate load (kN)	Failure mode
	Quantity	Spacing (mm)	Quantity	Spacing (mm)	Inclination of the CFRP	Anchorage in flange		
BV	-	-	-	-	-	-	181	SC
B90-7	-	-	2 no. 3	178	90	No	230	BF
B90-5	-	-	2 no. 3	127	90	No	255	BF
B90-5A	-	-	2 no. 3	127	90	Yes	371	SP
B45-7	-	-	2 no. 3	178	45	No	331	BF
B45-5	-	-	2 no. 3	127	45	No	356	SP
BSV	2 no. 3	355	-	-	-	-	306	SC
BS90-7A	2 no. 3	355	2 no. 3	178	90	Yes	414	SP+FF

SC = shear compression; BF = bond failure of NSM rods; SP = splitting of concrete cover; and FF = flexural failure.

The results have shown that in the absence of steel stirrups, an increase in load carrying capacity as high as 106% with respect to the control beam was observed. The failure of this beam was followed by the splitting of a bottom concrete cover region due to shear deformation of the longitudinal reinforcement that eventually led to cover delamination and loss of anchorage of the FRP rods. Based on the results, the authors concluded that the shear capacity of the strengthened beams with NSM technique can be increased by: decreasing the

space of the FRP rods; anchoring the rods into the flange of the beam; adopting an inclination of 45° for the rods.

Rizzo and De Lorenzis (2009) investigated the shear capacity of RC beams strengthened in shear with different type of NSM reinforcements (laminates and rods), spacing and inclination of the laminates/rods, and mechanical properties of the groove-filling epoxy. For bonding the FRPs, two types of epoxy paste were used, one, type *a*, of a tensile strength and secant tensile elastic modulus of 18.6 MPa and 4.15 GPa, respectively, and the other, type *b*, of 22.8 MPa and 12.87 GPa for these corresponding properties. One beam was strengthened in shear with EBR CFRP laminates. Figure 2-18 shows the geometry of the tested beams.

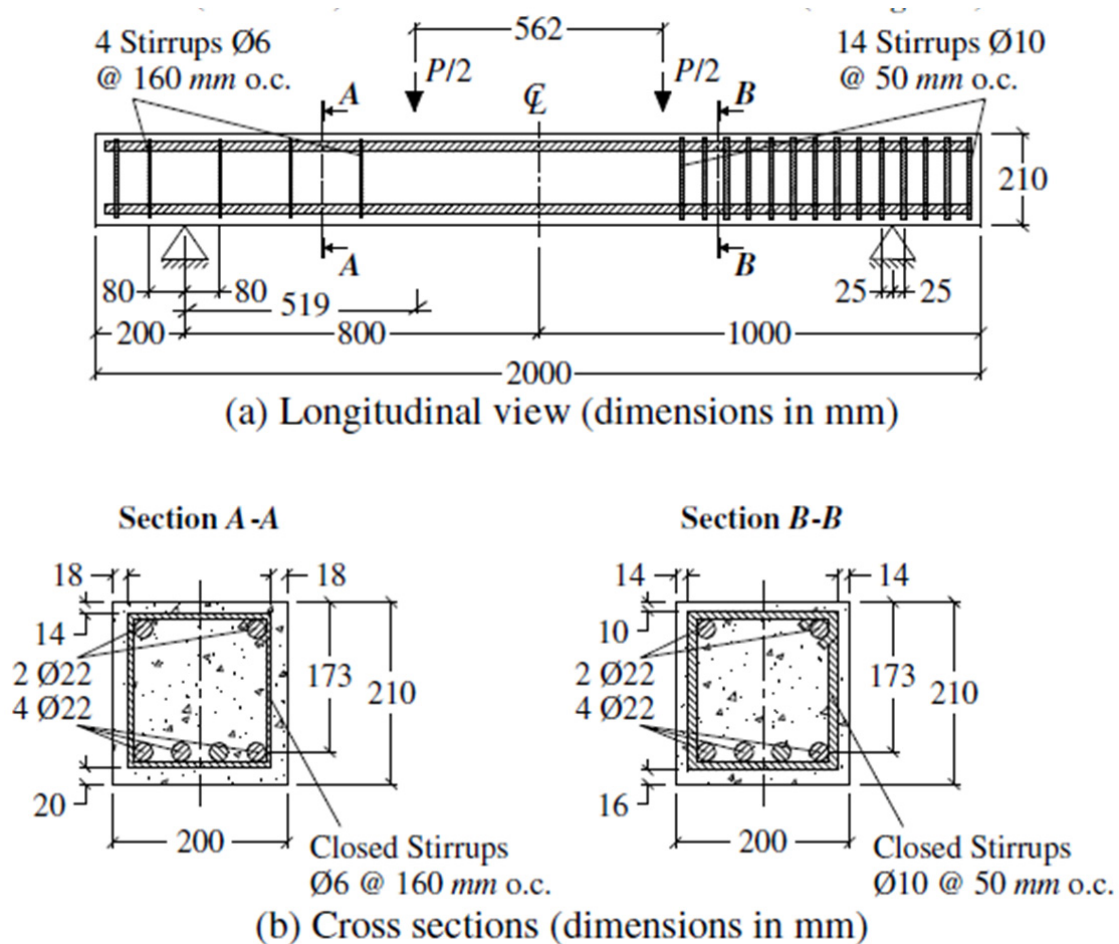


Figure 2-18: Geometrical details of the RC beams (Rizzo and De Lorenzis 2009)

Table 2-6 presents the strengthening and ultimate load of the tested beams.

Table 2-6: Details and results of the tested beams (Rizzo and De Lorenzis 2009)

Beam designation	Strengthening system	Type of groove-filling epoxy	Inclination of the CFRP fibers	Spacing of the strengthening system	Ultimate load (kN)
C	-	-	-	-	244
UW90	Externally bonded CFRP laminate	-	90	Continuous strengthening	283
NB90-73-a	NSM CFRP bars	a	90	73	353
NB90-73-b		b	90	73	297
NB90-45-b		b	90	45	301
NB45-146a		b	45	146	322
NB45-73a		a	45	73	300
NS90-73a	NSM CFRP strips	a	90	73	345
NS45-146a		a	45	146	310

The results show that the beams strengthened with NSM technique supported higher load capacity than beams strengthened with EBR technique. In EBR technique the strengthening potentialities of the CFRP were not fully mobilized due to premature debonding of the CFRP. The increase in shear capacity was about 16% for the beam strengthened with externally bonded U-wrapped strip, and ranged between 22% and 44% for the beams strengthened with NSM reinforcement.

Dias and Barros (2010) compared the performance of the RC beams strengthened in shear with NSM CFRP laminates and EBR technique. They examined 15 almost full scale T cross section beams under three point bending configuration. Nine beams were strengthened with different inclination and strips and percentage of the CFRP laminates. Figure 2-19 shows the geometry of the control beam (C-R).

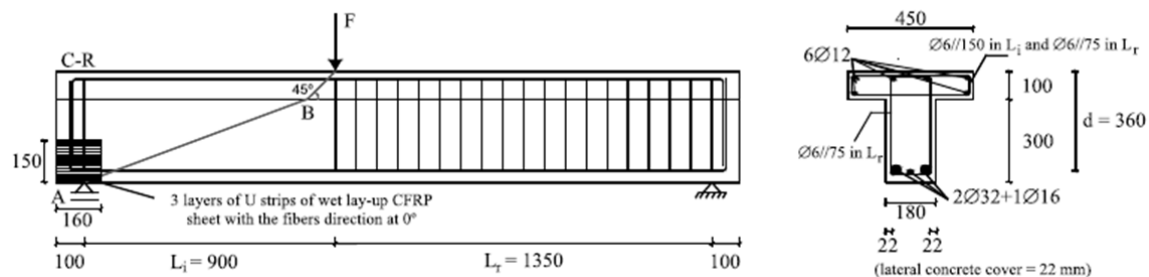


Figure 2-19: Geometry of the control beam (dimensions in mm) (Dias and Barros 2010)

Three beams were strengthened by EBR technique with different percentage of strips of the CFRP sheets. Table 2-7 presents the details and results of the tested beams.

Based on the results, these authors concluded that:

- NSM technique was more effective than EBR technique, since the NSM provided a larger increase of load carrying capacity after shear crack formation.

- The arrangement consisting of laminates at 45° was most effective in all the series with different CFRP percentage, and laminates at 60° were more effective than vertical laminates.
- The effectiveness level of the NSM technique is limited by concrete tensile strength, since at failure, a certain volume of concrete was attached to the CFRP laminates.

Table 2-7: Details and results of the tested beams (Dias and Barros 2010)

Beam designation	shear reinforcement system in the smaller beam shear span (L_s)					Ultimate load (kN)	
	Shear strengthening	Quantity	Percentage (%)	Spacing (mm)	Angle (°)		
C-R	-	-	-	-	-	207	
2S-R	NSM CFRP laminates	-	-	-	-	304	
7S-R		-	-	-	-	467	
2S-4LV		2×4 laminates (1.4×9.5 mm ²)	0.08	180	90°	337	
2S-7LV		2×7 laminates (1.4×9.5 mm ²)	0.13	114	90°	374	
2S-10LV		2×10 laminates (1.4×9.5 mm ²)	0.18	80	90°	398	
2S-4L45		2×4 laminates (1.4×9.5 mm ²)	0.08	275	45°	393	
2S-7L45		2×7 laminates (1.4×9.5 mm ²)	0.13	157	45°	422	
2S-10L45		2×10 laminates (1.4×9.5 mm ²)	0.19	110	45°	446	
2S-4L60		2×4 laminates (1.4×9.5 mm ²)	0.07	243	60°	386	
2S-6L60		2×6 laminates (1.4×9.5 mm ²)	0.11	162	60°	394	
2S-9L60		2×9 laminates (1.4×9.5 mm ²)	0.16	108	60°	413	
2S-4M		EBR CFRP wet lay-up sheets	4 strips of CFRP wet lay-up sheets U configuration – 1 layer (0.176×60mm ²)	0.07	180	90°	311
2S-7M (1)			7 strips of CFRP wet lay-up sheets U configuration – 1 layer (0.176×60mm ²)	0.10	114	90°	325
2S-7M (2)			7 strips of CFRP wet lay-up sheets U configuration – 2 layer (0.176×60mm ²)	0.21	114	90°	370

Analytical and numerical research have shown the NSM technique for the shear strengthening of the RC beams can be more effective if the FRP laminates are deeper installed into the slits. The depth of the slits is limited to the concrete cover, and in general does not exceed 30 mm. In the analytical model proposed by Bianco et al. (2014) it is assumed four failure modes for the NSM laminates crossing a critical shear crack: 1) debonding, 2) concrete semi-conical tensile fracture, 3) mixed shallow semi-conical plus

debonding, and 4) laminate tensile fracture. The semi-conical is formed when the axis of the laminate is assumed positioned at the surface of the beam's lateral face. According to theoretical fundamentals of this model, if the laminate is positioned deeper into the core of the beam's web, the concrete fracture is formed by higher surface than the one corresponding to the semi-cone, resulting higher resisting concrete fracture and, consequently, higher shear strengthening effectiveness for the NSM technique. Recently an experimental program was carried out to study the effectiveness of installing the laminates deeper into the slits by Barros and Dias (2013). This experimental program was composed of one reference beam (Figure 2-20) and four strengthened beams with CFRP laminates, where laminates were positioned at different depth/inclination into slits opened at lateral faces of the beam's web in the shorter span of the beam (a , as indicated in Figure 2-20).

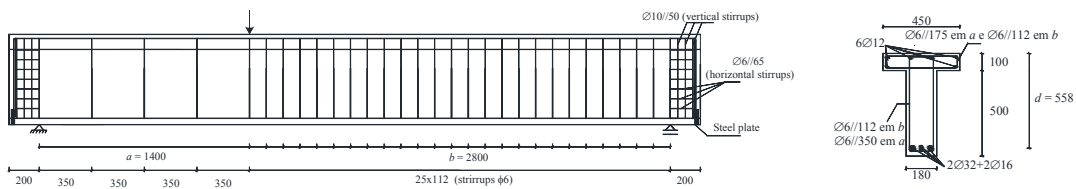


Figure 2-20: Geometry of the reference beam (dimensions in mm) (Barros and Dias 2013)

The details and results of the tested beams are represented in Figure 2-21 and Table 2-8.

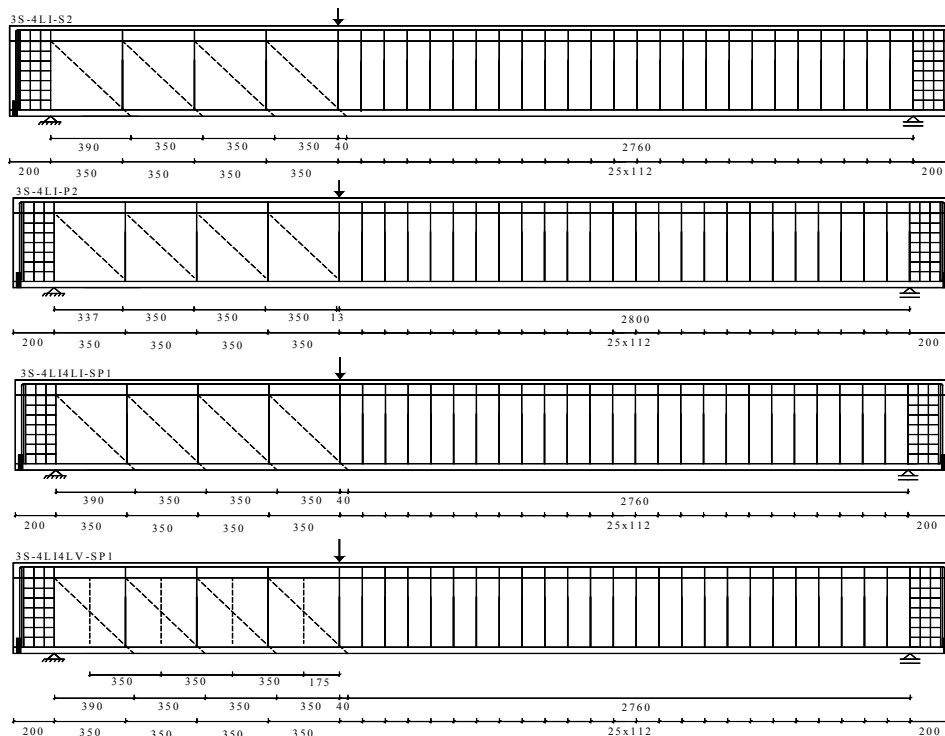


Figure 2-21: NSM shear strengthening configurations (CFRP laminates at dashed lines) (dimensions in mm) (Barros and Dias 2013)

Table 2-8: Details and results of the tested beams (Barros and Dias 2013)

Beam designation	<i>shear reinforcement system in the smaller beam shear span (a)</i>					Ultimate load (kN)	Deflection at maximum load (mm)
	Quantity	Percentage (%)	Depth of groove (mm)	Spacing (mm)	Angle (°)		
3S-R	-	-	-	-	-	331	10.7
3S-4LI-S2	2×4 laminates (1.4×20 mm ²)	0.113	21	350	52°	555	16.7
3S-4LI-P2	2×4 laminates (1.4×20 mm ²)	0.113	35	350	52°	599	17.5
3S-4LI4LI-SP1	2×8 laminates (1.4×10 mm ²)	0.113	35	350	52°	550	20.3
3S-4LI4LV-SP1	2×8 laminates (1.4×10 mm ²)	0.101	35(90°)/15(52°)	350/350	52°/90°	566	16

Based on the results, the 3S-4LI-P2 beam (2×4 laminates (1.4×20 mm²) and depth of 35 mm) has shown better behavior in terms of maximum load carrying capacity and also deflection corresponding to maximum load at loaded section. The option for having two independent laminates in each slits (3S-4LI4LI-SP1 beam), or use of CFRP configurations with two kinds of inclinations for the laminates installed at different depth inside the slits (3S-4LI4LV-SP1 beam) provided a more ductile behavior after peak load for the beam strengthened with NSM technique.

Based on the results reported in literature (De Lorenzis and Nanni 2001, Dias and Barros 2010, Chaallal et al. 2011, Dias and Barros 2013) debonding and concrete cover detachment are the failure modes that can compromise the shear strengthening effectiveness of NSM and EBR techniques. This is mainly caused by the relatively low concrete tensile strength that limits the force that can be transferred by bonding to the surrounding concrete (Chaallal et al. 2011).

2.3.3 Embedded Through Section

In the Embedded Through-Section (ETS) technique, steel or FRP bars are inserted into holes executed through the cross section and bonded with an appropriate epoxy adhesive (Figure 2-22). This technique can be more effective than the two previous techniques (EBR and NSM) due to the higher confinement that surrounding concrete provides to the ETS bars, and larger concrete fracture surface that is mobilized during the pull-out process applied to the ETS bars crossing the shear cracks.

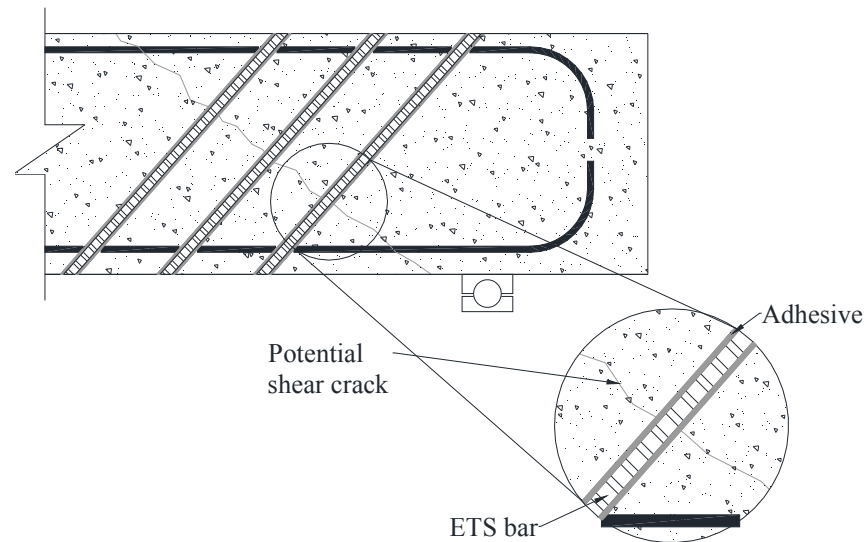


Figure 2-22: Embedded Through-Section (ETS) strengthening technique concept for the shear strengthening of reinforced concrete beams (Barros and Dalfre 2013)

The ETS technique is composed of the following steps:

- 1- The position of the longitudinal bars and stirrups has to be found by a rebar detector in order do not introduce any damage in these reinforcements during the execution of the holes for the installation of the ETS bars;
- 2- The position of the ETS bars has to be marked on the RC beams, and holes are made with the desire inclination through the core of the cross-section of the RC beams;
- 3- The holes are cleaned by compressed air;
- 4- The holes are filled by an appropriate adhesive epoxy (cement based adhesives have been also used when using ETS steel bars);
- 5- The bars are inserted into the holes and adhesive in excess is removed.

Chaallal et al. (2011) carried out an experimental program to assess the effectiveness of ETS technique by comparing the performance of EBR, NSM, and ETS shear strengthening techniques. The experimental program has involved twelve tests performed on T cross section beams. The details of the beams are presented in Figure 2-23. Two variables were examined in that experimental program:

- a) Effectiveness of the strengthening technique
- b) Presence of internal steel stirrups

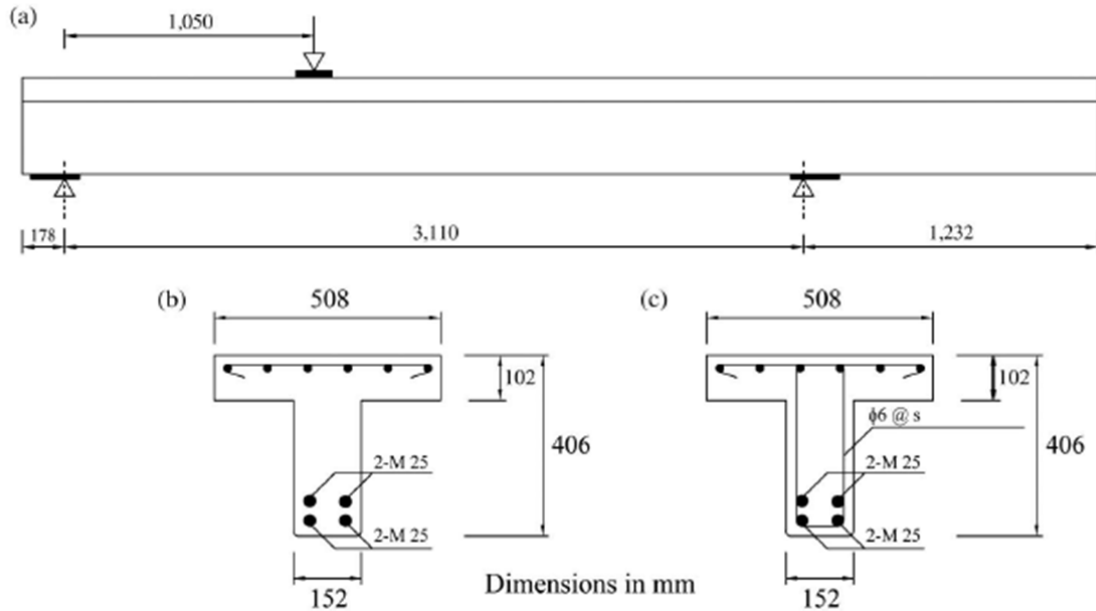


Figure 2-23: Details of tested beams: (a) longitudinal view; (b) cross-section with no transverse reinforcement; (c) cross-section with transverse steel stirrups (dimensions in mm) (Chaallal et al. 2011)

Series S0 is formed of beams without shear reinforcement. S1 and S3 consisted of the beams with transverse reinforcement, spaced at $s = d / 2$ for S1 series and $s = 3d / 4$ for S3 series, where $d = 350$ mm represents the effective depth of the beams. The average concrete strength was 25 MPa for S0 and S1 and 35 MPa for S3 series. Sand coated CFRP rods with nominal diameters of 9.5 mm and 12.7 mm are used for NSM and ETS strengthening methods, respectively. The average tensile strength and modulus of elasticity were 1870 MPa and 143.9 GPa, respectively. The CFRP sheet used for EB series is a unidirectional carbon fiber fabric that presents an ultimate stress and young's modulus of 3650 MPa and 231 GPa, respectively.

The main results of the experimental program are presented in Table 2-9. The results have shown that the average shear capacity of the strengthened beams has increased around 23%, 31%, and 60% when using the EB U-jacket sheet, NSM FRP rods, and ETS CFRP rods, respectively. The ETS technique was more efficient in term of mobilizing the tensile capacity of FRP systems. The failure of the strengthened beams with EBR and NSM techniques were FRP sheet debonding and concrete cover delamination, respectively, and all the corresponding beams failed in shear. In the series of ETS beams, the S1 and S3 failed in bending, while S0 failed in shear. At failure of the beams strengthened according to NSM and

EBR techniques, the maximum tensile strain of the FRP was much lower than their ultimate tensile strain.

Table 2-9: The main results of the experimental program (Chaallal et al. 2011)

Strengthening method	Beam designation	Shear strengthening system	Ultimate load (kN)	Total shear resistance (kN)	Failure mode
Control	S0-CON	-	123	81	Shear
	S1-CON	Stirrups@175mm	351	232	Shear
	S3-CON	Stirrups@263mm	294	194	Shear
EBR	S0-EB	Continuous sheets in the form of U-wraps	181	120	Shear
	S1-EB	Stirrups@175mm Continuous sheets in the form of U-wraps	378	251	Shear
	S3-EB	Stirrups@263mm Continuous sheets in the form of U-wraps	335	222	Shear
NSM	S0-NSM	NSM strengthening d=9.5mm @130mm	198	131	Shear
	S1-NSM	Stirrups@175mm NSM strengthening d=9.5mm@130mm	365	242	Shear
	S3-NSM	Stirrups@263mm NSM strengthening d=9.5mm@130mm	380	252	Shear
ETS	S0-ETS	ETS strengthening d=12.7mm @130mm	273	181	Shear
	S1-ETS	Stirrups@175mm NSM strengthening d=12.7mm@130mm	397	263	Flexural
	S3-ETS	Stirrups@263mm NSM strengthening d=12.7mm@130mm	425	282	Flexural

The presence of steel stirrups resulted in a decrease of the contribution of CFRP to the shear resistance for the beams strengthened with the EBR and NSM techniques. While the contribution of CFRP did not significantly decrease with the presence of transverse steel reinforcement in the specimens strengthened with the ETS technique.

Barros and Dalfre (2013) carried out a comprehensive experimental program composed of 14 RC beams. Two variables were examined in that experimental program:

1. Percentage of existing steel stirrups.
2. Inclination of the ETS steel bars (45° or vertical).

The experimental program was formed by two series of RC beams with different cross section (150×300 mm² and 300×300 mm²) with a total length of 2450 mm and a shear span of 900 mm. Figure 2-24 shows the configuration of the beams.

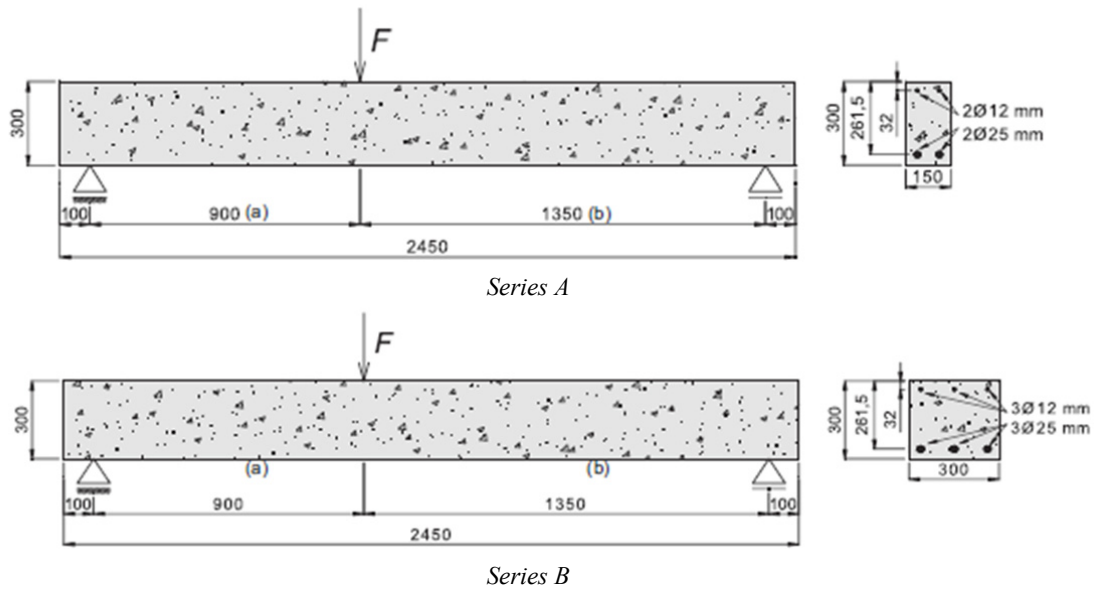


Figure 2-24: Geometry of the beams (dimensions in mm) (Barros and DalFre 2013)

Table 2-10 presents general information of series A and series B and also the results of the tested beams. The authors concluded that:

- Inclined ETS bars were more effective than vertical bars, and the shear strengthening effectiveness was increased with the percentage of ETS bars.
- For an ETS shear strengthening ratio of 0.16%, a ductile flexural failure mode was assured in beams of flexural reinforcement ratio of 1.88%.
- For the tested beams, the contribution of the ETS bars was limited by the concrete crushing or yielding of the longitudinal reinforcement.
- In the beams strengthened with ETS technique the strengthening effectiveness has increased with the percentage of the steel stirrups.

Table 2-10: General information and corresponding results of the tested beams (Barros and Dalfre 2013)

	Beam designation	Shear strengthening system	Ultimate load (kN)	Deflection corresponding to the maximum load (mm)
Series A	Reference	-	109	4.0
	S300.90	Stirrups@300mm	165	8.4
	E300.90	ETS strengthening (90°) 3 ϕ 10@300mm	161	7.0
	E300.45	ETS strengthening (45°) 3 ϕ 10@300mm	204	12
	S300.90/E300.90	Stirrups@300mm ETS strengthening (90°) 3 ϕ 10@300mm	231	13.1
	S300.90/E300.45	Stirrups@300mm ETS strengthening (45°) 3 ϕ 10@300mm	244	14.0
	S225.90	Stirrups@225mm	180	9.9
	S225.90/E225.90	Stirrups@225mm ETS strengthening (90°) 3 ϕ 10@225mm	244	14.5
Series B	Reference	-	203	4.5
	S300.90	Stirrups@300mm	232	5.6
	E300.90	ETS strengthening (90°) 3 ϕ 10@300mm	239	6.1
	E300.45	ETS strengthening (45°) 3 ϕ 10@300mm	336	9.4
	S300.90/E300.90	Stirrups@300mm ETS strengthening (90°) 3 ϕ 10@300mm	390	15
	S300.90/E300.45	Stirrups@300mm ETS strengthening (45°) 3 ϕ 10@300mm	397	20

Breveglieri et al. (2014) carried out an experimental program composed of 10 T-cross section RC beams, organized in two series: series A without steel stirrups; series B with two steel stirrups, spaced at 300 mm, in monitored shear span. The beams were designed in order they fail in shear. Figure 2-25 shows the reference beam with no steel stirrups in the monitored shear span.

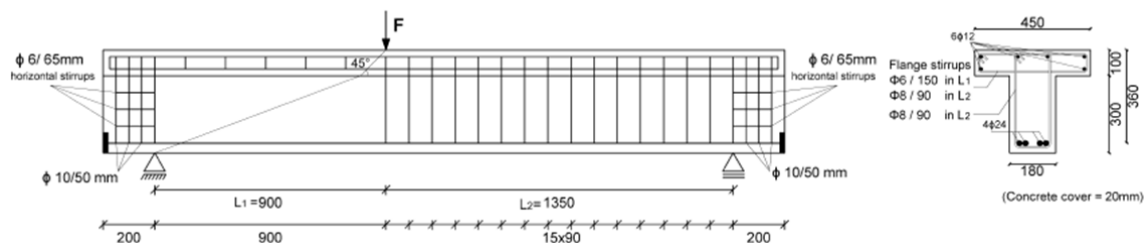


Figure 2-25: Tested beams: geometry, steel reinforcements applied in all beams (dimensions in mm) (Breveglieri et al. 2014)

The following variables were examined in this experimental:

- a) Inclination of the ETS bars
- b) Shear strengthening ratio

The details and results of the tested beams are presented in Table 2-11.

Table 2-11: General information and corresponding results of the tested beams (Breveglieri et al. 2014)

<i>Beam designation</i>	<i>Shear strengthening system</i>	<i>Ultimate load (kN)</i>	<i>Deflection corresponding to the maximum load (mm)</i>
<i>0S-Ref</i>	-	156	4.66
<i>0S-ETS300-90</i>	ETS strengthening (90°) 3φ10@300mm	218	4.37
<i>0S-ETS300-45</i>	ETS strengthening (45°) 3φ10@300mm	349	-
<i>0S-ETS180-90</i>	ETS strengthening (90°) 3φ10@300mm	257	4.31
<i>0S-ETS180-45</i>	ETS strengthening (45°) 3φ10@300mm	269	6.56
<i>2S-Ref</i>	Stirrups@300mm	242	4.70
<i>2S-ETS300-90</i>	Stirrups@300mm ETS strengthening (90°) 3φ10@300mm	316	5.32
<i>2S-ETS300-45</i>	Stirrups@300mm ETS strengthening (45°) 3φ10@300mm	407	7.03
<i>2S-ETS180-90</i>	Stirrups@180mm ETS strengthening (90°) 3φ10@300mm	407	8.27
<i>2S-ETS180-45</i>	Stirrups@180mm ETS strengthening (45°) 3φ10@300mm	505	8.37

The load carrying capacity of the strengthened beams increased more than 30%, and reached a maximum of 136% compared to control beam. The authors concluded that the inclined ETS bars (45°) were more effective than vertical ones due to the larger available resisting bond length assured. They also pointed out that the average inclination of the shear failure crack of the strengthened beams varied between 39° and 45°. Therefore, the ETS bars were almost orthogonal to the critical shear cracks. As mentioned in previous sections, the effectiveness of EBR and NSM techniques has decreased with the increase of the percentage of steel stirrups. In the ETS technique the strengthening effectiveness has increased with the percentage of the steel stirrups. The detrimental group effect observed in the two previous techniques (EBR and NSM) due to the mutual interaction consecutive FRP shear reinforcements did not occur in the ETS technique, even for minimum spacing of the ETS bars.

2.4 Fiber Reinforced Concrete for Shear Strengthening

Fiber Reinforced Concrete (FRC) is being used not only to restore the load carrying capacity and deflection of damaged structures, but also to increase the load carrying and energy dissipation performance of concrete and masonry structures. The relatively high post-cracking residual strength and energy absorption of FRC is taking into account for the use of this composite in the structural rehabilitation and strengthening. The results obtained by several researchers in experimental programs also show the potential reduction or, even the total replacement, of steel stirrups by taking advantage of the shear resistance of FRC (Kwak et al. 2002, Slater et al. 2012).

Recently, Strain Hardening Cementitious Composite (SHCC) is used to produce thin plates to increase the shear and flexural capacity of the RC beams (Esmaeeli et al. 2013a) and also energy dissipation of beam-column joint (Esmaeeli et al. 2014). SHCC is a class of fiber reinforced cement composites (FRCC) that exhibits ductile behavior under tensile load, with a strain hardening response rather than the tension softening character presented by conventional FRCC after crack initiation (Li 1998). In SHCC materials, the fiber bridging mechanisms developed during the crack opening process allow a gradual increase of tensile capacity from crack initiation up to a relatively high tensile strain (more than 1%), where a failure macro-crack finally occurs, followed by a strain-softening stage (Figure 2-26). The tensile strain hardening phase is accompanied by the formation of a diffuse crack pattern of very small crack width.

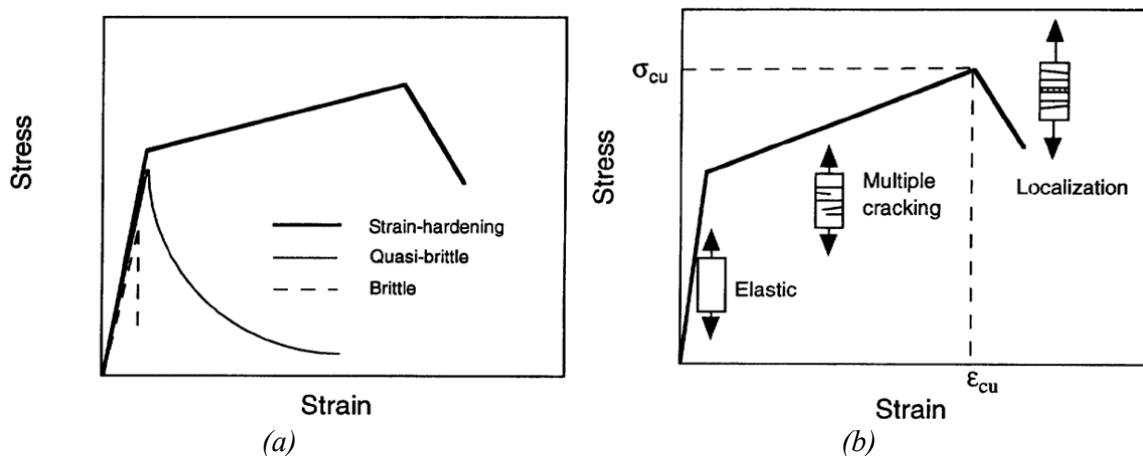


Figure 2-26: (a) Schematic illustration of uniaxial stress-strain curves for brittle, quasi-brittle, and strain-hardening cementitious materials, (b) Schematic of three deformation stages of a SHCC during a uniaxial tensile test

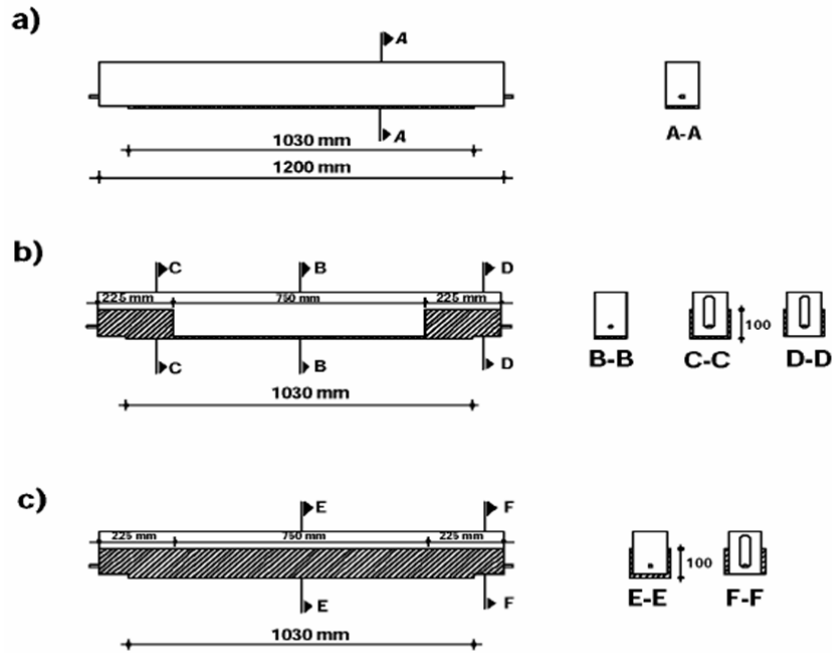


Figure 2-28: Retrofit configurations: (a) one plate bonded on the tensile face, (b) one plate bonded on the tensile face and four plates bonded on the vertical sides, and (c) one plate bonded on the tension face and two plates fully covering the vertical faces (Maheri et al. 2004)

The main results of the experimental program are presented in Table 2-13, demonstrating a noticeable strengthening effectiveness of the CARDIFRC plates on the stiffness and ductility of the repaired beams. The stiffness of repaired beams has increased with the thickness of retrofitting plates. This technique was able to change the failure mode of the beams from brittle shear to a ductile flexural failure.

Table 2-13: Details and main results of the tested beams (Maheri et al. 2004)

	<i>Retrofit configuration</i>	<i>Plate thickness (mm)</i>	<i>Mix type</i>	<i>Beam No.</i>	<i>Ultimate load (kN)</i>	<i>Maximum deflection (mm)</i>	<i>Failure mode</i>			
Non-ductile beams	<i>Control beam</i>	-	-	1	32	8.6	Flexure			
		-	-	2	29	4.1	Shear			
		-	-	3	30	4.9	Shear			
		-	-	4	26	3.3	Shear			
	<i>Figure 2-28a</i>	16	I	1	35	9.1	Flexure			
				2	31	8.0	Flexure			
			II	1	47	8.5	Flexure			
				2	40	3.5	Shear			
		20	II	1	41	8	Flexure			
				2	35	8.7	Flexure			
	<i>Figure 2-28b</i>	16	I	1	43	9.7	Flexure			
				2	46	9.1	Flexure			
				3	43	9.4	Flexure			
			II	1	53	9.3	Flexure			
				2	42	9.11	Flexure			
				3	54	20.1	Flexure			
		20	II	1	35	8.8	Flexure			
				2	37	8.8	Flexure			
				<i>Figure 2-28c</i>	16	I	1	76	9.4	Flexure
							2	85	9.9	Flexure
3	84	9.1	Flexure							
II	1	86	19.6			Flexure				
	2	80	9.3			Flexure				
	3	68	9.1			Flexure				
ductile beams	<i>Control beam</i>	-	-	1	42	23.8	Flexure			
		-	-	2	46	30.9	Flexure			
		-	-	3	45	26.2	Flexure			
	<i>Figure 2-28a</i>	16	I	1	57	25.5	Flexure			
				2	64	20.5	Flexure			
		20	I	1	77	17.4	Flexure			
				2	84	21	Flexure			
	<i>Figure 2-28b</i>	16	I	1	65	15.9	Flexure			
				2	61	14	Flexure			
		20	I	1	60	14.4	Flexure			
				2	58	20.4	Flexure			
	<i>Figure 2-28c</i>	16	I	1	130	14.2	Flexure			
				2	146	23.5	Flexure			
20		I	1	133	17.3	Flexure				

In a study conducted by Mostosi et al. (2011), the use of High Performance FRC (HPFRC) was investigated for the shear strengthening of RC beams. Two kinds of HPFRC were used: i) a HPFRC with a self-leveling rheology that can be cast with a thin thickness; and ii) a new thixotropic material. Figure 2-29 and Table 2-14 show the geometry of the beams and the specimens' characteristics, respectively. The HPFRC jacket was reinforced with a wire mesh of 2.05 mm diameter bent wires, assembled with a spacing of 25.4 mm. A perfect bond between the beam's concrete substrate and HPFRC jacket was assured by sandblasting.

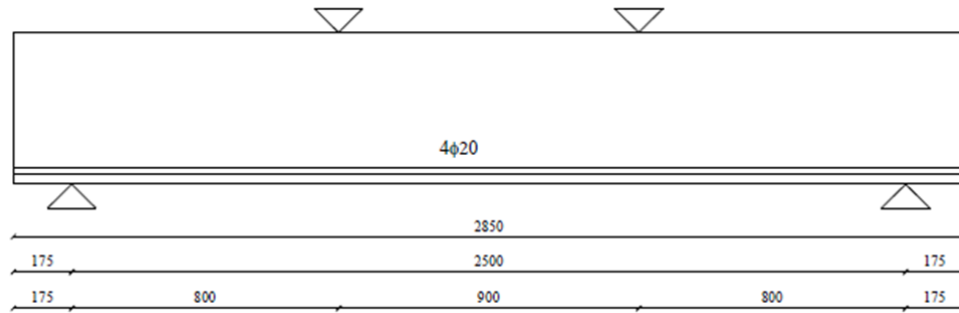


Figure 2-29: Beam geometry (dimensions in mm) (Mostosi et al. 2011)

Table 2-14: Specimens characteristics (Mostosi et al. 2011)

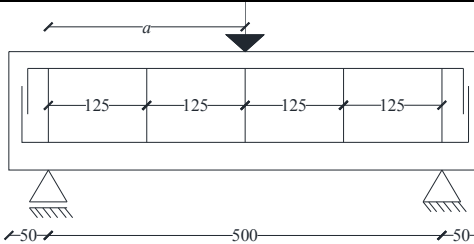
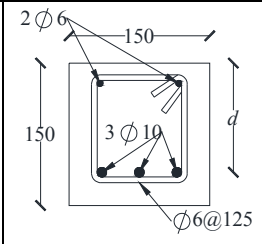
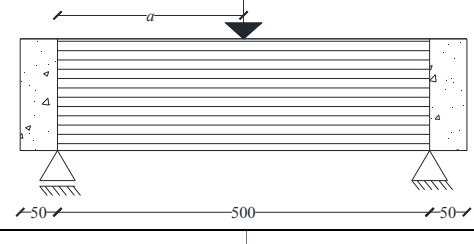
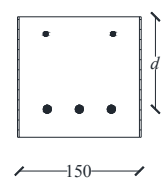
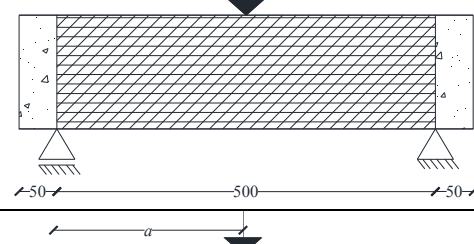
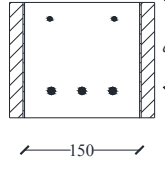
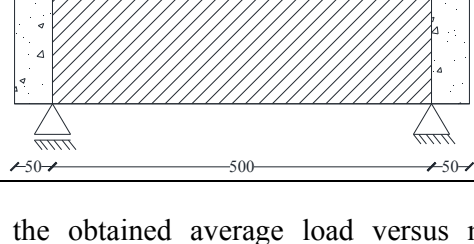
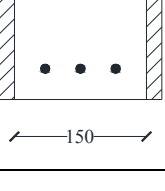
Beam designation			Thickness of the jacket	Material	Type Mesh	Ultimate load (kN)	Maximum deflection (mm)
Un-Reinforced beam		-	No reinforced	-	-	450	-
Beam B		Lower surface	50 mm	Self-leveling	Welded wire mesh U bent	773	11.9
		Lateral surface	50 mm	Self-leveling			
Beam D		Lower surface	50 mm	Self-leveling	Welded wire mesh U bent	741	12.1
		Lateral surface	50 mm	thixotropic			
Beam E		Lower surface	50 mm	Self-leveling	Welded wire mesh U bent to a height of 20 cm on lateral surfaces	670	16.9
		Lateral surface	30 mm	thixotropic			

For the beams strengthened with HPFRC jacket (beams B, D, and E), as opposed to reference beams, the failure mode was governed by flexural. The author concluded that the reinforced HPFRC jacket can have a contribution like the conventional shear reinforcement.

Esmaeeli et al. (2013a) investigated the potentialities of a hybrid composite plate (HCP) for the shear strengthening of RC beams with $a/d=2.15$. HCP was composed of CFRP sheet glued with epoxy adhesive to the interior surface of a thin plate of SHCC.

Table 2-15 shows the details of the strengthening configurations adopted in these beams that were tested under three point bending load.

Table 2-15: Shear strengthening schemes and beam's geometry and reinforcement (dimensions in mm) (Esmaeeli et al. 2013a)

Beam designation	Beam Type	Section	shear strengthening scheme
CB			Control Beam
BF			CFRP Shear strengthening
BH			HCP Shear strengthening
BS			SHCC Shear strengthening

According to the obtained average load versus mid-span deflection, Figure 2-30, the maximum load carrying capacity of the beam strengthened with HCPs (BH) was 19% more than the maximum load carrying capacity of the control beam (CB).

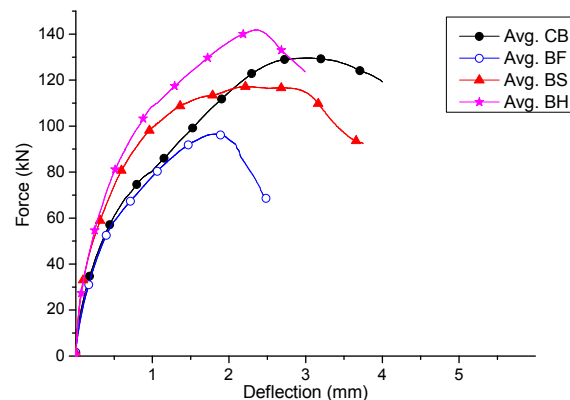


Figure 2-30: Load Deflection curves (Esmaeeli et al. 2013a)

The crack pattern of the beam strengthened with HCPs (BH) has more flexural cracks, visible on the external surface, than the beam strengthened with SHCC plate (BS) (Figure 2-31) due to the strengthening contribution of the CFRP sheet.



Figure 2-31: Typical cracks pattern and the failure modes of the beams (Esmaeeli et al. 2013a)

In a study conducted by Ruano et al. (2014), the performance of steel fiber reinforced concrete (SFRC) as a retrofitting material for reinforced concrete beams was assessed. The experimental program was composed of 18 RC beams with and without steel stirrups. Figure 2-32 shows one example of the RC beams with still stirrups, the test setup, and the repair/strengthening scheme. Eight beams with stirrups were damaged (up to failure load), and repaired with SFRC and loaded again. One beam without steel stirrups was tested as control beam, and the other beams were strengthened with FRC. Three types of high performance with self-compacting matrix were used as repair/strengthening materials: plain concrete, FRC with 30 kg/m^3 of steel fibers and FRC with 60 kg/m^3 of steel fibers.

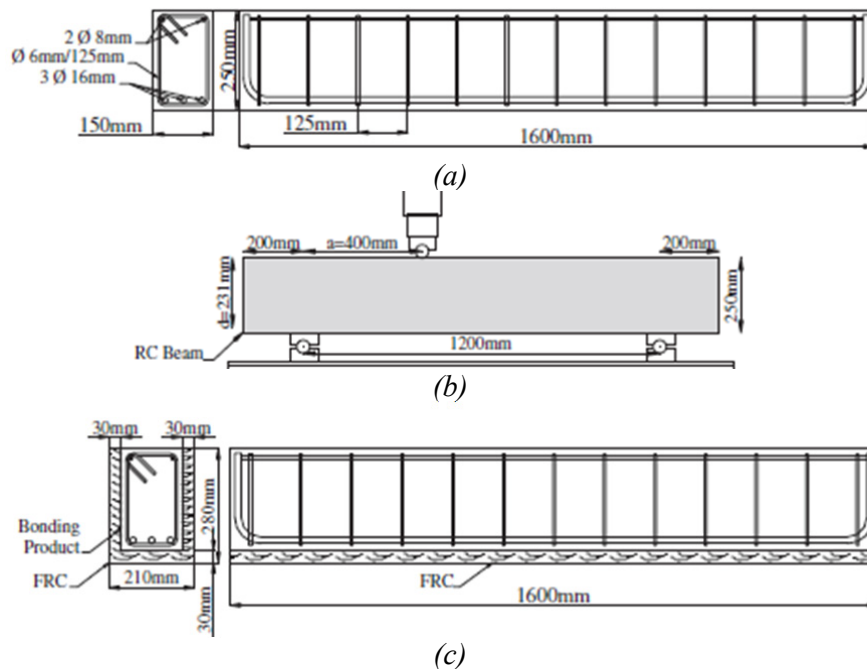


Figure 2-32: (a) one example of RC beams, (b) test setup, and (c) repair/strengthening scheme (dimensions in mm) (Ruano et al. 2014)

The results of the tested beams are presented in Table 2-16. The beam without steel stirrups strengthened with plain concrete jacketing (beam 3) presented debonding and spalling of the steel reinforcement. While, the SFRC jacketing prevented the debonding, preserving the integrity of the beam (beams 9 and 15). The beams with stirrups strengthened with fiber reinforced concrete increased their shear strength while for the case of beams strengthened with plain concrete no strength increase was found. The authors concluded reinforced concrete jacketing looks like an efficient method for shear strengthening of reinforced concrete beams with stirrups.

Table 2-16: Details and results of the tested beams (Ruano et al. 2014)

<i>Beam designation</i>	<i>Stirrups</i>	<i>Repaired</i>	<i>Jacketing</i>	<i>Load capacity before repairing (kN)</i>	<i>Ultimate load (kN)</i>
1	Yes	No	Plain concrete	-	245.4
2	Yes	No	Plain concrete	-	284.9
3	No	No	Plain concrete	-	172.9
4	Yes	Yes	Plain concrete	221.7	215.8
5	Yes	Yes	Plain concrete	221.7	248.1
6	Yes	Yes	Plain concrete	221.7	263.5
7	Yes	No	FRC 30kg/m ³	-	278.5
8	Yes	No	FRC 30kg/m ³	-	276.2
9	No	No	FRC 30kg/m ³	-	152.7
10	Yes	Yes	FRC 30kg/m ³	257.9	252.3
11	Yes	Yes	FRC 30kg/m ³	245.0	299.3
12	Yes	Yes	FRC 30kg/m ³	221.9	275.6
13	Yes	No	FRC 60kg/m ³	-	262.4
14	Yes	No	FRC 60kg/m ³	-	298.0
15	No	No	FRC 60kg/m ³	-	252.0
16	Yes	Yes	FRC 60kg/m ³	188.5	293.5
17	Yes	Yes	FRC 60kg/m ³	189.5	291.1
18	Control	No	-	-	116.1

2.5 Conclusion

Based on the literature, the following conclusions can be drawn in terms of the benefits provided by the use of FRP and FRC for the shear strengthening of RC beams:

- 1- The strengthening and repairing techniques based on the use of fiber reinforced polymer (FRP) and fiber reinforced concrete (FRC) materials have been recognized as very effective to increase the load and deformation capacity of Reinforced Concrete (RC) beams.
- 2- The ETS technique can be more effective in terms of increasing the load and deformation capacity of RC beams failing in shear than NSM and EBR techniques.
- 3- At failure of the beams strengthened according to NSM and EBR technique, the maximum tensile strain of adopted FRPs was, in general, much lower than their

ultimate tensile strain, due to the occurrence of premature debonding of the FRPs or/and concrete cover detachment.

- 4- The premature debonding in the NSM and EBR technique is caused by the relatively low tensile strength of the concrete substrate that limits the maximum load that can be transferable between FRPs and concrete element to be strengthened.
- 5- The contribution of the FRP systems in EBR and NSM techniques has decreased with the increase of the percentage of existing steel stirrups, while in ETS technique the strengthening effectiveness was not affected by the detrimental effect between steel stirrups and strengthening systems.
- 6- Shear strengthening technique based on the use of FRC is capable to transform a brittle shear failure in a ductile flexural failure.
- 7- FRC jacket/plate can increase the stiffness and the shear capacity of the RC beams without or low shear reinforcement.

Chapter 3

Shear Strengthening of Reinforced Concrete Beams with Hybrid Composite Plate

3.1 Introduction

In this chapter, the assessment of the Hybrid Composite Plate (HCP) for the shear strengthening of Reinforced Concrete (RC) beams is investigated. HCP is a thin plate of Strain Hardening Cementitious Composite (SHCC) reinforced with Carbon Fiber Reinforced Polymer (CFRP) laminates. These HCPs were capable of restoring, and even increase, the hysteretic response, energy dissipation, and also the load carrying capacity of beam-column joint that were previously damaged (Esmaeeli et al. 2015). HCPs were also very efficient for the increase of the flexural capacity of the RC beams (Esmaeeli et al. 2014). Besides the contribution of the SHCC for the strengthening efficiency of HCPs, the SHCC also assures some protection to the CFRP laminates and adhesive in terms of vandalism, aggressive environmental conditions, and fire. The combination of SHCC and CFRP grids was also explored in the context of the development of an innovative hybrid composite system for the structural rehabilitation, where the benefits of combining these materials in terms of load carrying capacity, ductility and cracking behavior were demonstrated (Orosz et al. 2013).

Due to the excellent bond conditions between SHCC and CFRP laminates, these reinforcements provide the necessary tensile strength capacity to the HCP, while the high post-cracking tensile deformability and resistance of SHCC avoids the occurrence of premature fracture failure of this cement composite in the stress transfer process between these two materials when the HCP is crossed by a shear crack.

The type of HCP schematically represented in Figure 3-1 was used in the experimental programs dedicated to the actual chapter. The HCP in these experimental programs is formed by a plate of SHCC of 20 mm thick reinforced with CFRP laminates that were applied according to the procedures adopted in the NSM technique (Dias and Barros 2010). Therefore, slits of a width and a depth of about 4 mm and 11 mm were opened on the lateral face of the SHCC plate that will be in contact with the concrete substrate. The slits were filled with an appropriate epoxy adhesive (S&P 220). The CFRP laminates were then inserted into the slits, and adhesive in excess was removed.

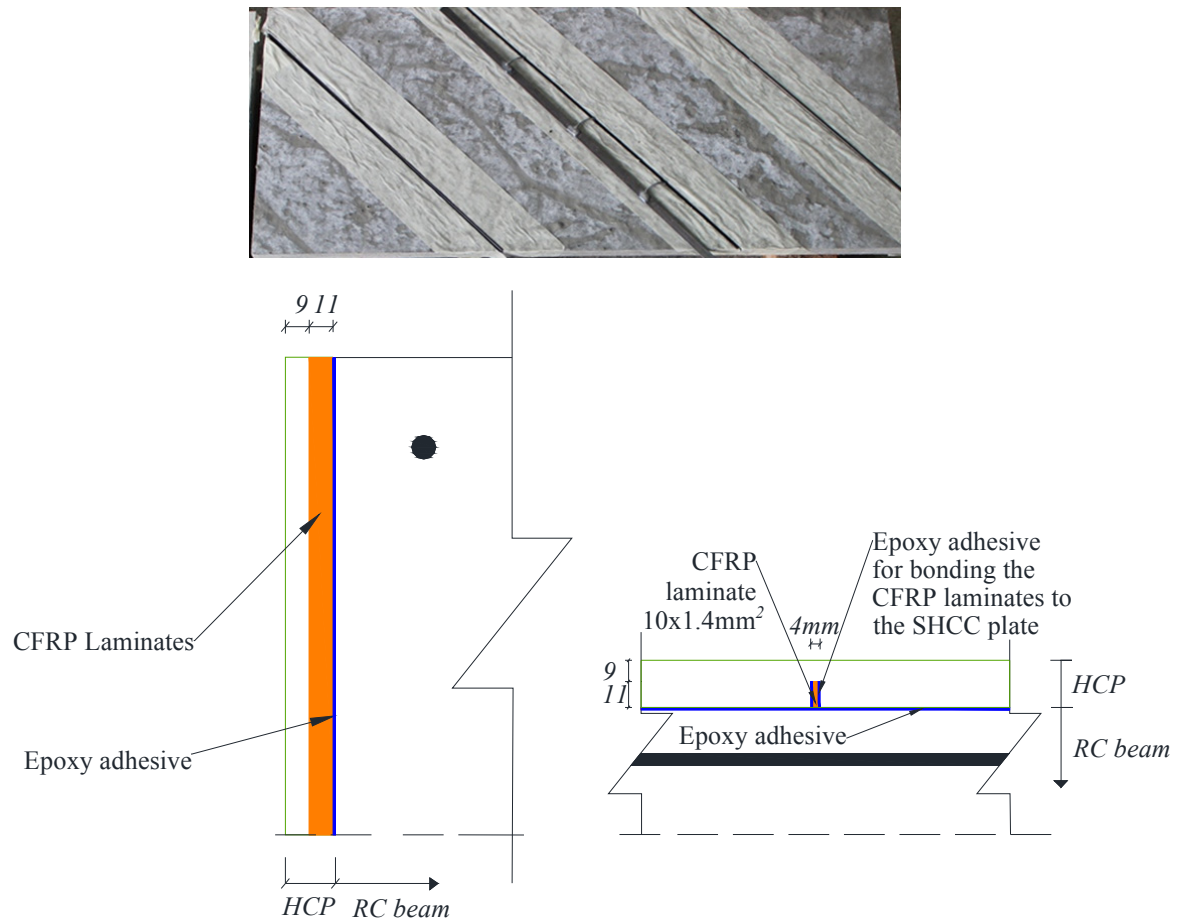


Figure 3-1: A schematic view of HCP (dimensions in mm)

3.2 Contextualization of the Experimental Programs

Besides the assessment of the effectiveness of HCPs for the shear strengthening of the RC beams, these experimental programs have also the purpose of investigating the influence on this effectiveness of the:

- Orientation of the CFRP laminates that reinforce the SHCC plate;
- CFRP shear strengthening ratio;
- Using mechanical anchors to install the HCPs;

Finally, the effectiveness of this technique is also explored for shear repairing of pre-damaged RC beams.

In the first experimental program six rectangular cross section RC beams were tested, composed of two control beams, one with seven steel stirrups in monitored shear span and

one without any shear strengthening in this beam's span, and four beams shear strengthened, one with NSM-CFRP laminates, another one with SHCC plates, and the others two with HCPs where the unique difference is the inclination of the CFRP laminates (45°, and 90°). The shear strengthening percentage of the CFRP laminates in the beams of this series (Series I) was $\rho_{fw} = 0.10\%$. The HCPs in this experimental were bonded using epoxy adhesive.

In the second experimental program (Series II) eight full scale T cross section beams were tested. It was composed of two control beams, one with seven steel stirrups in the monitored shear span and the other without any shear reinforcement in this beam's span, and six beams strengthened in shear by using the following three different techniques: NSM-CFRP laminates (one beam); SHCC plates (one beam); HCPs (four beams). The HCPs had different shear strengthening percentage of CFRP laminates ($\rho_{fw} = 0.08\%$ and $\rho_{fw} = 0.14\%$). Furthermore, the HCPs were bonded to substrate by the two following strategies: the HCPs were bonded by applying exclusively epoxy adhesive; besides epoxy adhesive, the HCPs were also fixed with mechanical anchors.

In the third series (Series III), the effectiveness of the HCPs to repair pre-damaged RC beams is assessed. For this purpose the damaged control beams (beams without any shear strengthening) tested in series I and II were repaired by using HCPs, and were tested again. The HCPs were bonded using both epoxy adhesive and mechanical anchors.

3.3 Series I: Beams of Rectangular Cross Section

3.3.1 Beams and test setup

The beams of this experimental program had a rectangular cross section (150×300 mm²) with the length of 2500 mm, and 2200 mm clear span (Figure 3-2). The longitudinal steel reinforcement consisted of 2φ20 laid at the bottom, and 2φ10 at the top as tensile and compression reinforcement, respectively, giving to the beam's cross section an effective depth (d) of 261 mm. The steel bars were anchored at the section of the supports with 90° hooks to prevent premature anchorage failure and sliding. To localize the shear failure in only one of the shear spans, a three point bending test setup with different length of the shear spans was selected (Figure 3-2). Since the monitored shear span (L_i) had a length of 800 mm, a shear span to effective depth ratio (L_i / d) of 3 was assured. A relatively high percentage of steel stirrups (φ8@100 mm) was applied in the other span (L_r) to avoid that shear failure

occurs in this span. Depending on the number of the steel stirrups in L_i , the beams were categorized in two different types. The type A was designed with steel stirrups $\phi 8@100$ mm, while type B did not include any transverse reinforcement in this span in an attempt of assuring flexural and shear failure mode for these respective beams. Four beams of type B were strengthened in shear with the following techniques: 1) NSM-CFRP laminates; 2) SHCC plates; and 3) HCPs with two inclinations of the CFRP laminate (45° and 90°).

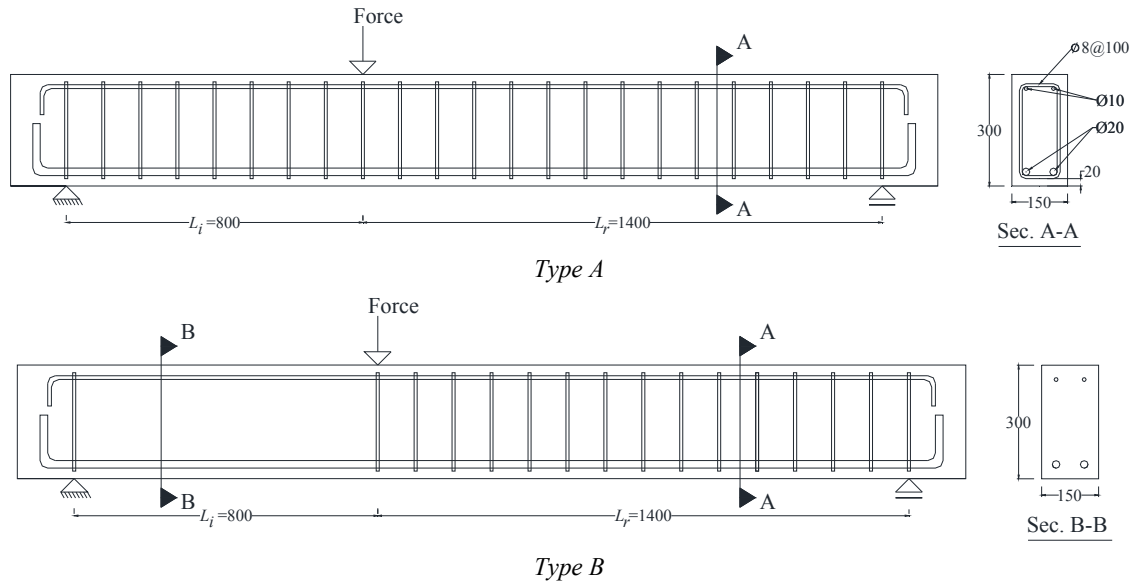


Figure 3-2: Geometry and reinforcement arrangement of the concrete beams (dimensions in mm)

The characteristics of the beams are presented in Table 3-1. The 7S-R-I beam had 7 stirrups in the L_i span in order to assure flexural failure. The C-R-I was a control beam without any type of shear reinforcement and strengthening in the L_i span. The NSM-4L90-I beam was shear strengthened with four vertical CFRP laminates in each lateral face of the L_i span, spaced at 180 mm, and applied according to the NSM technique. The SP-I beam was strengthened with SHCC plates applied in each lateral face of L_i span to investigate the effectiveness of these plates for the shear strengthening. These plates had overall dimensions of $720 \times 300 \times 20$ mm³ and were bonded to the concrete beam using an epoxy adhesive (S&P220). The SP-4L90-I and SP-3L45-I beams were strengthened by applying HCPs in each lateral face of L_i span. The HCP is a 20 mm thick SHCC plate that includes a strengthening system formed by CFRP laminates positioned at 90° (SP-4L90-I, Figure 3-3a) or 45° (SP-3L45-I, Figure 3-3b).

The NSM-4L90-I, SP-4L90-I, and SP-3L45-I beams had equal percentage of CFRP laminates. The CFRP shear strengthening percentage, ρ_{fw} , is:

$$\rho_{fw} = \frac{2a_f b_f}{b_w s_f \sin \theta_f} \quad (4.1)$$

where $b_w = 150$ mm is width of the beam's cross section, $a_f = 1.4$ mm and $b_f = 10$ mm are the dimensions of the NSM CFRP laminate cross section, s_f and θ_f represent the spacing and inclination of these laminates, respectively (Figure 3-3).

Table 3-1: Shear strengthening/reinforcement configurations applied in the L_i beam's shear span of the tested beams

Beam designation	Shear strengthening/reinforcement configuration	Quantity	Percentage of CFRP laminates (%)	Spacing, s_f , (mm)	Angle of CFRP laminates, θ_f , ($^\circ$)
C-R-I	-	-	-	-	-
NSM-4L90-I	NSM CFRP laminates of 1.4×10 mm ² cross section	2×4 CFRP laminates	0.10	180	90
SP-I	SHCC Plates	20 mm thickness of SHCC	-	-	-
SP-4L90-I	HCPs (20 mm thickness of SHCC reinforced with CFRP laminates of 1.4×10 mm ² cross section)	2×4 CFRP laminates	0.10	180	90
SP-3L45-I	HCPs (20 mm thickness of SHCC reinforced with CFRP laminates of 1.4×10 mm ² cross section)	2×3 laminates	0.10	250	45
7S-R-I	Steel stirrups	$\phi 8 @ 100$ mm	-	-	-

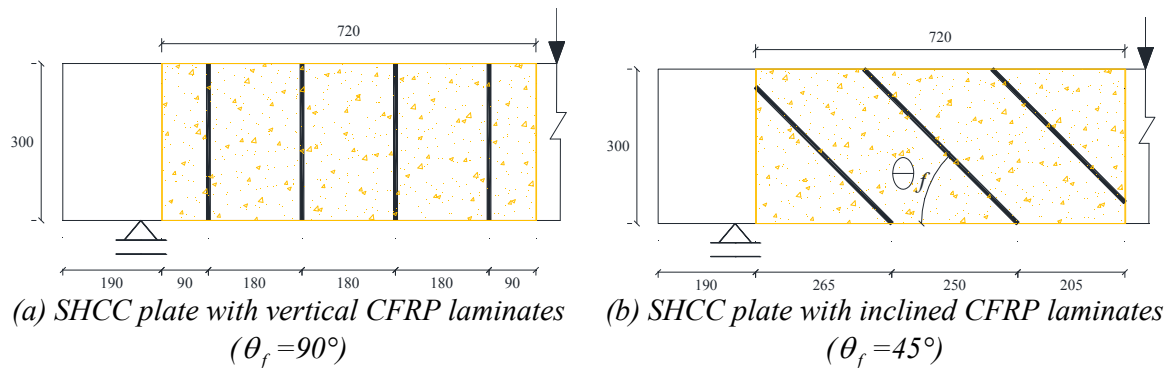


Figure 3-3: Configurations of the HCPs in beam: (a) SP-4L90-I, and (b) and SP-3L45-I (dimensions in mm)

The SHCC plates were cut from panels with a size of $800 \times 800 \times 20$ mm³ that were built, each one, with a batch of about 13 liters of SHCC. After casting, these panels were sealed by a plastic sheet and were kept in a room environment for 24 hours before de-molding. After

de-molding, all these panels were transferred to the climate room and were cured under the constant conditions of 20°C temperature and 80% humidity up to the age of 28 days, in order to follow the curing procedure recommended in Esmaeeli et al. (2012) for this type of panels. The load was applied by using a servo closed loop control equipment, taking the signal read in the displacement transducer (LVDT) of the servo-actuator to control the test at a deflection rate of 0.01 mm/s. The deflections of the beams at loaded section and at mid-span were measured by two LVDTs. These LVDTs were supported on an aluminum bar fixed at the alignments of the supports of the beams (Figure 3-4a) in order to avoid readings non related to the beam deflection, such as support settlements and deformability of the test reaction frame (Costa and Barros 2010). With the purpose of obtaining the strain variation along the laminates, strain gages (SG) were bonded to the CFRP laminates according to the arrangement represented in Figure 3-4b.

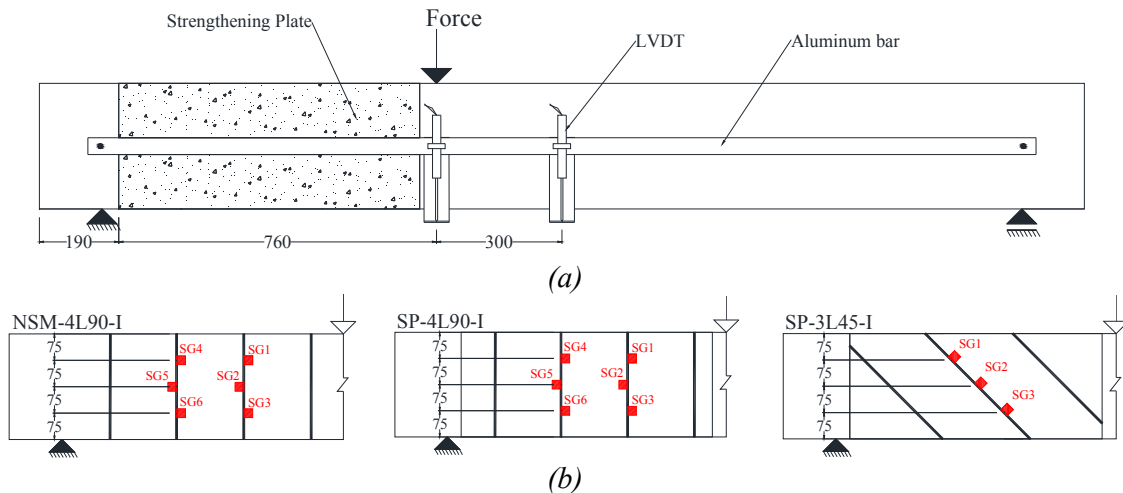


Figure 3-4: Monitoring system- position of the: (a) LVDTs, and (b) strain gages in CFRP laminates (dimensions in mm)

3.3.2 Material properties

The concrete compressive strength was evaluated at 28 days and 99 days by executing direct compression tests with cylinders of 150 mm diameter and 300 mm height according to EN206-1 recommendation (de Normalisation 2000). The values of tensile properties of the steel bars were obtained from uniaxial tensile tests executed according to EN10002-1 recommendations (ISO 1990). The tensile properties of the CFRP laminates and epoxy adhesive were characterized by executing uniaxial tensile tests according to the recommendations of ISO 527-5 (European Standard 1997) and ISO 527-2 (European Standard 1996), respectively.

The SHCC is composed of a cementitious mortar reinforced with 2% of volume of short discrete polyvinyl alcohol (PVA) fibers. The SHCC mix was prepared based on a previous study (Esmaeeli et al. 2013b). The dry ingredient materials (sand, S, cement, C, and fly ash, FA) were firstly mixed. In the second step, the superplasticizer (SP) and a quarter of the water (W) were combined and added to the dry ingredient materials. The rest of the water and the viscous modifier agent (VMA) were then combined and introduced into the mix. Finally, PVA fibers were added to the mortar. The SHCC mix procedure and proportions are presented in Table 3-2 and Table 3-3, respectively.

Table 3-2: SHCC mix procedure (Esmaeeli et al. 2013b)

Step	Mix ingredients in each step	Duration (s)
1	S+C+FA	30
2	0.25W+SP	150
3	0.75W+VMA	150
4	Fibers	300

Table 3-3: SHCC mix proportions based on the weight ratio percentage (Esmaeeli et al. 2013b)

Fly ash/Cement	Water/B*	Sand / B*	Admixtures/B*	PVA fibers**
120	30	50	2.2	2

*B: Binder (cement + fly ash)

**Percentage of total composite mix volume.

The envelope and the average tensile stress vs. crack opening displacement (COD) obtained in notched specimens are presented in Figure 3-5 (Esmaeeli et al. 2013b). According to these results, the average tensile stress at crack initiation and the average tensile strength of the SHCC were 2.7 and 3.5 MPa, respectively. Table 3-4 represents the average values obtained from the experimental programs for the assessment of the relevant properties of the concrete, steel bars, CFRP laminates, adhesive epoxy, and SHCC.

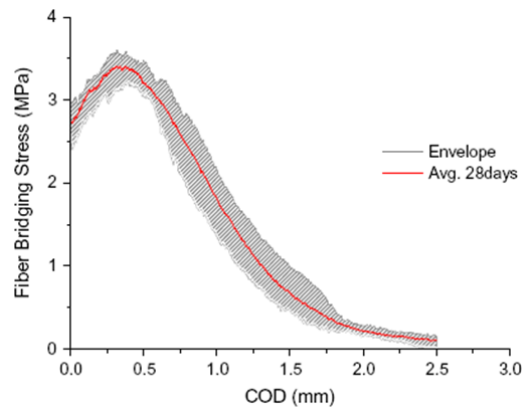


Figure 3-5: The envelope and the average tensile stress vs. crack opening displacement (COD) obtained in notched specimens (Esmaeeli et al. 2013b)

Table 3-4: Material properties

Concrete	Compressive strength			
	f_{cm} =24.5 MPa (at 28 days)		f_{cm} =32.7 MPa (at 99 days)	
	Tensile strength	$\phi 8$	$\phi 10$	$\phi 20$
Steel	f_{sym} (yield stress)	544 MPa	529 MPa	576 MPa
	f_{sum} (tensile strength)	610 MPa	625 MPa	640 MPa
CFRP laminate	Tensile strength	Elasticity modulus		Maximum strain
	f_{fum} =2617 MPa	E_{fm} =149 GPa		ε_{fu} =1.75%
Epoxy adhesive	Tensile strength	Elasticity modulus		Maximum strain
	f_{fum} =18 MPa	E_{fm} =6.8 GPa		ε_{fu} =0.4%
SHCC	Tensile stress at crack initiation	Tensile strength	Compressive strength	Young's modulus
	2.7 MPa	3.5 MPa	31.6 MPa	18.4 GPa

3.3.3 Preparation of the beams

The CFRP laminates were applied to the NSM-4L90-I beam according to the NSM technique described in Dias and Barros (2013). The slits that were opened on the lateral faces of the beam for the installation of the CFRP laminates had a width and a depth of about 5 mm and 15 mm, respectively.

The CFRP laminates adopted for the reinforcement of the SHCC plates have followed a procedure similar to the one taken for the NSM-4L90-I beam. However, in this case the slits on the SHCC plates had a width and a depth of about 4 mm and 11 mm, respectively, spaced at 180 mm and 250 mm for the SP-4L90-I ($\theta_f = 90^\circ$) and SP-3L45-I ($\theta_f = 45^\circ$) beams, respectively (Figure 3-3a and Figure 3-3b). The HCPs were applied to their corresponding beams 5 days after the application of the CFRP laminates in order to guarantee a proper curing of the adhesive.

To apply the SHCC plates and HCPs to the lateral faces of the concrete beams on L_i span, the following procedures were executed: 1) a 1-2 mm roughness with sandblast was executed to improve the bond conditions between SHCC/HCPs and concrete beams (the inspection of the tested beams showed that no slip occurred between substrate and SHCC/HCPs); 2) the surfaces of the beams were cleaned by compressed air; 3) an epoxy adhesive (S&P220) layer of a thickness of about 1 mm was homogenously applied on the surfaces of the concrete beams and SHCC/HCPs that will be in contact; 4) mechanical clamps were used to maintain the SHCC/HCPs pressed against the lateral surfaces of the beam up to the time that the epoxy resin developed its initial bond. To guarantee a proper curing of the adhesive, one week passed between the beams' strengthening operation and the beams' test.

3.3.4 Tests and results

3.3.4.1 Global Analysis

The load vs. deflection curves of the tested beams are represented in Figure 3-6a. The SP-4L90-I and SP-3L45-I beams presented higher load carrying capacity and stiffness than the other beams, except 7S-R-I beam, which reveals the shear strengthening effectiveness of the HCPs for the overall behavior of this type of beams.

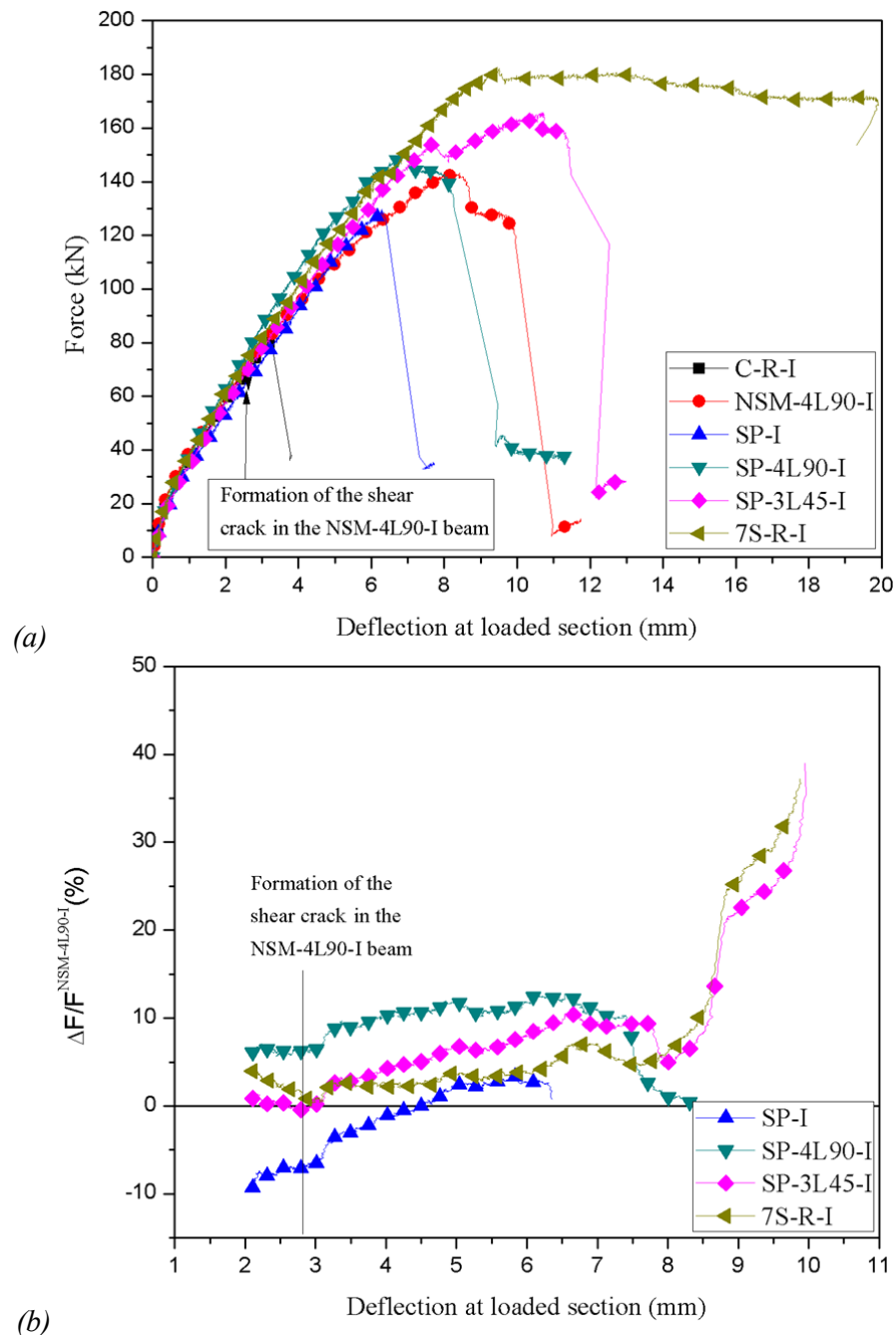


Figure 3-6: (a) Force vs. deflection at the loaded-section, and (b) $\Delta F / F^{NSM-4L90-I}$ vs. deflection at the loaded-section for the beams strengthened with SHCC plates and HCPs

The maximum load and its corresponding deflection of the tested beams are included in Table 3-5. The maximum deflection at the loaded section, at peak load, of the SP-3L45-I beam was 1.5 and 2.0 times higher than the corresponding deflection of the SP-4L90-I and SP-I beams, respectively.

Table 3-5: Relevant results in terms of load and deflection capacity

Beam designation	F_{\max} (kN)	Deflection at loaded section (mm)	Shear resistance (kN)	$(\frac{\Delta F}{F^{NSM-4L90-I}})_{\max}$ (%)	$\frac{\Delta F_{\max}}{F_{\max}^{C-R-I}}$ (%)	$\frac{F_{\max}}{F_{\max}^{7S-R-I}}$ (%)
C-R-I	81	3.3	51	-	-	44
NSM-4L90-I	143	8.2	91	0	77	79
SP-I	130	6.3	82	4	60	71
SP-4L90-I	151	8.3	96	14	87	83
SP-3L45-I	166	12.5	106	39	105	91
7S-R-I	182	19.9	116	37	125	100

From the obtained results the $\Delta F_{\max} / F_{\max}^{C-R-I} = (F_{\max} - F_{\max}^{C-R-I}) / F_{\max}^{C-R-I}$ ratio was evaluated, and the values are indicated in Table 3-5, where F_{\max}^{C-R-I} and F_{\max} are the maximum load capacity of the C-R-I beam and shear strengthened beams, respectively. For deflections greater than the corresponding to the formation of the first shear crack in the NSM-4L90-I beam, it was calculated the $\Delta F / F^{NSM-4L90-I}$ ratio where ΔF is the increase of the load provided by SHCC plates and HCPs ($\Delta F = F - F^{NSM-4L90-I}$), being $F^{NSM-4L90-I}$ the load capacity of the beam shear strengthened with CFRP laminates applied according to the NSM technique, and F is the corresponding (for the same deflection) load capacity of the other shear strengthened beams. The values of the $F_{\max} / F_{\max}^{7S-R-I}$ ratio are also presented, where F_{\max}^{7S-R-I} is the maximum load carrying capacity of the 7S-R-I beam.

The results show that the shear strengthening configuration formed by HCPs including CFRP laminates at 45° (SP-3L45-I) was the most effective in terms of maximum load carrying capacity ($\Delta F_{\max} / F_{\max}^{C-R-I}$), since an increase of 105% was obtained, while an increase of 87%, 77%, and 60% was determined for SP-4L90-I, NSM-4L90-I, and SP-I beams, respectively.

The results in Figure 3-6b and Table 3-5 show that, for deflections higher than the one corresponding to the first shear crack in the NSM-4L90-I (2.7 mm) the adopted HCPs provided an increase in the beams load carrying capacity and deflection performance. The decrease of the stiffness after the formation of the first shear crack in NSM-4L90-I beam was not so pronounced in the beams strengthened with HCPs.

By comparing the results of the SP-4L90-I and SP-3L45-I beams with those determined in the SP-I beam it is verified that the CFRP laminates have contributed for the higher shear strengthening effectiveness of HCPs, since the laminates have avoided the degeneration of the micro-cracks in the SHCC plates on macro-cracks, which had also a positive effect in terms of the stiffness preservation of the beam.

The obtained experimental results show that SP-3L45-I and SP-4L90-I beams had a maximum load of 91% and 83% of the maximum load of the 7S-R-I reference beam (F_{\max}^{7S-R-I}), respectively, the one designed for flexural failure.

3.3.4.2 Detailed Analysis

C-R-I beam

The C-R-I beam does not include any steel stirrups in the monitored shear span. During the loading of the beam, three cracks became visible at a load level of approximately 61 kN. One of these cracks, of flexural-shear nature, initiated at 250 mm from the support section, and the other two have formed at the center of the shear span. By increasing the load, the crack closer to the support section has converted in the shear failure crack, while the other cracks entered in a closing process. The crack pattern of the beam at a load of 61 kN and at failure load (81 kN) are represented in Figure 3-7a and Figure 3-7b, respectively. The maximum deflection at loaded section of the beam at failure load was 3.3 mm.

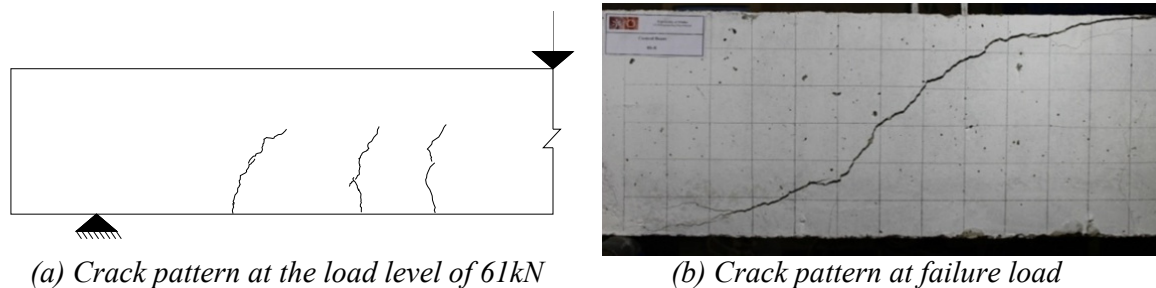
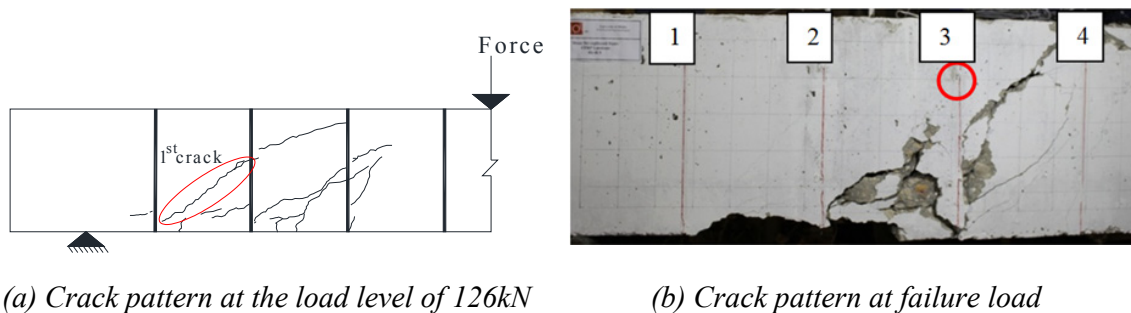


Figure 3-7: Crack patterns and failure modes of the C-R-I beam

NSM-4L90-I beam

In the NSM-4L90-I beam the first shear crack became visible at 260 mm from the support section, at the same load of the formation of the first shear crack in the reference beam (61 kN). With the increase of load, more shear cracks were formed (Figure 3-8a) in the shear span. At a load of 126 kN, cracks were formed along the longitudinal steel bars due to the dowel resistance offered by these bars to the propagation of the shear crack. Figure 3-8b shows that the laminate number 3 has crossed the shear failure crack. After the shear

contribution of this laminate has been exhausted, a sudden failure has occurred with the widening of this crack. This was followed by the splitting of a bottom concrete cover region due to the shear deformation of the longitudinal bars that have offered dowel resistance to the propagation of the shear failure crack. An ultimate load of 143 kN was achieved at a deflection of 8.2 mm. The maximum shear capacity of this beam was 77% greater than the one of the reference beam. The highest longitudinal strain reached in the CFRP laminates was recorded in the SG1 (Figure 3-4b) positioned at 81 mm from the shear failure crack (marked with a circle in Figure 3-8b), and was approximately 0.66%, which corresponds to 40% of the ultimate strain of the CFRP. This strain value and all those herein reported are not necessarily the maximum values, since they are dependent on the relative position of the SGs with respect to the shear cracks. Figure 3-9 represents the curves of the load vs. the strain in the SG where the maximum CFRP strain was registered in the strengthened beams. Up to the formation of the shear crack the maximum strain has increased almost linearly with the applied load, but did not exceed the strain value of 0.01% demonstrating that these CFRP laminates have marginal shear strengthening contribution during this stage, as expected. However, at the formation of the shear failure crack an abrupt increase of strain occurred.



(a) Crack pattern at the load level of 126kN

(b) Crack pattern at failure load

Figure 3-8: Crack patterns and failure modes of the NSM-4L90-I beam

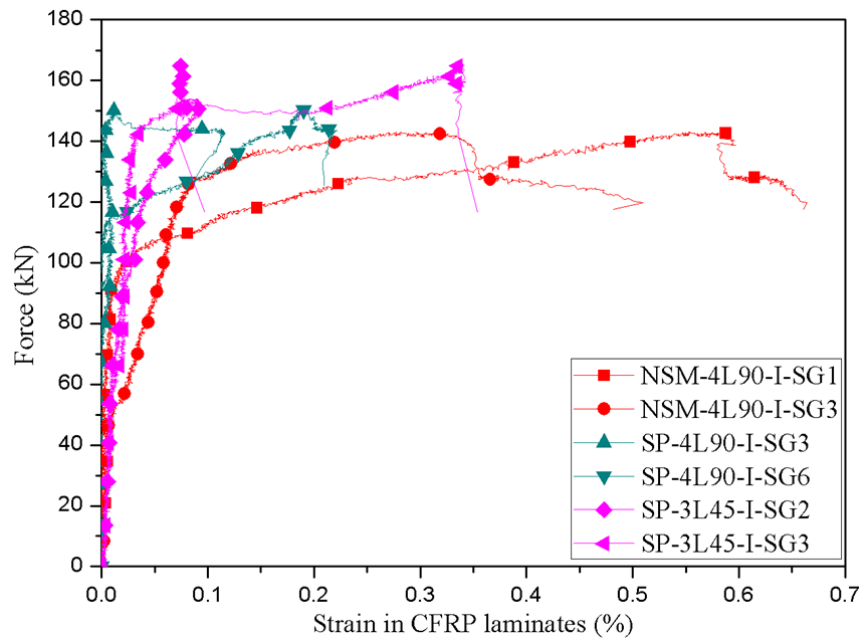
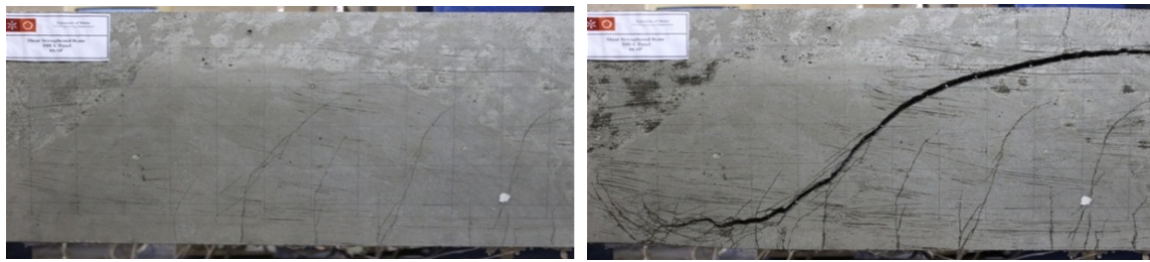


Figure 3-9: Force vs. strain in monitored laminates in SGs where the maximum strains were registered

SP-I beam

The SP-I beam was strengthened with two $720 \times 300 \times 20$ mm³ SHCC plates with weight of around 7.7 kg for each plate. During the loading process several micro-cracks have formed on the surface of the SHCC plates. Figure 3-10a and Figure 3-10b show the crack patterns a load level of about 124 kN and at failure, respectively. At a load level of 124 kN the cracks are visible by spraying oil (WD-40) on the surface of the SHCC plates. At a load of 130 kN a shear failure crack became well visible and shear failure occurred. By applying the SHCC plates to the lateral faces of the beam, the weight and width of the SP-I beam's cross section became 5% and 27%, respectively, more than the one of the control beam. However, the shear resistance and the maximum deflection of the SP-I beam increased 60% and 92% compared to the control beam, respectively. In Figure 3-11 the crack patterns of C-R-I (gray color) and SP-I (black color) beams are compared at their corresponding maximum load. The shear failure crack in both beams has quite similar configuration, but SP-I beam presents much more flexural cracks, whose energy in its formation, as well as the resistance of the SHCC plate on the propagation of the shear failure crack have contributed for the significant increase in terms of load carrying capacity registered in this beam. Both beams presented a brittle behavior, with an abrupt load decay at peak load. As already indicated, the SHCC was reinforced with 2% in volume of PVA fibers of 40 μ m diameter and 8 mm length. The

reinforcement mechanisms of these fibers were not able to absorb in a stable way the huge amount of energy released in the formation process of critical shear cracks.



(a) After spraying the oil on the surface of the SHCC plates of SP-I beam

(b) Crack pattern at failure load of the SP-I beam

Figure 3-10: Crack patterns and failure modes of the SP-I beam

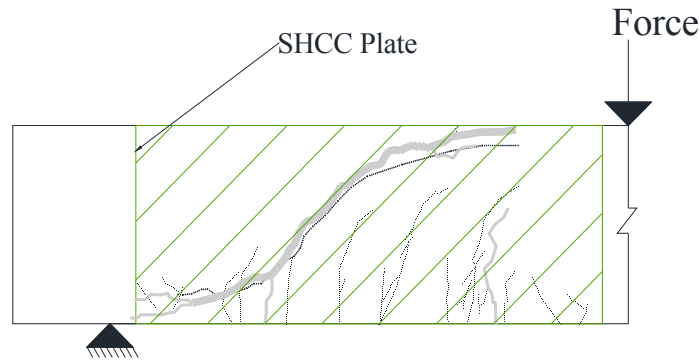
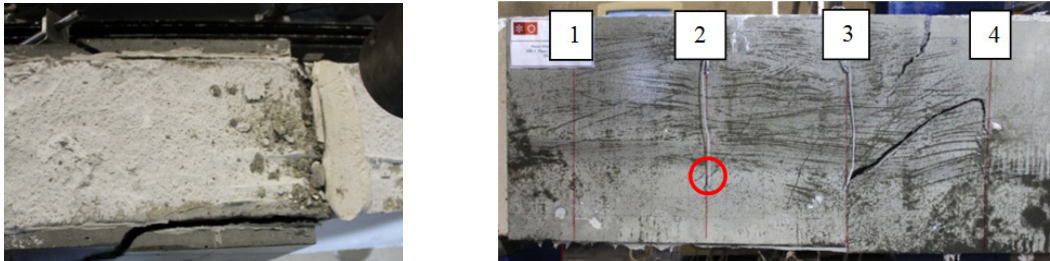


Figure 3-11: Crack patterns of the C-R-I (gray color) and SP-I (black color) at failure load

SP-4L90-I beam

The SP-4L90-I beam had no steel stirrups in the monitored shear span, and was strengthened with HCPs applied on the beam's lateral faces in this span. The HCPs were formed by SHCC plates strengthened by four vertical ($\theta_f = 90^\circ$) CFRP laminates spaced at 180 mm (Figure 3-3a). Vertical lines in Figure 3-12b represent the position of the CFRP laminates. Like in SP-I beam, by increasing the load several micro-cracks have formed on the surface of the HCPs. This beam failed at a load level of 151 kN with the formation of a shear failure crack between the two CFRP laminates closest to the point load (number 3 and 4), followed of the detachment of a part of the HCP that also included some concrete cover (Figure 3-12a and Figure 3-12b). This alteration on the failure mode, assured by the HCP, has provided an increase of load carrying capacity (17%) and its corresponding deflection (33%) when compared to the SP-I beam, due to the contribution of the CFRP laminates. The highest longitudinal strain reached in the CFRP laminates was recorded by the SG6 (Figure 3-4b) at 15 mm from a diagonal thin crack, and was approximately 0.21%, which corresponds to

12.7% of the ultimate strain of the CFRP laminate. The position of this strain gage is illustrated in Figure 3-12b by a circle. The premature detachment of the HCPs justifies the relatively low collaboration of the CFRP laminates for the shear strengthening, demonstrated by the too low maximum strain registered (Figure 3-9).



(a) Detachment of the HCPs in SP-4L90-I beam

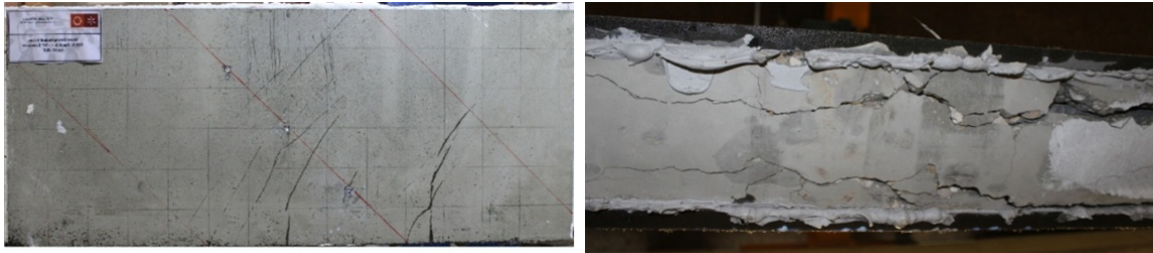
(b) Failure mode of the SP-4L90-I beam

Figure 3-12: Crack patterns and failure modes of the SP-4L90-I beam

SP-3L45-I beam

Although the shear CFRP strengthening ratio has been the same in the SP-3L45-I and SP-4L90-I beams ($\rho_{fw}^{SP-4L90-I} = \rho_{fw}^{SP-3L45-I} = 0.10\%$), the inclination of the CFRP laminates was different, leading to differences on the contribution of these laminates for the shear strengthening of this type of beams. The HCPs of the SP-3L45-I beam were formed by SHCC plates strengthened with three $\theta_f = 45^\circ$ CFRP laminates spaced at 250 mm (Figure 3-3b). The inclined lines in Figure 3-13a represent the position of the CFRP laminates. The first shear crack was detected at a load level of 76 kN. Figure 3-13a shows the crack pattern of this beam at a load level of 123 kN, where it is visible the formation of flexural and flexural-shear cracks. The failure of the beam is governed by the detachment of the HCPs (Figure 3-13b), each one bringing together part of the concrete cover of the lateral surface of the beam, which is a failure mode already reported in Dias and Barros (2013) when high percentage of CFRP laminates are used on the shear strengthening of RC beams. Like in the SP-4L90-I beam, the load carrying capacity of the SP-3L45-I beam was limited by this typical failure mode. However, the better orientation of the CFRP laminates in relation to the shear cracks formed in the concrete core of the SP-3L45-I beam has assured a larger area of concrete fracture during the detachment process of the HCPs (as is clearly visible when Figure 3-12a and Figure 3-13b are compared), which caused a higher load carrying capacity and its corresponding deflection in this beam, when compared to the SP-4L90-I beam. In fact failure occurred at a load level of 166 kN, indicating an increase of 105%, 16%, 28%, and

10% compared with C-R-I, NSM-4L90-I, SP-I, and SP-4L90-I, respectively. The maximum longitudinal strain reached in the CFRP laminates (SG3, Figure 3-4b) was approximately 0.35%, which corresponds to 21% of the ultimate strain of the CFRP. Like already pointed out for the SP-4L90-I beam, the detachment of the HCPs also occurred in the SP-3L45-I beam has avoided the mobilization of the shear strengthening potentialities of the CFRP laminates.



(a) Crack pattern in the lateral surface of SP-3L45-I beam at the load level of 123kN

(b) Crack pattern in the bottom surface at failure load of SP-3L45-I beam

Figure 3-13: Crack patterns and failure modes of the SP-3L45-I beam

7S-R-I beam

As expected, the beam shear reinforced in the shear span with steel stirrups of $\phi 8@100$ (7S-R-I) failed in bending with the yielding of the flexural reinforcement (at 182 kN), followed by the concrete crushing (at about 170 kN and a deflection of 20 mm) in the loaded zone (Figure 3-14).



Figure 3-14: Crack patterns and failure modes of the 7S-R-I beam

3.4 Series II: Beams of T Cross Section

3.4.1 Beams and test setup

Figure 3-15 presents the T cross section of the tested beams. The reinforcement systems were designed to assure shear failure mode for the beams. The longitudinal reinforcement consisted of $2\phi 32$ and $1\phi 16$ laid at the bottom, and $6\phi 12$ at the flange of the beams as tensile and compression reinforcement, respectively, giving to the beam cross section an effective depth of 355 mm. To localize the shear failure in only one of the shear span, a three point bending test setup with different shear span lengths was adopted. The length of the monitored shear span (L_i) was 2.5 times the effective beam's depth. To avoid shear failure in the other span a relatively high percentage of steel stirrups ($\phi 6@75$) was applied in this span (L_r). The experimental program was made up of one beam with steel stirrups $\phi 6@112.5$ mm (7S-R-II beam, $\rho_{sw} = 0.28\%$), and seven beams with no steel stirrups in L_i shear span.

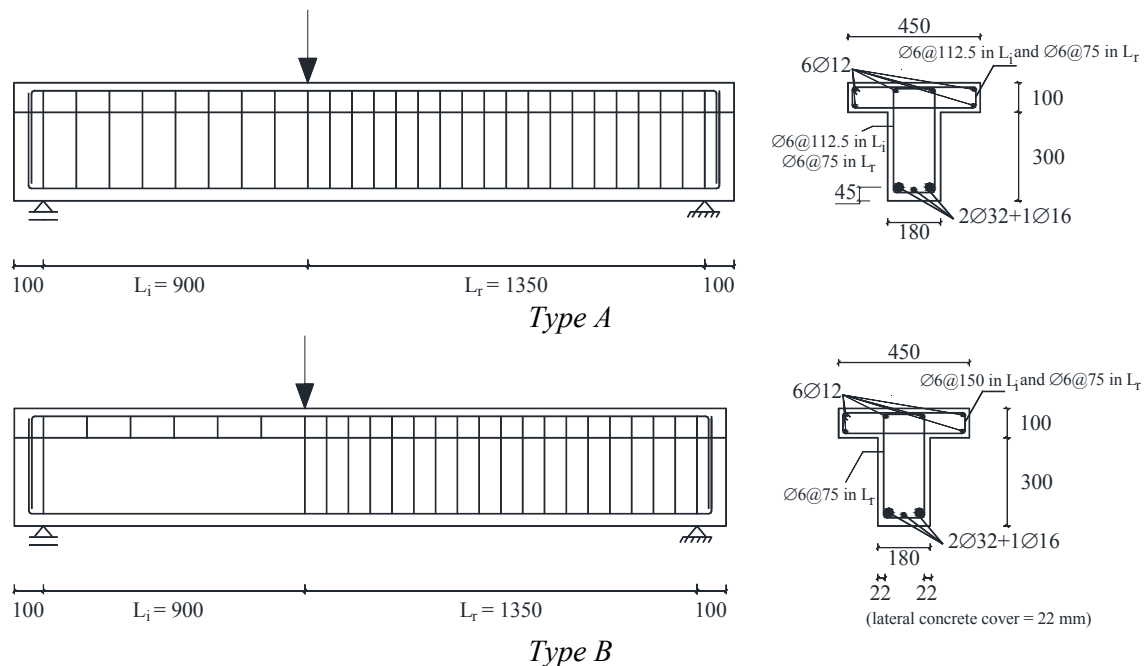


Figure 3-15: Geometry and reinforcement arrangement of the concrete beams (dimensions in mm)

The shear strengthening effectiveness of the following variables is aimed to be examined in this experimental program:

- CFRP shear percentage ($\rho_{fw} = 0.08\%$ and 0.14%);
- Application of mechanical anchors;

The characteristics of the beams are presented in Table 3-6. The C-R-II was a reference beam without any type of shear reinforcement and strengthening in the L_i shear span. The NSM-3L45-II was a beam without steel stirrups in the L_i span, and was strengthened according to the NSM technique with 3 inclined CFRP laminates ($\theta = 45^\circ$) in each lateral face of L_i span, spaced at 275 mm (s_f). The SP-II was a beam strengthened with SHCC plates to study the effectiveness of these plates for the shear strengthening of T cross section beams. Each plate had overall dimension and weight of $800 \times 300 \times 20$ mm³ and 8.6 kg, respectively. The SHCC plates were bonded to concrete substrate by using epoxy adhesive (S&P 220). By applying the SHCC plates to the lateral faces of the beam the weight and width of beam's cross section became, respectively, 5% and 22%, larger than the corresponding ones of the control beam (C-R-II).

Table 3-6: Shear strengthening/reinforcement in the monitored shear span of the tested beams

<i>Beam designation</i>	<i>Shear strengthening/reinforcement configuration</i>	<i>Quantity</i>	<i>Connection of the SHCC/HCP to substrate</i>	<i>Percentage of CFRP laminates (%)</i>	<i>Spacing, s_f, (mm)</i>
<i>C-R-II</i>	-	-	-	-	-
<i>NSM-3L45-II</i>	NSM CFRP laminates of 1.4×10 mm ² cross section	2×3 CFRP laminates	-	0.08	275
<i>SP-II</i>	SHCC Plates	20mm thickness of SHCC	Adhesive	-	-
<i>SP-3L45-II</i>	HCPs (20 mm thickness of SHCC reinforced with CFRP laminates of 1.4×10 mm ² cross section)	2×3 CFRP laminates	Adhesive	0.08	275
<i>SP-5L45-II</i>		2×5 CFRP laminates		0.14	157
<i>SP-3L45-B-II</i>	HCPs (20 mm thickness of SHCC reinforced with CFRP laminates of 1.4×10 mm ² cross section)	2×3 CFRP laminates	Adhesive and mechanical anchors	0.08	275
<i>SP-5L45-B-II</i>		2×5 CFRP laminates		0.14	157
<i>7S-R-II</i>	Steel stirrups	φ6		-	-

Based on the results of the beams tested in previous section (rectangular cross section), and considering the recommendations in the literature about the influence of the orientation of NSM CFRP systems on the shear strengthening effectiveness of RC beams (De Lorenzis and Nanni 2001, Dias and Barros 2010), the arrangement consisting of laminates at 45° was selected for this experimental program since it is expected as the most effective. The SP-3L45-II and SP-5L45-II beams were strengthened by applying HCPs in each lateral face of the L_i shear span using epoxy adhesive. As shown in Figure 3-16, the HCP is a 20 mm thick SHCC plate that was reinforced with three or five inclined CFRP laminates, spaced at 275 mm (SP-3L45-II series) and 157 mm (SP-5L45-II series).

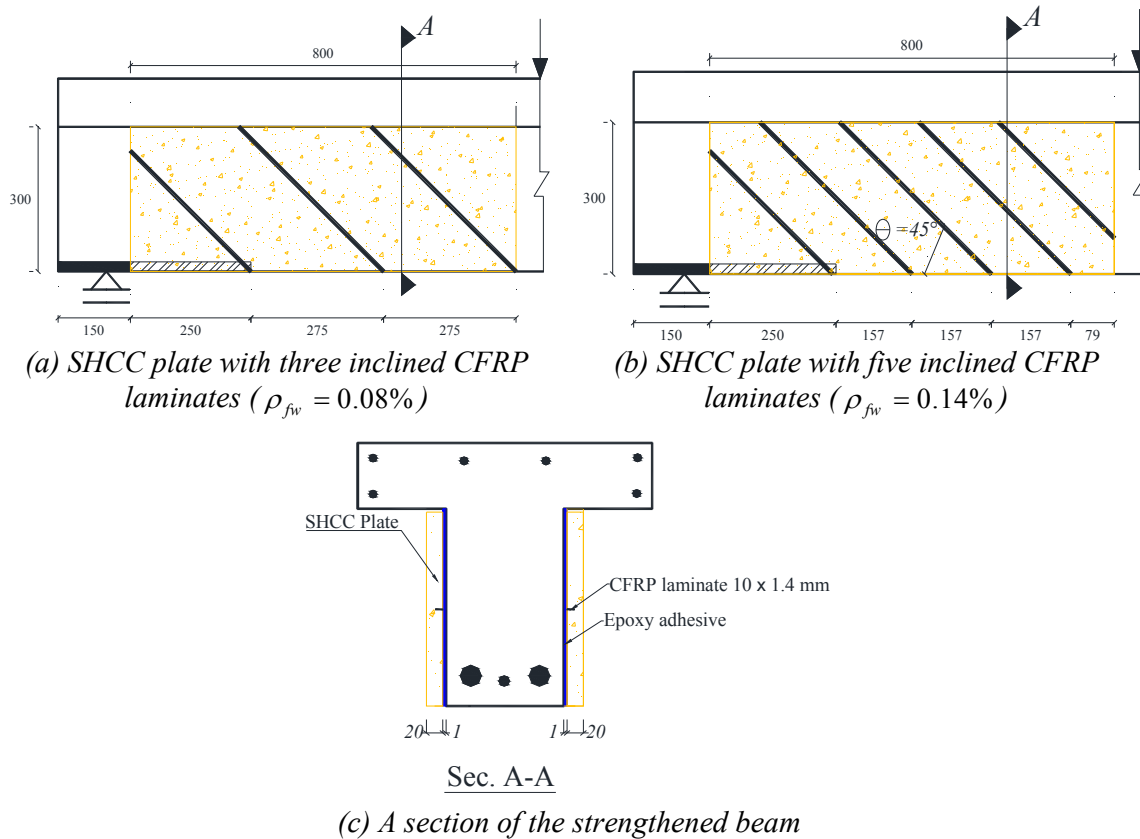


Figure 3-16: Position of the CFRP laminates of the HCPs in: (a) SP-3L45-II beam, (b) SP-5L45-II beam, (c) a section of the strengthened beam with HCP (dimensions in mm)

Based on the results of the tested beams in previous section, the shear strengthening contribution of the HCPs can be limited by the tensile strength of the concrete substrate. In order to full explore the shear strengthening potentialities of HCPs, in this program the HCPs applied in the SP-3L45-B-II and SP-5L45-B-II beams were not only bonded to lateral faces of these beams using epoxy adhesive, but also fixed to the beams with 12 bolts of 10 mm diameter, according to the configuration represented in Figure 3-17. The application of these mechanical anchors aims to prevent a premature debonding of the HCPs, and since the bolts were applied with a torque meter device, a certain concrete confinement can be introduced in the zone of the beam to be strengthened, resulting favorable effects in terms of shear strengthening.

The load was applied by using a servo closed loop control equipment, taking the signal read in the displacement transducer (LVDT) of the servo-actuator to control the test at a deflection rate of 0.01 mm/s. The deflections of the beams at loaded section and at mid-span were measured by two LVDTs that were supported on an aluminum bar fixed at the alignments of the supports of the beams (Figure 3-18a). With the purpose of obtaining the strain variation in

the laminates, strain gages (SG) were bonded to the CFRP laminates according to the arrangement represented in Figure 3-18b.

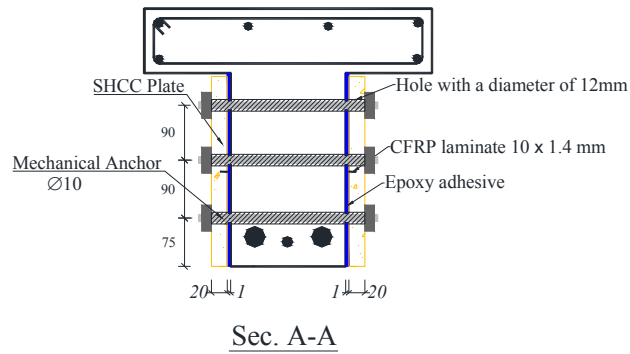
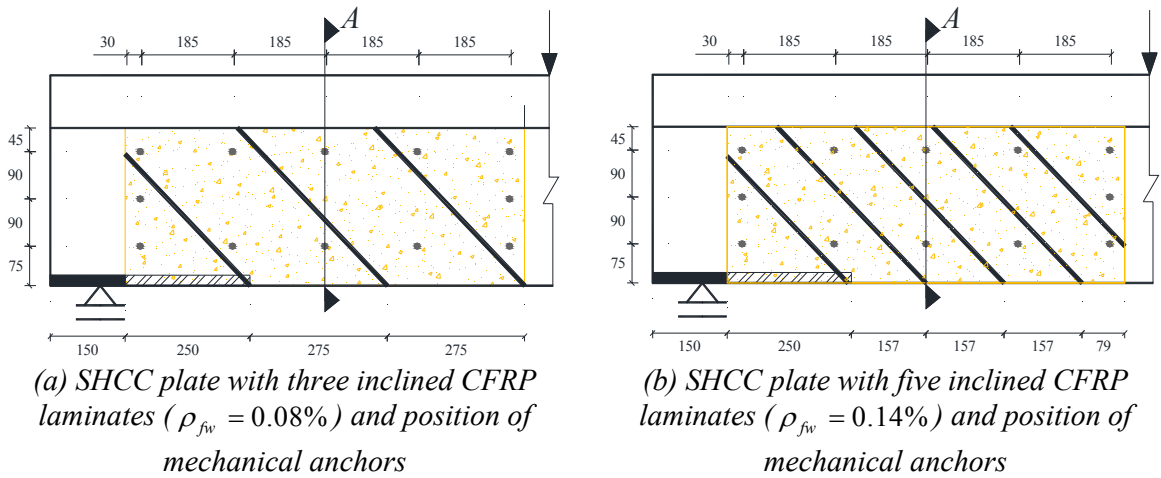


Figure 3-17: Position of the CFRP laminates and mechanical anchors (a) SP-3L45-B-II, (b) SP-5L45-B-II, (c) position of the bolts inside of the RC beams (dimensions in mm)

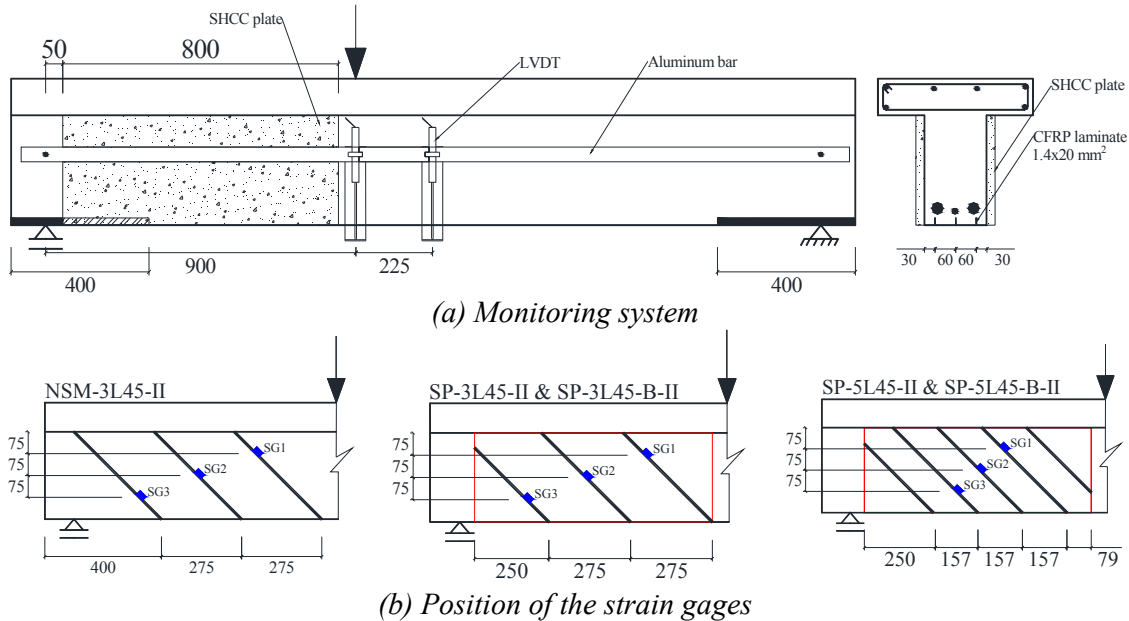


Figure 3-18: Monitoring system- position of the: (a) LVDTs, and (b) strain gages in CFRP laminates (dimensions in mm)

Table 3-7 includes the average values obtained from the experimental programs for the assessment of the relevant properties of the concrete, steel bars, CFRP laminates, epoxy adhesive, and SHCC.

Table 3-7: Values of the properties of intervening materials

Concrete	Compressive strength				
	$f_{cm} = 32.7$ MPa (at 45 days)				
Steel bars	Tensile strength	$\phi 6$	$\phi 12$	$\phi 16$	$\phi 32$
	f_{sym} (yield stress)	500 MPa	490 MPa	470 MPa	625 MPa
	f_{sum} (tensile strength)	594 MPa	591 MPa	566 MPa	905 MPa
CFRP laminate	Tensile strength	Elasticity modulus		Maximum strain	
	$f_{fum} = 2617$ MPa	$E_{fm} = 149$ GPa		$\epsilon_{fu} = 1.75\%$	
Epoxy adhesive	Tensile strength	Elasticity modulus		Maximum strain	
	$f_{fum} = 18.00$ MPa	$E_{fm} = 6.8$ GPa		$\epsilon_{fu} = 0.4\%$	
SHCC	Tensile stress at crack initiation	Tensile strength	Tensile strain at tensile strength	Compressive strength	Young's modulus
	2.7 MPa	3.5 MPa	1.3%	31.6 MPa	18.4 GPa

3.4.2 Preparation of the beams

The NSM CFRP laminates, SHCC plates, and HCPs were applied to the RC beams adopting the same procedures applied in the corresponding RC beams of the previous experimental program. However, in the SP-3L45-B-II and SP-5L45-B-II beams, twelve holes were drilled

through web of the beams with a diameter of 12 mm for the installation of mechanical anchors as illustrated in Figure 3-17. The HCPs were also fixed to the concrete substrate of these beams with 12 mechanical fasteners composed of bolts and nuts, by applying a torque of 20 N.m in the nuts on both sides of the beams. To guarantee a proper curing of the adhesive, one week passed between the beams' strengthening operation and the beams' test. To improve the anchorage conditions of the longitudinal reinforcement, and therefore avoid concrete spalling at the beam support section, a strengthening system based on the use of longitudinal NSM CFRP laminates of $1.4 \times 20 \text{ mm}^2$ cross section, and with a total length of 400 mm, was applied on the bottom face of the beams, as illustrated in Figure 3-18a.

3.4.3 Tests and results

3.4.3.1 Global Analysis

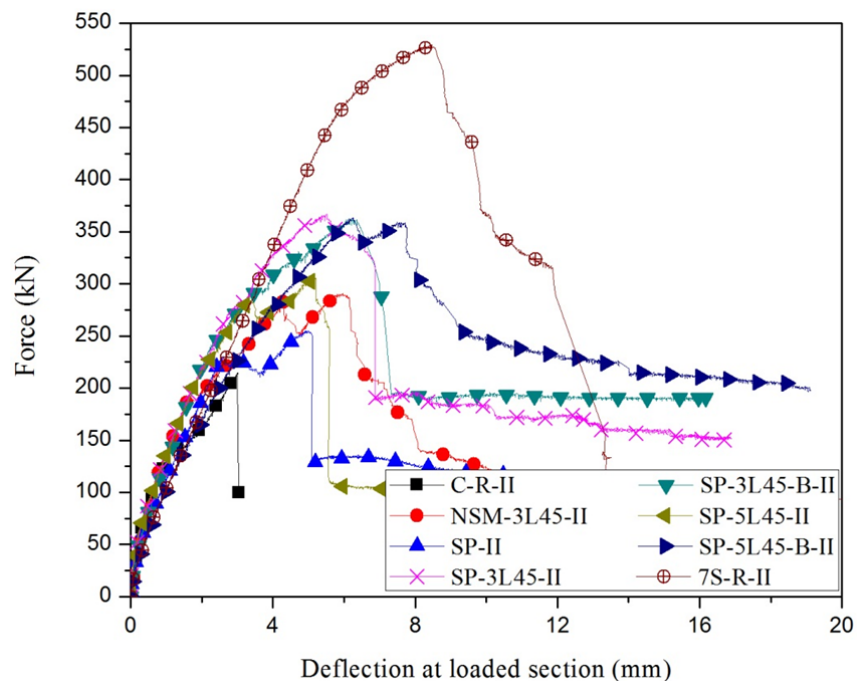
The relationships between force and deflection of the tested beams are presented in Figure 3-19:a. The SP-3L45-II, SP-3L45-B-II, and SP-5L45-B-II beams presented higher load carrying capacity compared to other beams, except 7S-R-II beam, which shows the effectiveness of HCPs for the shear strengthening. The loaded section deflection at peak load of the SP-5L45-B-II beam was around 1.1 and 1.3 times higher than the corresponding deflection of the NSM-3L45-II and SP-II beams, respectively.

From the obtained results the $\Delta F_{\max} / F_{\max}^{SP-II} = (F_{\max} - F_{\max}^{SP-II}) / F_{\max}^{SP-II}$ ratio was evaluated, and the values are indicated in Table 3-8, where F_{\max}^{SP-II} and F_{\max} are the maximum load capacity of the beam strengthened with SHCC plates and of the other shear strengthened beams, respectively. For deflections greater than the corresponding to the formation of the first shear crack in the NSM-3L45-II and SP-II beams, it was calculated the $\Delta F^{NSM-3L45-II} / F^{NSM-3L45-II}$ and $\Delta F^{SP-II} / F^{SP-II}$ ratios, where ΔF is the increase of the load provided by HCPs ($\Delta F^{NSM-3L45-II} = F - F^{NSM-3L45-II}$, $\Delta F^{SP-II} = F - F^{SP-II}$), being $F^{NSM-3L45-II}$ and F^{SP-II} the load capacity of the beam strengthened with NSM CFRP laminates and SHCC plates, respectively, and F is the corresponding load capacity (for the same deflection) of the other strengthened beams with HCPs. These ratios were calculated up to $3\Delta_u^{SP-II}$ of the SP-II beam, where Δ_u^{SP-II} is the deflection corresponding to the maximum load of the SP-II beam. The values of the $F_{\max} / F_{\max}^{7S-R-II}$ ratio are also presented in Table 3-8, where $F_{\max}^{7S-R-II}$ is the maximum load carrying capacity of the 7S-R-II beam.

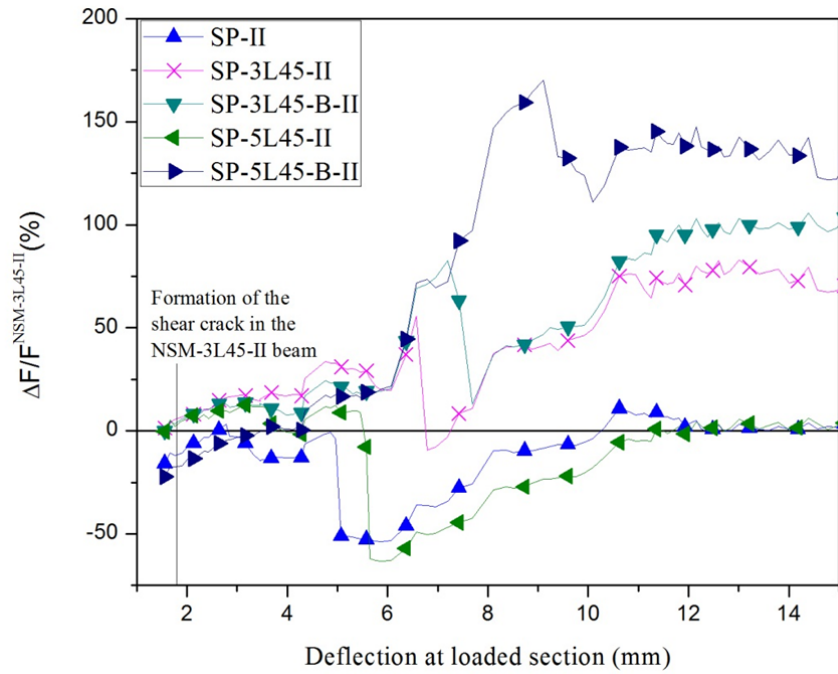
The results in Table 3-8 and Figure 3-19:b and Figure 3-19:c show that, for deflection higher than the one corresponding to the first shear crack in the NSM-3L45-II (1.8 mm) and SP-II (2.6 mm) beams, respectively, the adopted HCPs provided an increase in the beams load carrying capacity and deflection performance. The load of the SP-5L45-B-II and SP-3L45-B-II beams at deflection of about 15 mm is around 125% and 100% higher than the load of NSM-3L45-II and SP-II beams, respectively. These results show the effectiveness of the HCPs and also of the mechanical anchors in terms of post peak load carrying and deformability capacity. In fact, apart SP-5L45-II beam, the post-peak performance of the beams shear strengthened with HCPs was much higher than the performance of the NSM-3L45-II and SP-II beams.

Table 3-8: Relevant results in terms of load and deflection capacity

Beam designation	F_{\max} (kN)	Deflection at loaded section Δ_u (mm)	Shear resistance (kN)	$\left(\frac{\Delta F^{NSM-3L45-II}}{F^{NSM-3L45-II}}\right)_{\max}$ (%)	$\left(\frac{\Delta F^{SP-II}}{F^{SP-II}}\right)_{\max}$ (%)	$\frac{\Delta F_{\max}}{F_{\max}^{SP-II}}$ (%)	$\frac{F_{\max}}{F_{\max}^{7S-R-II}}$ (%)
C-R-II	214	3.0	128	-	-	-	-
NSM-3L45-II	291	5.9	174	0	-	14	55
SP-II	255	5.0	153	11	0	0	50
SP-3L45-II	367	5.5	220	85	176	44	70
SP-3L45-B-II	363	6.2	218	106	178	43	70
SP-5L45-II	306	5.1	184	14	131	20	58
SP-5L45-B-II	364	6.3	218	174	196	43	70
7S-R-II	530	8.4	318	444	-	108	100

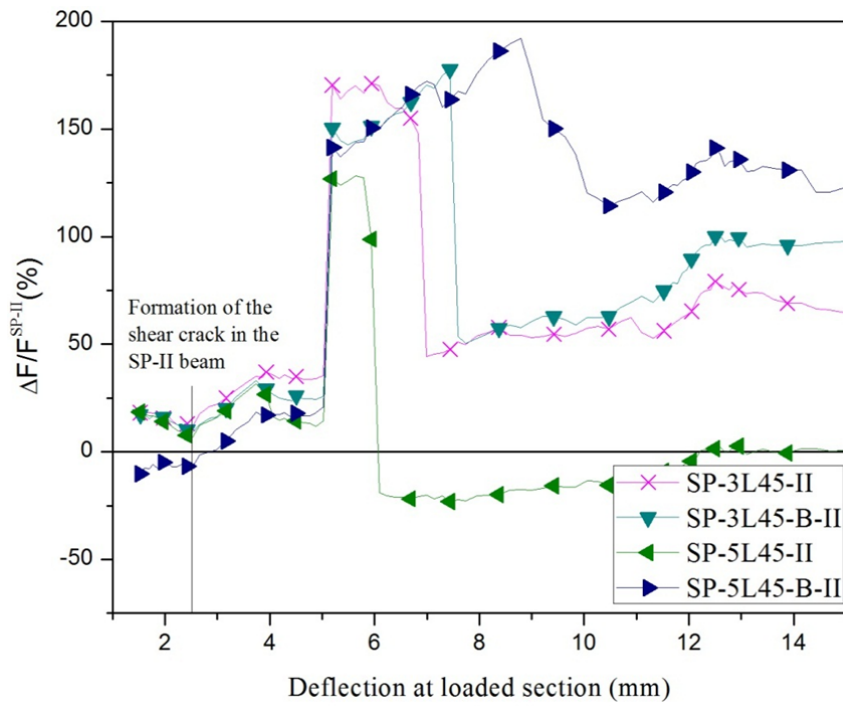


(a)



(b)

Figure 3-19: (a) Force vs. deflection at the loaded-section, (b) $\Delta F / F^{NSM-3L45-II}$ vs. deflection at the loaded-section for the beams strengthened with SHCC/HCPs, and (c) $\Delta F / F^{SP-II}$ vs. deflection at the loaded-section for the beams strengthened with HCPs



(c)

Figure 3-19: (Continued.)

By comparing the results of the strengthened beams with HCPs with those determined in the SP-II beam ($\Delta F_{\max} / F_{\max}^{SP-II}$) it is verified that the CFRP laminates have contributed for the higher shear strengthening effectiveness of HCPs, as mentioned, the laminates have avoided the degeneration of the micro-cracks in the SHCC plates on macro-cracks, which had also a positive effect in terms of the stiffness preservation of the beam.

The obtained experimental results show that, apart SP-5L45-II beam, the beams strengthened with HCPs had a maximum load of about 70% of the maximum load of the 7S-R-II reference beam ($F_{\max}^{7S-R-II}$).

3.4.3.2 Detailed analysis

C-R-II beam

The C-R-II beam had no steel stirrups in monitored shear span. At a load of about 100 kN, two cracks became visible. One crack initiated at the support section (splitting crack), and the other one formed at the center of the shear span (Figure 3-20a). By increasing the load, the cracks widened and propagated up to load of 214 kN. At this load the beam failed at the support section before shear failure of the beam occurred (Figure 3-20b). This failure mode was not expected and was caused by a deficient execution of the anchorage length of the longitudinal reinforcement. As mentioned, the other beams were strengthened by three longitudinal CFRP laminates with length of 400 mm at support to avoid failure of the beams at supports (Figure 3-18a).

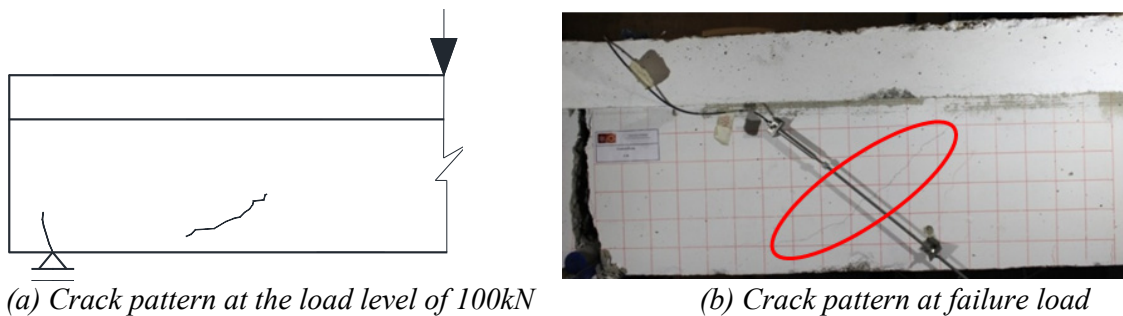


Figure 3-20: Crack patterns and failure modes of the C-R-II beam

The C-R-II beam in this experimental had the same configuration and geometry to the C-R beam in the experimental program that was carried out by Dias and Barros (2010). They reported the C-R-II beam in their experimental program failed in shear at a load of 207 kN. As shown in Figure 3-20b by a red ellipse, at a load of 214 kN and deflection of 3.0 mm the critical shear crack formed, and it did not degenerate in a shear failure crack due to the unexpected splitting failure crack at the support of the beam due to the aforementioned

reasons. The results obtained in the numerical simulations of these tested beams (as it will be shown in chapter 4), the shear failure load of the C-R-II beam would be 215kN.

7S-R-II beam

As shown in Figure 3-15, the 7S-R-II beam has seven steel stirrups $\phi 6@112.5$ mm ($\rho_{sw} = 0.28\%$) in the monitored shear span. The first shear crack became visible at the center of the L_i span (160 kN), Figure 3-21a. As indicated in Mofidi and Chaallal (2011), in a RC beam with an adequate percentage of steel stirrups, the shear crack pattern tends to be distributed over a large width. In fact, another shear crack was formed at a load of 230 kN, almost parallel to the first shear crack, at around 500 mm from the support section (Figure 3-21a). By increasing the load these two cracks have widened and propagated up to failure load. This beam failed at a load level of 530 kN (Figure 3-21b) when the deflection was 8.4 mm. The beam presented a shear brittle behavior, with an abrupt load decay at peak load.

As shown in Figure 3-19:a, after an abrupt load decay, the load was stabilized at a load level of about 100 kN (19% of maximum load).

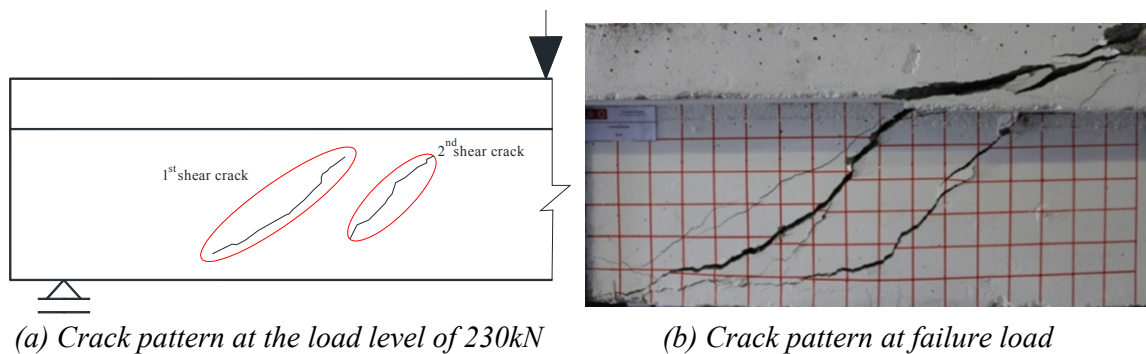
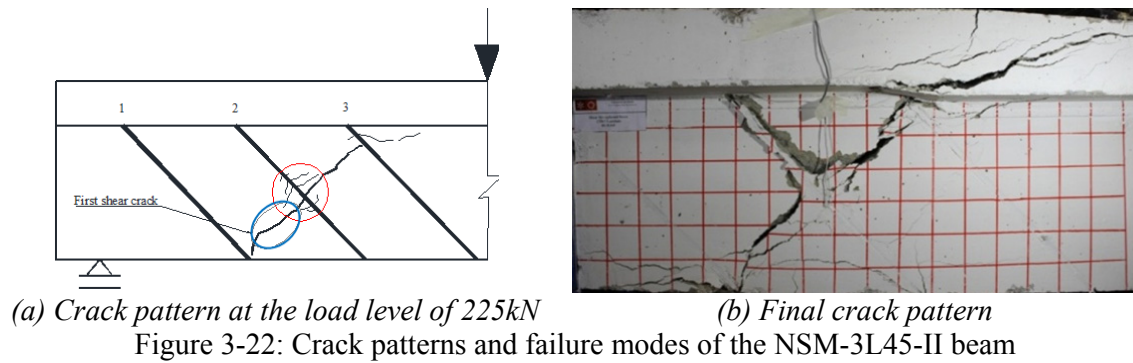


Figure 3-21: Crack patterns and failure modes of the 7S-R-II beam

NSM-3L45-II beam

The NSM-3L45-II beam had no steel stirrups in the monitored shear span. This beam was strengthened with three inclined (45°) CFRP laminates in each lateral face of monitored shear span, spaced at 275 mm. The CFRP shear strengthening percentage of this beam was $\rho_{fw} = 0.08\%$. The first shear crack became visible at around 350 mm from the support section (between laminates number 1 and 2, blue ellipse in Figure 3-22a), at a load level of about 173 kN.



As reported in Bianco et al. (2011), the failure mode of a NSM CFRP laminate subjected to an imposed end slip can be categorized into four groups: a) debonding, b) tensile rupture of laminate, c) concrete semi-pyramid tensile fracture, and d) a mixed shallow semi-pyramid plus debonding failure mode (Figure 3-23). These modes of failure are dependent on the relative mechanical and geometric properties of the materials involved. When principal tensile stresses transferred to the surrounding concrete attain its tensile strength, concrete fractures along a surface, envelope of the compression isostatics, whose shape can be assumed as a semi-cone (Bianco et al. 2010) or a semi-pyramid (Bianco et al. 2014). As shown in Figure 3-22a by a red circle, by increasing the load, some cracks were formed around the laminate number 2, and the aforementioned mixed failure mode has occurred in this laminate. Due to the quite low bond transfer length of the other two laminates, they did marginal contribution for the ultimate shear capacity of this beam. At a load and deflection of about 275 kN and 4.1 mm, respectively, the laminate number 2 failed and the load was decreased of about 7%. After that, the load started increasing due to propagation of the shear crack through the flange of the beam towards the load area. An ultimate load of 291 kN was achieved at a deflection of 5.2 mm. In this beam only one single shear crack formed due to the relatively low shear reinforcement.

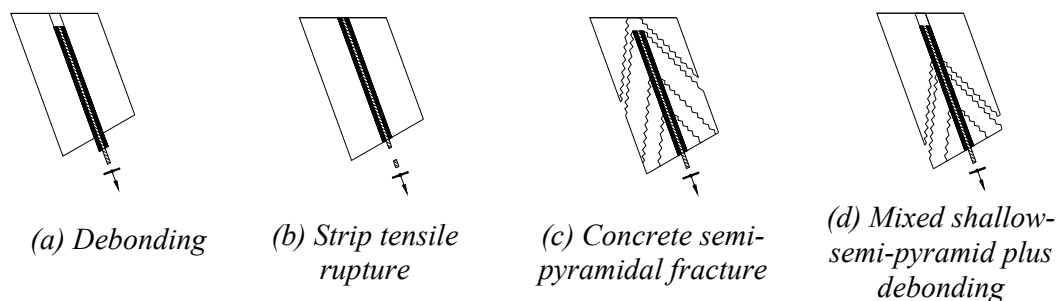


Figure 3-23: The mode of failure of an NSM CFRP laminate subjected to an imposed end slip (Bianco et al. 2010)

At the failure, the beam's load carrying capacity decreased and was stabilized at a load level of about 32% of the maximum load. Due to the crack pattern formed at the failure of the NSM-3L45-II beam (Figure 3-22b), the highest longitudinal strain in the CFRP laminates was recorded in the SG2 (Figure 3-18b) positioned almost coinciding with the shear failure crack, and was approximately 1.04%, which corresponds to 63% of the ultimate strain of the CFRP laminate. Figure 3-24 represents the relationship between applied load and strain in the SGs where the maximum CFRP strain was registered in the strengthened beams.

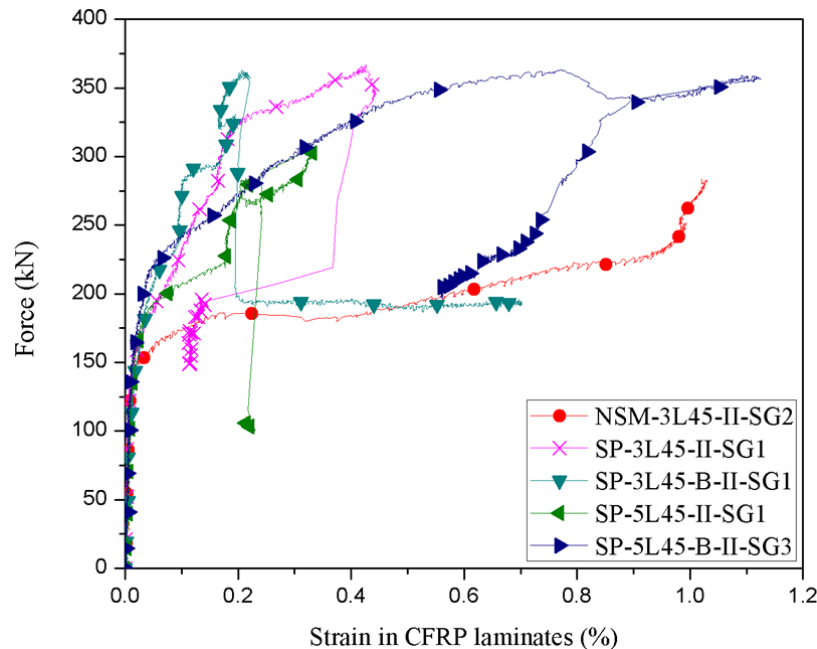


Figure 3-24: Force vs. strain in monitored laminates in SGs where the maximum strains were registered

SP-II beam

The SP-II beam was strengthened with two $800 \times 300 \times 20 \text{ mm}^3$ SHCC plates that were bonded to each lateral face in L_i shear span using epoxy adhesive. The first shear crack became visible by spraying oil (WD-40) on the surface of the SHCC plate (Figure 3-25a). This shear crack formed at a load level of about 230 kN for a deflection of 2.6 mm. In this stage, the load was maintained almost constant up to deflection of around 3.5 mm, with the widening of this shear crack and the formation and propagation of some new cracks near the major shear crack. After that, the load started increasing due to the propagation of the shear failure crack through the flange of the beam towards the loaded area, and collapse has occurred at a load level of about 255 kN and a deflection of 5.0 mm (Figure 3-25b). This beam presented a brittle behavior, with an abrupt load decay in the post peak.

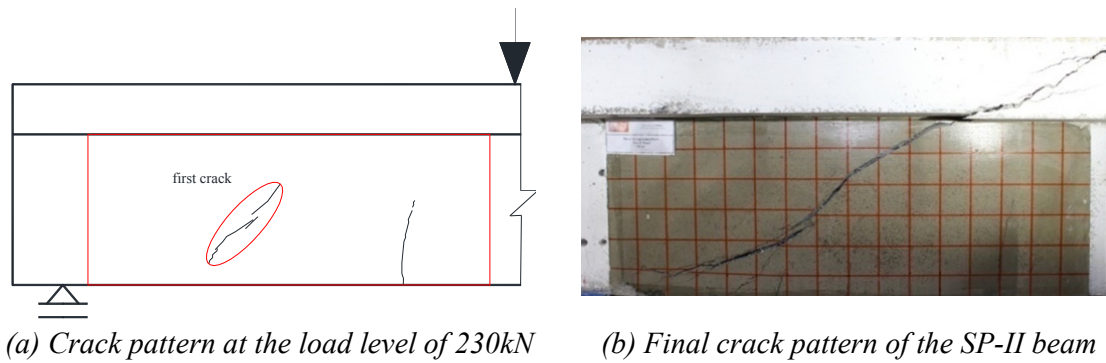


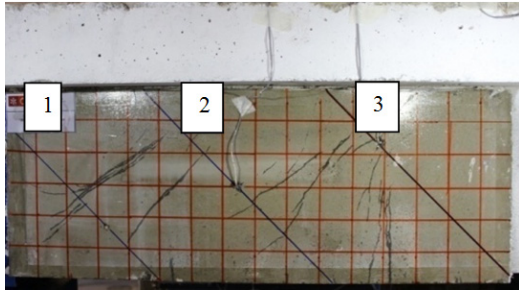
Figure 3-25: Crack patterns and failure modes of the SP-II beam

SP-3L45-II beam

The SP-3L45-II beam had no steel stirrups in L_i shear span, and was strengthened with HCPs bonded to each lateral face in the monitored shear span using epoxy adhesive. As shown in Figure 3-16a, the HCPs formed by SHCC plates reinforced with three inclined CFRP laminates, spaced at 275 mm. The inclined lines in Figure 3-26a show the position of the CFRP laminates.

The first shear crack formed at a load level of about 220 kN between laminates number 1 and 2, almost in the same location of the first shear crack in the NSM-3L45-II beam. By increasing the load, several micro-cracks formed on the surface of the HCPs Figure 3-26a shows the crack pattern of this beam at failure load.

The beam failed at a load of about 367 kN and deflection of 5.5 mm. The failure of the beam was governed by the detachment of HCPs (Figure 3-26b). As mentioned, the effectiveness level of this technique was limited by the tensile strength of the concrete cover, as shown in Figure 3-26b by red ellipse, since at failure load, part of concrete cover was attached to the HCPs and local detachment has occurred. After local detachment, the load was stabilized at a level of 42% of the maximum load (155 kN). This load level was higher than the load of the previous beams (7S-R-II and NSM-3L45-II), since HCPs had connection in the other parts, Figure 3-26c shows the local detachment of HCPs. The HCPs caused an increase of the load carrying capacity (44%) and its corresponding deflection (10%), when compared to the effect of the SHCC plates in the SP-II beam. The highest longitudinal strain in the CFRP laminates was recorded by the SG1 (Figure 3-18b), and was approximately 0.41%, which corresponds to 25% of the ultimate strain of the CFRP laminate. The detachment of the HCPs justifies the relatively low collaboration of the CFRP laminates for the shear strengthening, demonstrated by the relatively small maximum strain registered (Figure 3-24).



(a) Crack pattern at the load level of 350kN of the SP-3L45-II beam



(b) Final crack pattern of the SP-3L45-II beam when HCP was peeled off after the test

Figure 3-26: Crack patterns and failure modes of the SP-3L45-II beam



(c) Local detachment of HCPs at failure load

Figure 3-26: (Continued.)

SP-3L45-B-II beam

The SP-3L45-B-II beam was identical to SP-3L45-II beam, except that the HCPs were bonded using epoxy adhesive and fixed by 12 through bolts and nuts. A torque of 20 N.m was applied to tighten the nuts on both sides of the beam. Figure 3-17a and Figure 3-17c show the position of the CFRP laminates and bolts, respectively.

The first shear crack was detected at a load level of about 246 kN in the same position of the first crack in SP-3L45-II beam (between laminates number 1 and 2). By increasing the load, this crack has widened and propagated. Figure 3-27 shows the crack pattern of this beam at failure load. At the load of 363 kN the major shear crack was opened, with an abrupt load decay at peak load. After this abrupt load decay, the resisting load was almost maintained, at a load level of about 52% of maximum load (190 kN) up to the end of the test (a deflection of about 16 mm). The anchors have contributed for the higher shear strengthening effectiveness of the HCPs in the post peak stage of the beam, avoiding the detachment of the HCPs. The deflection at maximum load of this beam was 13% and 24% higher than the deflection at maximum load of SP-3L45-II and SP-II beams, respectively.

As shown in Figure 3-27, the laminate number 1 was torn off. However, since the SG3 did not function properly during the test, the highest longitudinal strain was recorded in the SG1

(Figure 3-18b), and was approximately 0.69%, which corresponds to 42% of the ultimate strain of the CFRP laminate.

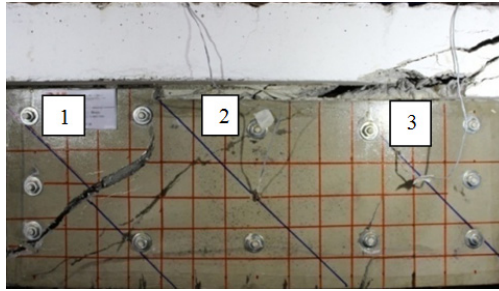


Figure 3-27: Final crack pattern of the SP-3L45-B-II beam

SP-5L45-II beam

The SP-5L45-II beam was strengthened with HCPs reinforced with five CFRP laminates ($\rho_{fw} = 0.14\%$), spaced at 157 mm (Figure 3-16b). The first flexural-shear crack formed at a load level of 166 kN. By increasing the load, several micro-cracks formed on the surface of the HCPs. The crack pattern in this beam presents much more cracks than in the other two previous beams, which is assumed to be caused by the higher percentage of CFRP laminates. The failure of this beam was premature debonding of the HCPs at the load of 306 kN and deflection of 5.1 mm. After the abrupt load decay at peak load, the beam's carrying capacity stabilized at a load level of about 30% of the maximum load (94 kN). The crack pattern of HCPs of this beam at failure load is shown in Figure 3-28. Due to the premature detachment of the HCPs, no shear failure crack is visible on the surface of the HCPs, which indicates that the NSM CFRP laminates were not mobilized effectively. In fact, the highest tensile strain was recorded by the SG1 (Figure 3-18b), and was approximately 0.33%, which corresponds to only 20% of the ultimate strain of the CFRP laminate.

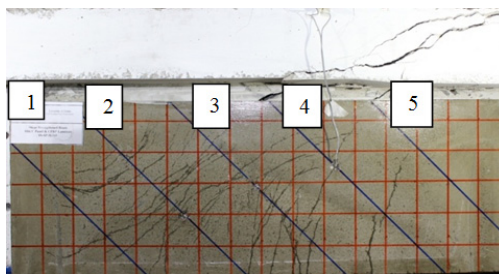


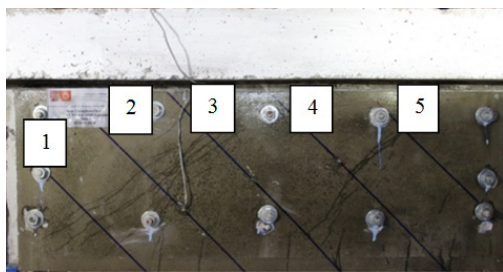
Figure 3-28: Final crack pattern of the SP-5L45-II beam

SP-5L45-B-II beam

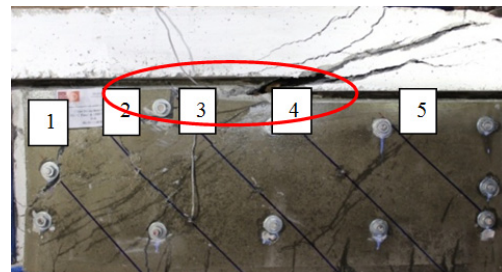
In SP-5L45-B-II beam the HCPs were bonded to the lateral faces of the beam using epoxy adhesive and applying 12 mechanical anchors (Figure 3-17b), like the procedure adopted in

the SP-3L45-B-II beam. The first shear crack was detected at a load of about 220 kN, intersecting the laminate number 4 (Figure 3-29a). The crack pattern of the HCPs presents much more shear and flexural-shear cracks, whose energy in their formation, as well as the resistance of the HCPs to the propagation of the shear failure crack have contributed for the significant increase in terms of ductility registered in this beam. In SP-5L45-B-II beam, the reinforcement effectiveness of the CFRP laminates has avoided the degeneration of the micro cracks into macro-shear failure crack on the SHCC, and the mechanical anchors prevented the premature detachment and debonding of the HCPs, and the failure was localized at the web-flange zone of the beam (marked with a red ellipse in Figure 3-29b). Since a strengthening discontinuity exists in this web-flange transition zone, and considering that no internal stirrups are available to offer resistance to the propagation of this type failure crack, the beams strengthened with HCPs fixed with adhesive and anchors cannot exceed the maximum load attained by the SP-5L45-B-II beam, regardless the percentage of CFRP used and number of bolts. However, as it is visible in the post-peak stage of this beam, the load decay was much smoother, and the residual load carrying capacity of this beam (55% of the maximum load) was much higher than the one registered in previous beams, due to the larger fracture surface mobilized in the failure mode of the SP-5L45-B-II beam.

The maximum longitudinal strain measured in the CFRP laminates (SG3, Figure 3-18b) was 1.12% (Figure 3-24), which corresponds to 68% of the ultimate strain of the CFRP, that is higher than the maximum strain recorded in the NSM-3L45-II beam. This result shows the effectiveness of the mechanical anchors to avoid premature detachment of the HCPs and to assure higher collaboration of the CFRP laminates for the shear strengthening.



(a) Crack pattern at the load level of 355kN of the SP-5L45-B-II beam



(b) Final crack pattern of the SP-5L45-B-II beam

Figure 3-29: Crack patterns and failure modes of the SP-5L45-B-II beam

3.5 Series III: Repair of Existing RC beams

3.5.1 Beams and test setup

The experimental program of this series is formed by two series of the beams, composed of beams with a rectangular cross section (Figure 3-2) and T cross section (Figure 3-15). The characteristics of the beams are presented in Table 3-9.

Table 3-9: Shear strengthening/reinforcement in the monitored shear span of the tested beams

	<i>Beam designation</i>	<i>Shear strengthening/reinforcement configuration</i>	<i>Quantity</i>	<i>connector of the web - flange</i>	<i>Spacing, S_f (mm)</i>
<i>Rectangular</i>	<i>R-SP-3L45-III</i>	HCPs (20 mm thickness of SHCC reinforced with CFRP laminates of 1.4×10mm ² cross section)	2×3CFRP laminates		150
	<i>SP-5L45-III</i>	HCPs (20 mm thickness of SHCC reinforced with CFRP laminates of 1.4×10mm ² cross section)	2×5CFRP laminates	4 steel bars ϕ 10	157
<i>T</i>	<i>R-SP-5L45-III</i>	HCPs (20 mm thickness of SHCC reinforced with CFRP laminates of 1.4×10mm ² cross section)	2×5CFRP laminates	4 steel bars ϕ 10	157

In the first step the control beams in previous experimental programs (C-R-I and C-R-II) were loaded up to failure load and then fully unloaded. In next step they were repaired by applying HCPs to each lateral face of the monitored shear span using a combination of epoxy adhesive and mechanical anchors. The repaired beams, designated by R-SP-3L45-III (Figure 3-30a) and R-SP-5L45-III (Figure 3-30b), were subjected to the same test configuration adopted in their virgin state. To prevent the localization of failure in web-flange zone (as occurred in the SP-5L45-B-II beam of the previous experimental program) the SP-5L45-III and R-SP-5L45-III beams were strengthened with 4 steel bars connectors (Figure 3-30b and Figure 3-30c).

With the purpose of obtaining the strain variation in the laminates, strain gages (SG) were bonded to the CFRP laminates according to the arrangement represented in Figure 3-30.

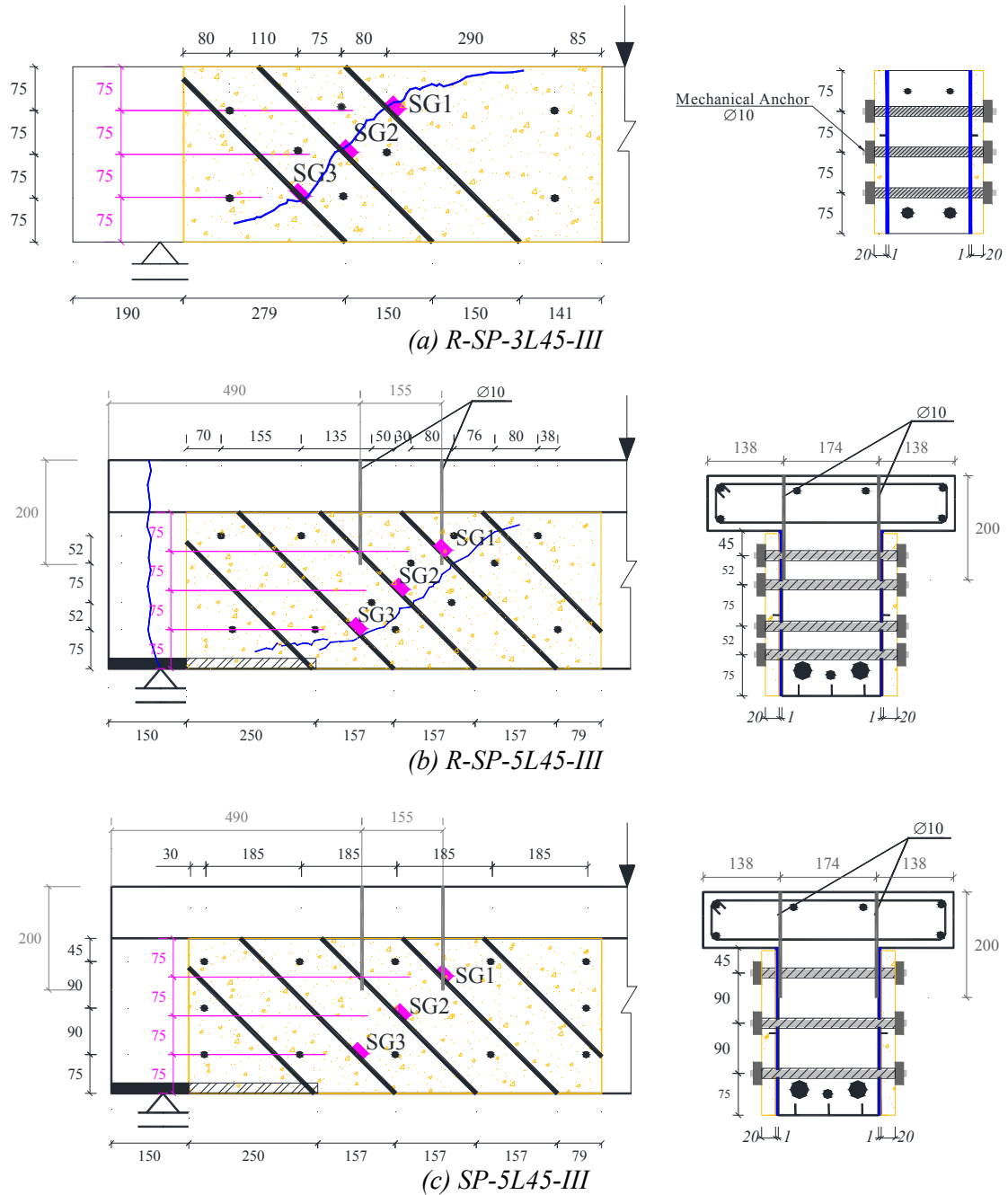


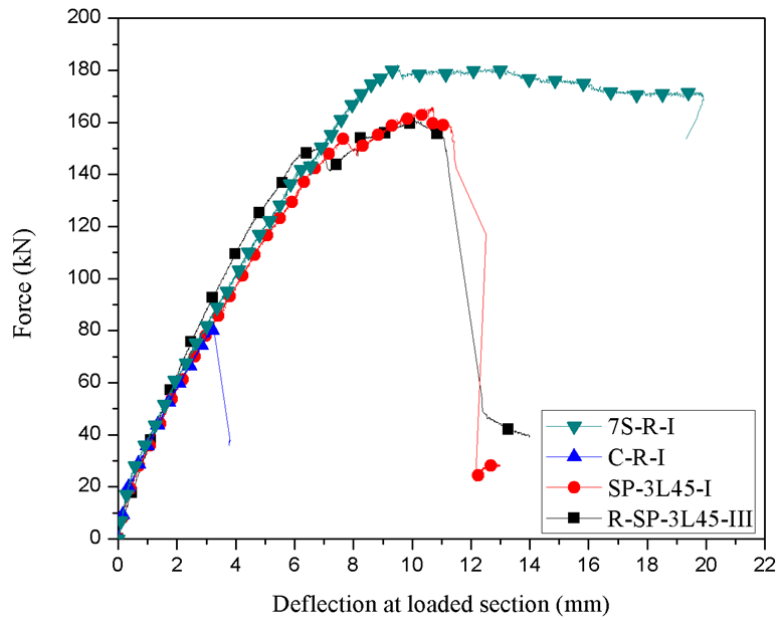
Figure 3-30: Geometry of the repaired beams

3.5.2 Test and results

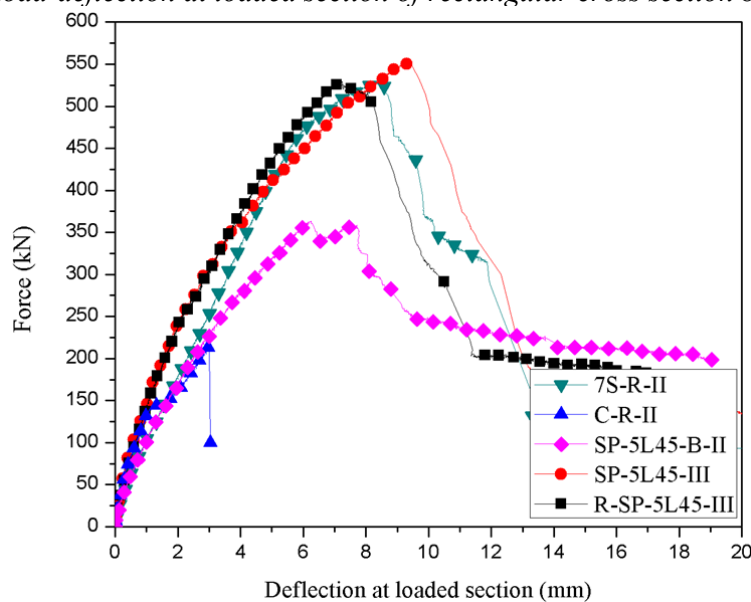
3.5.2.1 Global Analysis

The relationship between load and deflection at loaded section of the beams are presented in Figure 3-31a and Figure 3-31b. The maximum load and its corresponding deflection of the tested beams and their failure modes are presented in Table 3-10. The values of the

$F_{\max} / F_{\max}^{7S-R}$ ratio are also presented in Table 3-10, this ratio is the maximum load capacity of the beam strengthened with HCPs (F_{\max}) to its corresponding beam with seven steel stirrups (F_{\max}^{7S-R}) in previous sections. The results in Table 3-10 reveal that, in absence of the steel stirrups, the maximum load carrying capacity of the pre-damaged rectangular beam was 88% of the rectangular beam with seven steel stirrups. The failure mode of the R-SP-3L45-III beam was detachment of the HCPs.



(a) Load-deflection at loaded section of rectangular cross section beams



(b) Load-deflection at loaded section of T cross section beams

Figure 3-31: Load-deflection at loaded section (a) rectangular cross section, and (b) T cross section beams

Table 3-10: Relevant results in terms of load and deflection capacity

	<i>Beam designation</i>	F_{\max} (kN)	<i>Deflection at loaded section (mm)</i>	<i>Shear resistance (kN)</i>	$\frac{F_{\max}}{F_{\max}^{7S-R}}$ (%)	<i>Failure mode</i>
<i>Rectangular</i>	<i>C-R-I</i>	81	3.3	51	45	Shear
	<i>SP-3L45-I</i>	166	12.5	105	91	Detachment
	<i>R-SP-3L45-III</i>	161	10.1	103	88	Detachment
	<i>7S-R-I</i>	182	19.9	116	100	Flexural
<i>T</i>	<i>C-R-II</i>	214	3.0	128	40	Concrete spalling
	<i>SP-5L45-B-II</i>	364	6.3	218	67	Web-flange
	<i>SP-5L45-III</i>	552	9.4	331	104	Shear
	<i>R-SP-5L45-III</i>	530	7.2	318	100	Shear
	<i>7S-R-II</i>	530	8.4	318	100	Shear

The shear strength of the T cross section beam without steel shear connectors in the web-flange zone (SP-5L45-B-II) was 70% of the corresponding beam with 7 steel stirrups. By adding steel shear connector bars, the shear strength of the beams increased significantly in both the virgin and pre-damaged beams, with a maximum load almost equal to the one of the 7S-R-II beam. The SP-5L45-III and R-SP-5L45-III beams failed in shear.

3.5.2.2 Detailed analysis

R-SP-3L45-III

After has been tested, the C-R-I beam was strengthened with two HCPs according to the arrangement indicated in Figure 3-30a. It should be noticed that no repairing material was used in an attempt of sealing the existing cracks. For assuring a better bond conditions, an emery was passed on the lateral faces of the beam, in the zones where the HCPs were planned to be installed, for removing the cement past on the concrete substrate. To prevent detachment of HCPs, they were bonded to substrate using an epoxy adhesive and fixed by eight through bolts of 10 mm diameter. A torque of 20 N.m was applied to the bolts in both sides of the beam that through the action of the corresponding nuts introduces a confinement pressure to the concrete between the HCPs. The position of the laminates and mechanical anchors were designed in order to provide an effective resistance to the propagation of the existing shear crack (Figure 3-30a).

The first shear crack was detected at a load of about 50 kN at the position of the existing shear crack on the damaged beam. By increasing the load, the shear crack on the surface of the HCP was propagated and widened. At the load of about 80 kN, a new shear crack was formed at the same position of the first shear crack in the SP-3L45-I beam. Due to excellent bond conditions between SHCC and CFRP laminates, this reinforcement provided the

necessary tensile strength capacity to the HCP, while the high post-cracking tensile deformability and resistance of the SHCC avoided the occurrence of premature fracture failure of this cement composite in the stress transfer process between these two materials when HCP was crossed by the shear crack. Due to this effect, the failure crack was localized at the zone of the HCPs without any CFRP laminate. The failure occurred at a load level of 161 kN and deflection of 10.1 mm (Figure 3-32).

The maximum shear capacity of this beam was almost two times higher than the one of the C-R-I reference beam. The maximum load carrying capacity and deflection at maximum load of this beam were 97% and 81% of the SP-3L45-I beam, respectively. In spite of the intense state of damage of the C-R-I beam after it has been tested, the stiffness of the R-SP-3L45-III beam was even higher than the SP-3L45-I beam up to a load level of 150 kN, which means that the strengthening intervention adopted in the R-SP-3L45-III was capable of surpass the stiffness of the SP-3L45-I beam.

The maximum longitudinal strain in the CFRP laminates was recorded in SG2 (Figure 3-30a), and was approximately 18% of the ultimate strain of the CFRP laminates.

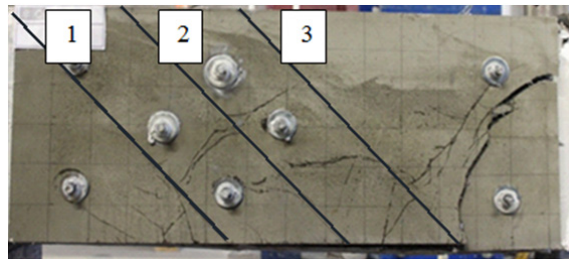


Figure 3-32: Final crack pattern of R-SP-3L45-III beam

SP-5L45-III beam

The SP-5L45-III beam was identical to SP-5L45-B-II beam, except that to offer resistance to the crack propagation through the web-flange zone (a type of failure observed in the SP-5L45-B-II beam), four $\phi 10$ steel bars of 200 mm length (two per each face) were applied to the beam as shown in Figure 3-30c. For this purpose, holes of 12 mm were opened in the flange of the beam, in the alignment coinciding with the middle surface of the concrete cover thickness of the lateral faces of the beam. The holes were cleaned by compressed air. Sikadur 32 adhesive was prepared according to supplier recommendation, and the bars were introduced into the holes that were previously filled with this adhesive. A period of 7 days was dedicated to cure the adhesive prior to testing the beam. The first crack was detected between laminates number 2 and 3 at a load of 146 kN (Figure 3-33). The HCP presents a

more diffuse crack pattern than in the previous beam, with a preponderancy for flexural cracks, whose energy in its formation, as well as the resistance of the SHCC for the propagation of a shear failure crack have contributed for the significant increase in terms of load carrying capacity and deflection performance registered in this beam.

The maximum load carrying capacity of this beam was 552 kN, which was 4% and 52% greater than the load carrying capacity of the 7S-R-II and SP-5L45-B-II beams, respectively. In terms of deflection, whose value at peak load was 9.4 mm, this comparative increase was 12% and 50%, respectively. The failure of this beam was governed by shear failure, unlike the SP-5L45-B-II, this justifies the high strengthening contribution of the steel bars applied in the SP-5L45-III beam.

The maximum tensile strain in CFRP laminate was recorded in the SG2 (Figure 3-30c), and was 1.8%, which correspond to the ultimate tensile strain of the CFRP laminates, which indicates that this laminate was almost in its rupture stage. This value is higher than values registered by Dias and Barros (2010), and the tested beams in previous series. The failure of the tested beams was governed by the detachment of the CFRP laminates and HCPs, respectively, which has avoided the mobilization of the shear strengthening potentialities of the CFRP laminates.

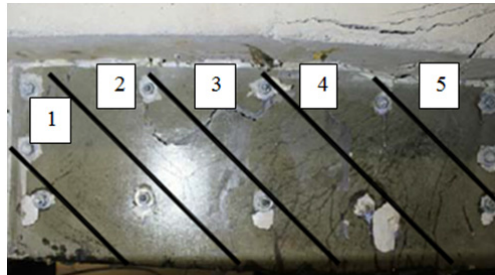


Figure 3-33: Final crack pattern of the SP-5L45-III beam

R-SP-5L45-III beam

As mentioned in previous section, the C-R-II beam exhibited an incipient shear failure at the support cross section. The crack at the support was repaired by sealing it with epoxy-based adhesive (Sikadur 32). For closing this crack as much as possible, after it has been filled with the adhesive, a mechanical clamping system was applied for 48 hours. To improve the anchorage conditions of the longitudinal reinforcement, three longitudinal NSM CFRP laminates of $1.4 \times 20 \text{ mm}^2$ cross section were applied in the beam's support zone with length of 400mm (Figure 3-30b). Like it was done in the SP-5L45-III beam, to avoid premature failure at the web-flange zone, four $\phi 10$ steel bars were applied to the beam as shown in

Figure 3-30b. This repaired beam was shear strengthened with HCPs technique. In this respect it should be mentioned that the shear crack already existing in this beam was not submitted to any treatment. The HCPs of this beam had a same configuration of the HCPs of the SP-5L45-B-II and SP-5L45-III beams, however the arrangement of the bolts was different. In fact, as shown in Figure 3-30b, in the strengthened C-R-II beam, herein designated as R-SP-5L45-III, the numbers of bolts were also 12, but their disposition was designed in order to provide an effective resistance to the propagation of the existing shear crack.

Two micro cracks were detected by sparing oil (WD-40) on the surface of the HCP at a load of about 141 kN, in the zone of the existing shear crack on the C-R-II damaged beam. By increasing the load, these cracks have propagated and widened followed by the formation of more micro cracks in that zone that were not degenerated in macro-cracks due to the reinforcement contribution of the CFRP laminates.

The maximum load carrying capacity of this beam was 530 kN that was 96% and 100% of the maximum load carrying capacity of the SP-5L45-III and 7S-R-II beams, respectively. The final crack pattern of this beam is presented in Figure 3-34.

The SG1 and SG3 did not function during the test. The maximum longitudinal strain recorded in the CFRP laminate was registered in the SG2 (Figure 3-30b), and was 0.45%, which correspond to 29% of the ultimate strain of the CFRP.



Figure 3-34: Final crack pattern of the R-SP-5L45-III beam

3.6 Conclusions

The effectiveness of Hybrid Composite Plates (HCPs) for the shear strengthening of reinforced concrete (RC) beams was investigated by carrying out three experimental programs.

When the HCP was bonded with epoxy adhesive, the effectiveness of the HCP technique was limited by the tensile strength of the concrete substrate of the RC beams, since at failure, a concrete cover layer of an average thickness that varied between 5 and 10 mm was attached to the HCPs. The detachment of HCPs has avoided the mobilization of the shear strengthening potentialities of the CFRP laminates. In fact, the HCPs bonded with epoxy to the concrete substrate of the RC beams have detached prematurely, having been registered a maximum tensile strain in the CFRP laminates that did not exceed 25% of the ultimate strain of these laminates. However, when the HCPs were bonded with epoxy and fixed with mechanical anchors, this type of failure mode was avoided, and the tensile capacity of the CFRP laminates of the HCPs was effectively mobilized, since maximum tensile strains in the CFRP closely to its ultimate tensile strain were measured. The results have also shown that for deflections higher than the one corresponding to the formation of the first shear crack in the beam strengthened with NSM technique, the adopted HCPs have increased the beam's load carrying capacity and deflection performance.

The load carrying capacity of T cross section RC beams shear strengthened with HCPs was limited by the shear strengthening discontinuity at the web-flange of the beam, since in these strengthened beams the failure crack had propagated through this zone. By applying steel shear connectors in this zone, and adopting an optimized configuration for the bolts, it was demonstrated to be possible to attain an increase of 146% in the shear capacity of a damaged beam that had been previously loaded to its maximum load capacity.

The HCPs were capable of increasing not only the load carrying and deflection capacity, but also the post-peak resisting load, with favorable effects in terms of energy absorption capacity.

Chapter 4

Numerical Simulation and Parametric Study

4.1 Introduction

In the present work is described a multi-directional fixed smeared crack model capable of simulating with high accuracy the RC beams failing in shear. The main innovative aspect in this constitutive model is the treatment of the concrete fracture mode II by using a softening diagram to simulate the crack shear stress vs. crack shear sliding in the context of a smeared crack approach.

Advanced numerical simulations are carried out to contribute for a better understanding of the effectiveness of the shear strengthening technique with HCPs. By using the properties obtained from the experimental program for the characterization of the relevant properties of the intervening materials, the data for defining the crack shear softening diagram of the adopted multi-directional fixed smeared crack constitutive model was derived from inverse analysis by simulating the beams tested experimentally. These simulations have fitted with high accuracy the deformational response and the crack pattern of the tested beams. Thus, an extensive parametric study is carried out for the evaluation of the influence on the load carrying capacity and failure mode of the following conditions: arrangement of CFRP laminates; shear strengthening ratio; the use of mechanical anchors for fixing the HCP to the RC beam; using mortar instead of SHCC; and different confinement of the concrete core.

In the following section a brief description of the model is provided, since the detailed exposition can be found elsewhere (Ventura-Gouveia et al. 2008).

4.2 Multi-Directional Fixed Smeared Crack Model

When the material behavior is considered to be nonlinear, its constitutive matrix depends on the stress or strain levels. In this case, an incremental-iterative technique is normally used. The external load is applied incrementally and the relationship between incremental strain and stress is given by the following equation:

$$\Delta\sigma = \underline{D}\Delta\varepsilon \quad (4.1)$$

where $\Delta\sigma$ represents the stress increment, $\Delta\varepsilon$ is the strain increment and \underline{D} is the tangent constitutive matrix.

In a smeared crack approach the total incremental strain of cracked material is decomposed into an incremental strain vector of the uncracked material, $\Delta \underline{\underline{\varepsilon}}^{co}$, and the incremental strain vector of the cracked material, $\Delta \underline{\underline{\varepsilon}}^{cr}$:

$$\Delta \underline{\underline{\varepsilon}} = \Delta \underline{\underline{\varepsilon}}^{co} + \Delta \underline{\underline{\varepsilon}}^{cr} \quad (4.2)$$

For the three dimensional case, the incremental local crack strain vector, $\Delta \underline{\underline{\varepsilon}}_l^{cr}$, is defined by :

$$\Delta \underline{\underline{\varepsilon}}_l^{cr} = \left\{ \Delta \varepsilon_n^{cr}, \Delta \gamma_{t_1}^{cr}, \Delta \gamma_{t_2}^{cr} \right\}^T \quad (4.3)$$

and, in global coordinate system:

$$\Delta \underline{\underline{\varepsilon}}^{cr} = \left\{ \Delta \varepsilon_1^{cr}, \Delta \varepsilon_2^{cr}, \Delta \varepsilon_3^{cr}, \Delta \gamma_{23}^{cr}, \Delta \gamma_{31}^{cr}, \Delta \gamma_{12}^{cr} \right\}^T \quad (4.4)$$

Eq. (4.5) represents the relation between global strain ($\Delta \underline{\underline{\varepsilon}}^{cr}$) and local strain ($\Delta \underline{\underline{\varepsilon}}_l^{cr}$):

$$\Delta \underline{\underline{\varepsilon}}^{cr} = \left[\underline{\underline{T}}^{cr} \right]^T \Delta \underline{\underline{\varepsilon}}_l^{cr} \quad (4.5)$$

where $\underline{\underline{T}}^{cr}$ is the transformation matrix:

$$\underline{\underline{T}}^{cr} = \begin{bmatrix} a_{11}^2 & a_{12}^2 & a_{13}^2 & 2a_{12}a_{13} & 2a_{11}a_{13} & 2a_{11}a_{12} \\ a_{11}a_{21} & a_{12}a_{22} & a_{13}a_{23} & a_{12}a_{23} + a_{13}a_{22} & a_{11}a_{23} + a_{13}a_{21} & a_{11}a_{22} + a_{12}a_{21} \\ a_{11}a_{31} & a_{12}a_{32} & a_{13}a_{33} & a_{13}a_{32} + a_{12}a_{33} & a_{13}a_{31} + a_{11}a_{33} & a_{12}a_{31} + a_{11}a_{32} \end{bmatrix} \quad (4.6)$$

The components a_{11} , a_{12} , and a_{13} form a vector that follows the direction of the n local axis; a_{21} , a_{22} , and a_{23} form a vector that defines the t_1 local axis; and a_{31} , a_{32} , and a_{33} form a vector that defines the t_2 local axis. All these vectors are defined in the global coordinate system (Figure 4-1).

In the global coordinate system the incremental stress components are:

$$\Delta \underline{\underline{\sigma}} = \left\{ \Delta \sigma_1, \Delta \sigma_2, \Delta \sigma_3, \Delta \tau_{23}, \Delta \tau_{31}, \Delta \tau_{12} \right\}^T \quad (4.7)$$

Eq. (4.8) represents the relation between $\Delta \underline{\underline{\sigma}}$ and $\Delta \underline{\underline{\sigma}}_l^{cr}$:

$$\Delta \underline{\underline{\sigma}}_l^{cr} = \underline{\underline{T}}^{cr} \Delta \underline{\underline{\sigma}} \quad (4.8)$$

where $\Delta \underline{\underline{\sigma}}_l^{cr}$ is the local incremental stress vector:

$$\Delta \underline{\underline{\sigma}}_l^{cr} = \left\{ \Delta \sigma_n^{cr}, \Delta \tau_{t_1}^{cr}, \Delta \tau_{t_2}^{cr} \right\}^T \quad (4.9)$$

where $\Delta \sigma_n^{cr}$ is the mode I incremental crack normal stress, $\Delta \tau_{t_1}^{cr}$ and $\Delta \tau_{t_2}^{cr}$ are the sliding mode incremental crack shear stress in \hat{t}_1 and \hat{t}_2 direction, respectively.

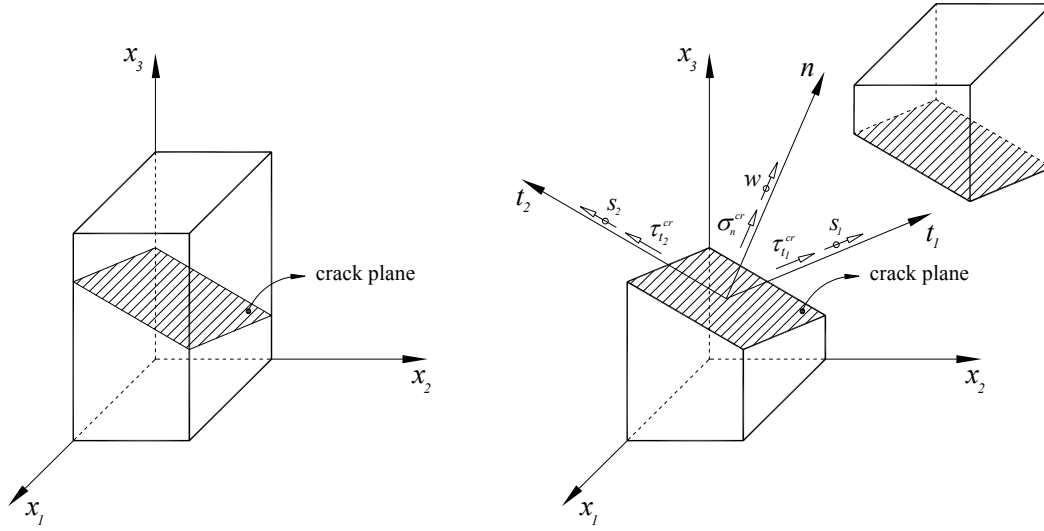


Figure 4-1: Crack stress components (Ventura-Gouveia et al. 2008)

According to the multi-directional fixed smeared crack concept, stress and strain are related by the following equation:

$$\Delta \underline{\sigma} = \underline{D}^{crco} \Delta \underline{\varepsilon} \quad (4.10)$$

Due to the decomposition of the total strain into an elastic concrete part and a crack part, $\Delta \underline{\varepsilon} = \Delta \underline{\varepsilon}^{co} + \Delta \underline{\varepsilon}^{cr}$, in Eq. (4.10) the cracked concrete constitutive matrix, \underline{D}^{crco} , is obtained with the following equation (Sena-Cruz 2004):

$$\underline{D}^{crco} = \underline{D}^{co} - \underline{D}^{co} \left[\hat{\underline{T}}^{cr} \right]^T \left(\hat{\underline{D}}^{cr} + \hat{\underline{T}}^{cr} \underline{D}^{co} \left[\hat{\underline{T}}^{cr} \right]^T \right)^{-1} \hat{\underline{T}}^{cr} \underline{D}^{co} \quad (4.11)$$

where \underline{D}^{co} is the constitutive matrix of concrete, assuming a linear behavior:

$$\underline{D}^{co} = \frac{E_c}{(1+\nu_c)(1-2\nu_c)} \begin{bmatrix} (1-\nu_c) & \nu_c & \nu_c & & & \\ \nu_c & (1-\nu_c) & \nu_c & & & 0 \\ \nu_c & \nu_c & (1-\nu_c) & & & \\ & & & \frac{1-2\nu_c}{2} & 0 & 0 \\ & & & 0 & \frac{1-2\nu_c}{2} & 0 \\ & & & 0 & 0 & \frac{1-2\nu_c}{2} \end{bmatrix} \quad (4.12)$$

being E_c and ν_c the Young's modulus and the Poisson's ratio of undamaged concrete, respectively. In Eq. (4.11) $\hat{\underline{T}}^{cr}$ is the matrix that transforms the stress components from the coordinate system of the finite element to the local crack coordinate system (a subscript is

used to identify entities in the local crack coordinate system). If m cracks occur at an Integration Point (IP):

$$\underline{\hat{T}}^{cr} = [\underline{T}_1^{cr} \dots \underline{T}_i^{cr} \dots \underline{T}_m^{cr}]^T \quad (4.13)$$

In Eq. (4.11) $\underline{\hat{D}}^{cr}$ is a matrix that includes the constitutive law of the m cracks:

$$\underline{\hat{D}}^{cr} = \begin{bmatrix} \underline{D}_1^{cr} & \underline{0} & \dots & \underline{0} \\ \underline{0} & \underline{D}_2^{cr} & \dots & \underline{0} \\ \dots & \dots & \dots & \dots \\ \underline{0} & \underline{0} & \dots & \underline{D}_m^{cr} \end{bmatrix} \quad (4.14)$$

with D_i^{cr} being the crack constitutive matrix of the i^{th} crack:

$$\underline{D}^{cr} = \begin{bmatrix} D_n^{cr} & 0 & 0 \\ 0 & D_{t_1}^{cr} & 0 \\ 0 & 0 & D_{t_2}^{cr} \end{bmatrix} \quad (4.15)$$

where D_n^{cr} , $D_{t_1}^{cr}$ and $D_{t_2}^{cr}$ represent the modulus correspondent to the fracture mode I (normal), the sliding mode stiffness modulus in the \hat{t}_1 direction and the sliding mode stiffness modulus in the \hat{t}_2 direction, respectively.

The behavior of non-completely closed cracks formed at an IP is governed by the following relationship:

$$\Delta \underline{\sigma}_i^{cr} = \underline{D}^{cr} \Delta \underline{\varepsilon}_i^{cr} \quad (4.16)$$

In this approach, a new crack is arisen in an IP when the angle formed between the new crack and the already existing cracks, α_{new}^{cr} , exceeds a certain threshold angle, α_{th} (a parameter of the constitutive model that in general ranges between 30 and 60 degrees (Sena-Cruz 2004)).

The crack opening propagation is simulated with the tri-linear diagram represented in Figure 4-2, which is defined by the normalized stress, α_i , and strain, ξ_i , parameters that define the transition points between the linear segments of this diagram. The ultimate crack strain, $\varepsilon_{n,u}^{cr}$, is defined as a function of the parameters α_i and ξ_i , fracture energy, G_f^I , tensile strength, $f_{ct} = \sigma_{n,1}^{cr}$, and crack band width, l_b , as follows (Sena-Cruz 2004):

$$\varepsilon_{n,u}^{cr} = \frac{2}{\xi_1 + \alpha_1 \xi_2 - \alpha_2 \xi_1 + \alpha_2} \frac{G_f^I}{f_{ct} l_b} \quad (4.17)$$

being $\alpha_1 = \sigma_{n,2}^{cr} / \sigma_{n,1}^{cr}$, $\alpha_2 = \sigma_{n,3}^{cr} / \sigma_{n,1}^{cr}$, $\xi_1 = \varepsilon_{n,2}^{cr} / \varepsilon_{n,u}^{cr}$ and $\xi_2 = \varepsilon_{n,3}^{cr} / \varepsilon_{n,u}^{cr}$.

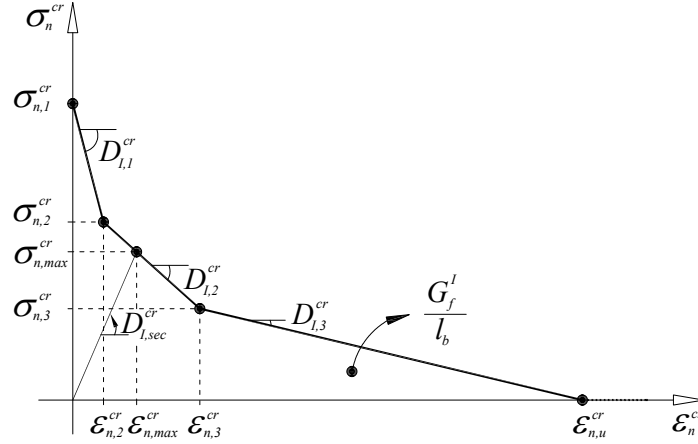


Figure 4-2: Tri-linear stress-strain diagram to simulate the fracture mode I crack propagation (Barros et al. 2013)

To simulate the fracture mode II modulus, a shear retention factor is used:

$$D_{t_1}^{cr} = D_{t_2}^{cr} = \frac{\beta}{1-\beta} G_c \quad (4.18)$$

where G_c is the concrete elastic shear modulus and β is the shear retention factor. The parameter β is defined as a constant value or as a function of the current crack normal strain, ε_n^{cr} , and of the ultimate crack normal strain, $\varepsilon_{n,u}^{cr}$, as follows:

$$\beta = \left(1 - \frac{\varepsilon_n^{cr}}{\varepsilon_{n,u}^{cr}}\right)^{P_1} \quad (4.19)$$

when $P_1 = 1$ a linear decrease of β with the increase of ε_n^{cr} is assumed. Larger values of the exponent P_1 correspond to a more pronounced decrease of the β parameter.

In structures governed by flexural failure modes, this strategy leads to simulations with good accuracy (Barros et al. 2011). Exceptions occur in structures that fail by the formation of a critical shear crack. To simulate accurately the deformational response and the crack pattern up to the failure of this type of structures, the adoption of a softening crack shear stress vs. crack shear strain relationship was implemented to model the crack shear transfer in \hat{t}_1 and \hat{t}_2 direction (Ventura-Gouveia et al. 2008).

The implemented crack shear diagrams are represented in Figure 4-3. The crack shear stress increases linearly until the crack shear strength is reached, $\tau_{t,p}^{cr}$, (first branch of the shear crack diagram), followed by a decrease in the shear residual strength (softening branch). The diagram represented in Figure 4-3 is defined by the following equations:

$$\tau_t^{cr}(\gamma_t^{cr}) = \begin{cases} D_{t,1} \gamma_t^{cr} & 0 < \gamma_t^{cr} \leq \gamma_{t,p}^{cr} \\ \tau_{t,p}^{cr} - \frac{\tau_{t,p}^{cr}}{(\gamma_{t,u}^{cr} - \gamma_{t,p}^{cr})} (\gamma_t^{cr} - \gamma_{t,p}^{cr}) & \gamma_{t,p}^{cr} < \gamma_t^{cr} \leq \gamma_{t,u}^{cr} \\ 0 & \gamma_t^{cr} > \gamma_{t,u}^{cr} \end{cases} \quad (4.20)$$

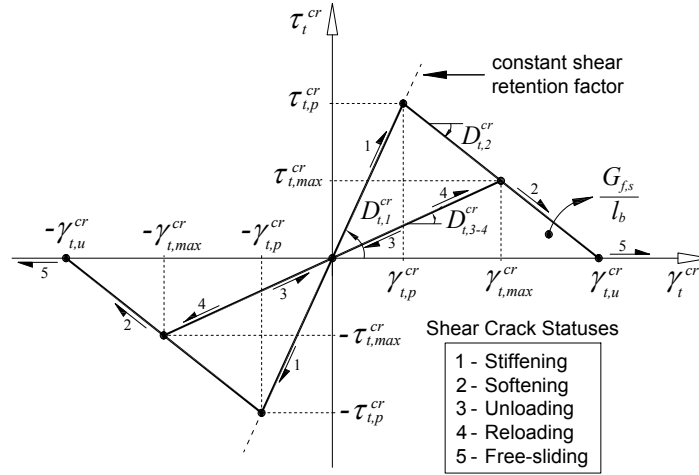


Figure 4-3: Diagrams to simulate the relationship between the crack shear stress and crack shear strain component, and possible shear crack statuses (Barros et al. 2013)

The initial shear fracture modulus, $D_{t,1}^{cr}$, is defined by Eq. (4.18) ($D_{t_1}^{cr}$ is replaced by $D_{t,1}^{cr}$) by assuming for β a constant value in the range $]0,1[$. The peak crack shear strain, $\gamma_{t,p}^{cr}$, is obtained using the crack shear strength (from the input data), $\tau_{t,p}^{cr}$, and the crack shear modulus:

$$\gamma_{t_1,p}^{cr} = \gamma_{t_2,p}^{cr} = \frac{\tau_{t,p}^{cr}}{D_{t,1}^{cr}} \quad (4.21)$$

The ultimate crack shear strain, $\gamma_{t,u}^{cr}$, depends on the crack shear strength, $\tau_{t,p}^{cr}$, on the shear fracture energy (mode II fracture energy), $G_{f,s}$, and on the crack bandwidth, l_b :

$$\gamma_{t_1,u}^{cr} = \gamma_{t_2,u}^{cr} = \frac{2G_{f,s}}{\tau_{t,p}^{cr} l_b} \quad (4.22)$$

In this approach it is assumed that the crack bandwidth, used to assure that the results are independent of the mesh refinement (Rots 1988), is the same for both fracture mode I and mode II processes.

When the softening constitutive law represented in Figure 4-3 is used to evaluate the fracture mode II softening modulus $D_{t_1}^{cr} = D_{t_2}^{cr}$ of Eq. (4.15), its value depends on the branches

defining the diagram. For this reason five shear crack statuses are proposed and their meaning is schematically represented in Figure 4-3.

The crack mode II modulus of the first linear branch of the diagram is defined by Eq. (4.18), the second linear softening branch is defined by:

$$D_{t_1}^{cr} = D_{t_2}^{cr} = D_{t,2}^{cr} = -\frac{\tau_{t,p}^{cr}}{\gamma_{t,u}^{cr} - \gamma_{t,p}^{cr}} \quad (4.23)$$

and the crack shear modulus of the unloading and reloading branches is obtained from:

$$D_{t_1}^{cr} = D_{t_2}^{cr} = D_{t,3-4}^{cr} = \frac{\tau_{t,max}^{cr}}{\gamma_{t,max}^{cr}} \quad (4.24)$$

being $\gamma_{t,max}^{cr}$ and $\tau_{t,max}^{cr}$ the maximum crack shear strain already attained and the corresponding crack shear stress determined from the softening linear branch. Both components are stored to define the unloading/reloading branch (see Figure 4-3).

In free - sliding status ($|\gamma_t^{cr}| > |\gamma_{t,u}^{cr}|$) the crack mode II stiffness modulus, $D_{t_1}^{cr} = D_{t_2}^{cr} = D_{t,5}^{cr}$, is null. To avoid numerical instabilities in the calculation of the stiffness matrix and in the calculation of the internal forces, when the crack shear status is free - sliding, a residual value is assigned to this term. A free - sliding status is assigned to the shear crack status when $\varepsilon_n^{cr} > \varepsilon_{n,u}^{cr}$ (Barros et al. 2013).

4.3 Modeling Beam Shear Strengthened with NSM Technique

To assess the predictive performance of the model for RC beams failing in shear, in the context of structural strengthening, it was used on the simulation of the experimental tests carried out by Dias and Barros (2010), where a series of RC beams were shear strengthened with NSM CFRP laminates. The general information about the beams of the experimental program and finite element adopted for these beams are presented in Figure 4-4 and Figure 4-5, respectively. More information about the experimental program can be found in Dias and Barros (2010).

Beams ID	Shear strengthening system	Shear strengthening arrangements
2S-R	Reference beam without CFRP	
2S-4LV	NSM CFRP laminates at 90° (2 × 4 laminates: $\rho_{fv} = 0.08\%$)	
2S-7LV	NSM CFRP laminates at 90° (2 × 7 laminates: $\rho_{fv} = 0.13\%$)	
2S-10LV	NSM CFRP laminates at 90° (2 × 10 laminates: $\rho_{fv} = 0.18\%$)	
2S-4LI45	NSM CFRP laminates at 45° (2 × 4 laminates: $\rho_{fv} = 0.08\%$)	
2S-7LI45	NSM CFRP laminates at 45° (2 × 7 laminates: $\rho_{fv} = 0.13\%$)	
2S-10LI45	NSM CFRP laminates at 45° (2 × 10 laminates: $\rho_{fv} = 0.19\%$)	
2S-4LI60	NSM CFRP laminates at 60° (2 × 4 laminates: $\rho_{fv} = 0.07\%$)	
2S-6LI60	NSM CFRP laminates at 60° (2 × 6 laminates: $\rho_{fv} = 0.11\%$)	
2S-9LI60	NSM CFRP laminates at 60° (2 × 9 laminates: $\rho_{fv} = 0.16\%$)	

Figure 4-4: General information about the beams of the experimental program (dimensions in mm) (Barros et al. 2013)

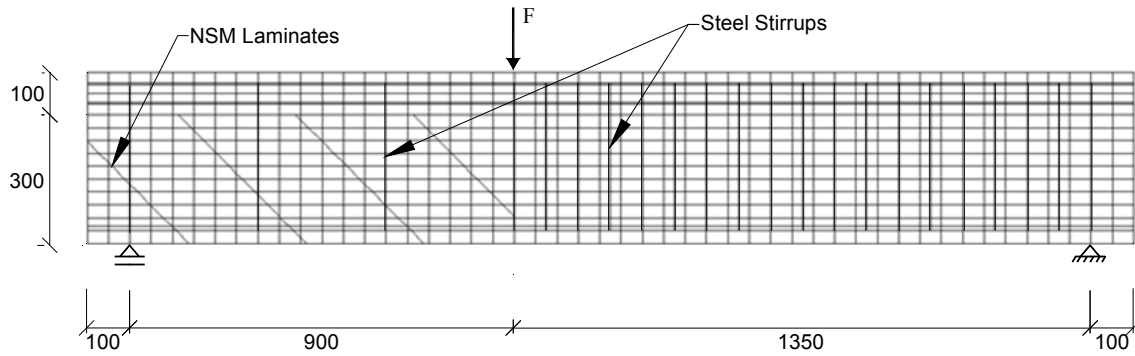


Figure 4-5: Finite element mesh of the beam 2S-4LI45 (dimensions in mm)
(Barros et al. 2013)

To simulate the crack initiation and the fracture mode I propagation of reinforced concrete, the tri-linear tension-softening diagram represented in Figure 4-2 was adopted. The values that define this diagram are indicated in Table 4-1, and were obtained from the experimental program for the characterization of the relevant properties of the intervening materials. In this table is also included the data necessary to define the shear-softening diagram represented in Figure 4-3, adopted to simulate the degradation of crack shear stress transfer after crack initiation. Since no available experimental results exist to characterize the crack shear softening diagram, the adopted values were obtained by inverse analysis by fitting the experimental results as best as possible.

Table 4-1: Values of the parameters of the constitutive model for the concrete

Property	Value
Poisson's ratio	0.15
Compressive strength	39.7 N/mm ²
Initial Young's Strength	33271 N/mm ²
Tri-linear tension softening diagram of concrete	$f_{ct}=2.2 \text{ N/mm}^2$, $\zeta_1=0.005$, $\zeta_2=0.1$, $\alpha_1=0.30$, $\alpha_2=0.30$, $G_{fn}=0.086 \text{ N/mm}$
Parameter defining the mode I fracture energy available to the new crack	$P_2=3$
Softening crack shear stress-strain diagram	$\tau_{t,p}^{cr}=1.1 \text{ N/mm}^2$, $G_{fs}=0.05 \text{ N/mm}$, $\beta=0.40$
Crack band width	Square root of the area of Gauss integration point
Threshold angle	$\alpha_{th}=30^\circ$
Maximum number of cracks per integration point	2

The numerical simulations of this section it was used the 2D version of the multi-directional smeared crack model described in previous section. A detailed description of this model can be found in Sena-Cruz (2004). The beams are modeled with a mesh of 4-noded serendipity plane stress finite elements. The longitudinal steel bars, stirrups and the NSM CFRP

laminates are modeled with 2-noded perfect bonded embedded cables (one degree-of-freedom per each node).

For modeling the behavior of the longitudinal and transversal steel bars, the stress-strain relationship represented in Figure 4-6 was adopted. The curve (under compressive or tensile loading) is defined by the points PT1= $(\epsilon_{sy}, \sigma_{sy})$, PT2= $(\epsilon_{sh}, \sigma_{sh})$, and PT3= $(\epsilon_{su}, \sigma_{su})$, and a parameter P that defines the shape of the last branch of the curve. Unloading and reloading linear branches with slope $E_s = (\sigma_{sy} / \epsilon_{sy})$ are assumed in the present approach. The values of the parameters of the constitutive model for the steel are indicated in Table 4-2.

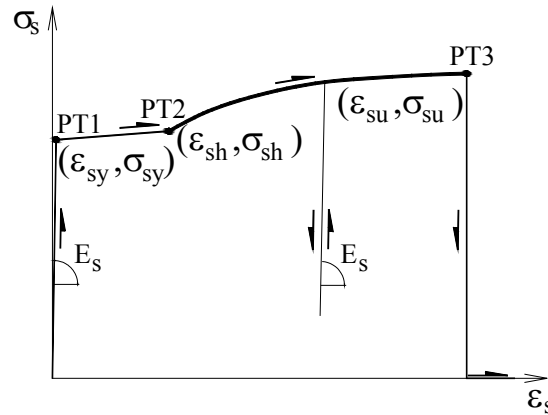


Figure 4-6: Uniaxial constitutive model for the steel bars (Barros et al. 2013)

Table 4-2: Values of the parameters of the steel constitutive model (Barros et al. 2013)

Property	ϕ6	ϕ12	ϕ16	ϕ32
f_{sym} (N/mm ²)	500	490	470	625
f_{sum} (N/mm ²)	594	591	566	905
ϵ_{sy} (‰)	2.3	2.5	2.6	3
σ_{sy} (N/mm ²)	500	490	470	625
ϵ_{sh} (‰)	20	30	30	10
σ_{sh} (N/mm ²)	537	490	470	845
ϵ_{su} (‰)	45	215	220	50
σ_{su} (N/mm ²)	594	591	566	905
Third branch exponent	1	1	1	1

For modeling the NSM CFRP laminates, a linear elastic stress-strain relationship was adopted. Table 4-3 present the values obtained in experimental tests with CFRP laminates specimens.

Table 4-3: Properties of CFRP laminates

<i>properties</i>	<i>Value</i>
<i>Maximum tensile strength</i>	2741.7 MPa
<i>Young's Modulus</i>	170.9 GPa
<i>Maximum strain</i>	1.60%

The experimental and the numerical relationships between the applied load and the deflection at the loaded section for the tested beams are compared in Figure 4-7. The crack patterns of these beams at the end of the analysis (at the end of the last converged load increment) are compared with the obtained experimental crack patterns in Figure 4-8. These two figures show that the numerical model is able to capture with good accuracy the deformational response of the beams and captured with good precision the localization and profile of the shear failure crack.

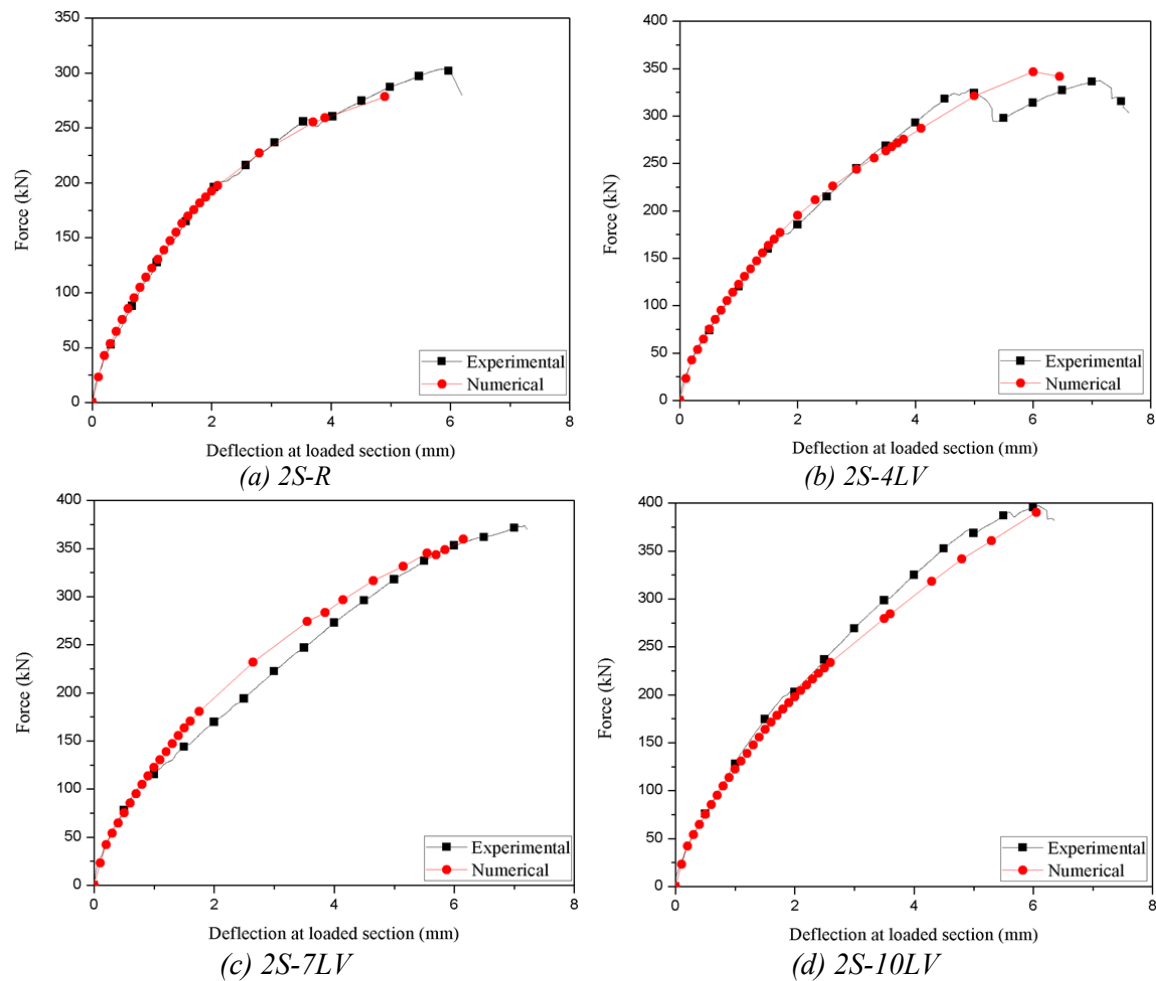


Figure 4-7: Comparison between experimental and numerical force vs. deflection at the loaded section relationships

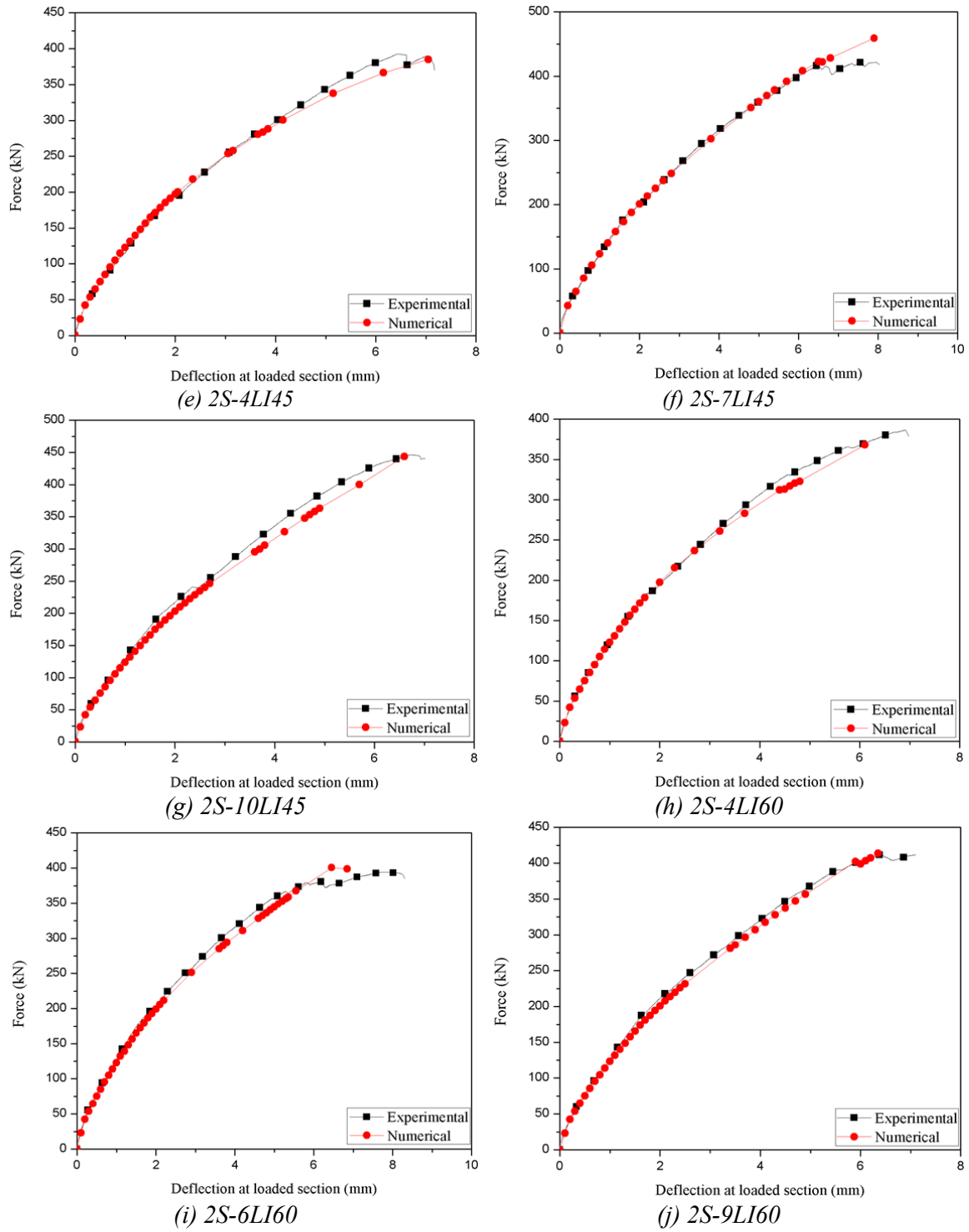


Figure 4.7: (Continued.)

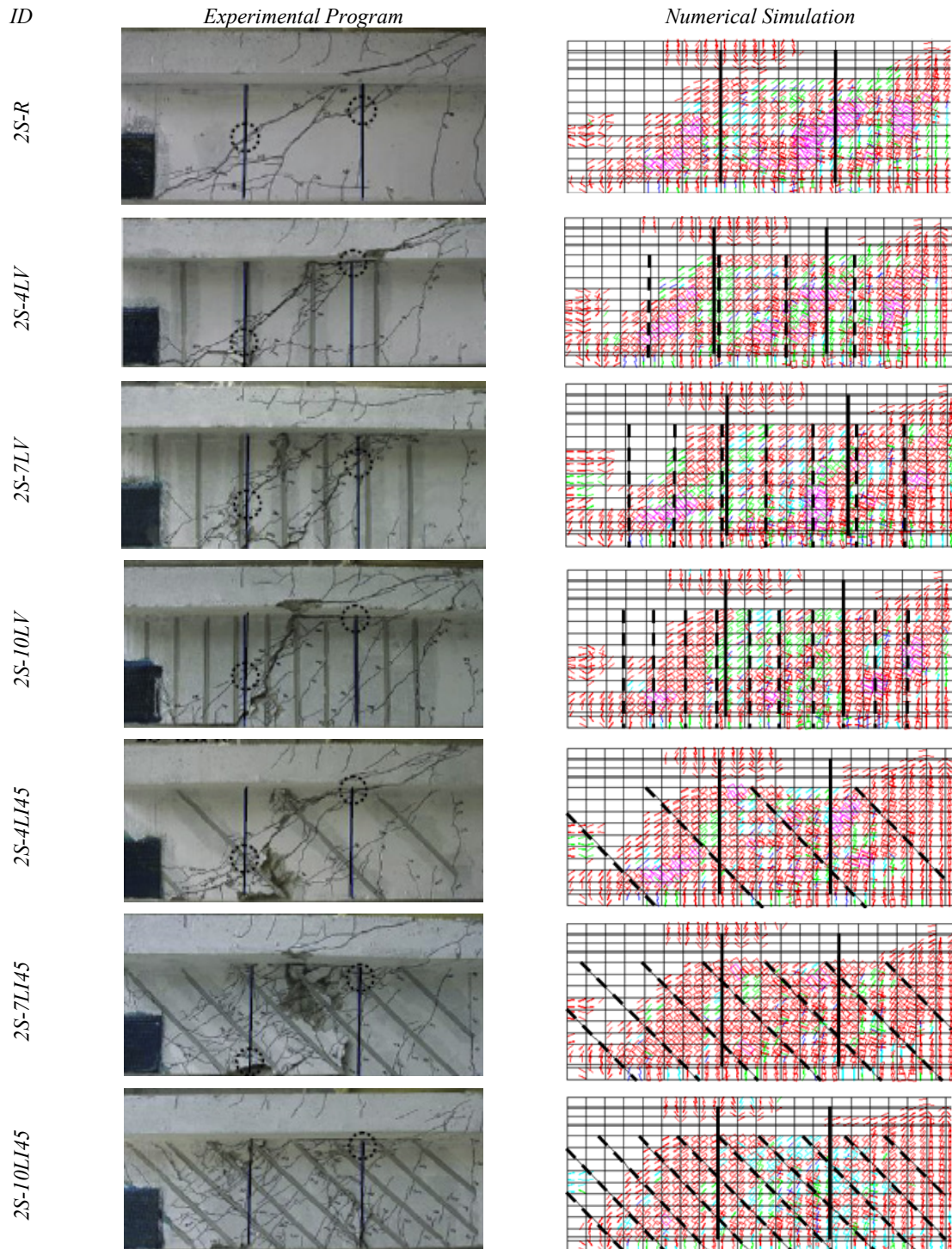


Figure 4-8: Crack patterns of the beams (in pink color: crack completely open; in red color: crack in the opening process; in cyan color: crack in the reopening process; in green color: crack in the closing process; in blue color: closed crack)

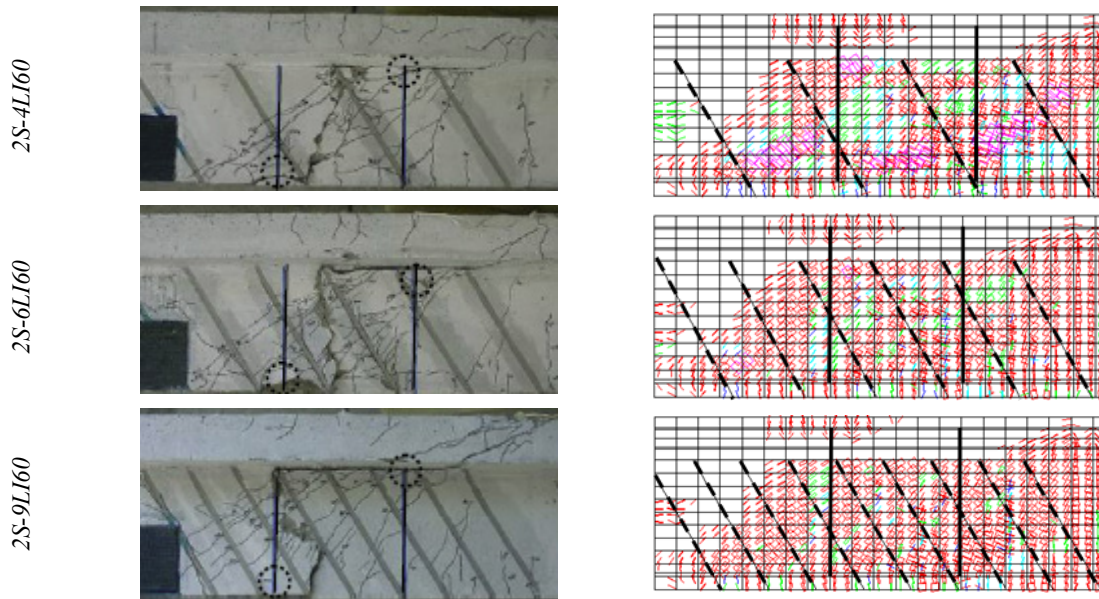


Figure 4-8: (Continued.)

4.4 Modeling of the Beams of Series I

The three dimensional multi-directional fixed smeared crack model described in section 4.2 was used in the numerical simulations of the beams of series I, II and III, whose tests and results were presented in Section 3.3, 3.4, 3.5, respectively. To simulate the crack initiation and the fracture mode I propagation of plain concrete and SHCC, the tri-linear tension-softening diagram represented in Figure 4-2 was used. The values of this diagram are indicated in Table 4-4 and Table 4-5 for plain concrete and SHCC, respectively. These tables also include the data necessary to define the shear-softening diagram (Figure 4-3). The data for the shear softening diagram of plain concrete was determined by fitting as best as possible the force-deflection relationship registered in the control beam tested experimentally (C-R-I), while for the SHCC this data was obtained by simulating the SP-I beam and considering the results obtained by Iosipescu shear tests (as it will be explained in Chapter 5). For the analysis of the remaining beams of the experimental program the values of the constitutive model applied to each intervening material were preserved constant.

Figure 4-9 represents the finite element mesh adopted for the RC beam. In the numerical simulations, this finite element mesh was only altered in order to take into account the strengthening provided by NSM laminates (NSM-4L90-I beam), the SHCC plate (SP-I beam), HCPs (SP-4L90-I and SP-3L45-I beams), and the use of more steel stirrups (7S-R-I beam).

Table 4-4: Values of the parameters of the constitutive model for the concrete

<i>Property</i>	<i>Value</i>
<i>Poisson's ratio</i>	0.19
<i>Compressive strength</i>	32.67 N/mm ²
<i>Initial Young's Strength</i>	31381 N/mm ²
<i>Tri-linear tension softening diagram of concrete</i>	$f_{ct}=2.1 \text{ N/mm}^2$, $\zeta_1=0.005$, $\zeta_2=0.1$, $\alpha_1=0.30$, $\alpha_2=0.30$, $G_{fn}=0.08 \text{ N/mm}$
<i>Parameter defining the mode I fracture energy available to the new crack</i>	$P_2=3$
<i>Softening crack shear stress-strain diagram</i>	$\tau_{t,p}^{cr}=1.1 \text{ N/mm}^2$, $G_{fs}=0.045 \text{ N/mm}$, $\beta=0.6$
<i>Crack band width</i>	<i>Cube root of the volume of the integration point</i>
<i>Threshold angle</i>	$\alpha_{th}=30^\circ$
<i>Maximum number of cracks per integration point</i>	2

Table 4-5: Values of the parameters of the constitutive model for the SHCC

<i>Property</i>	<i>Value</i>
<i>Poisson's ratio</i>	0.32
<i>Compressive strength</i>	31.60 N/mm ²
<i>Initial Young's Strength</i>	18420 N/mm ²
<i>Tri-linear tension softening diagram of concrete</i>	$f_{ct}=2.7 \text{ N/mm}^2$, $\zeta_1=0.98$, $\zeta_2=0.99$, $\alpha_1=1.16$, $\alpha_2=1.0$, $G_{fn}=0.46 \text{ N/mm}$
<i>Parameter defining the mode I fracture energy available to the new crack</i>	$P_2=3$
<i>Softening crack shear stress-strain diagram</i>	$\tau_{t,p}^{cr}=0.9 \text{ N/mm}^2$, $G_{fs}=1.7 \text{ N/mm}$, $\beta=0.50$
<i>Crack band width</i>	<i>Cube root of the volume of the integration point</i>
<i>Threshold angle</i>	$\alpha_{th}=30^\circ$
<i>Maximum number of cracks per integration point</i>	2

Only half of the full size beam was modeled, taking advantage of the symmetry of the beams in order to reduce the computational time of the numerical simulations. Serendipity 8 nodes solid elements with $2 \times 2 \times 2$ Gauss-Legendre integration scheme were used for both the concrete and SHCC (three degrees-of-freedom per node). The steel stirrups, longitudinal steel bars and CFRP laminates were modeled with 3D embedded cables of 2 nodes (one degree-of-freedom per node), by using a 2 Gauss-Legendre integration scheme, and perfect bond to the surrounding medium was assumed. The tested beams showed that no slip occurred between concrete substrate and SHCC plates, thus the assumption of perfect bond between substrate and SHCC plates was assumed.

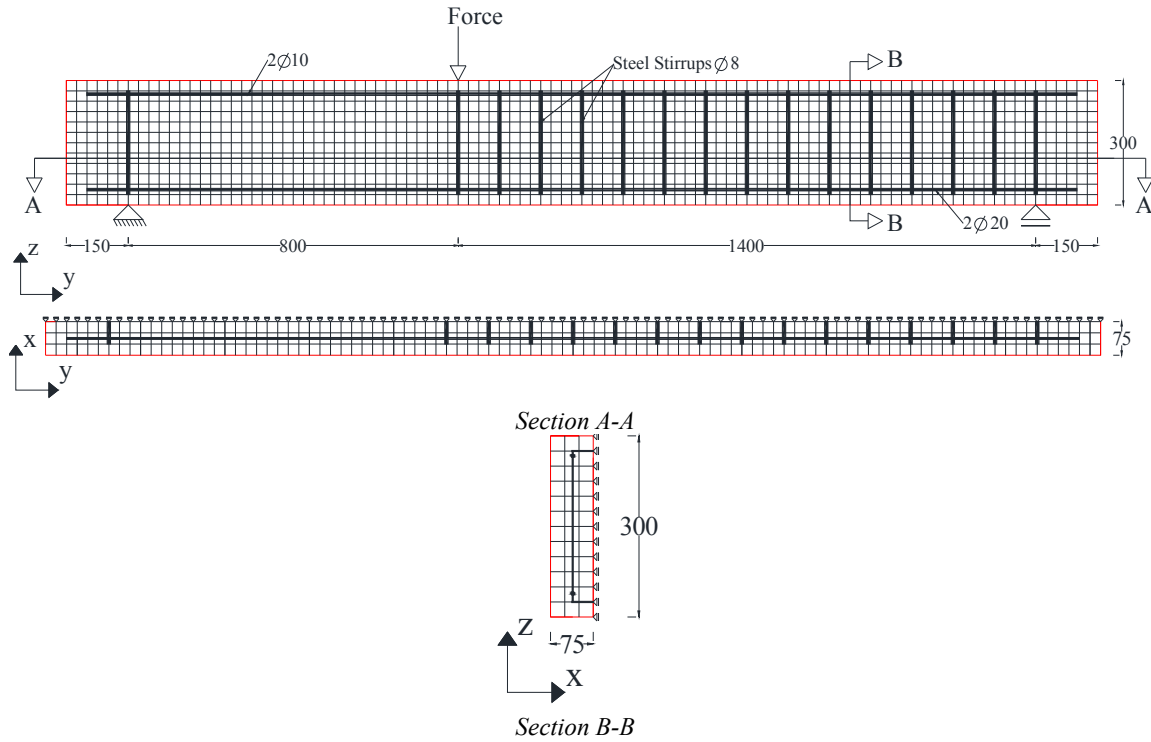


Figure 4-9: Geometry, mesh and support condition of C-R-I beam (dimensions in mm)

The values of the parameters of the constitutive model for the steel bars are indicated in Table 4-6. For modeling the NSM CFRP laminates, a linear elastic stress-strain relationship was adopted.

Table 4-6: Values of the parameters of the steel constitutive model

Property	$\phi 8$	$\phi 10$	$\phi 20$
$f_{sym} (N/mm^2)$	546	529	576
$f_{sum} (N/mm^2)$	610	625	640
$\epsilon_{sy} (\%)$	2.4	2.5	2.6
$\sigma_{sy} (N/mm^2)$	546	529	576
$\epsilon_{sh} (\%)$	35	30	35
$\sigma_{sh} (N/mm^2)$	558	529	579
$\epsilon_{su} (\%)$	100	150	100
$\sigma_{su} (N/mm^2)$	610	625	640
Third branch exponent	1	1	1

The experimental and the numerical relationships between the applied load and the deflection at the loaded section for the tested beams are compared in Figure 4-10. The crack pattern of these beams at the end of the analysis is represented in Figure 4-11. For the beams

strengthened with SHCC/HCP, the crack pattern is represented for the concrete substrate of the lateral surface, as well as for the SHCC/HCP. In Figure 4-11j a section view of the crack pattern of the SP-3L45-I beam is also represented in order to demonstrate the capability of the model to reproduce the localization of failure cracks at the concrete region close to the HCP/beam interface.

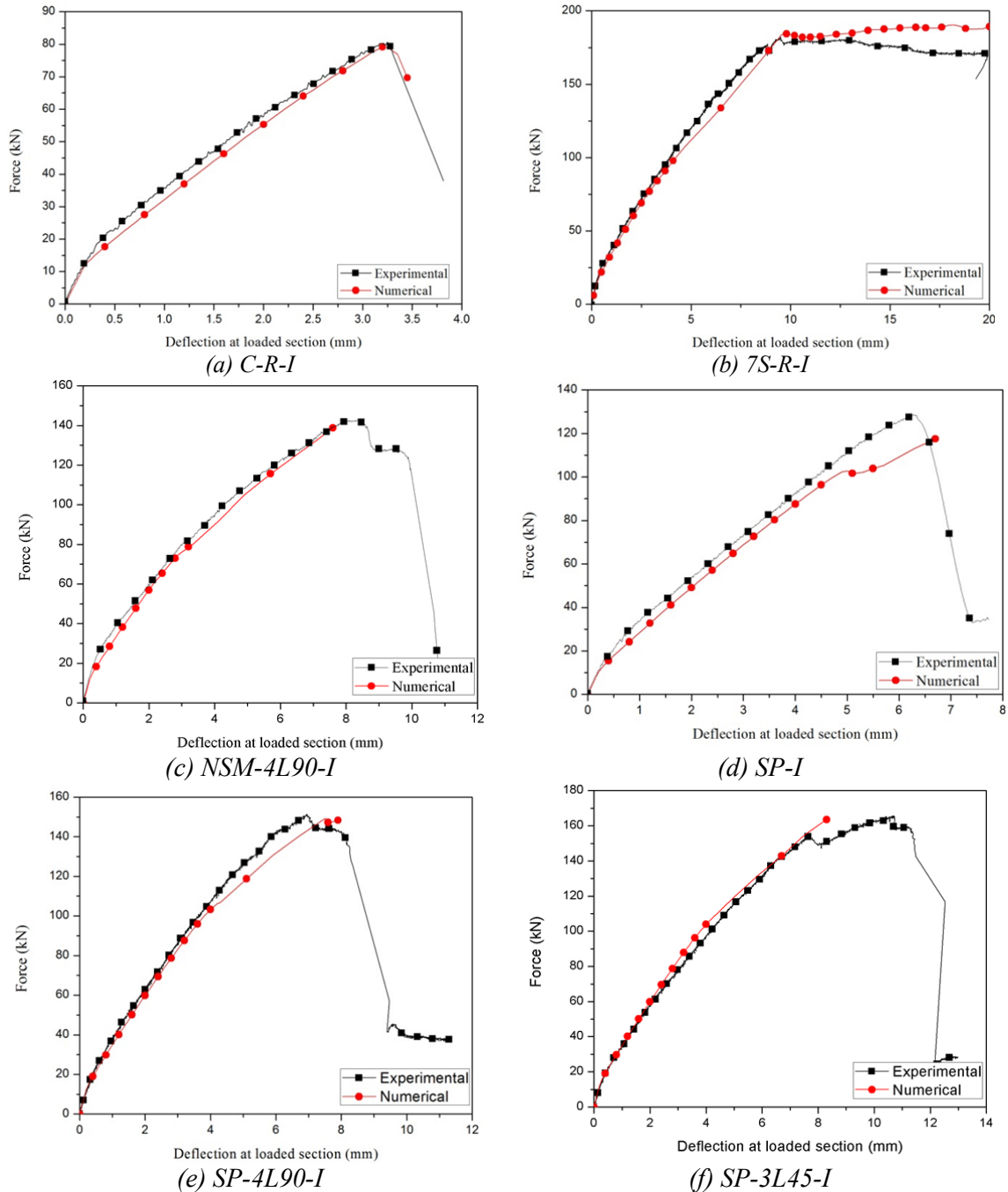


Figure 4-10: Comparison between experimental and numerical force vs. deflection at the loaded section relationships

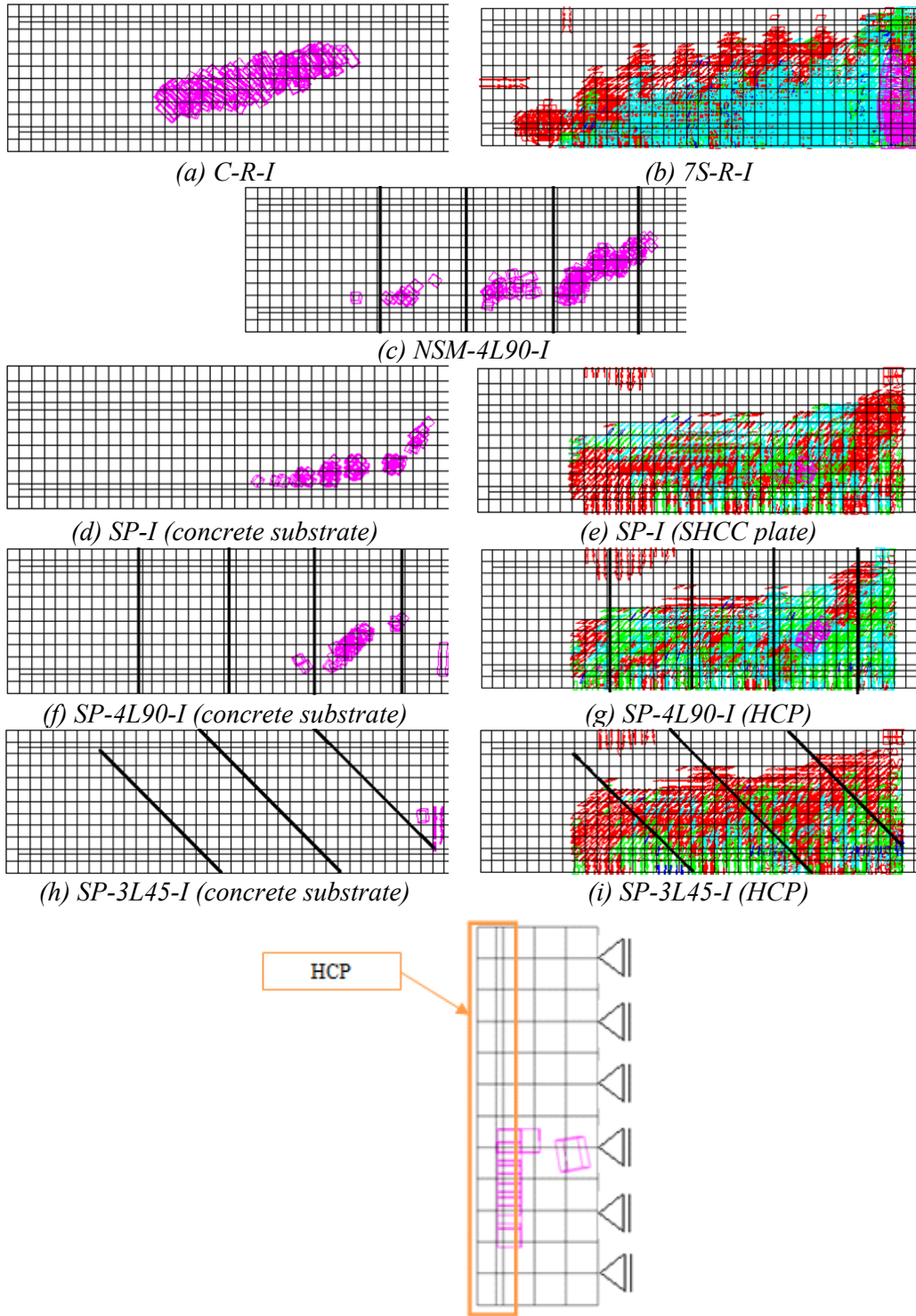


Figure 4-11: Crack patterns of the beams

4.5 Modeling of the Beams of Series II

The values of the tri-linear tension-softening and the shear-softening diagrams are indicated in Table 4-7 and Table 4-8 for plain concrete and SHCC, respectively. The data for the shear softening diagram of plain concrete was determined by fitting as best as possible the force-deflection relationship registered in the control beam tested experimentally (C-R-II), while for the SHCC this data was obtained by simulating the SP-II beam and considering the results obtained by Iosipescu shear tests. For the analysis of the remaining beams of the experimental program the values of the constitutive model applied to each intervening material were preserved constant.

Table 4-7: Values of the parameters of the constitutive model for the concrete

<i>Property</i>	<i>Value</i>
<i>Poisson's ratio</i>	0.19
<i>Compressive strength</i>	32.67 N/mm ²
<i>Initial Young's Strength</i>	31381 N/mm ²
<i>Tri-linear tension softening diagram of concrete</i>	$f_{ct}=2.1 \text{ N/mm}^2$, $\zeta_1=0.005$, $\zeta_2=0.1$, $\alpha_1=0.30$, $\alpha_2=0.30$, $G_{fn}=0.08 \text{ N/mm}$
<i>Parameter defining the mode I fracture energy available to the new crack</i>	$P_2=3$
<i>Softening crack shear stress-strain diagram</i>	$\tau_{t,p}^{cr}=1.1 \text{ N/mm}^2$, $G_{fs}=0.045 \text{ N/mm}$, $\beta=0.60$
<i>Crack band width</i>	<i>Cube root of the volume of the integration point</i>
<i>Threshold angle</i>	$\alpha_{th}=30^\circ$
<i>Maximum number of cracks per integration point</i>	2

Table 4-8: Values of the parameters of the constitutive model for the SHCC

<i>Property</i>	<i>Value</i>
<i>Poisson's ratio</i>	0.32
<i>Compressive strength</i>	31.60 N/mm ²
<i>Initial Young's Strength</i>	18420 N/mm ²
<i>Tri-linear tension softening diagram of concrete</i>	$f_{ct}=2.7 \text{ N/mm}^2$, $\zeta_1=0.98$, $\zeta_2=0.99$, $\alpha_1=1.18$, $\alpha_2=1.0$, $G_{fn}=0.46 \text{ N/mm}$
<i>Parameter defining the mode I fracture energy available to the new crack</i>	$P_2=3$
<i>Softening crack shear stress-strain diagram</i>	$\tau_{t,p}^{cr}=0.8 \text{ N/mm}^2$, $G_{fs}=1.7 \text{ N/mm}$, $\beta=0.50$
<i>Crack band width</i>	<i>Cube root of the volume of the integration point</i>
<i>Threshold angle</i>	$\alpha_{th}=30^\circ$
<i>Maximum number of cracks per integration point</i>	2

Figure 4-12 represents the finite element mesh adopted for the T cross section RC beam. In the simulations, this finite element mesh was altered in order to take into account the

strengthening provided by NSM laminates (NSM-3L45-II beam), the SHCC plate (SP-II beam), HCPs, and the use of more steel stirrups (7S-R-II beam).

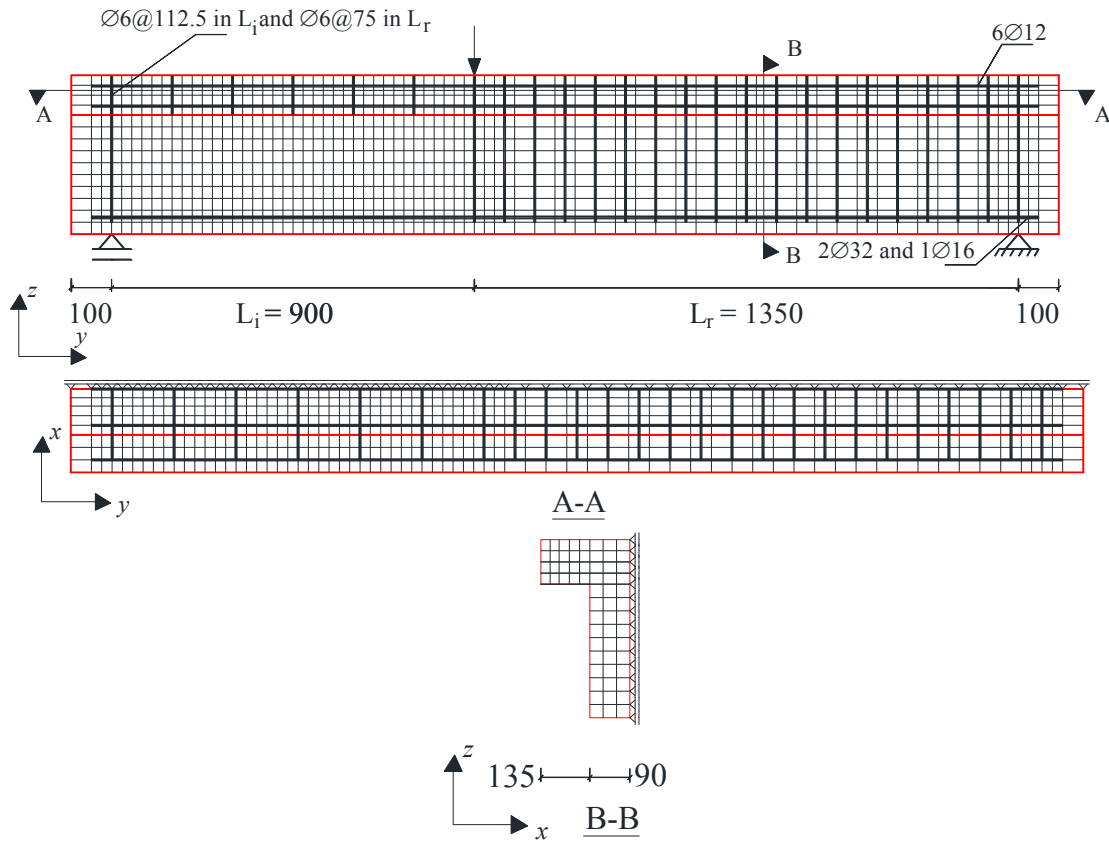


Figure 4-12: Finite element mesh of the C-R-II beam (dimensions in mm)

Only half of the full size beam was modeled. Serendipity 8 nodes solid elements with $2 \times 2 \times 2$ Gauss-Legendre integration scheme were used for both the concrete and SHCC (three degrees-of-freedom per node). The steel stirrups, longitudinal steel bars and CFRP laminates were modeled with 3D embedded cables of 2 nodes (one degree-of-freedom per node), by using a 2 Gauss-Legendre integration scheme, and perfect bond to the surrounding medium was assumed. The bolts were modeled with 3D two-node truss elements, and torque was simulated by applying a temperature decrease of -25.5°C in these elements, evaluated according to the following equation:

$$\begin{aligned}
 F &= \frac{\tau}{r} & F &= \frac{20}{0.005} = 4000 \text{ N} \\
 \sigma &= \frac{F}{A} & \sigma &= \frac{4000}{78.5} = 51 \text{ MPa} \\
 \varepsilon &= \frac{\sigma}{E} = T \cdot \alpha & \varepsilon &= \frac{51}{200000} = T \times 10^{-5}
 \end{aligned} \tag{4.25}$$

where τ is torque (N.m), and r , A , and E are the radius, cross sectional area, and elasticity modulus of the bolt (5 mm, 78.5 mm², 200 GPa), respectively. In these equations T and α are the temperature variation and the coefficient of thermal expansion, respectively.

The values of the parameters of the constitutive model for the steel bars are indicated in Table 4-9.

Table 4-9: Values of the parameters of the steel constitutive model

<i>Property</i>	$\phi 6$	$\phi 12$	$\phi 16$	$\phi 32$
f_{sym} (N/mm ²)	500	490	470	625
f_{sum} (N/mm ²)	594	591	566	905
ϵ_{sy} (‰)	2.3	2.5	2.6	3
σ_{sy} (N/mm ²)	500	490	470	625
ϵ_{sh} (‰)	20	30	30	10
σ_{sh} (N/mm ²)	537	490	470	845
ϵ_{su} (‰)	45	215	220	50
σ_{su} (N/mm ²)	594	591	566	905
<i>Third branch exponent</i>	1	1	1	1

The experimental and the numerical relationships between the applied load and the deflection at the loaded section for the tested beams are compared in Figure 4-13. The crack pattern of these beams at the end of the analysis is represented in Figure 4-14. These two figures show that the numerical model is able of predicting with high accuracy the load vs. deformational response of the beams, and to capture with a good precision the localization and profile of the failure cracks. For the beams strengthened with SHCC/HCP, the crack pattern is represented for the lateral surface of the concrete substrate, as well as for the SHCC/HCP. The higher load predicted for the SP-5L45-II indicates that the assumed perfect bond conditions between HCPs and concrete substrate was not assured in this beam. As mentioned in previous chapter (Chapter 3), the crack pattern of the beams strengthened with HCP shows the tendency of the failure crack to propagate at the web-flange interface due to the discontinuity of beam's cross section stiffness and shear strengthening contribution of the HCP. Figure 4-14 shows that the numerical model is able to capture with high accuracy this crack pattern.

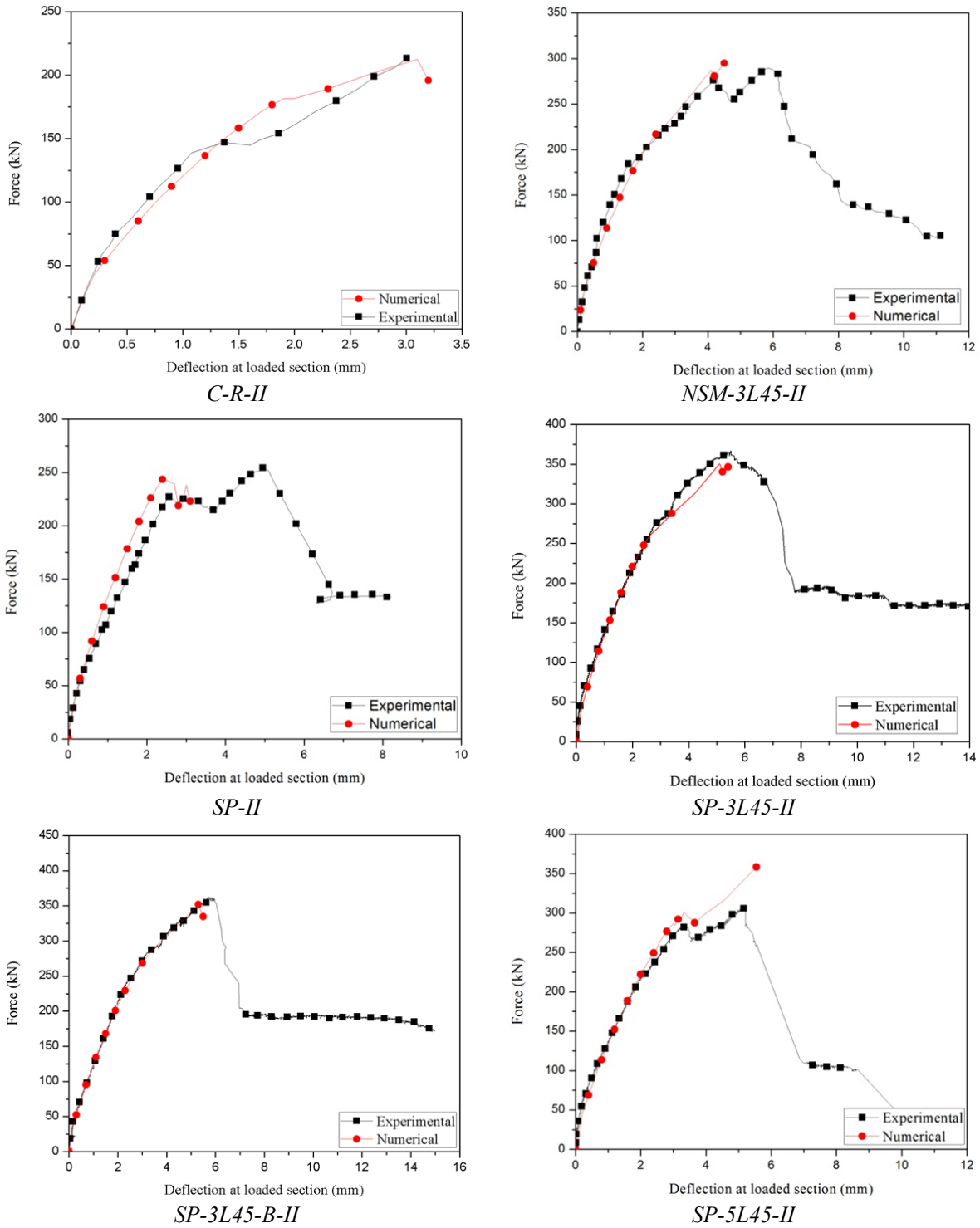


Figure 4-13: Comparison between experimental and numerical force vs. deflection at the loaded section relationships

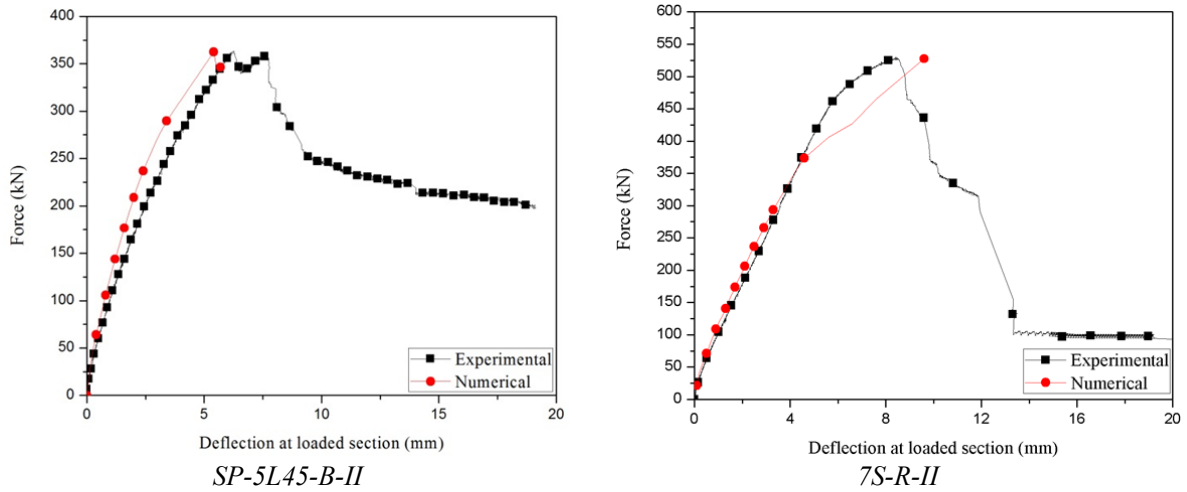


Figure 4-13: (Continued.)

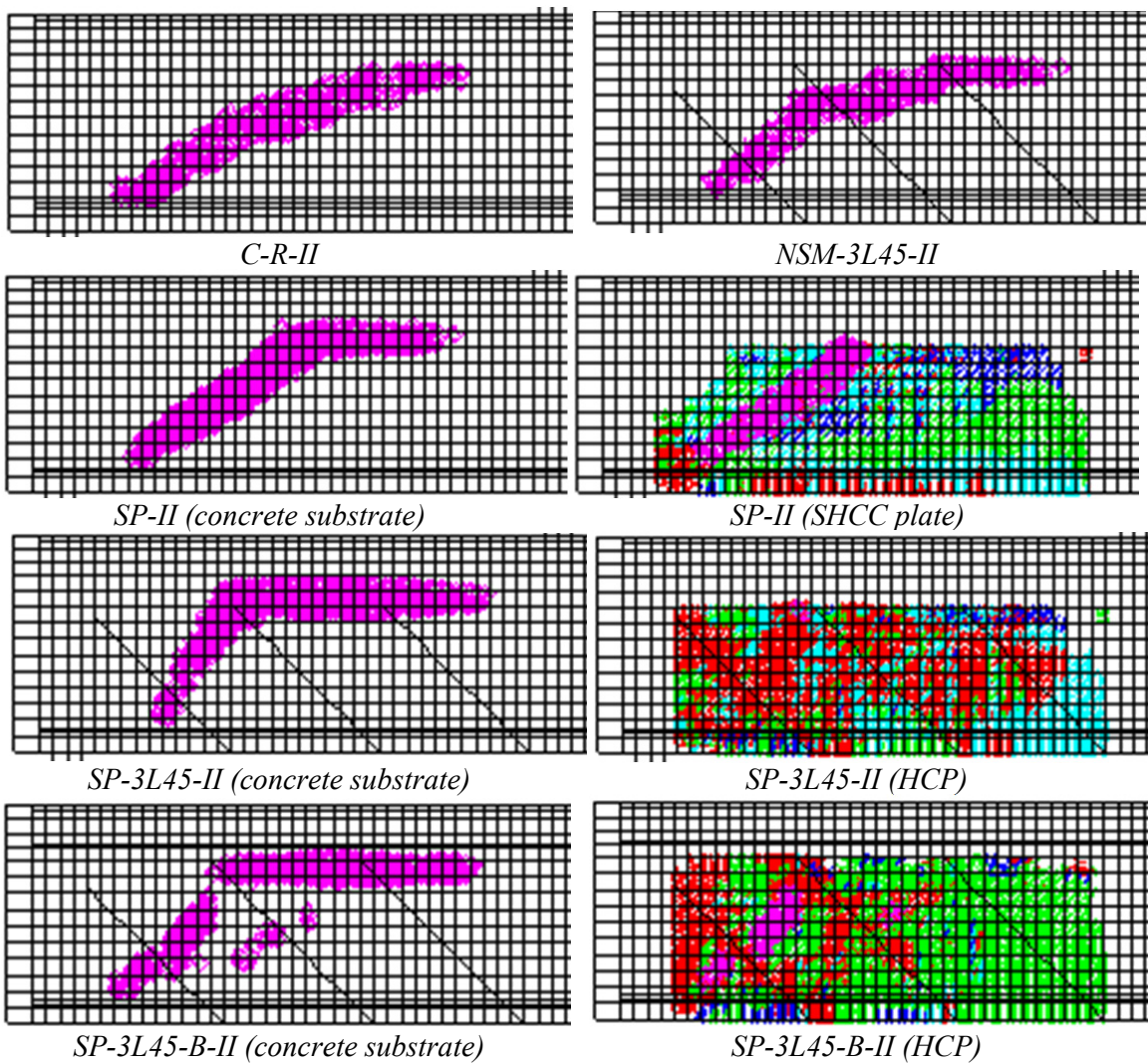


Figure 4-14: Crack patterns of the beams

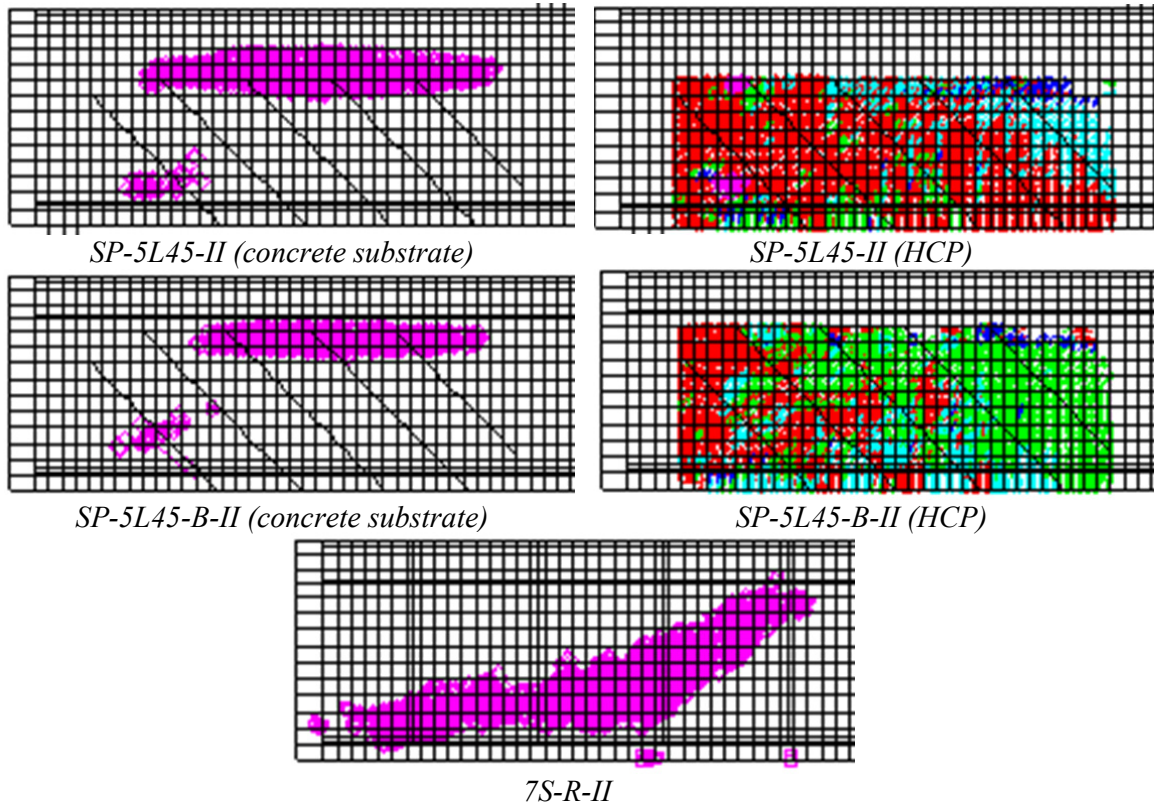


Figure 4-14: (Continued.)

4.6 Modeling of the Beams of Series III

In order to introduce the main shear crack in the model for simulating, as better as possible, the level of damages already existing in the R-SP-3L45-III and R-SP-5L45-III beams before have been strengthened, for the elements crossing this shear crack a much lower tensile strength and mode I fracture energy was assumed (0.1 N/mm^2 and 0.0007 N/mm , respectively) in order these elements behave in a very brittle nature, forcing the occurrence of the observed shear crack almost from the beginning of the loading process of these beams. For the other parameters of the constitutive model, values equal to the remaining concrete elements were adopted.

The experimental and numerical relationships between the applied load and the deflection at the loaded section for the tested beams are compared in Figure 4-15. The crack pattern of these beams at the end of the analysis is represented in Figure 4-16. These figures show that the numerical model is able of predicting with high accuracy the relationship between load and deflection and failure cracks of the repaired beams.

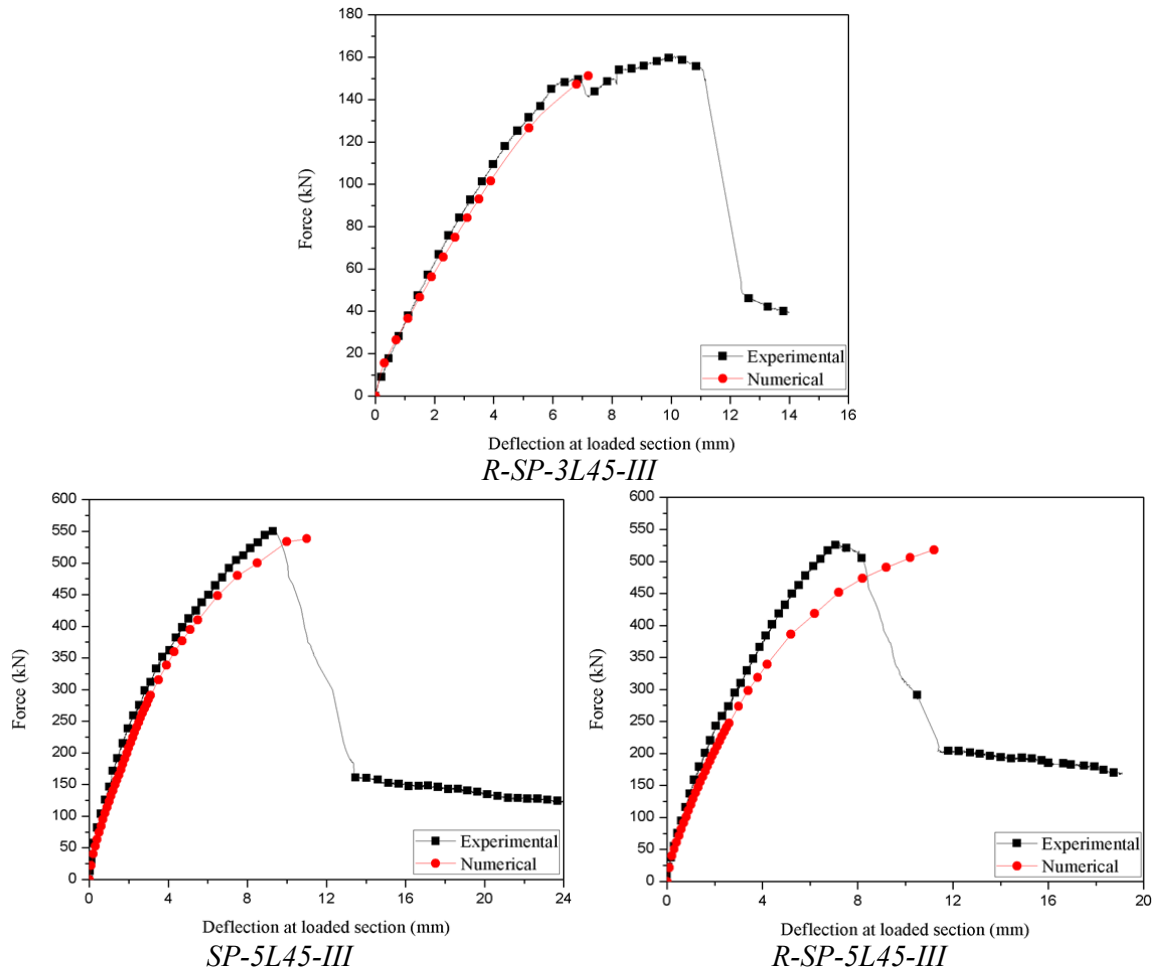


Figure 4-15: Comparison between experimental and numerical force vs. deflection at the loaded section relationships

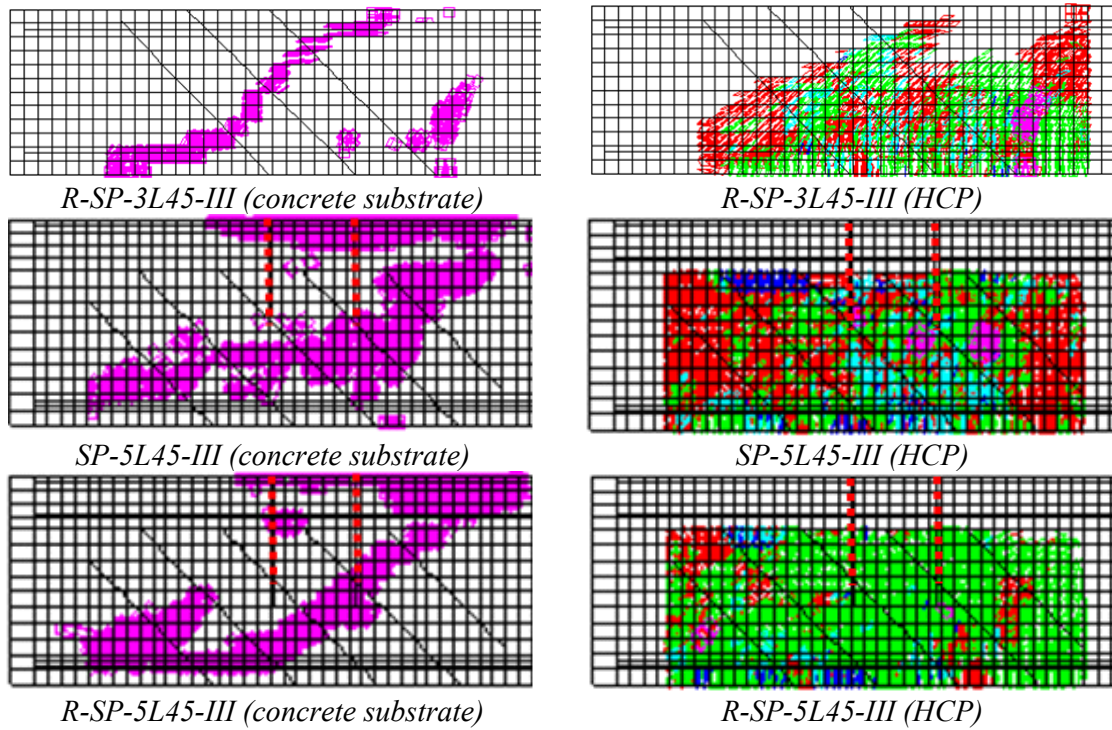


Figure 4-16: Crack patterns of the beams

4.7 Parametric Study for Assessing the Potentialities of the Developed Strengthening Technique

The computer program, whose good predictive performance for the simulation of the behavior of the structures under consideration was confirmed in the previous section, was adopted to execute a parametric study for the evaluation of the influence on the load carrying capacity and failure mode of the following parameters: arrangement of CFRP laminates and its shear strengthening ratio; the influence of mechanical anchors for fixing the HCP to the RC beam and concrete confinement; advantages of using SHCC instead of mortar.

The rectangular cross section beams simulated in the parametric study are shown in Figure 4-17. The T cross section beams that simulated in this section have the same mesh of the SP-5L45-III beam. The arrangement of the steel reinforcement, the material properties of concrete, SHCC and CFRP laminates, the support and load conditions, and the finite element mesh were the same of the ones adopted in the numerical simulations of the previous sections.

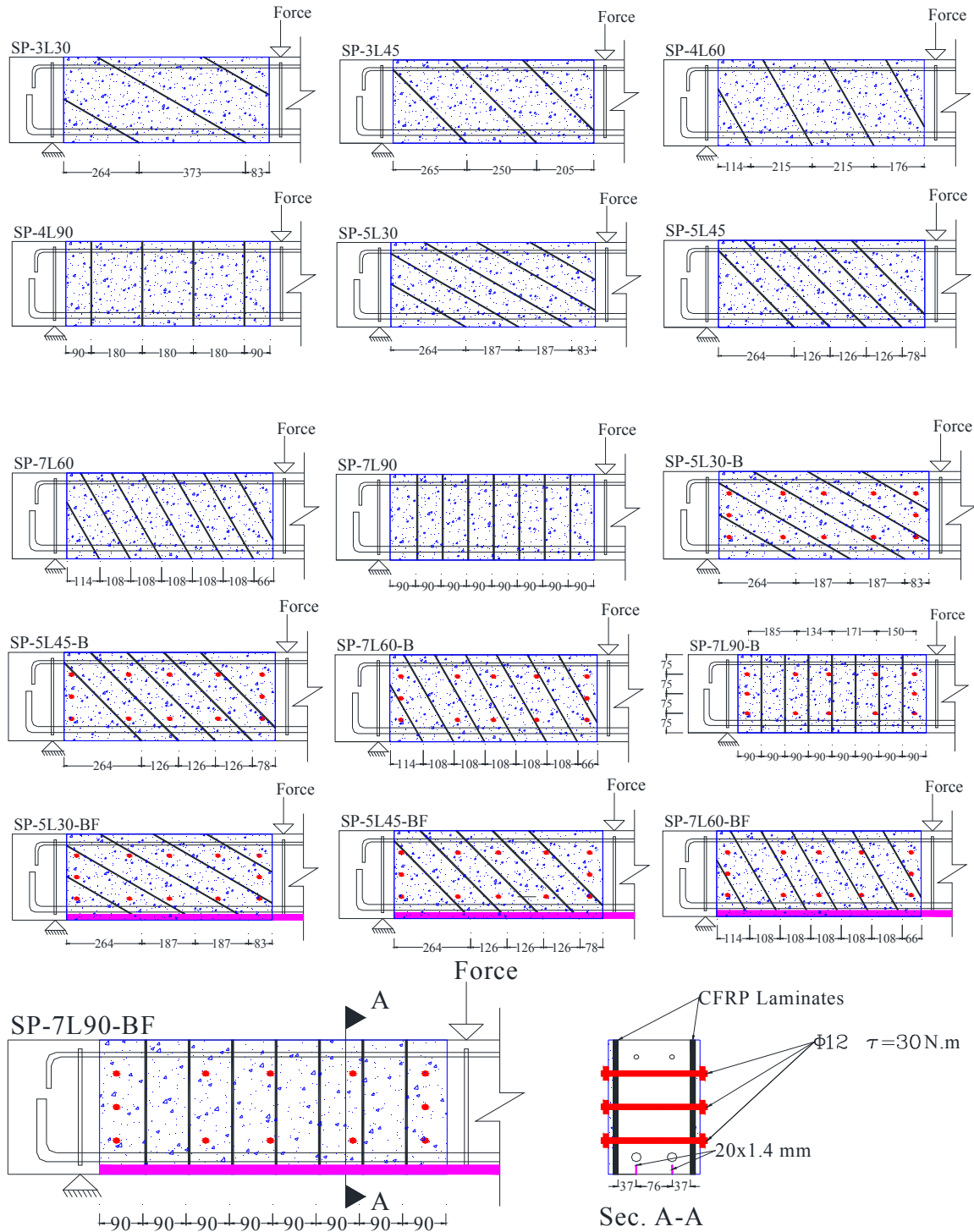


Figure 4-17: Strengthening scheme of the specimens (dimensions in mm)

Two shear strengthening ratios ($\rho_{fw} = 0.10\%$ and $\rho_{fw} = 0.20\%$) and four arrangements of CFRP laminates (30° , 45° , 60° , 90°) were studied. To prevent premature debonding of the HCPs and also to provide some confinement to the concrete core, the efficiency of using

mechanical anchors for fixing the HCP to the rectangular beam was also evaluated. A hybrid strengthening configuration composed of HCP for the shear reinforcement and longitudinal NSM CFRP laminates for the flexural reinforcement was also investigated for assuring a relatively high increase of load carrying capacity of RC beams. It was assumed that the longitudinal CFRP laminates had the same material properties of CFRP laminates for the shear strengthening. The designation of the beams composing this parametric study is indicated in Figure 4-17.

The mortar was considered as having material properties equal to the plain concrete of the beam to be strengthened (Table 4-7). The concrete confinement level was taken by simulating different torque applied to the mechanical anchors. Two different level of torque were chosen: 10 N.m and 40 N.m.

4.7.1 Influence of strengthening configuration and percentage of CFRP laminates

Figure 4-18 compares the relationship between the load and deflection curves at loaded section obtained for two different values of the shear strengthening ratio ($\rho_{fv} = 0.10\%$ and $\rho_{fv} = 0.20\%$) and four types of shear strengthening arrangements of the CFRP laminates (30° , 45° , 60° , 90°). The HCPs of SP-3L30, SP-3L45, SP-4L60, and SP-4L90 beams were strengthened with $\rho_{fv} = 0.10\%$, while the HCPs of SP-5L30, SP-5L45, SP-7L60, and SP-7L90 beams were strengthened with $\rho_{fv} = 0.20\%$. Figure 4-19 also compares the crack patterns of these beams (at the end of the last converged load increment). The crack patterns revealed that by increasing the CFRP percentage the failure mode shifted to detachment of the HCPs.

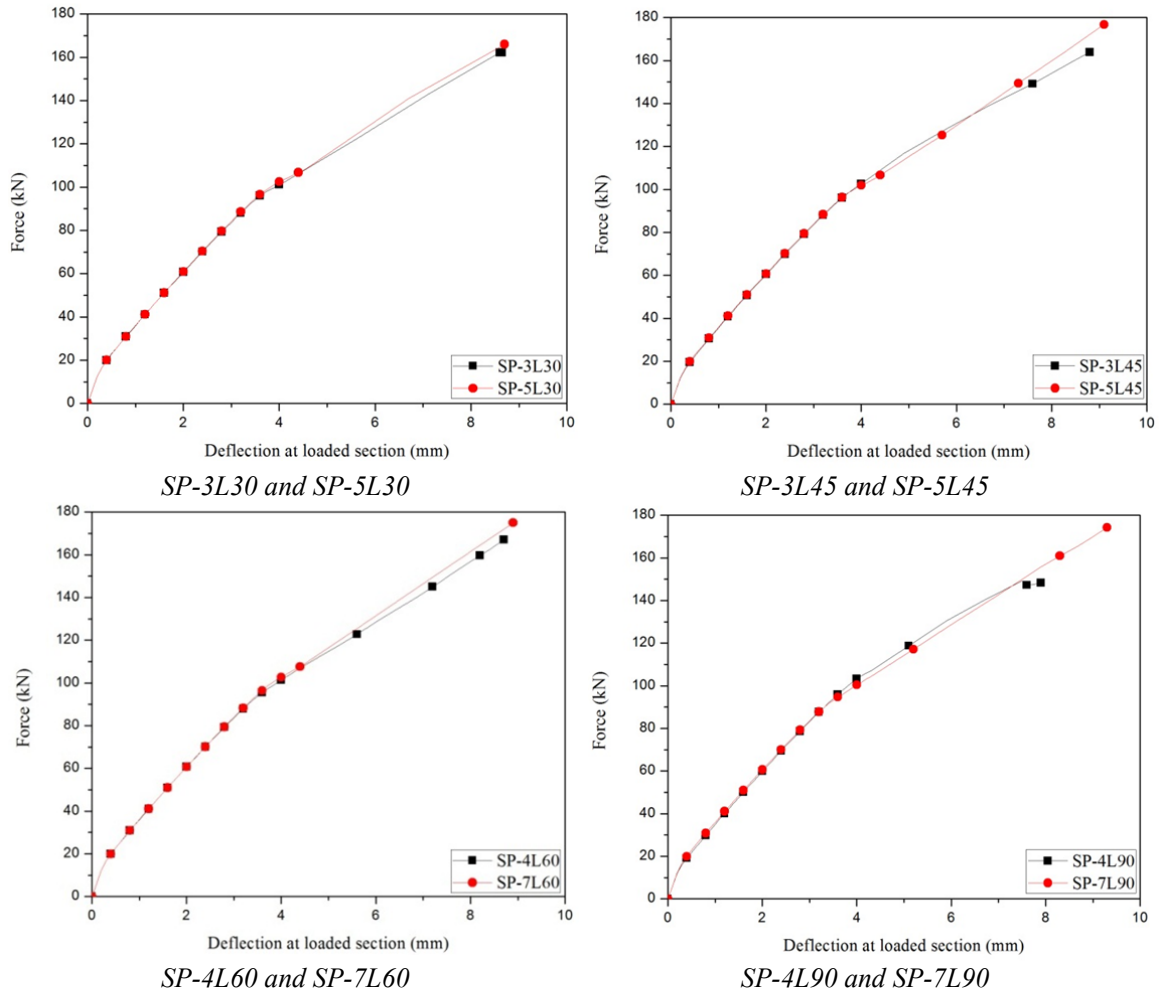


Figure 4-18: Influence of inclination and percentage of the CFRP laminates on the relationship between the force and the deflection at loaded section

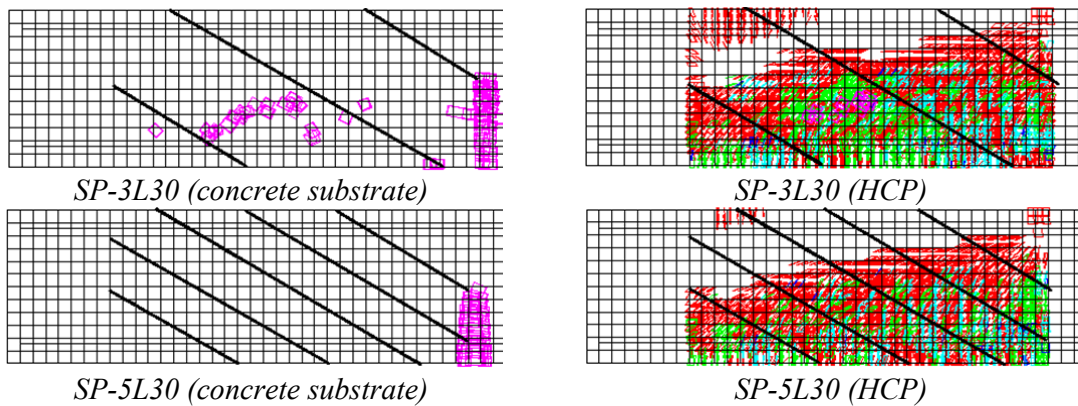


Figure 4-19: Influence of inclination and percentage of the CFRP laminates on the crack patterns

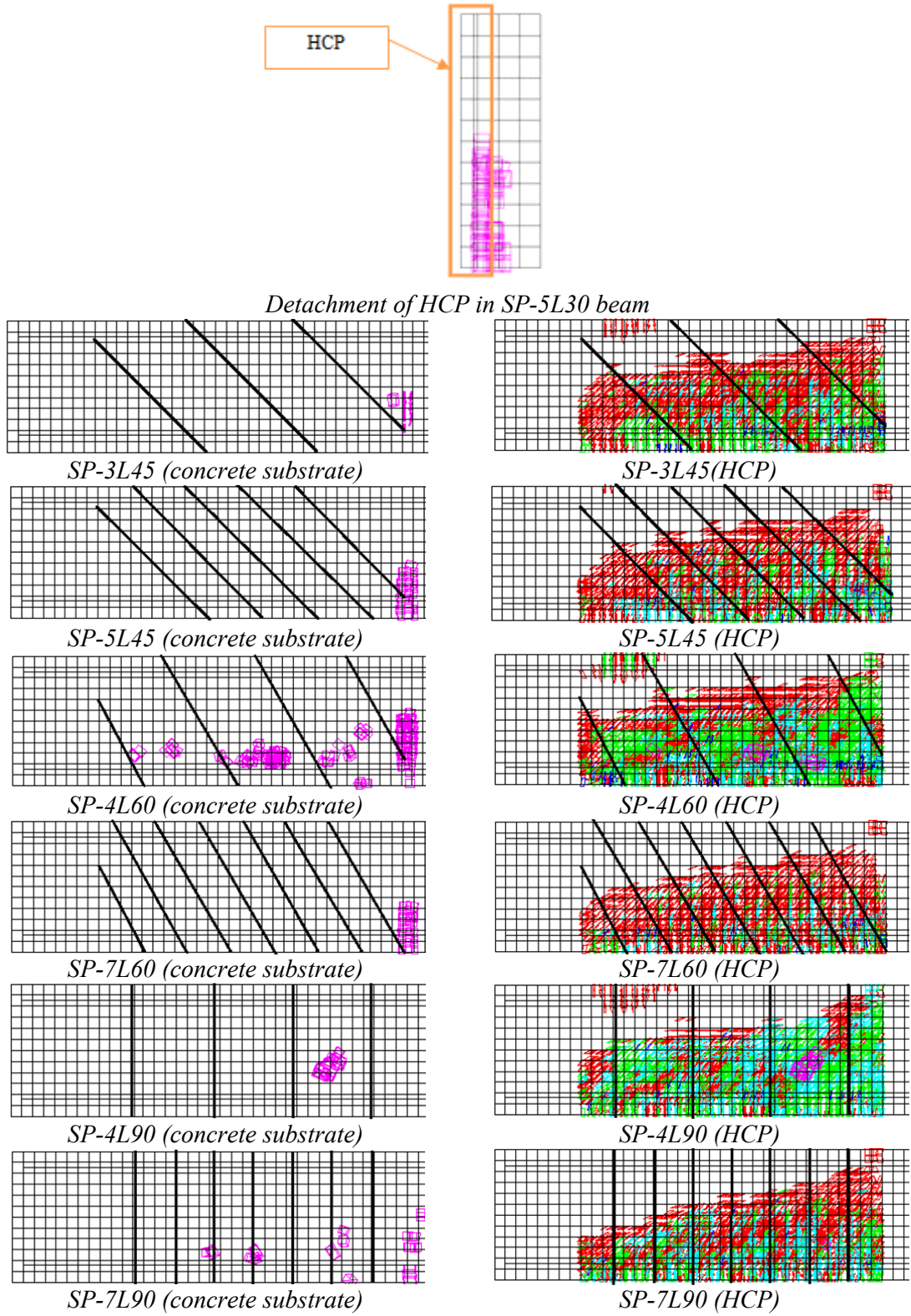


Figure 4-19: (Continued.)

4.7.2 Influence of mechanical anchors

Figure 4-20 compares the load-deflection curves obtained for two different procedures adopted to apply the HCPs to the concrete substrate of the lateral faces of the beam. In the first case, it is assumed the HCPs have been attached using an adhesive epoxy (full bond), while in the second case the HCPs are bonded using epoxy adhesive and fixed with 12 mechanical anchors. Figure 4-17 shows the position of the bolts. The diameter of the bolts is assumed 12 mm and a torque of 30 N.m is applied to tighten the bolts on both sides of the beam. The bolts are modeled with 3D two-node truss elements, and the torque was simulated by applying a temperature decrease of -23°C in these elements (based on the Eq. (4.25)). By applying the mechanical anchors, the load carrying capacity of the beams increased and the failure mode was changed from premature detachment of the HCPs to flexural failure (Figure 4-21).

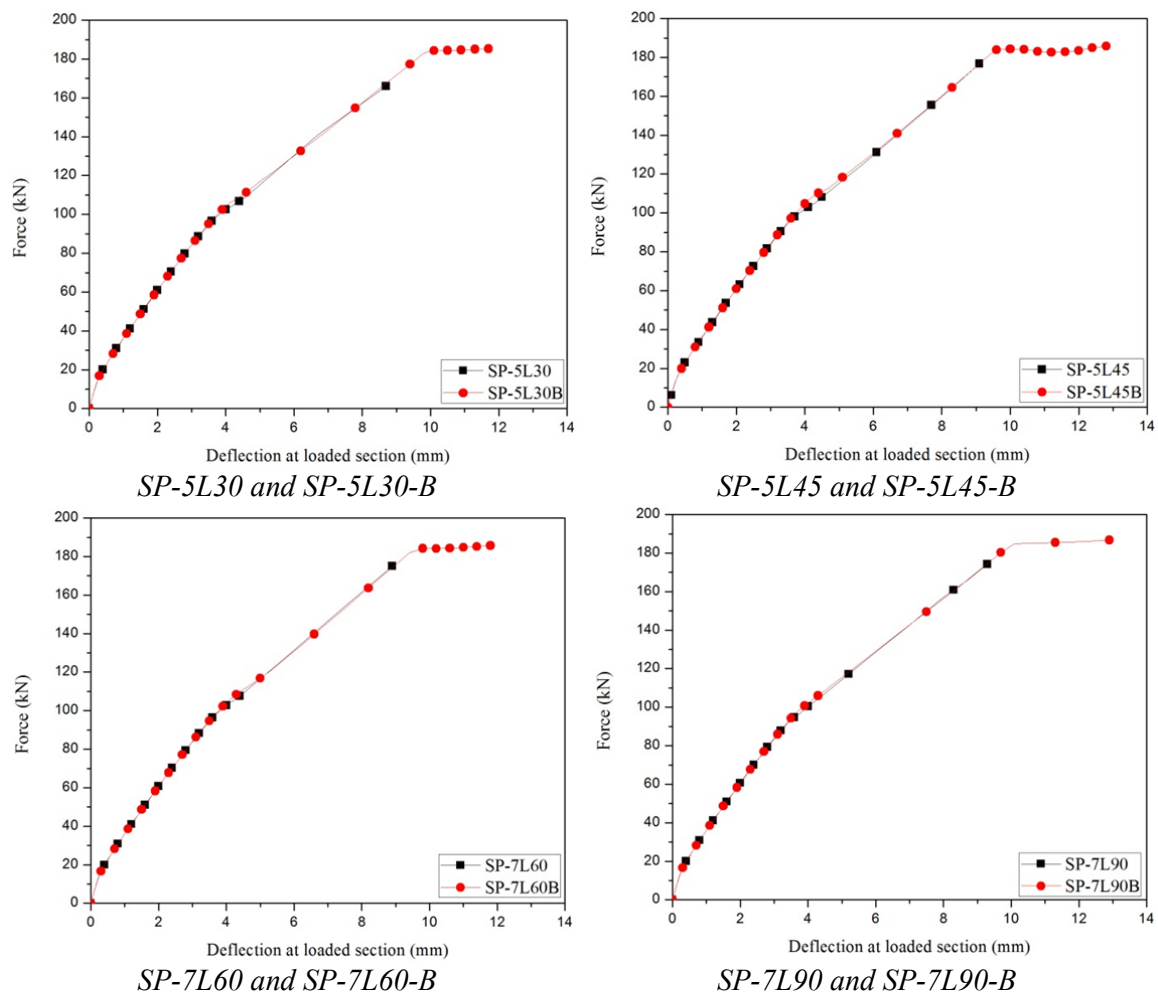


Figure 4-20: Influence of through bolts on the relationship between the force and the deflection at loaded section

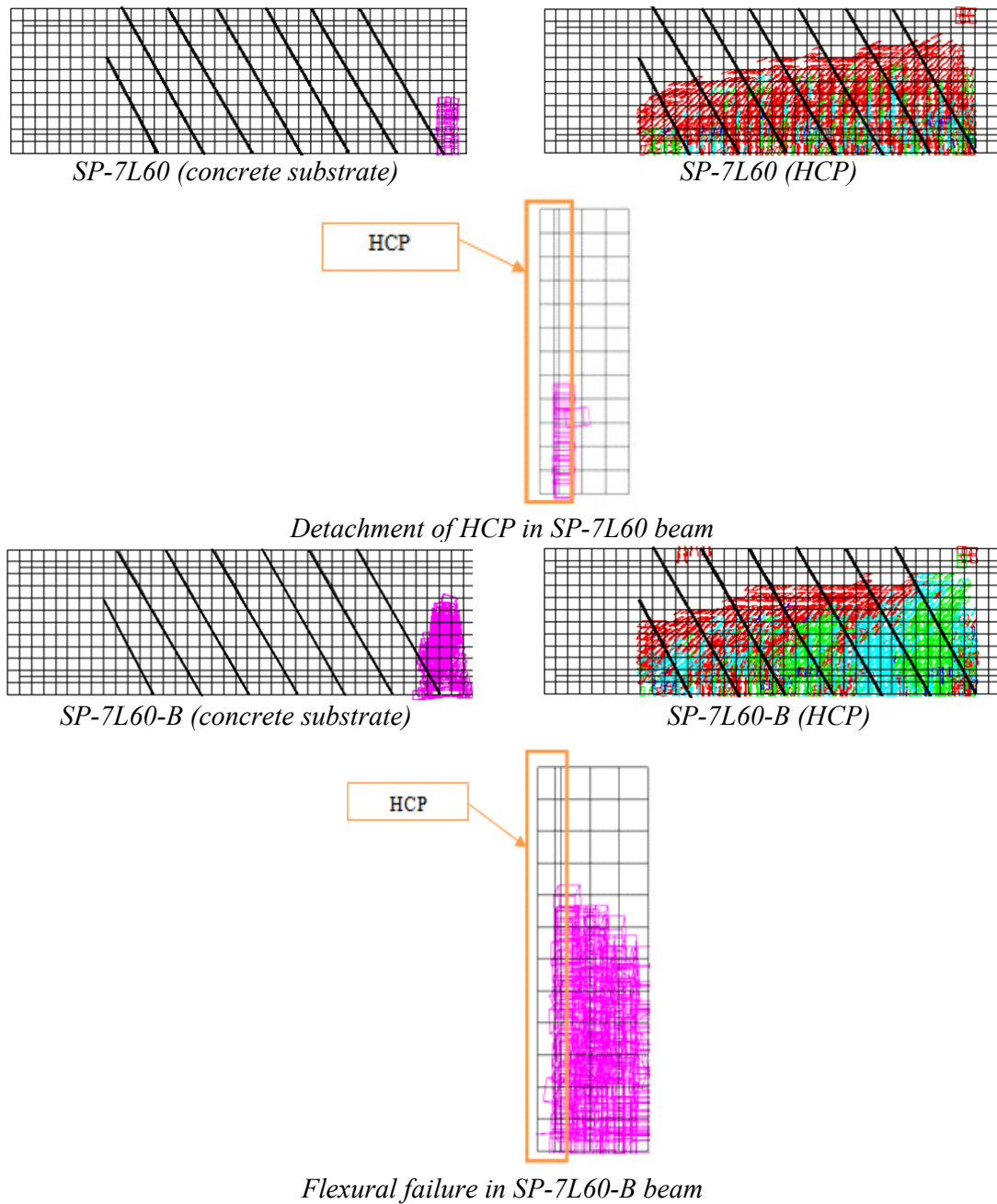


Figure 4-21: Influence of through bolts on the failure of the beams

4.7.3 Flexural strengthening of the beams

Based on the results in the previous section, by fixing with bolts the HCPs reinforced with the higher percentage of CFRP laminates, the beams have failed in bending, which avoided to exploit the full strengthening potential of these HCPs. Thus, to assess the shear strengthening effectiveness of these HCPs, it is essential to increase the flexural capacity of the beams. For

this purpose, the beams were also strengthened in bending by using two longitudinal CFRP laminates (Figure 4-17) of $20 \times 1.4 \text{ mm}^2$ cross sectional area and material properties equal to those used in the HCPs. Figure 4-22 and Figure 4-23 compare the relationship between load and deflection at the loaded section, as well as the crack patterns of the simulated beams (at the end of the last converged load increment). As the results show, this hybrid strengthening arrangement has provided a significant increase of the beam's load carrying capacity, with the highest increase registered in the beam shear strengthened with HCPs reinforced with laminates at 45° . The laminates at 60° are more effective than laminates at 90° .

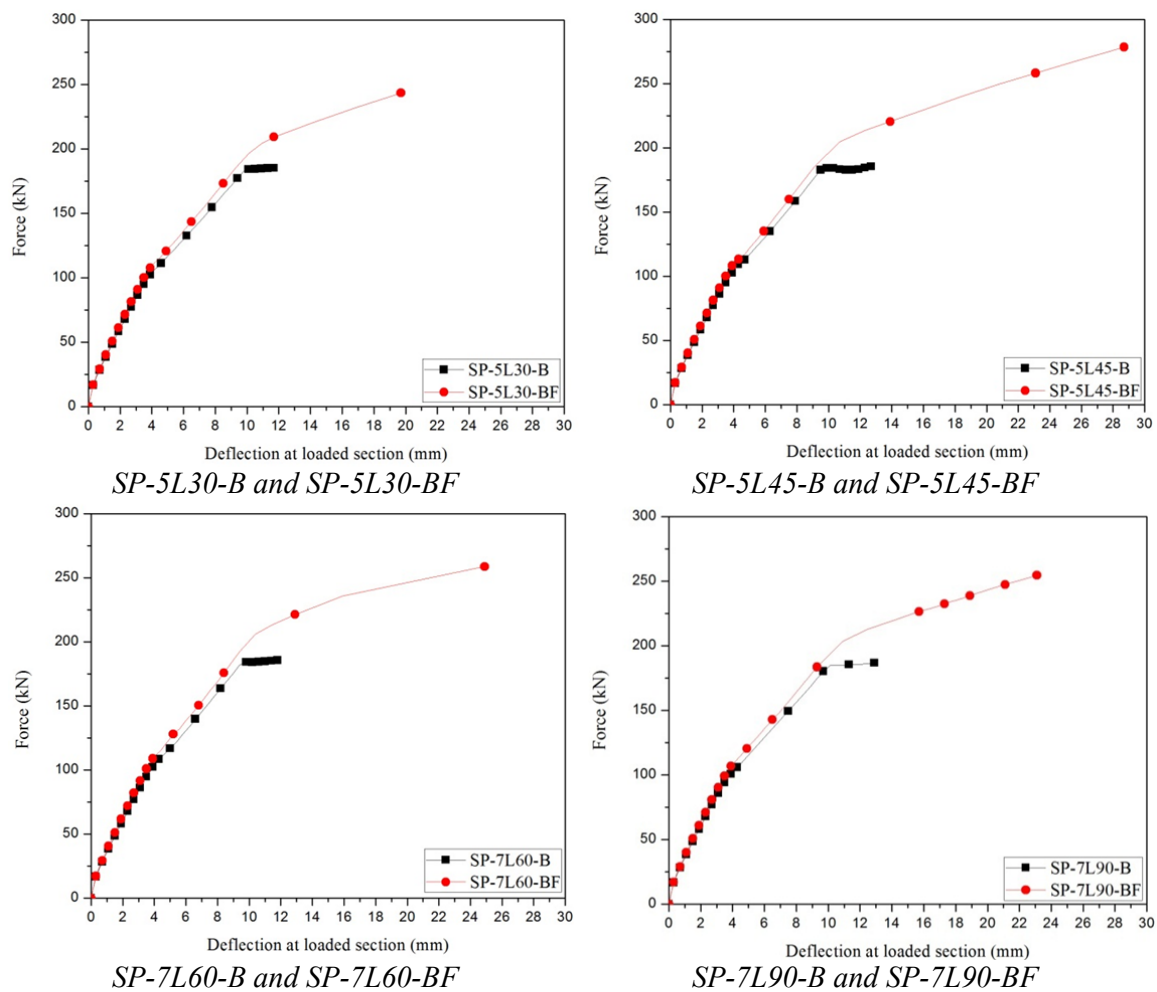


Figure 4-22: Influence of Shear and Flexural strengthening of the RC beams on the relationship between load and deflection

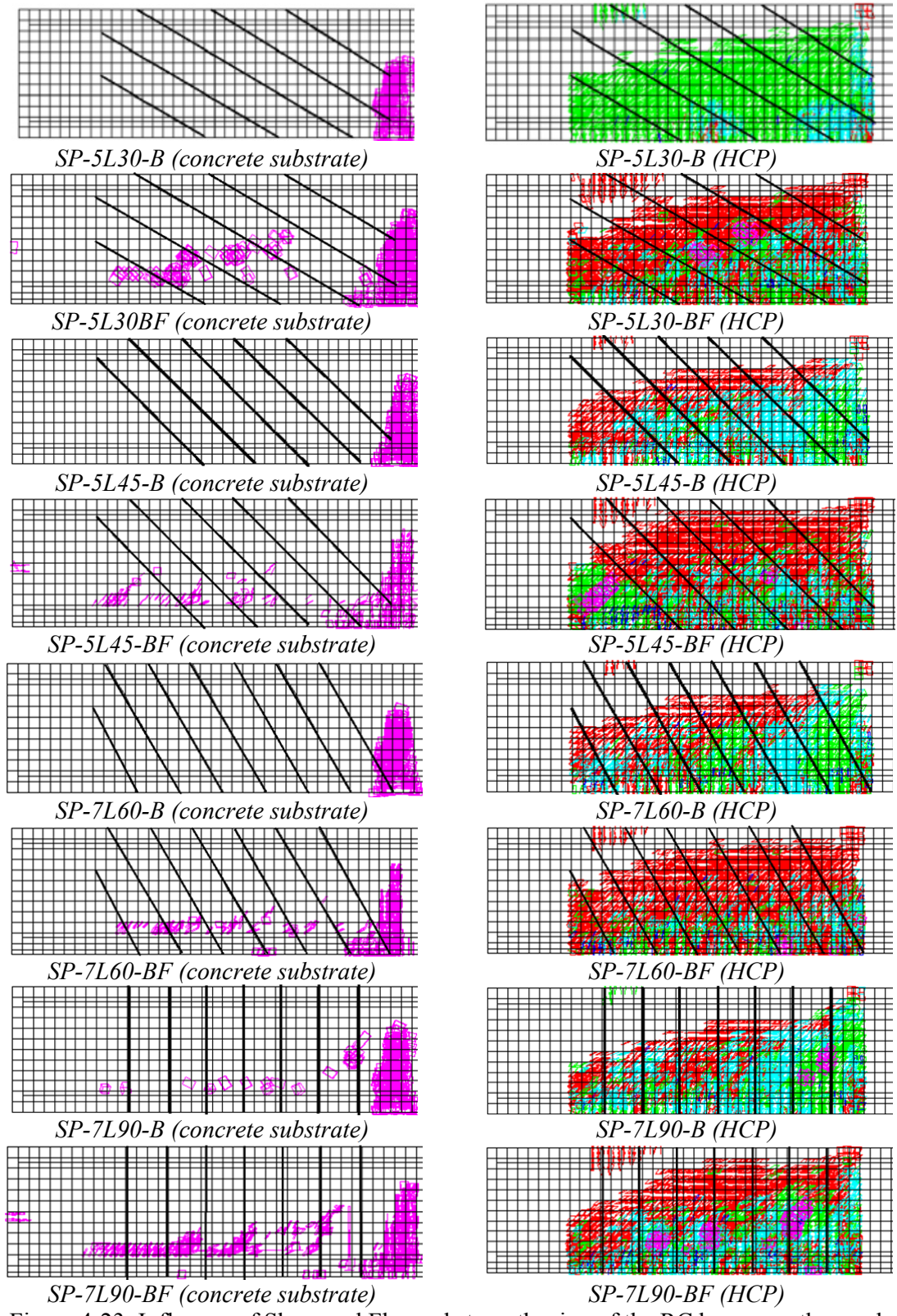


Figure 4-23: Influence of Shear and Flexural strengthening of the RC beams on the crack patterns

4.7.4 Influence of SHCC instead of Mortar

Figure 4-24 compares the relationship between the load and the deflection at loaded section obtained for the beam strengthened with HCPs (SP-5L45-III) and mortar plates (MP-5L45). It is assumed the mortar plate has the same dimensions ($800 \times 300 \times 20 \text{ mm}^3$) and CFRP reinforcement of the HCPs, and also it has the same material properties of the concrete substrate. As expected, the beam consisting of mortar failed at a lower load than of the beam strengthened with HCPs. This beam failed at a load of 474kN for a deflection of 7.3 mm. Figure 4-25 also compares the crack patterns of these beams at maximum load of the MP-5L45 beam. The crack pattern of the mortar plate includes more fully open cracks than HCPs due to the much more brittle nature of the mortar.

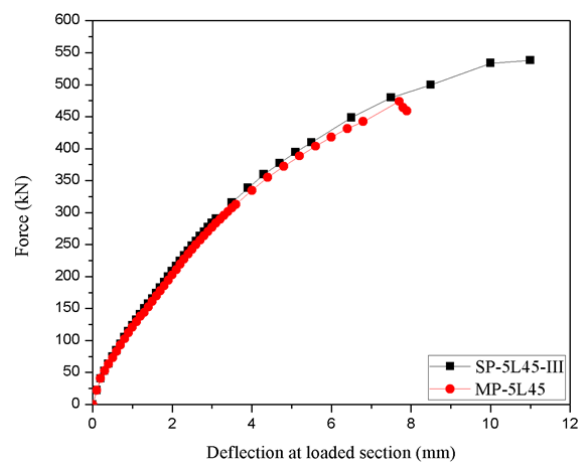


Figure 4-24: Influence of SHCC instead of mortar on the relationship between the force and the deflection at loaded section

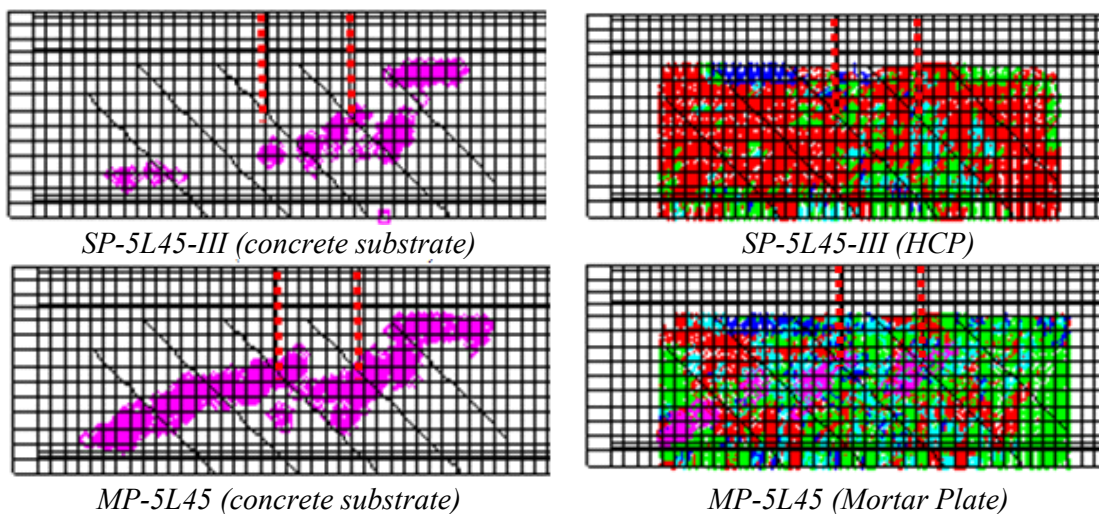


Figure 4-25: Influence of mortar instead of SHCC on the crack patterns at ultimate load of the strengthened beam with mortar plates

4.7.5 Influence of the torque level applied to the mechanical anchors

As aforementioned, the mechanical anchors can prevent the premature debonding of the HCPs, and increase the confinement of concrete core, with consequent benefits in terms of shear resistance. As explained in the previous section, torque was simulated by applying a temperature decrease of -12.75°C , -23°C , and -51°C (10N.m, 20N.m, and 40N.m, respectively) in these elements, by following Eq. (4.25). Figure 4-26 compares the load-deflection curves obtained for three different torque levels applied to the mechanical anchors. As expected, the load carrying capacity of the beam and its ultimate deflection have increased with the torque level. Figure 4-27 shows the crack patterns of the beams at the ultimate load of the beam with the lowest torque level (SP-5L45-T10). Based on this figure by increasing the torque the crack opening is decreased in a same load and SP-5L45-T40 beam has the minimum full opening crack than other beams.

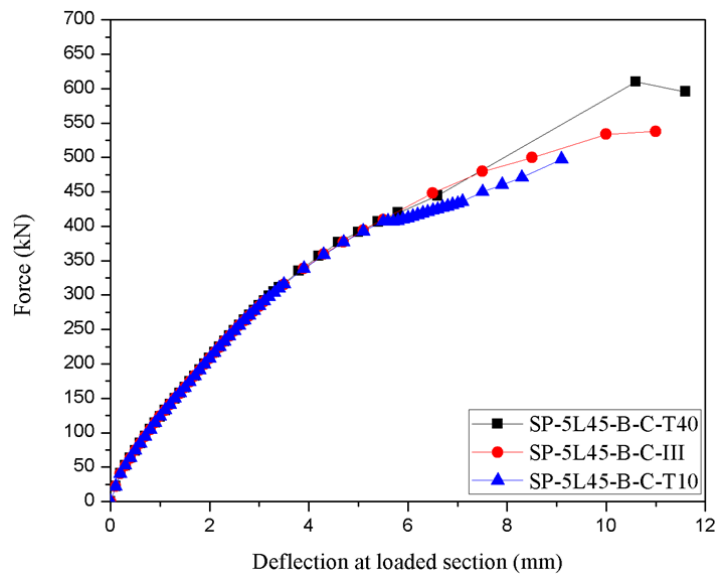


Figure 4-26: Influence of concrete confinement on the relationship between the force and the deflection at loaded section

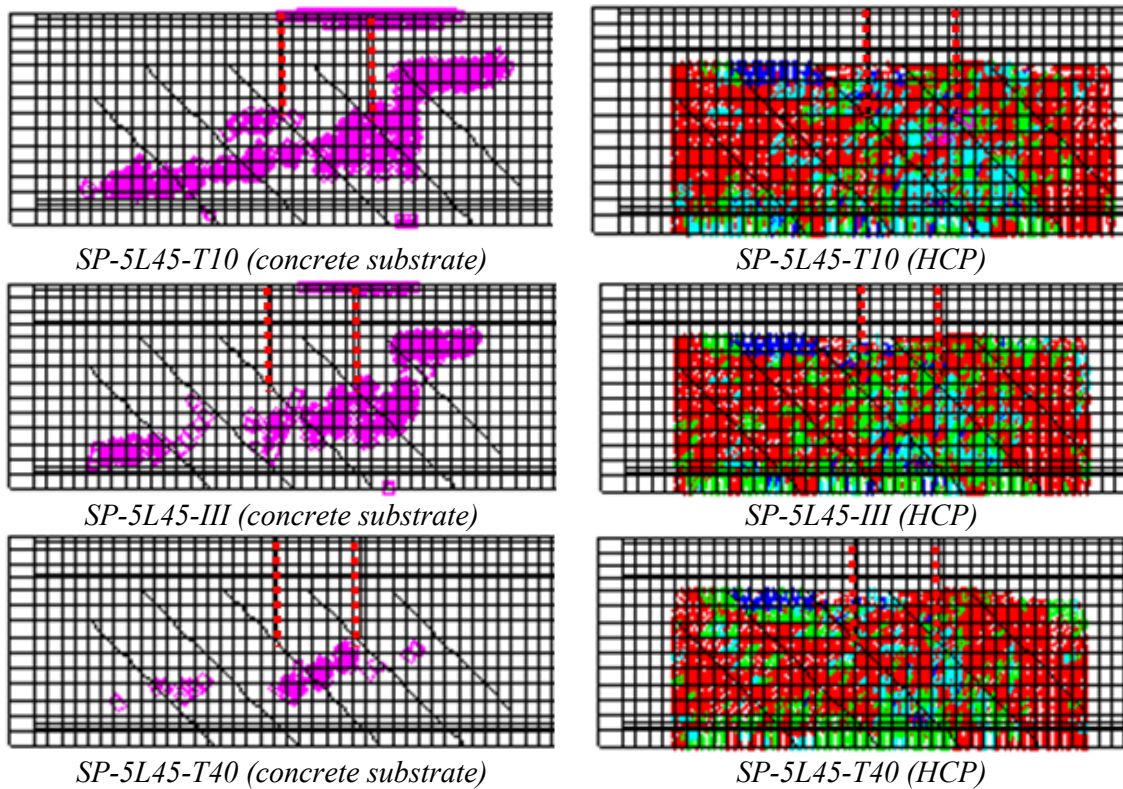


Figure 4-27: Influence of the torque level applied on the mechanical bolts on the crack patterns at the ultimate load of the beam with the lowest torque level (SP-5L45-T10)

4.8 Conclusions

The capability of a FEM-based computer program to predict with high accuracy the behavior of the beams strengthened in shear with hybrid composite plates (HCPs) up to its collapse was demonstrated. The shear crack softening diagram available in the multi-directional fixed smeared crack model allowed a good prediction of the load carrying capacity, crack patterns and failure modes of the tested beams. Due to the lack of specific experimental tests, the data to define the shear crack softening diagram was obtained by inverse analysis. It can be concluded that by adopting the shear softening diagram in the multi-directional fixed smeared crack model available in the FEMIX computer program has assured the prediction with high accuracy the behavior of structures failing in shear or in flexural/shear.

To simulate the existing shear crack of the beams to be strengthened (series III), a very small tensile strength and mode I fracture energy was attributed to the finite elements crossing this shear crack.

To evaluate the influence on the beam's load carrying capacity of the shear strengthening arrangement and ratio of CFRP laminates, the effectiveness of mechanical anchors, and

advantages of SHCC instead of mortar to produce HCP an extensive parametric study was carried.

By increasing the shear strengthening ratio of CFRP laminates, and fixing the HCPs to the beam's concrete substrate by mechanical anchors, failure mode can be shifted from shear failure and detachment of the HCPs to flexural failure. It was also verified that HCP's with laminates at 45° was the most effective arrangement in terms of shear strengthening with the proposed technique. The hybrid technique composed of HCPs for the shear strengthening and NSM CFRP laminates for the flexural strengthening was capable of increasing significantly the load carrying capacity of RC rectangular beams by highly mobilizing the potentialities of these reinforcement systems.

When mortar was used instead of SHCC, the beam has failed at a lower load, since the strain hardening character of the SHCC assured a much more diffuse crack pattern in the HCP, with a consequent better mobilization of the high tensile capacity of the CFRP laminates.

The load carrying capacity and deformability performance of this type of strengthened beams have increased with the torque level applied to the mechanical bolts due to the higher concrete confinement.

Chapter 5

Shear Behavior of SHCC Material

5.1 Introduction

The assessment of the shear behavior of SHCC is a challenging task due to lack of accurate test methods. The great difficulty lies in developing a test setup capable of introducing a pure shear stress field. There are several shear tests proposed by various researchers in an attempt of capturing the shear behavior of materials (Ohno 1957, Iosipescu 1967, Banks-Sills and Arcan 1983, Reinhardt et al. 1997, Boulifa et al. 2013). Iosipescu test was proposed for determining shear properties of metal and welded joints (Iosipescu 1967). This test method was considered appropriate for composite materials, and it was adopted by ASTM standard D-5379 (1993). The Iosipescu specimens are loaded in antisymmetric four points bending with a double notch in a region with high shear and low bending moment. The Iosipescu specimens consist of a small beam height (h_0), angle of notch root (α), and tip radius at notches (r) (Figure 5-1). This geometry of the specimen can assure a uniform shear distribution in the notched plane.

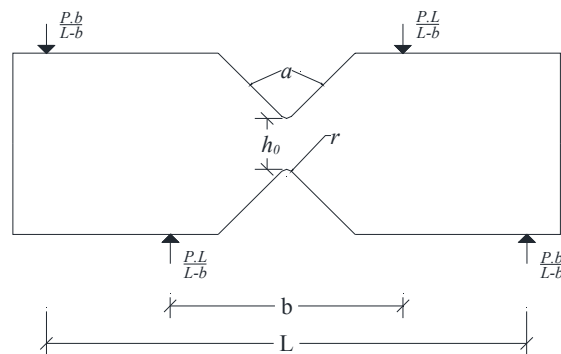


Figure 5-1: Concept of Iosipescu Shear Test

In this chapter, the shear behavior of the SHCC is investigated by Iosipescu shear test method. For this purpose, an experimental program of V-double edge notched was carried out. The experimental program is detailed and the obtained results are presented and discussed.

Advanced numerical simulation was carried out to contribute for a better understanding of the shear behavior of the SHCC. These simulations have fitted the average shear stress-sliding relationship of the tested specimens.

A parametric study was carried out by executing a nonlinear analysis with FEM-based computer program, FEMIX, to study influence of shear retention factor defining the first branch of shear softening diagram, to illustrate the advantages of SHCC *vs.* mortar and also effect of notch tip radius.

5.2 Review of Mode II Testing Methods

Pure shear panel test method was developed to measure the relationship between principal stresses and corresponding principal strains (Collins and Mitchell 1991). In this method several loads are applied in two directions to transfer a vertical load to a pure shear force directly on specimen (Figure 5-2a). In this test shear stress distribution on panel is not uniform, shear stress has a maximum value at each surface and decreases along the diagonal, and has a minimum value at the center of the specimen. This method was used for plain concrete, lightweight aggregate concrete, and FRC.

Double edge notched compression test has been proposed for materials made by high compressive strength ($f'_c = 85$ MPa and $f_t = 5$ MPa) (Reinhardt et al. 1997). As shown in Figure 5-2b, one side of the specimen is loaded in compression and the other side is free. After mode II crack initiation at the tip of the notch, diagonal shear bonds form that cause failure of concrete in compression before the mode II crack extended to its full size. Hence, this technique is not able to measure fracture energy of mode II.

Axisymmetric punch shear test has been used for mortar and concrete due to easy handling (Figure 5-2c) (Tada et al. 1985). However, numerical simulation showed that large tensile stresses occur at the crack tips. A recent study has shown that increasing the number and depth of the notches can decrease the tensile stress at the crack tips (Reinhardt et al. 1997).

Short beam shear test is one of the simplest tests (Figure 5-2d) and is widely used for composites materials (ASTM 2000). However, the short beam shear test cannot give acceptable results due to non-uniform shear stress distribution and the presence of normal flexural stress.

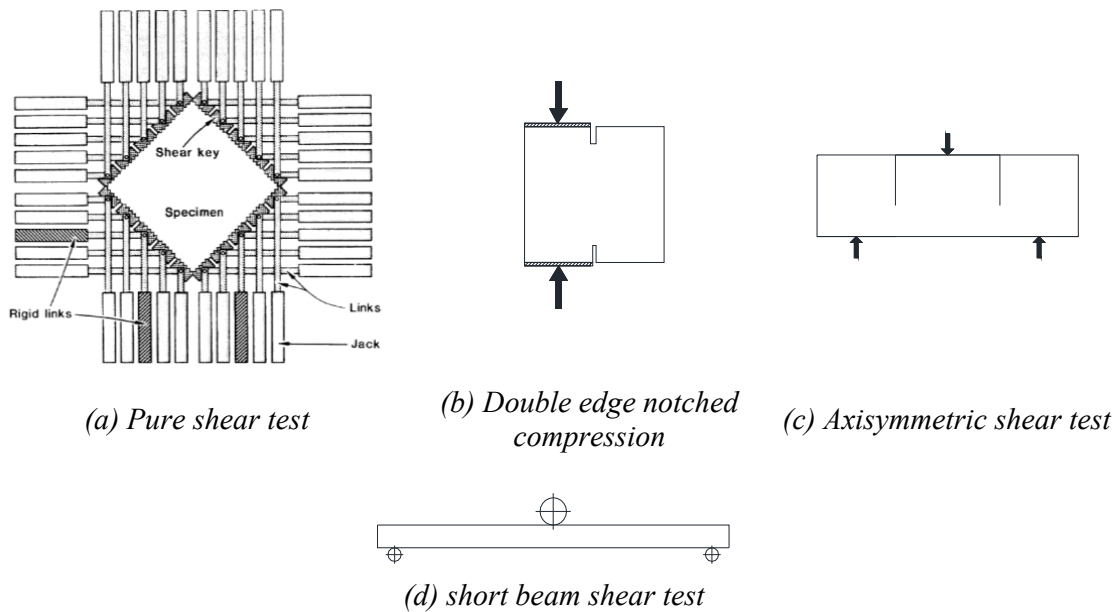


Figure 5-2: Different mode II test setups: (a) Pure shear panel test (Collins and Mitchell 1991); (b) Double-Edge Notched compression (Reinhardt et al. 1997); (c) Axisymmetric shear specimen according to Tada et al. (1985); (d) short beam shear test (ASTM 2000)

Ohno shear beam test was developed to create a pure shear zone (Ohno 1957). The concept of the Ohno shear beam test is shown in Figure 5-3a. Based on the shear force (Figure 5-3b) and bending moment diagrams (Figure 5-3c), a state of pure shear exists at the center of the beam where the bending moment is zero. Bending moment varies along the beam with the maximum ($p.a/2$) and minimum values (0) at the two inner loading points (Figure 5-3c). Thus, the failure of the specimen becomes uncertain. Shear failure, flexural failure or a combination of the shear and flexural failure may occur during this test (Shang and Zijl 2007). In an improvement on the Ohno shear test, a notched specimen was proposed by Iosipescu (1967), whereby a uniform shear stress distribution in the pure shear zone is possible to assure.

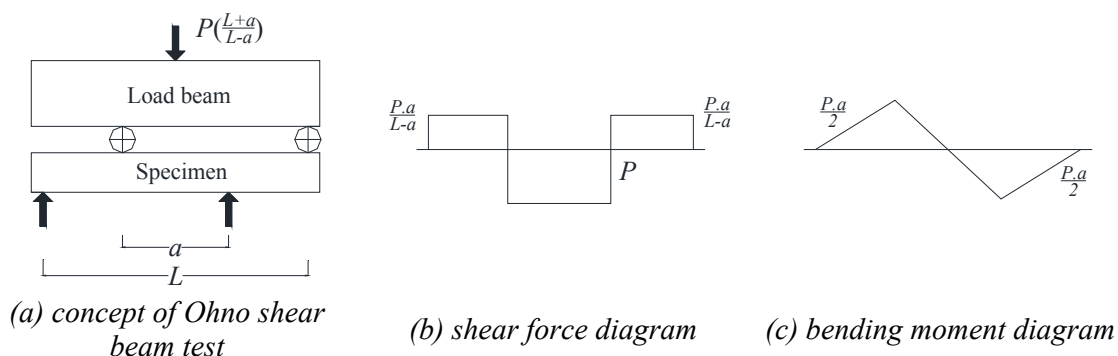


Figure 5-3: Shear force and moment diagram for Ohno shear beam test

5.3 Iosipescu Shear Test

This test method was proposed by the ASTM D-5379 (1993) standard for composite materials. The Iosipescu test method has been also used for fiber plastic materials (Morton et al. 1992) and wood (Xavier et al. 2004). As shown in the Figure 5-4 the concept and mechanism of the Iosipescu shear test is similar to Ohno shear beam test. However, the Iosipescu specimens consist of a double V-edge notched with small beam height (h_0), angle of notch root (α), and tip radius (r) at the pure shear section (Figure 5-1), whose values are defined in an attempt of assuring a uniform shear distribution in the notched plane. Based on the Figure 5-4 a state of pure shear exists at the center of the specimen, where the bending moment is zero.

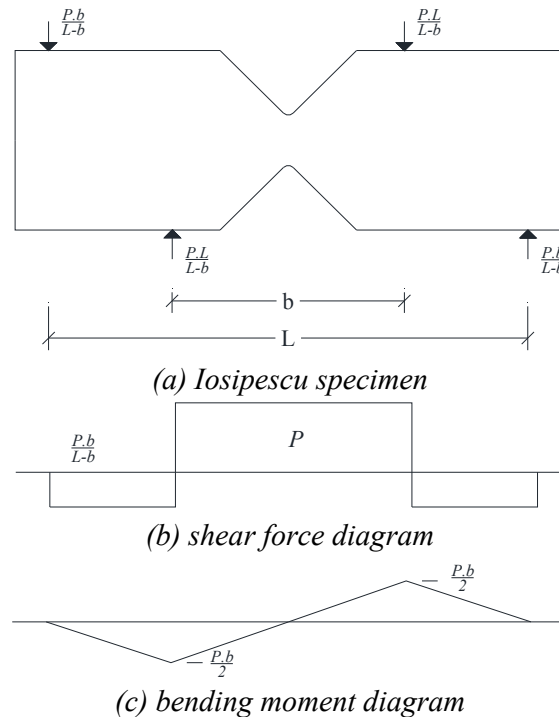


Figure 5-4: Internal force and bending moment in Iosipescu specimen

A notable amount of experimental research and numerical analysis dedicated to the Iosipescu shear test have been performed either with a single notch (Figure 5-5) or double notch (Figure 5-4) (Swartz et al. 1987, Ballatore et al. 1990, Barr and Derradj 1990, Ho et al. 1993, Derradj and Kaci 2008). The results of the single notch specimens have shown that cracks initiate in mode II but quickly change to a mixed mode, although finite element simulation has shown the mode I is the dominant crack propagation mode, and single notched specimen is not suitable for the determination of mode II fracture parameters (Swartz et al. 1987).

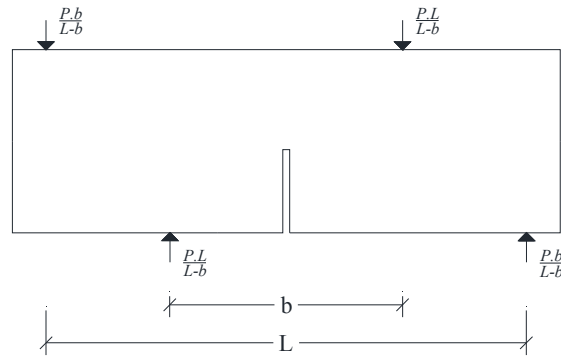


Figure 5-5: Single notch specimen

Krishnan et al. (2009) performed a numerical study to measure the variation of the shear stress along the center of Iosipescu and full specimen (Ohno shear beam test). Both specimens had the same sectional area at the pure shear section. As shown in Figure 5-6, the variation of shear stress for Ohno shear test beam is parabolic, while in Iosipescu specimen is almost constant at the critical section (notched plane).

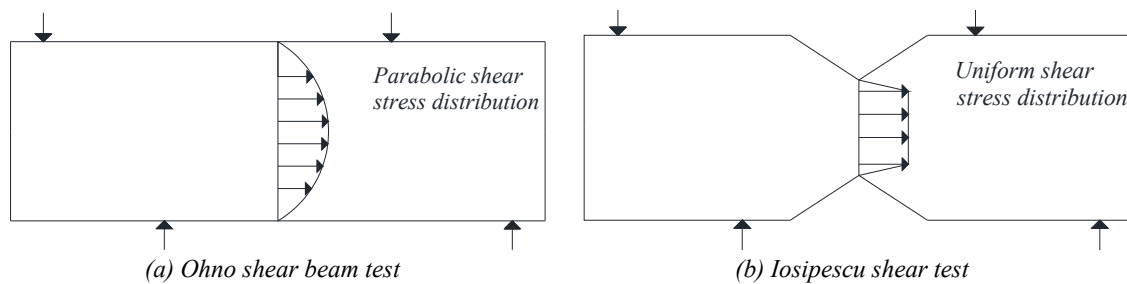


Figure 5-6: Comparison between (a) Ohno shear beam test and (b) Iosipescu shear test (Krishnan et al. 2009)

A modified Iosipescu shear SHCC specimen has been investigated by linear finite element analysis by considering the material properties of SHCC (Shang and Zijl 2007). Notch radius (r), height of the specimen at notched section (h_0), and angle of notch roots (α) have been studied to find a uniform shear stress distribution along the critical section.

5.4 Experimental Program

5.4.1 Development of fixture and specimen

Two versions of the Iosipescu shear fixture and specimen have been developed for composite materials (Ho et al. 1993) (Figure 5-7a and Figure 5-7b). The original fixture and specimen (Figure 5-7a) produced a very small region of uniform shear stress due to small depth of

notched section and significant normal strains in the specimen test section. To overcome these deficiencies a modified fixture and specimen were developed (Figure 5-7b). The modified fixture could produce a larger test section, larger fixture-to-specimen contact regions and the innermost fixture-to-specimen contact points were moved farther away from the test section. The uniform shear stress region increased but normal strains still exist in the test section.

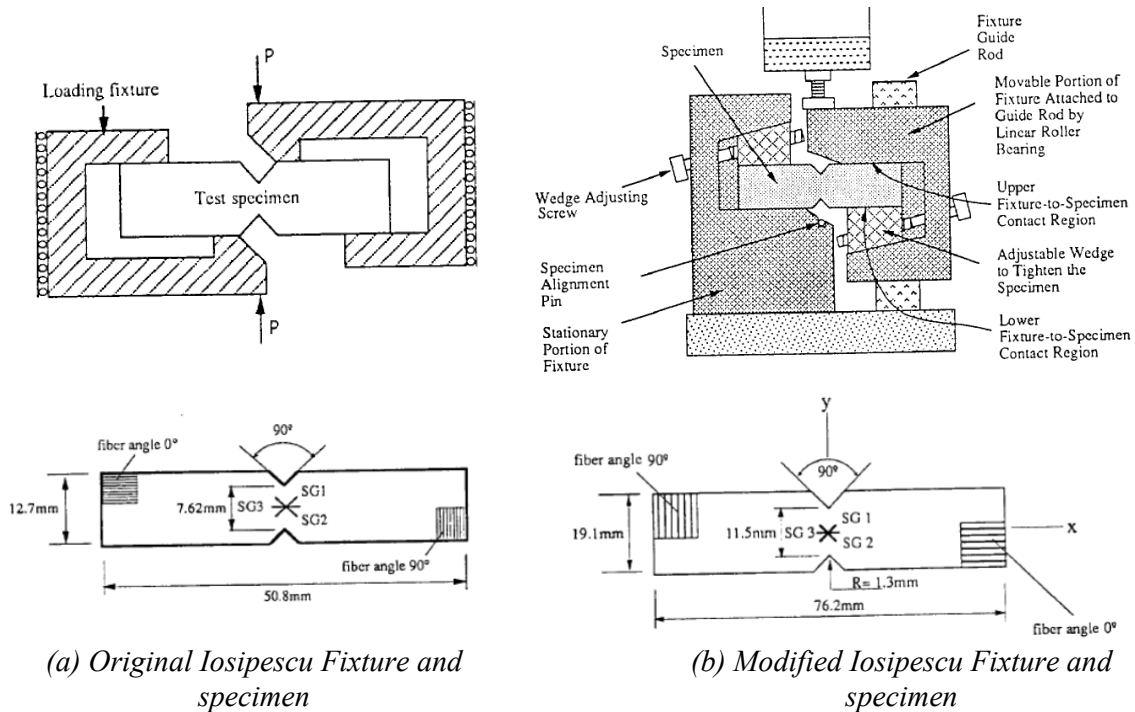


Figure 5-7: Developed Iosipescu fixtures and specimens (Ho et al. 1993)

The device developed in the scope of the research carried out in this PhD thesis is identical to the modified Iosipescu fixture (Figure 5-8a), and its details are provided in Annex A. This fixture covers the entire contact regions of the specimen.

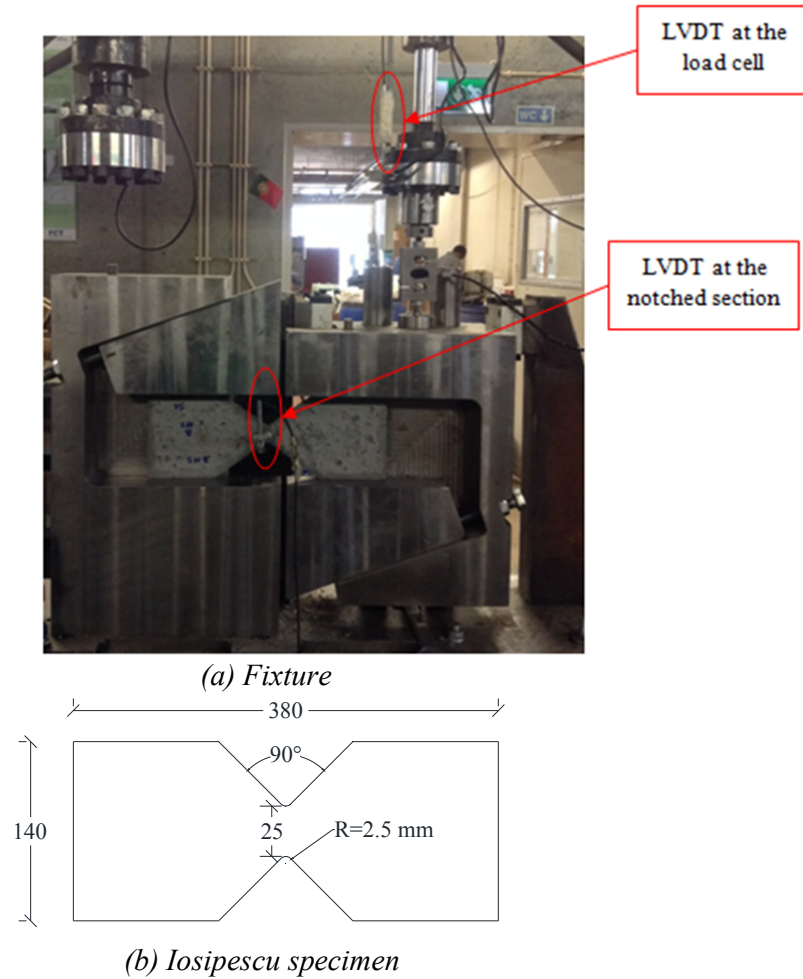


Figure 5-8: Developed Iosipescu fixture and specimen at university of Minho

The tests to carry out aim, mainly, to study the shear strength and shear stress evaluation with the crack sliding of SHCC material and also fracture energy of mode II, G_{f_s} . The dimensions of the specimens were $380 \times 140 \times 14.5 \text{ mm}^3$ with depth of the notch roots (h_0) 25 mm, angle of notch root (α) 90° , and tip radius at notches (r) 2.5 mm (Figure 5-8b). The specimen was designed by considering the results obtained by Shang and Zijl (2007) due to their study to modify the geometry of Iosipescu specimen for SHCC material.

The specimens were casted as the same time with the panels of the beams in Chapter 3. The average tensile stress at crack initiation and average tensile strength of the SHCC were 2.7 and 3.5 MPa, respectively. Table 5-1 presents the SHCC material properties.

Table 5-1: Values of the properties of SHCC materials

<i>Tensile stress at crack initiation</i>	<i>Tensile strength</i>	<i>Tensile strain at tensile strength</i>	<i>Compressive strength</i>	<i>Young's modulus</i>
2.7 MPa	3.5 MPa	1.3%	31.6 MPa	18.4 GPa

5.4.2 Test setup and monitoring system

The load was applied (10 kN load cell) by using a servo closed loop control equipment, taking the signal read in the displacement transducer (LVDT) of the servo-actuator to control the test at a deflection rate of 0.005 mm/s. The value registered in the load cell was calibrated by taking into account the weight and slight friction of the movable portion of fixture. For this purpose, in the first step, the servo-actuator registered the weight and slight friction of movable portion with no specimen installed inside. Then, the value showed by the load cell in this case was used to rectify the value of load cell during the test. Thus, the final value recorded from the load cell during the tests was considered as shear force in the notched section of the specimens. One LDVT was installed at the loaded section to measure the displacement of the specimens (Figure 5-8a), and another one was installed at notched section (as shown in Figure 5-9) to measure the sliding of the crack.

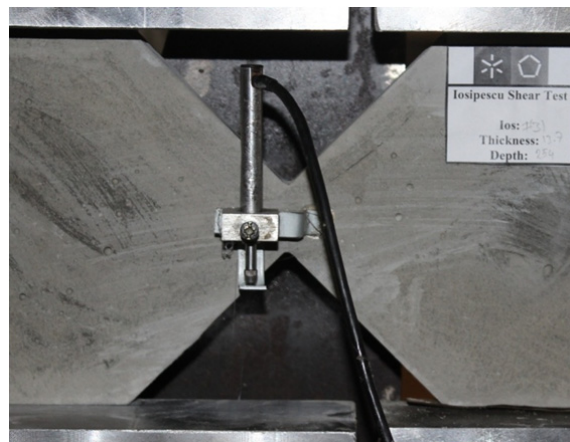


Figure 5-9: The position of the LVDT to measure sliding of the shear crack at notched section

5.4.3 Test results and discussion

Eight coupon specimens were tested. The average shear stress is determined by dividing the total applied load (P) (measured by the load cell) by the area of the cross section between two notches:

$$\tau_{avg} = \frac{P}{A} \quad (5.1)$$

The envelope and the average curve corresponding to the average shear stress vs. sliding relationship of the specimens are plotted in Figure 5-10. Figure 5-11 shows the typical crack patterns of these specimens.

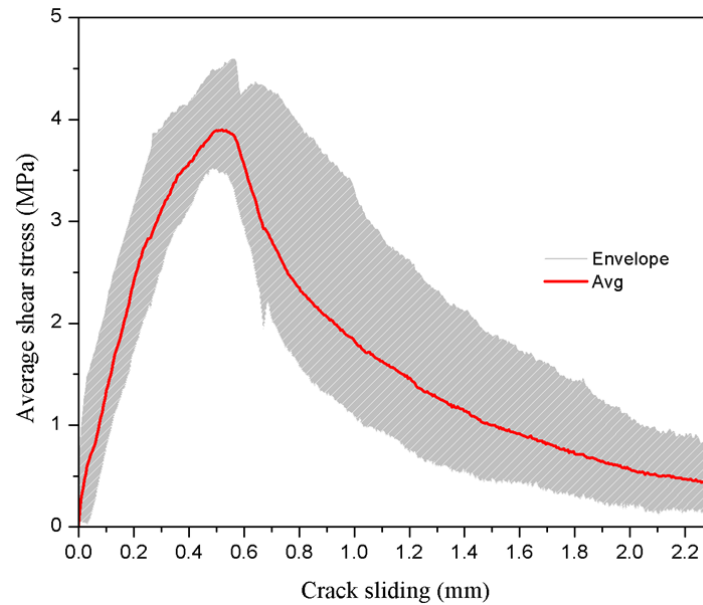
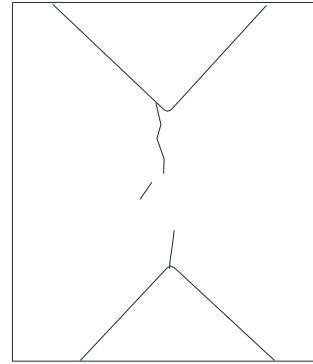
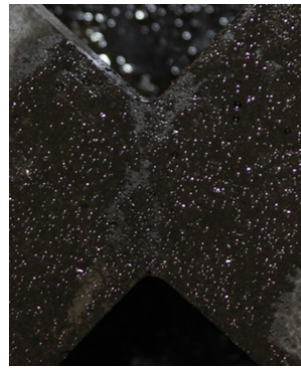


Figure 5-10: The envelope and average stress vs. crack sliding

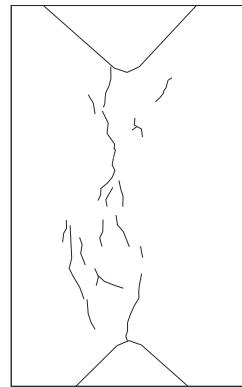


Figure 5-11: Typical crack patterns Iosipescu specimens tested

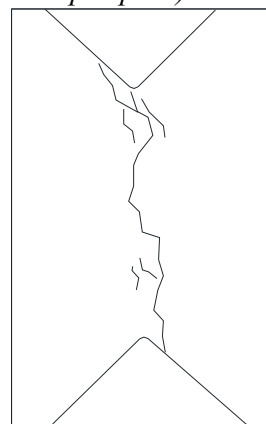
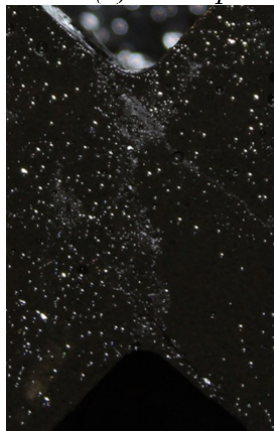
Iosipescu specimens had similar failure mode and their shear stress-sliding curves introduce three phases. The first phase corresponds to the linear behavior up to a shear stress of about 0.7 MPa (0.08 mm) and formation of initial vertical cracks (Figure 5-12a). These cracks were detected by spraying oil (WD-40) on the surface of the specimens. In the second phase more micro cracks were formed up to peak load (Figure 5-12b). When specimens reached their maximum load, the micro cracks connected to each other and the load started decreasing (softening stage) (Figure 5-12c) up to end of the test (Figure 5-11). Based on Figure 5-10, for an average slip 2 times the average slip at peak load the SHCC was still capable of supporting 50% of the average shear strength, which denotes the ductility of this composite material when subjected to shear deformations.



(a) Crack pattern at first phase (Linear pre-peak up to sliding of around 0.08 mm)



(b) Crack pattern at second phase (nonlinear pre-peak)



(c) Crack pattern at shear softening (nonlinear pre-peak)

Figure 5-12: Crack pattern of one specimen at different phase

By calculating the area under the curve of average shear stress versus sliding (shown in Figure 5-10), the fracture energy mode II of SHCC material was estimated about 1.4 N/mm, which corresponds to 40% of its mode I fracture energy.

5.5 Numerical Simulation

A numerical simulation based on the finite element method (FEM) of the Iosipescu beams test was carried out to define the fracture mode II of the constitutive model described in chapter 4. To simulate the crack initiation and fracture mode I propagation of SHCC, the tri-linear tension-softening diagram presented in Figure 4-2 was adopted. The values to define this diagram are indicated in Table 5-2. This table also includes the data necessary to define the shear-softening diagram in Figure 4-3. The crack shear strength corresponds to formation of initial vertical cracks and equal to 0.7 MPa (Figure 5-10 and Figure 5-12a). Also, fracture energy mode II was taken as 1.4 N/mm as it mentioned in the previous section, while the shear retention factor was assumed be equal of 0.5 as it will be discussed in the next section.

Table 5-2: Values of the parameters of the SHCC constitutive model

Property	Value
<i>Poisson's ratio</i>	0.32
<i>Compressive strength</i>	31.60 N/mm ²
<i>Initial Young's Strength</i>	18420 N/mm ²
<i>Tri-linear tension softening diagram of concrete</i>	$f_{ct} = 2.7 \text{ N/mm}^2$, $\xi_1 = 0.11$, $\xi_2 = 0.54$, $\alpha_1 = 1.27$, $\alpha_2 = 0.11$, $G_{fn} = 3.5 \text{ N/mm}$
<i>Parameter defining the mode I fracture energy available to the new crack</i>	$P_2 = 3$
<i>Softening crack shear stress-strain diagram</i>	$\tau_{t,p}^{cr} = 0.7 \text{ N/mm}^2$, $G_{fs} = 1.4 \text{ N/mm}$, $\beta = 0.5$
<i>Crack band width</i>	<i>Square root of the area of Gauss integration point</i>
<i>Threshold angle</i>	$\alpha_{th} = 30^\circ$

Figure 5-13 represents the finite element mesh used for the simulation of the specimen. The FE mesh was composed of 2015 nodes and 1920 serendipity 4 nodes plain stress elements with 2×2 Gauss-Legendre integration scheme. The adopted mesh refinement was adopted after some preliminary simulations in terms of assuring mesh objectivity of the results. This figure also shows the support and load conditions. The SHCC specimens can be considered as isotropic material in its plane due to random orientation nature of the short fibers (Shang and Zijl 2007). In fact, due to the relatively small thickness of the specimens from which the Iosipescu beam specimens were extracted, it is assumed fibers are oriented primarily in the plane. The force P is the sum of all vertical forces in each node in contact with the movable part of the fixture. This force represents the uniform load imposed on specimens and measured by the load cell in the experimental tests.

The experimental and the numerical relationship between average shear stress and the sliding of the crack at the notched plane for the tested specimens are compared in Figure 5-14. The

crack pattern of this specimen at the end of the analysis is represented in Figure 5-15. The first crack appeared experimentally and numerically at a load of about 0.31kN and 0.4kN, respectively. And softening stage started at a load of 1.3kN and 1.35kN for experimental and numerical, respectively. As it shown, the numerical model is able to capture with an acceptable accuracy the shear behavior of the tested specimens for a set of relevant material properties.

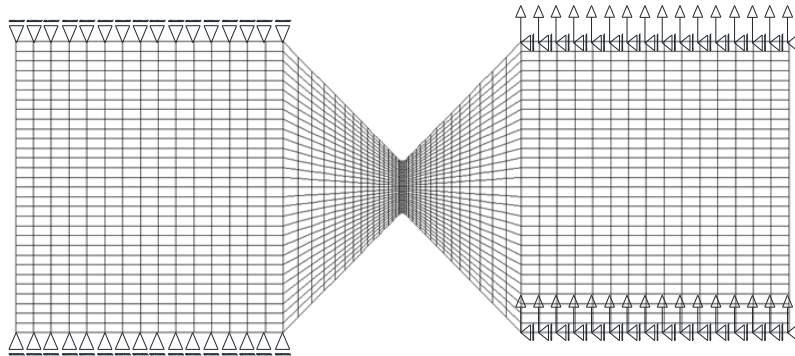


Figure 5-13: Finite element mesh of the Iosipescu specimen

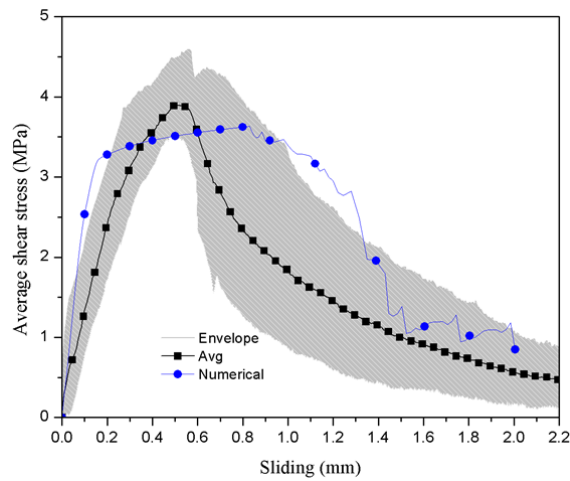


Figure 5-14: Comparison between experimental and numerical average shear stress vs. sliding relationship

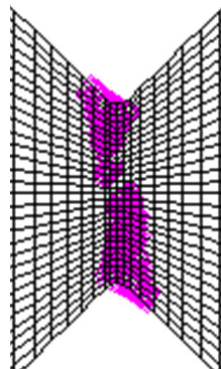


Figure 5-15: Crack patterns of the specimens

5.6 Parametric Study

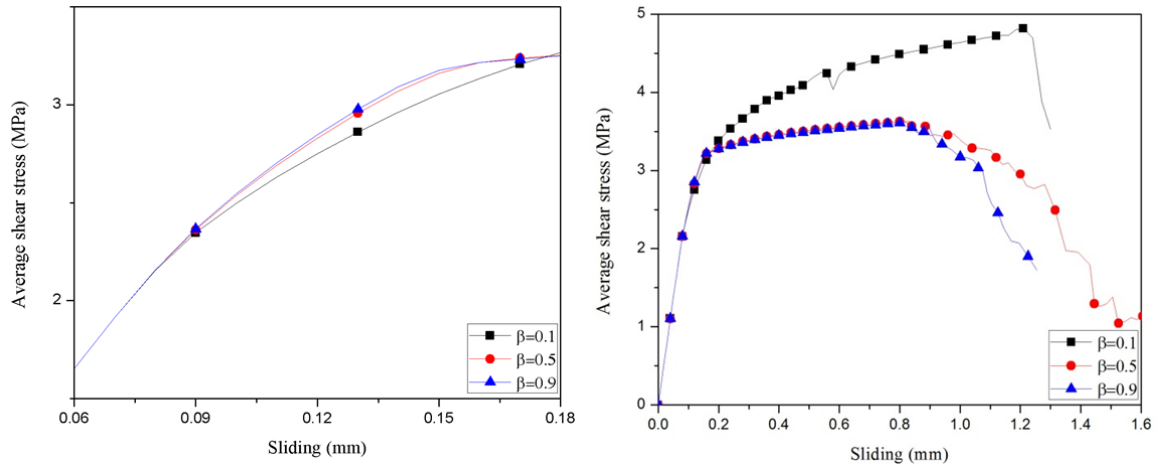
Linear and nonlinear analyses were carried out by using FEMIX computer program to investigate the influence of β parameter that define the first branch of the shear softening diagram, $\tau_t^{cr} - \gamma_t^{cr}$, as well as advantages of SHCC vs. plain cementitious material (PCM), and also effect of notch tip radius on shear stress distribution at critical section.

The finite element mesh, support, and load conditions were as the same adopted for the numerical simulation of the specimen in previous section.

5.6.1 Influence β parameter defining the first branch of the $\tau_t^{cr} - \gamma_t^{cr}$ diagram

In Figure 5-16 the influence of β parameter on the average shear stress *versus* sliding response of the specimens is represented by adopting the following three values for this parameter: 0.1, 0.5, and 0.9 (all the remaining parameters were maintained the same). The first one is lower and the last one is higher than the value considered in the analysis of the specimen.

The results show that, from 0.08 mm sliding (that corresponds to the formation of first shear crack at the notched plane) up to sliding of about 0.18mm the average shear stress capacity of the specimens increases with β (Figure 5-16a), while for larger sliding (when the influence of softening branch of the $\tau_t^{cr} - \gamma_t^{cr}$ diagram becomes relevant) when β reduces $\gamma_{t,p}^{cr}$ increases and consequently the crack enters in its shear softening stage at larger crack shear strain, leading to higher shear capacity to the specimen (Figure 5-17).



(a) Sliding between 0.06mm up to 0.18mm (b) Influence of shear retention factor
 Figure 5-16: Influence of shear retention factor on average shear stress

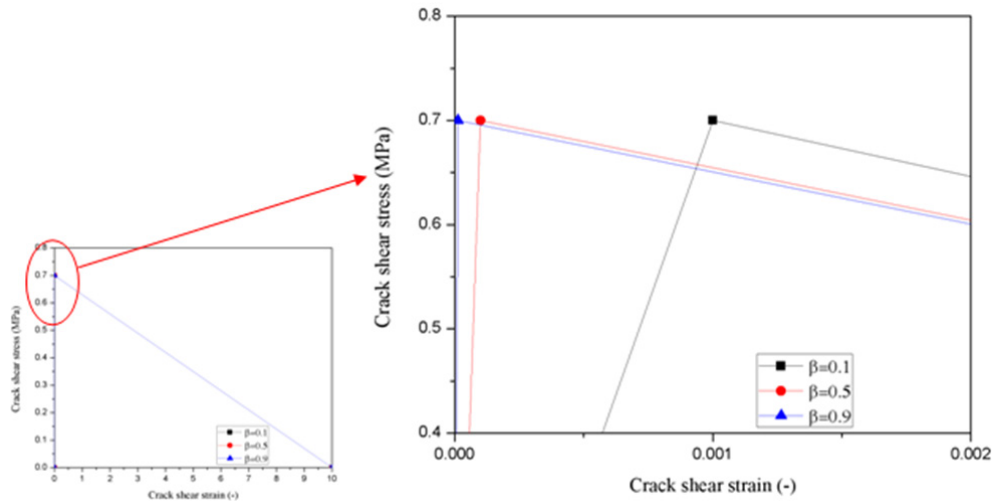


Figure 5-17: Representation of the crack shear stress-crack shear strain diagram for the β equal to 0.1, 0.5 and 0.9

5.6.2 Shear retention factor versus softening diagram for modeling the crack shear behavior

The relationship between the average shear stress and sliding for specimen when using the concept of shear retention factor, β , (Eq. (4.19) with $P_1=3$) and adopting the $\tau_i^{cr} - \gamma_i^{cr}$ diagram is presented in Figure 5-18. Up to a sliding of about 0.10 mm (that corresponds to the formation of first shear crack at the notched plane) the responses are similar, but above this sliding limit the two approaches start diverging significantly. By using β obtained according to Eq. (4.19), the load carrying capacity was much higher than the one predicted by using the

$\tau_i^{cr} - \gamma_i^{cr}$ diagram. Then, the concept of the shear retention factor is not capable of simulating the decrease of the crack shear stress transfer (τ_i^{cr}) with the increase of the crack shear strain (γ_i^{cr}). Figure 5-19 compares the crack patterns of the specimen with β factor and $\tau_i^{cr} - \gamma_i^{cr}$ diagram. As expected, shear retention factor approach has incorrectly predicted failure mode and crack pattern.

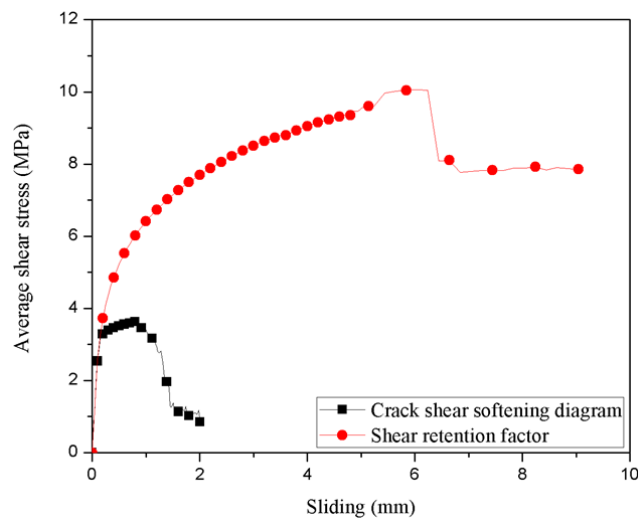


Figure 5-18: Influence of using the crack shear softening diagram vs. shear retention factor with $P_1 = 3$

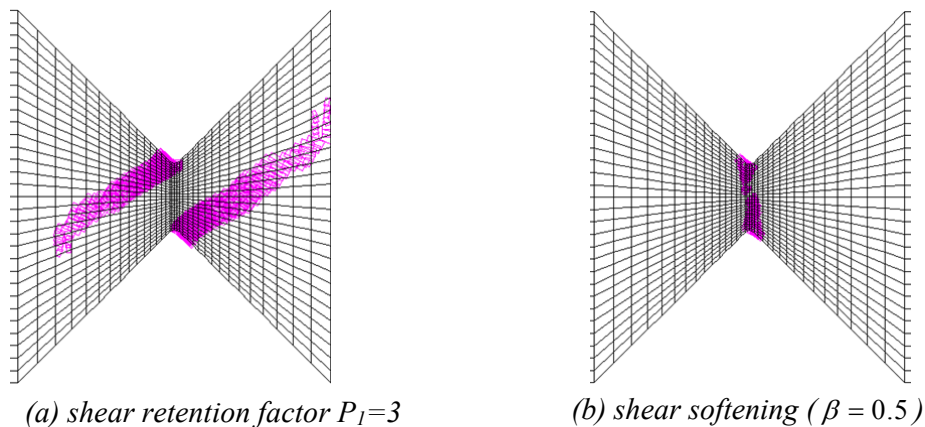


Figure 5-19: Influence of using the crack shear softening diagram vs. shear retention factor with $P_1 = 3$ on crack pattern

5.6.3 Plain cementitious material

Figure 5-20 compares the shear stress vs. sliding relationship obtained for plain cementitious material (PCM) and SHCC specimen. The material properties of the PCM are presented in Table 4-7. As mentioned, all the remaining parameters were the same adopted in the numerical simulations of the previous section. As expected, the specimen consisting of PCM

failed at a lower shear stress than of the specimen with SHCC. The specimen with PCM has a brittle behavior, with an abrupt load decay at peak load, while the SHCC specimen followed a softening behavior after peak load. The typical failure mode of PCM that reported by Shang and Zijl (2007) is presented in Figure 5-21a and compared with the result of the numerical simulation. First cracks are formed near the notch tips (red circle in Figure 5-21b), and cracking has propagated to flexural zone with 45° inclination to the axial horizontal axial of the specimen.

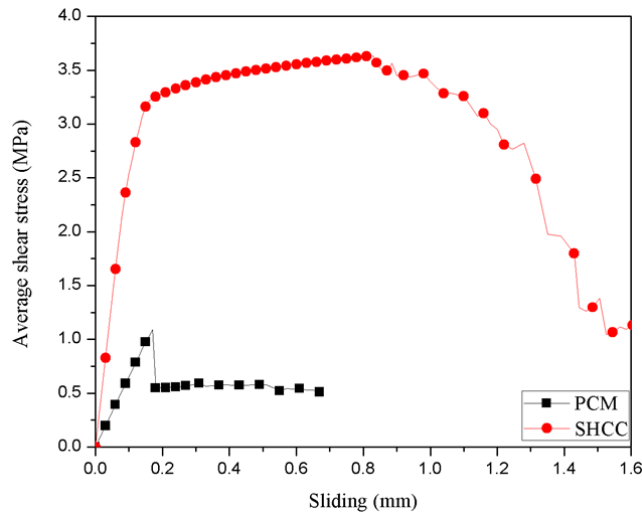
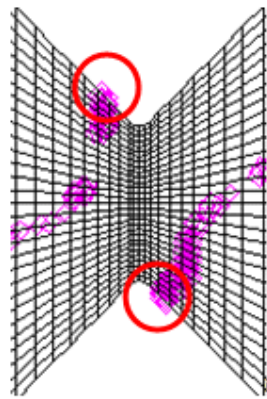


Figure 5-20: A comparison between SHCC and Plain Cementitious Material (PCM) on shear stress



(a) final crack pattern of PCM (Shang and Zijl 2007)



(b) crack pattern of the PCM

Figure 5-21: Influence of PCM instead of SHCC on the crack patterns

5.6.4 Influence of notch tip radius

As aforementioned, the notches contribute for the localization of the shear failure in the aimed zone, and alter the shear stress distribution from parabolic to a more uniform distribution in the notched section (Figure 5-6) (Krishnan and Xu 2009). However, a sharp notch favors the development of a shear stress gradient at notch tips.

In this study three different notch tip radius were simulated: $r=0.0$ mm, $r=2.5$ mm, and $r=4.0$ mm. The Linear and nonlinear analyses were carried out to study the shear stress distribution along the yellow line (Figure 5-23) and shear stress-sliding of the specimens, respectively.

The normalized shear stress (shear stress/average shear stress) distribution along the yellow line and shear stress distribution for different notch tip radius are presented in Figure 5-22 and Figure 5-23, respectively, when performing linear analysis. It can be seen from the Figure 5-23, the shear stress concentration at the roots is reduced (light blue) by increasing tip radius and since the specimen with $r=4.0$ mm has the minimum shear stress concentration at the notch tip. However, shear stress distribution of the $r=2.5$ mm along the yellow line (Figure 5-23) is more uniform than the one of the $r=4.0$ mm (Figure 5-22).

The average shear stress-sliding relationships of the specimens are presented in Figure 5-24. The specimen with sharp notch ($r=0$ mm) shows an abrupt load decay at peak load due to all the cracks at notched section suddenly opened. Figure 5-25 shows the shear stress distribution at crack initiation, peak load, and softening stage (80% of the maximum load) for the three radius values. The crack patterns for these last two situations are compared also in Figure 5-25. Based on this figure $r=2.5$ mm has a better shear stress distribution than other specimens before and after crack initiation and also peak load.

The softening stage of the specimen with $r=2.5$ mm was more ductile than the specimen of $r=4.0$ mm due to shear stress distribution of $r=2.5$ mm at notched section was more uniform than one of the $r=4.0$ mm.

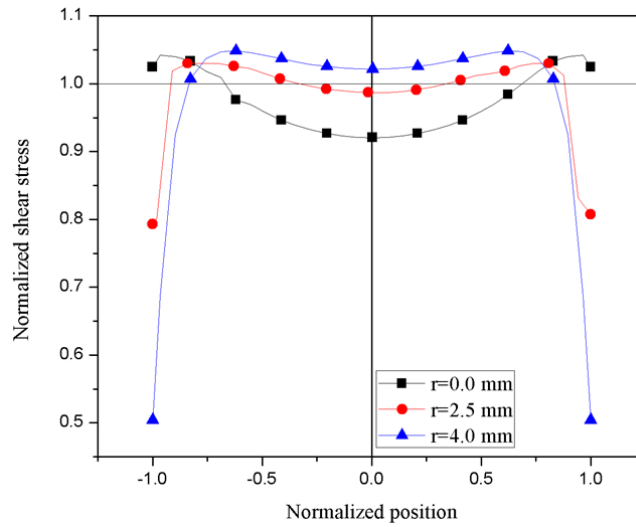


Figure 5-22: Normalized shear stress variation along pure shear section for different notch tip radius

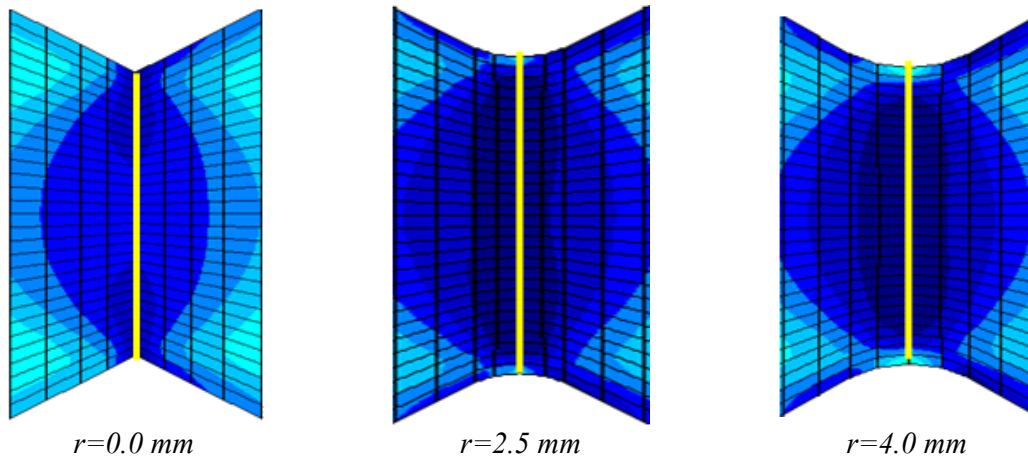


Figure 5-23: Shear stress distribution for different notch tip radius (dark blue: maximum shear stress, and light blue minimum shear stress)

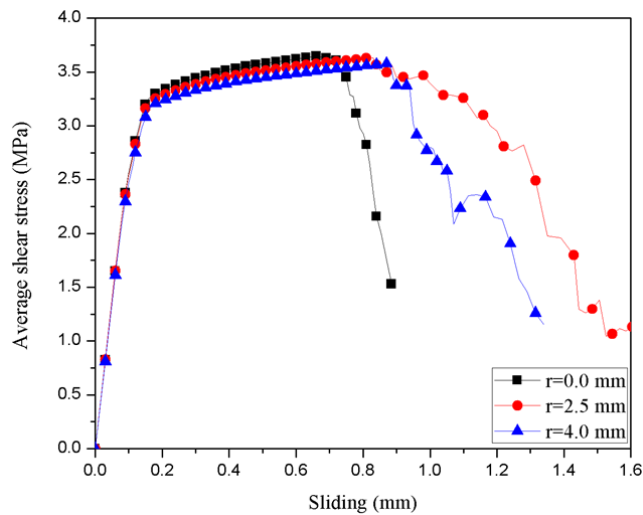


Figure 5-24: Influence of notch tip radius on shear stress-sliding relationship

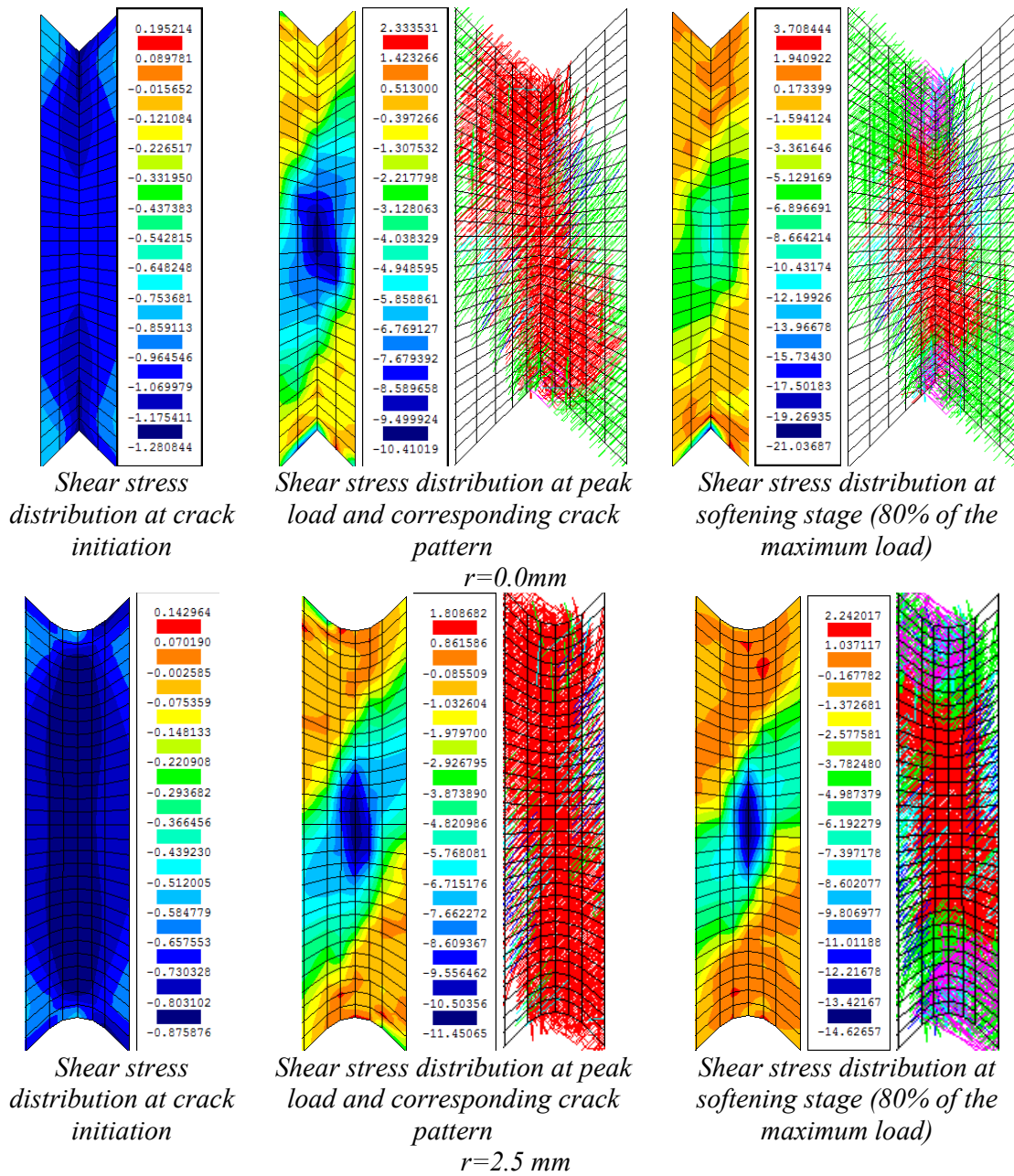
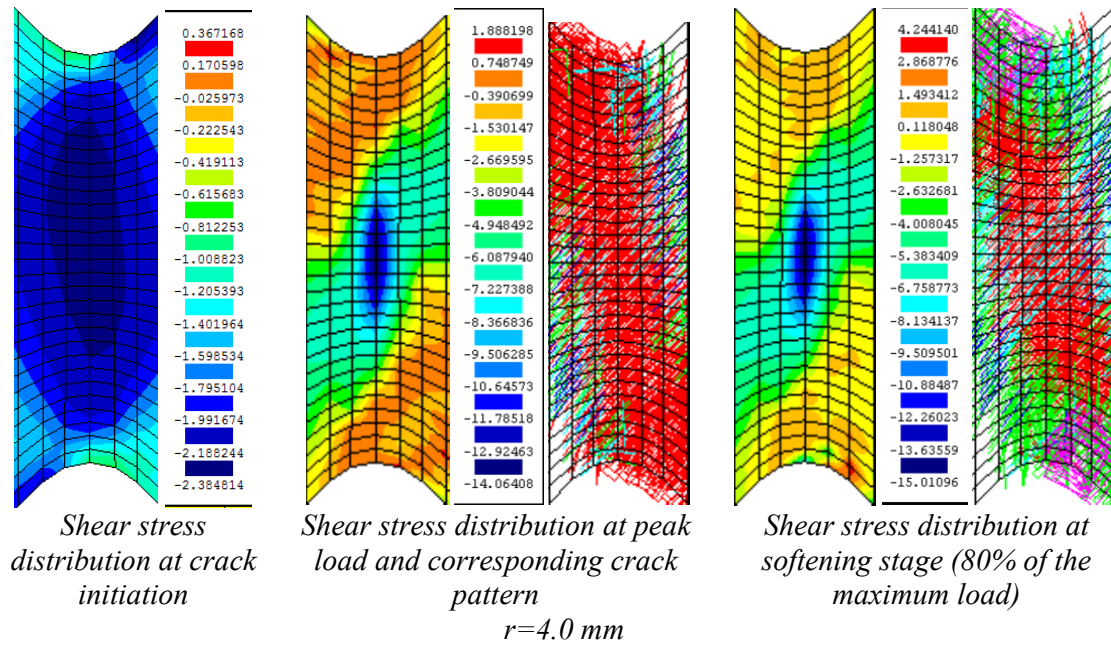


Figure 5-25: Shear stress distribution and crack pattern of specimens with different radius at different stages (in pink color: crack completely open; in red color: crack in the opening process; in cyan color: crack in the reopening process; in green color: crack in the closing process; in blue color: closed crack)



5.7 Conclusion

This chapter presented the experimental and numerical simulation of the Iosipescu shear test to study shear behavior of the SHCC. Based on the boundary condition and applied load in Iosipescu shear test a state of pure shear exists at the center of the specimen where the bending moment is zero. The Iosipescu specimens consisted of a double V-edge notched with small beam height, angle of notch, and tip radius at center of the specimen that can make sure a uniform shear distribution.

After formation of the first shear crack at notched section, by increasing the load more micro cracks were formed, and at the maximum load, the micro cracks connected to each other and the load start decreasing by following a softening branch.

The capability of a FEM-based computer program to predict the behavior of this type of structures up to its failure was studied. The shear crack softening diagram available in the multi-directional fixed smeared crack model implemented in the FEMIX computer program, allowed to simulate the shear behavior of the Iosipescu specimen.

A parametric study was carried: i) to study influence of shear retention factor defining the first branch of shear softening diagram, ii) to illustrate the advantages of SHCC versus mortar, iii) and also effect of notch tip radius.

It was verified that the shear stress of the specimens decrease by increasing the shear retention factor, β , due to the higher crack shear stress transfer. by using the concept of shear retention factor, β , for modeling the crack shear stress transfer, an abnormal high load carrying capacity is estimated, with an incorrectly predicted failure mode, while adopting softening diagram, not only the response of the specimen, but also the failure mode and the crack pattern were correctly estimated.

The specimen consisting of plain cementitious material (PCM) failed at a lower shear stress than of the specimen with SHCC. The specimen with PCM had a brittle behavior, with an abrupt load decay at peak load.

The results have shown the shear stress concentration at the roots is reduced by increasing the tip radius. And crack in specimen with sharp root ($r=0.0$ mm) formed at a lower load than the other specimen.

Chapter 6

Analytical Model to Predict Shear Capacity of Reinforced Concrete Beams Strengthened with NSM and HCPs

6.1 Introduction

There are two prominent models that are used to predict the shear capacity of concrete beams: Truss Model (TM) and Modified Compression Field Theory (MCFT). This chapter is focused on the MCFT; however, a short description of the TM is also herein given.

Two available analytical models to predict the contribution of NSM CFRP laminates/rods for the shear strengthening of RC beams (Nanni et al. and Bianco et al. formulations) are also explained and combined with Simplified MCFT to predict the shear capacity of RC beams strengthened with NSM technique. Then, the new formulations are described and developed to predict the shear capacity of the RC beams strengthened with Hybrid Composite Plates (HCPs), whose tests and results are presented in Chapter 3.

6.2 Truss Model

The Truss model is physically based on the interpretation of the crack patterns formed during the loading process of a RC beam.

In the TM the tensile reinforcement is regarded as a tension chord, the uncracked concrete compression zone in the beam is assumed to be the top chord, the diagonal compressive stress fields are intended to be the diagonal compression struts, and the vertical stirrups transfer the tensile forces from the flexural reinforcement to the uncracked concrete compression zone like tensile ties (Figure 6-1) (Blanksvärd 2009).

This model was explained by Ritter (1899) and Morsch (1908). They assumed 45 degrees for the diagonal compression struts before and after cracking of the cross section. They also neglected the concrete tensile strength (Blanksvärd 2009).

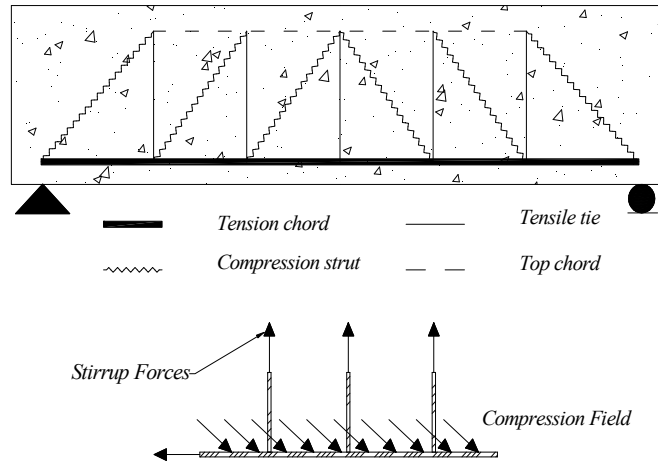


Figure 6-1: Truss models (Brown et al. 2005)

The equilibrium configuration for the 45 degrees of diagonal shear crack model is shown in Figure 6-2. The shear stresses are distributed over the width, b_w , and effective depth of the cross section, z . As shown in Figure 6-2, the total diagonal compressive force (F_2) is

$$f_2 b_w z / \sqrt{2}, \text{ and } V = \sqrt{2} F_2 / 2 :$$

$$f_2 = \frac{2V}{b_w z} \tag{6.1}$$

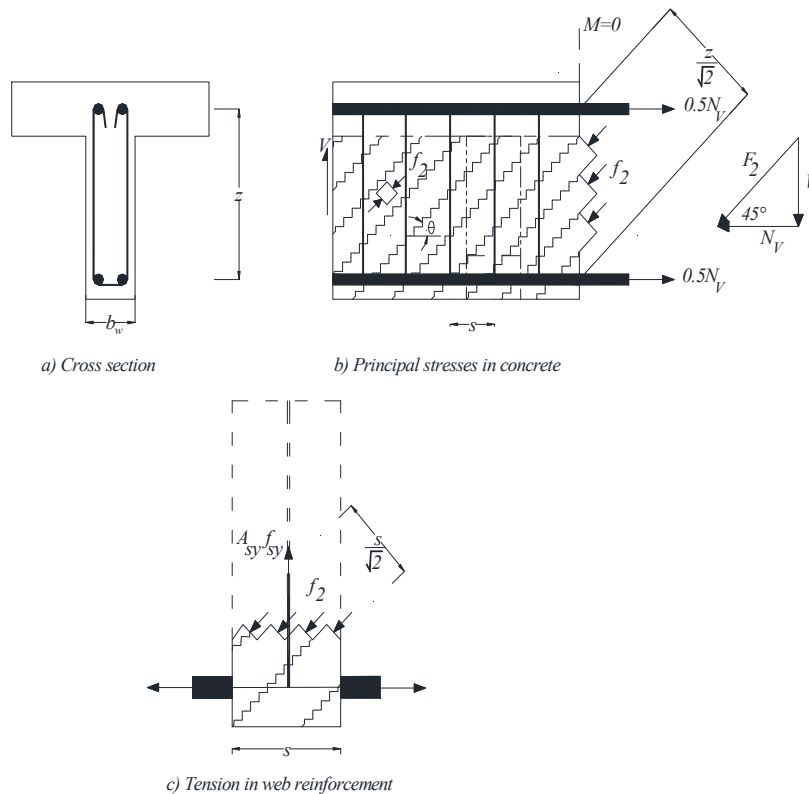


Figure 6-2: Equilibrium conditions for a truss of 45° angle (Collins and Mitchell 1991)

In Figure 6-2 s and z are the horizontal distance between stirrups and vertical distance between longitudinal reinforcements, respectively. The horizontal component of the diagonal compression is equilibrated by tension in the longitudinal reinforcement:

$$N_V = V \cot \theta \quad (6.2)$$

As shown in Figure 6-2, the vertical component of the diagonal compressive force is taken by stirrups. By projecting the force in the compression strut in vertical direction, and considering that shear force is $f_2 b_w s / 2$ it is obtained:

$$V = \frac{A_{sy} f_{sy}}{s} z \quad (6.3)$$

The truss model become the basis for many codes such as: ACI Committee 440 (2000), British Standards Institution (2001), ASSHTO (1998), and Swedish code BBK 94 (1994).

6.3 Compression Field Theory (CFT)

In truss model was assumed that the shear in cracked concrete beams is resisted by diagonal compression struts, and these struts are inclined at an angle of 45 degrees to the longitudinal axis of the concrete member. This approach ignores any contribution of the concrete tensile ties, thus the results of truss model can give conservative estimates of shear strength for RC concrete members (Bentz et al. 2006).

In 1929, Wanger developed the Tension Field Theory (TFT) in analogy to the post-buckling shear resistance of thin-webbed metal girder. He assumed that after buckling the thin-webbed girder, it has no resistance to compression and the shear is carried out by diagonal tension, and it was assumed that the inclination of the diagonal tensile stresses coincides with the inclination of principal tensile strains (Sang-Yeol 1999).

Vecchio and Collins (1986) applied the TFT to reinforced concrete. They assumed that after cracking, the concrete carries no tension, and the shear is carried out by a field of diagonal compressive stresses. The Compression Field Theory (CFT) considers the following assumptions:

- For each strain state there is only one corresponding stress state;
- Stresses and strains can be considered in terms of average values, when taken over areas or distance large enough to include several cracks;
- The concrete and bars are perfectly bonded together;
- The longitudinal and transverse reinforcement bars are uniformly distributed over the concrete elements.

By considering these assumptions, and assuming that the three strain components ε_x , ε_y and γ_{xy} (ε_x is the longitudinal strain, ε_y is the transverse strain and γ_{xy} is shear strain, in case of plane stress state) are known, then the strain in any other direction can be obtained by applying the Mohr's circle, Figure 6-3.

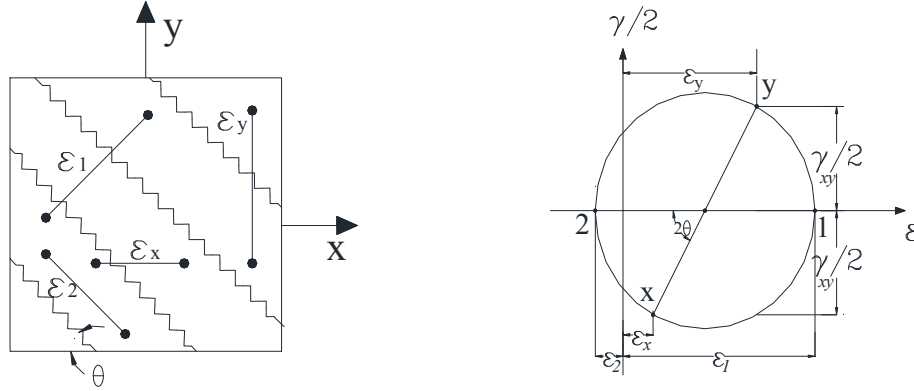


Figure 6-3: Mohr's circle for average strain

From the Mohr's circle the following equations can be derived:

$$\varepsilon_x + \varepsilon_y = \varepsilon_1 + \varepsilon_2 \quad (6.4)$$

$$\gamma_{xy} = 2(\varepsilon_1 - \varepsilon_y) \cot \theta = 2(\varepsilon_x - \varepsilon_2) \cot \theta \quad (6.5)$$

$$\gamma_{xy} = 2(\varepsilon_1 - \varepsilon_x) \tan \theta = 2(\varepsilon_y - \varepsilon_2) \tan \theta \quad (6.6)$$

where ε_1 is the diagonal tensile strain and ε_2 is the diagonal compressive strain. Tensile strains are positive, while compressive strains are negative. By dividing Eq. (6.5) and Eq. (6.6) the following noticeable relation is obtained:

$$\tan^2 \theta = \frac{\varepsilon_1 - \varepsilon_y}{\varepsilon_1 - \varepsilon_x} = \frac{\varepsilon_x - \varepsilon_2}{\varepsilon_y - \varepsilon_2} \quad (6.7)$$

that provides the inclination of the diagonal compressive stress, θ .

6.4 Modified Compression Field Theory (MCFT)

Because the CFT neglects the resisting contribution of cracked concrete in tension, conservative estimates of shear strength are predicted. The Modified Compression Field Theory (MCFT) is an enhancement of the CFT, since it takes into account the resisting contribution of cracked concrete in tension (Vecchio and Collins 1986). The equilibrium condition is considered at a cross section in a RC beam where bending moment is zero (pure shear).

The key simplifying assumption of the MCFT is that the principal strains and principal stresses are coaxial, i.e. they have the same orientation. This was justified by an experimental program. Figure 6-4a and Figure 6-4b show the test setup and one specimen of this experimental program, respectively. Figure 6-5 presents experimental results in terms of the inclination of principal strain (θ) vs. inclination of principal stress (θ_c), where it is verified that $\theta_c = \theta \pm 10^\circ$.

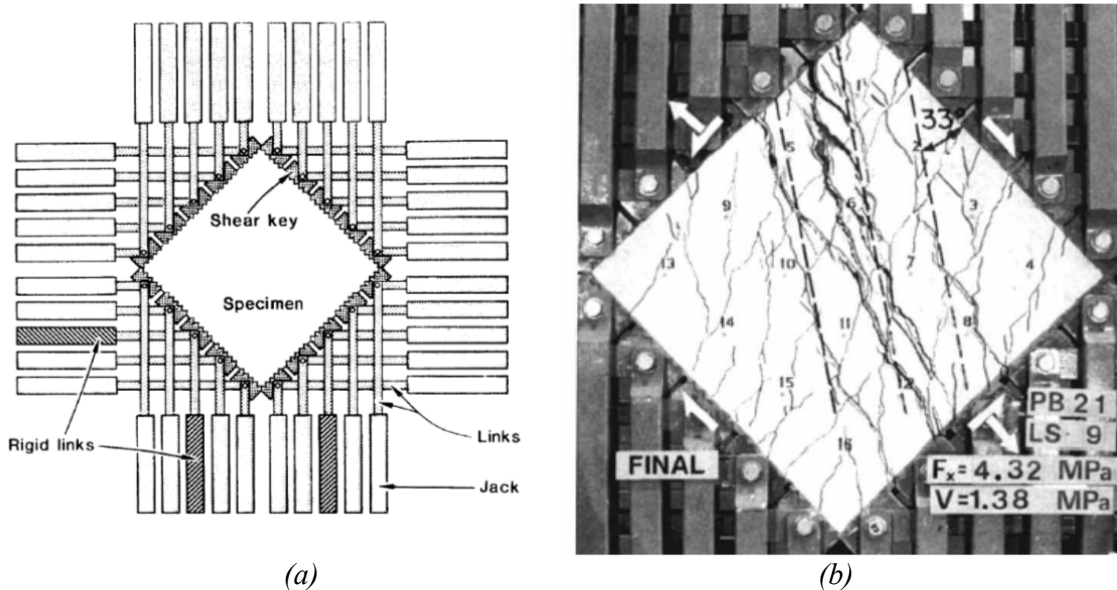


Figure 6-4: (a) test setup used to apply shear and normal stress (Vecchio and Collins 1986), (b) one specimen under loading (ACI-ASCE Committee 445 1999)

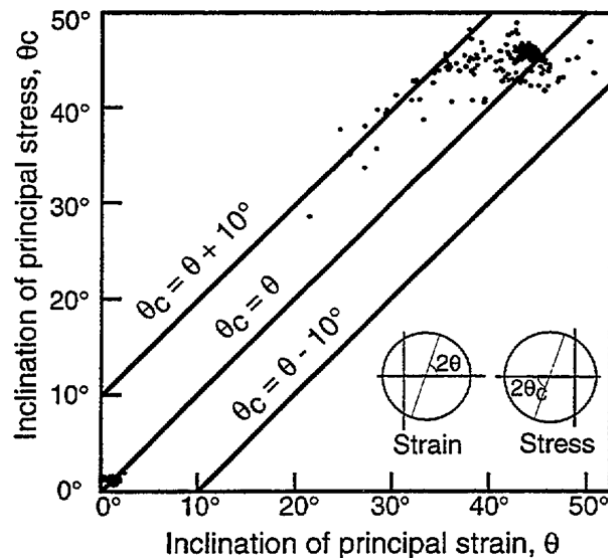


Figure 6-5: Comparison principal stress and principal strain (Vecchio and Collins 1986)

Vecchio and Collins (1986) studied the relationship between diagonal compressive stress, f_2 , and diagonal compressive strain, ε_2 . They found that principal compressive stress is not only function of the principal compressive strain but also of the coexisting principal tensile strain, ε_1 . The uniaxial compressive stress-strain relationship is approximated by a parabola according to (Figure 6-6):

$$f_2 = \left[2 \left(\frac{\varepsilon_2}{\varepsilon_c'} \right) - \left(\frac{\varepsilon_2}{\varepsilon_c'} \right)^2 \right] f_{2max} \quad (6.8)$$

where ε_c' is the strain at the peak compressive strength (that varies between 0.002 and 0.0035, depending on the concrete strength class), and:

$$f_{2max} = \frac{f_c'}{0.8 + 170\varepsilon_1} \leq f_c' \quad (6.9)$$

where f_c' represents the concrete compressive strength.

Eq. (6.8) describes the typical strain softening behavior of concrete in uniaxial compression as shown in Figure 6-6:

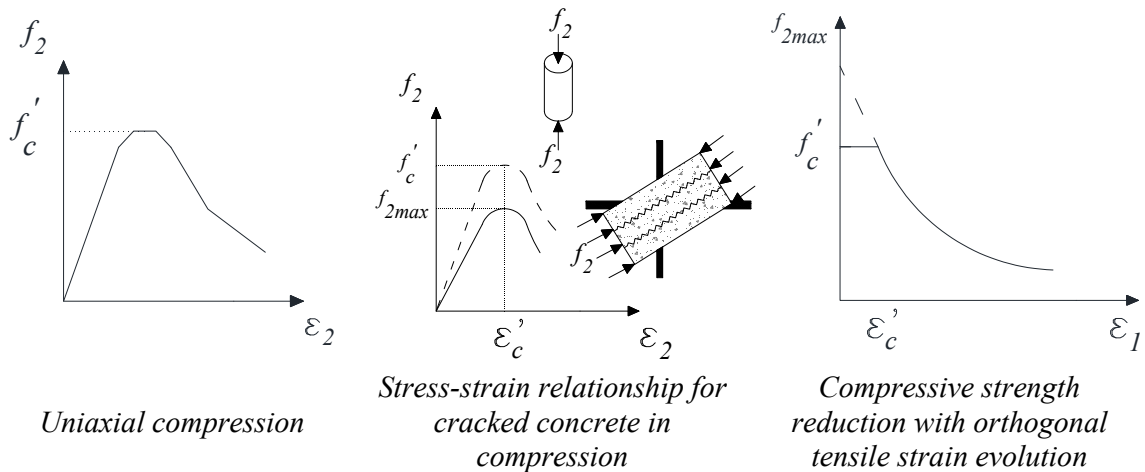


Figure 6-6: Stress- strain relationship for cracked concrete

As shown in Figure 6-7, the relationship between the average tensile stress and the average tensile strain in the concrete before cracking is linear, thus the tensile stress before cracking can be determined as follows:

$$f_1 = E_c \varepsilon_1 \quad (6.10)$$

where E_c is the modulus of elasticity of the concrete. After cracking, the average principal tensile stress in concrete is function of the average principal tensile strain as follows (Collins and Mitchell 1991):

$$f_1 = \frac{\alpha_1 \alpha_2 f_{cr}}{1 + \sqrt{500 \varepsilon_1}} \quad (6.11)$$

where f_{cr} is the cracking stress that can be taken as $0.33\sqrt{f'_c}$, while α_1 and α_2 are factors related to bond characteristics of the reinforcement and the type of loading, whose proposed values are:

$$\begin{aligned} \alpha_1 &= 1 \text{ for rough surface reinforcing bars} & \alpha_2 &= 1 \text{ for short-term monotonic loading} \\ \alpha_1 &= 0.7 \text{ for plain surface bars, wire or} & \alpha_2 &= 0.7 \text{ for sustained and/or repeated loads} \\ & \text{bonded strands} & & \\ \alpha_1 &= 0 \text{ for unbonded reinforcement} & & \end{aligned}$$

The third phase of the tensile stress-strain response will be discussed later.

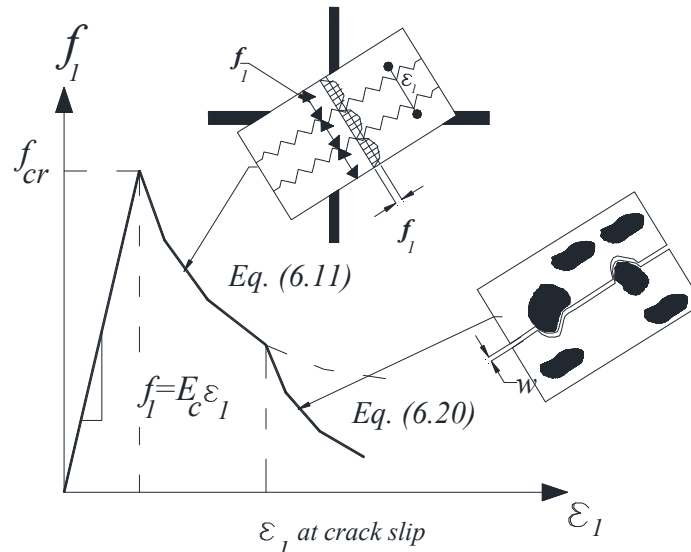


Figure 6-7: Average stress-strain relationship for cracked concrete in tension (Collinset al. 1996)

6.4.1 Equilibrium between cracks

As mentioned previously, a RC beam concrete resists to shear due to the formation of diagonal compressive struts delimited by diagonal shear cracks (Figure 6-8b). As shown in this figure, the tensile stresses vary from zero at the cracks to a maximum between cracks.

From the Mohr circle (Figure 6-8c):

$$\text{In rectangular } A1y: \overline{A1} = v \tan \theta$$

$$\text{In rectangular } A2y: \overline{A2} = v \cot \theta$$

$$f_1 + f_2 = \overline{A1} + \overline{A2} = v(\tan \theta + \cot \theta) \quad (6.12)$$

$$\text{where } v = \frac{V}{b_w z}$$

The vertical components of compressive and tensile forces in the concrete struts have to be supported by the stirrup. The equilibrium can be expressed as (Figure 6-8d):

$$A_{sy} f_{sy} = (f_2 \sin^2 \theta - f_1 \cos^2 \theta) b_w s \quad (6.13)$$

From Eq. (6.12):

$$v = \frac{f_1}{\tan \theta + \cot \theta} + \frac{f_2}{\tan \theta + \cot \theta}$$

and from Eq. (6.13):

$$f_2 = \frac{\left(\frac{A_{sy} f_{sy}}{b_w s} + f_1 \cos^2 \theta \right)}{\sin^2 \theta}$$

From above equations:

$$v = \frac{f_1}{\tan \theta + \cot \theta} + \frac{1}{\tan \theta + \cot \theta} \times \left(\frac{A_{sy} f_{sy}}{b_w s} + f_1 \cos^2 \theta \right)$$

$$v = \frac{A_{sy} f_{sy}}{b_w s} \times \frac{1 + \cot^2 \theta}{\tan \theta + \cot \theta} + \frac{f_1}{\tan \theta + \cot \theta} (1 + \cot^2 \theta)$$

$$V = v b_w z = \frac{A_{sy} f_{sy}}{b_w s} b_w z \times \frac{1 + \cot^2 \theta}{\tan \theta + \cot \theta} + \frac{f_1}{\tan \theta + \cot \theta} (1 + \cot^2 \theta) b_w z$$

$$V = \frac{A_{sy} f_{sy}}{s} z \times \cot \theta + b_w z f_1 \times \cot \theta \quad (6.14a)$$

$$V = V_{steel} + V_{concrete} \quad (6.14b)$$

Similarly, as shown in Figure 6-8d, the longitudinal imbalance f_1 between the diagonal tensile and compression in the concrete must be carried out by the longitudinal steel reinforcement.

$$A_{sx} f_{sx} = (f_2 \cos^2 \theta - f_1 \sin^2 \theta) b_w z \quad (6.15)$$

where A_{sx} is the cross sectional area of the longitudinal reinforcement, and f_{sx} is the average stress in the longitudinal reinforcement. Introducing Eq. (6.12) into Eq. (6.15) gives the force in the longitudinal reinforcement as:

$$A_{sx} f_{sx} = V \cot \theta - f_1 b_w z \quad (6.16)$$

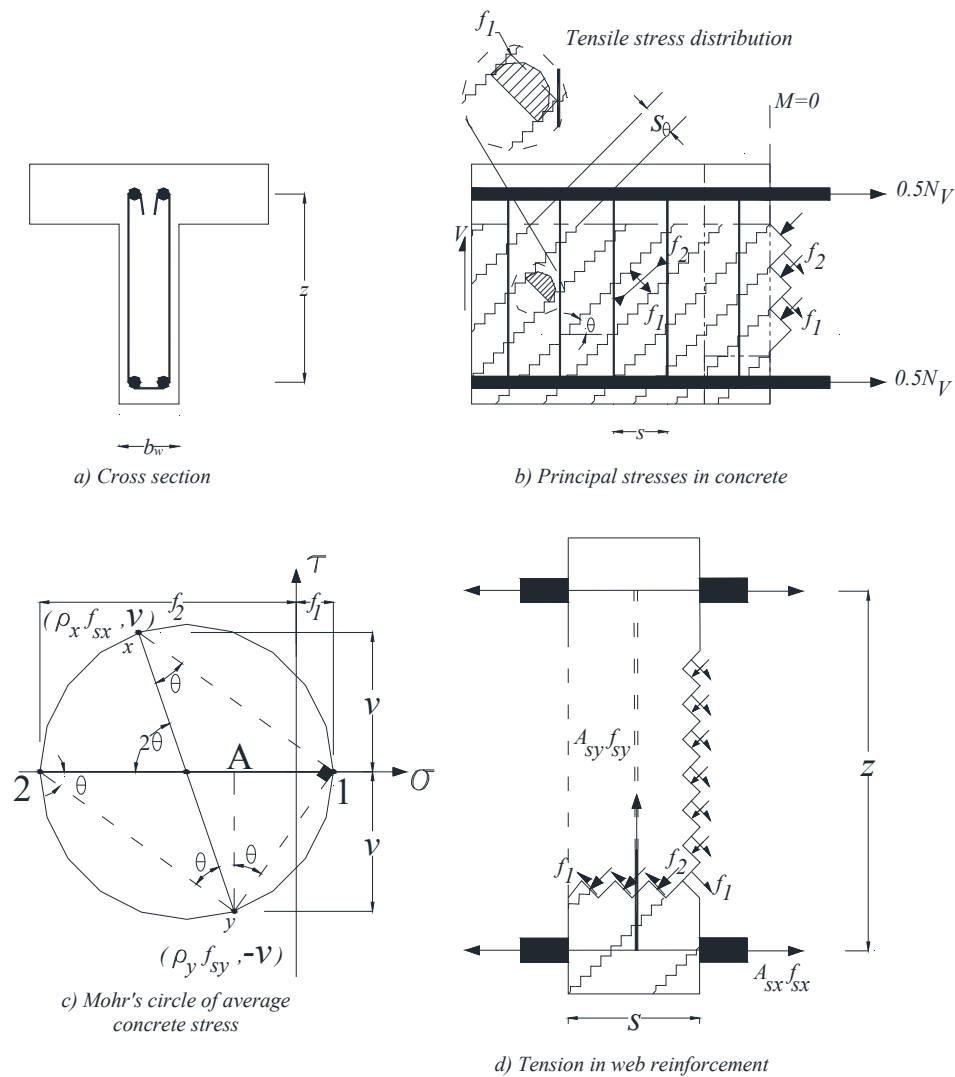


Figure 6-8: Principal stresses in concrete and variation of tensile stresses in the compressive struts

6.4.2 Equilibrium across cracks

Failure of the RC element may not be governed by average stresses, but it can occur at a crack due to local stress gradient. At low shear values, tension is transmitted across cracks by local increase of stresses in the reinforcement bridging the cracks. At a certain shear force, the stress in the web reinforcement just reaches yield at crack locations. Above this shear force, the shear resistance is only assured by aggregate interlock, herein designated as local stress, v_{ci} . The 'crack check' in MCFT represents an explicit check to ensure that the average stress levels can be resisted locally at a crack location. 'Crack check' is done by looking at the stress state in the cracks and between the cracks (Figure 6-9). It limits the average

principal tensile stress in concrete to a maximum allowable value, determined by considering the steel stress at the crack and the ability of crack surface to resist shear stress (Bentz 2000).

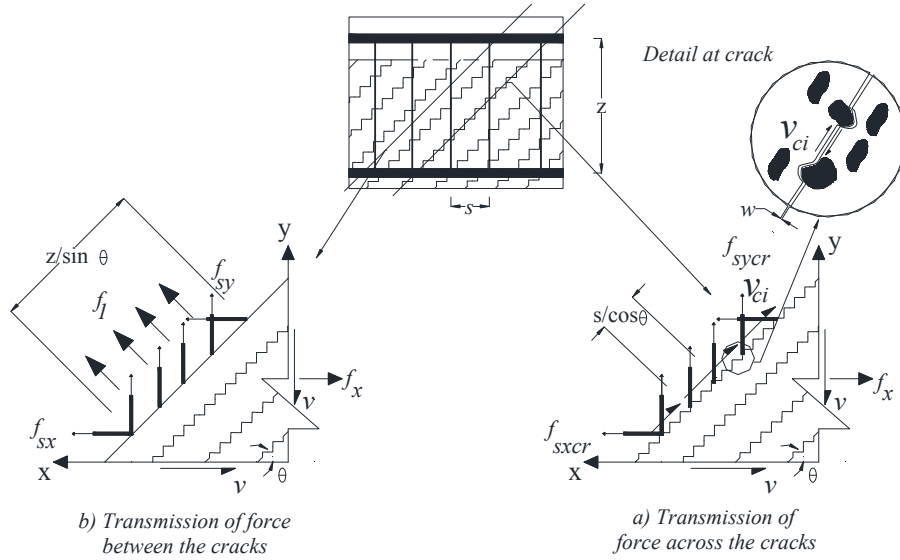


Figure 6-9: Force transmission a) across the crack, b) between the cracks (Collins et al. 1996)

In Figure 6-9, f_{sy} and f_{sxc} represent the stress in the transverse and longitudinal reinforcement at a crack surface, respectively. Vecchio and Collins (1986) proposed an equation for shear stress at crack, v_{ci} , based on the compressive strength of concrete, maximum diameter of aggregates and crack width:

$$v_{ci} = \frac{0.18\sqrt{f'_c}}{0.31 + \frac{24w}{a_g + 16}} \quad (6.17)$$

where w is the crack width and a_g is the maximum aggregate size in mm.

The two sets of stresses, at cracks and between cracks, must be statically equivalent. Equivalence of vertical forces at crack and between cracks (Figure 6-9) requires:

$$A_{sy}f_{sy} \frac{z/\sin\theta}{s/\cos\theta} + f_1 b_w \frac{z}{\sin\theta} \cos\theta = A_{sy}f_{sy} \frac{z/\sin\theta}{s/\cos\theta} + v_{ci} b_w \frac{z}{\sin\theta} \sin\theta$$

$$A_{sy}f_{sy} \frac{z}{s \tan\theta} + f_1 b_w z \cot\theta = A_{sy}f_{sy} \frac{z}{s \tan\theta} + v_{ci} b_w z \quad (6.18)$$

In the concrete elements is assumed that the transverse steel reinforcement yields at the crack, $f_{sy} = f_{y\text{yield}}$. To maintain this equality, the average tensile stress, f_1 , must be:

$$A_{sy}f_{sy} \frac{z}{s \tan\theta} + f_1 b_w z \cot\theta = A_{sy}f_{y\text{yield}} \frac{z}{s \tan\theta} + v_{ci} b_w z$$

$$f_1 b_w \cot \theta = \frac{A_{sy}}{s} \cot \theta (f_{y \text{ yield}} - f_{sy}) + v_{ci} b_w$$

$$f_1 = v_{ci} \tan \theta + \frac{A_{sy}}{b_w s} (f_{y \text{ yield}} - f_{sy}) \quad (6.19)$$

If the stirrups reach to their yield stress and the crack begins to slip (Collins et al. 1996):

$$f_1 = v_{ci} \tan \theta \quad (6.20)$$

The use of Eq. (6.17) requires an estimate of the crack width, w . It can be taken as the product of the principal tensile strain ε_1 and average spacing of the diagonal cracks, s_θ (Figure 6-10):

$$w = \varepsilon_1 s_\theta \quad (6.21)$$

where:

$$s_\theta = \frac{1}{\frac{\sin \theta}{s_{mx}} + \frac{\cos \theta}{s_{my}}} \quad (6.22)$$

As shown in Figure 6-10, s_{mx} and s_{my} are the longitudinal and the transverse crack spacing, respectively.

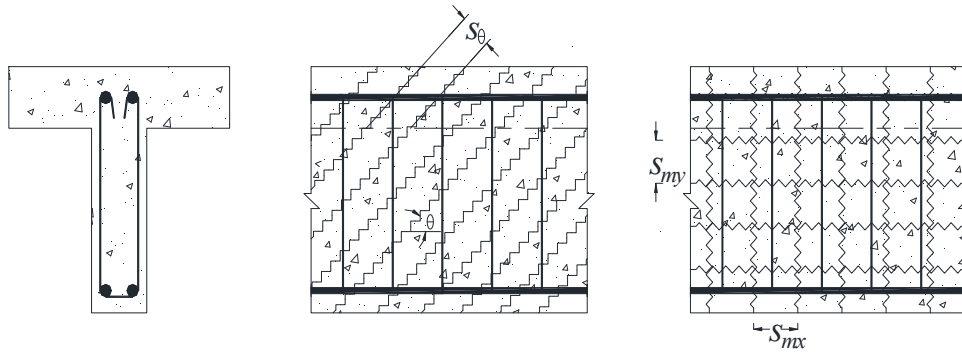


Figure 6-10: Crack spacing in reinforced concrete (Duthinh and Carino 1996)

Finally, imposing the equilibrium of the horizontal forces at a crack and between cracks (Figure 6-9), a limit of the magnitude of the concrete tension can be obtained in order to take into account the yield initiation of longitudinal steel at the crack surface ($f_{sxcr} = f_{x \text{ yield}}$):

$$A_{sx} f_{sxcr} - v_{ci} \times \cos \theta \times \frac{z}{\sin \theta} b_w \geq A_{sx} f_{sx} + f_1 b_w \frac{z}{\sin \theta} \sin \theta$$

From Eq. (6.19):

$$v_{ci} = \left[f_1 - \frac{A_{sy}}{b_w s} (f_{y \text{ yield}} - f_{sy}) \right] \times \cot \theta$$

$$A_{sx} f_{x\text{yield}} \geq A_{sx} f_{sx} + f_1 b_w z + \left[f_1 - \frac{A_{sz}}{b_w s} (f_{y\text{yield}} - f_{sy}) \right] b_w z \cot^2 \theta \quad (6.23)$$

Figure 6-11 gives 15 equations used in MCFT.

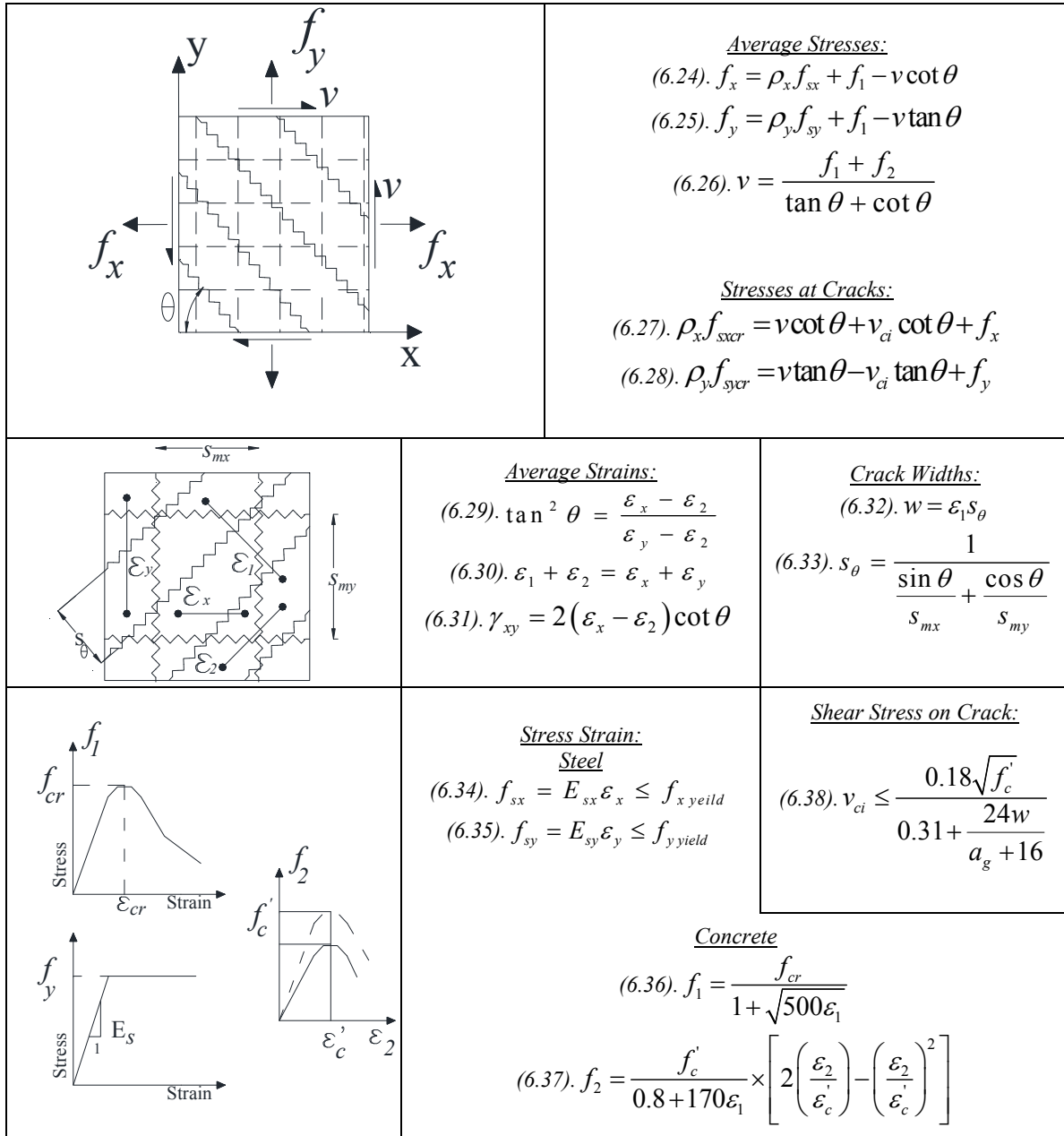


Figure 6-11: Equations of modified compression field theory

6.4.3 Solution technique for MCFT

Vecchio and Collins (1986) and Sang-Yeol (1999) gave a solution to calculate the shear resistance based on MCFT:

Step 1: Estimate θ .

Step 2: Choose a value for ε_1 . It is recommended ε_1 can be less than $\varepsilon_1 = 0.05 \times 10^{-3}$ (Vecchio and Collins 1986)

Step 2: Estimate θ .

Step 3: Calculate w from Eq. (6.21) and Eq. (6.22), the crack spacing is estimated from suggestion of CEB-FIP (1993):

$$s_{mx} = 2 \left(c_x + \frac{s_x}{10} \right) + 0.25k \frac{d_x}{\rho_x} \quad (6.39)$$

$$s_{my} = 2 \left(c_y + \frac{s}{10} \right) + 0.25k \frac{d_y}{\rho_y} \quad (6.40)$$

where:

d_x and d_y are longitudinal and transverse bars diameters, respectively.

c_x and c_y are the clear distance to the longitudinal and transverse reinforcement, respectively.

s_x and s = bar spacing.

$$\rho_y = \frac{A_{sy}}{b_w s} \text{ and } \rho_x = \frac{A_{sx}}{A_c}$$

A_c = area of concrete cross section.

$k = 0.4$ for deformed bars and 0.8 for plain bars.

Figure 6-12 defines the parameters related to crack spacing.

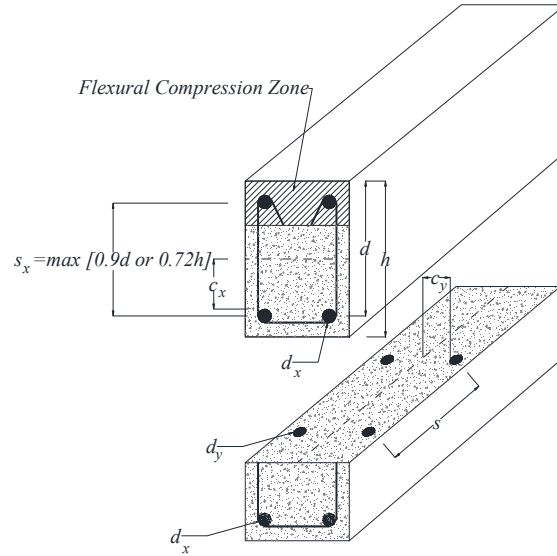


Figure 6-12: Parameters influencing crack (Collins and Mitchell 1991, Kuchma et al. 2008)

Step 4: Estimate average stress in transverse reinforcement, f_{sy} .

Step 5: Calculate the average tension in the concrete, f_1 , using Eq. (6.10) and Eq. (6.11);

Take the smallest value.

$$\varepsilon_1 \leq \varepsilon_{cr} \text{ then } f_1 = E_c \varepsilon_1 .$$

$$\varepsilon_1 > \varepsilon_{cr} \text{ then } f_1 = \frac{\alpha_1 \alpha_2 f_{cr}}{1 + \sqrt{500 \varepsilon_1}}$$

Step 6: Calculate V from Eq. (6.14a).

Step 7: Calculate f_2 from Eq. (6.12).

Step 8: Calculate the $f_{2\max}$ from Eq. (6.9).

Step 9: Check if $\frac{f_2}{f_{2\max}} \leq 1$; if f_2 is higher than $f_{2\max}$, return to step 1 and choose a θ closer to 45° .

Step 10: Calculate ε_2 :

$$f_2 = \left[2 \left(\frac{\varepsilon_2}{\varepsilon_c} \right) - \left(\frac{\varepsilon_2}{\varepsilon_c} \right)^2 \right] f_{2\max} \Rightarrow$$

$$\varepsilon_2^2 - 2\varepsilon_2 \varepsilon_c + \frac{f_2}{f_{2\max}} \varepsilon_c^2 = 0$$

$$\varepsilon_2 = \varepsilon_c' \left(1 \pm \sqrt{1 - \frac{f_2}{f_{2\max}}} \right)$$

Collins suggested to take the smaller value (Collins and Mitchell 1991):

$$\varepsilon_2 = \varepsilon_c' \left(1 - \sqrt{1 - \frac{f_2}{f_{2\max}}} \right) \quad (6.41)$$

Step 11: Calculate ε_y and ε_x :

$$\varepsilon_x + \varepsilon_y = \varepsilon_1 + \varepsilon_2 \Rightarrow \varepsilon_x = \varepsilon_1 + \varepsilon_2 - \varepsilon_y$$

$$\tan^2 \theta = \frac{\varepsilon_x - \varepsilon_2}{\varepsilon_y - \varepsilon_2}$$

$$\tan^2 \theta = \frac{\varepsilon_1 + \varepsilon_2 - \varepsilon_y - \varepsilon_2}{\varepsilon_y - \varepsilon_2} = \frac{\varepsilon_1 - \varepsilon_y}{\varepsilon_y - \varepsilon_2}$$

$$\varepsilon_y + \varepsilon_y \tan^2 \theta = \varepsilon_1 + \varepsilon_2 \tan^2 \theta$$

$$\varepsilon_y = \frac{\varepsilon_1 + \varepsilon_2 \tan^2 \theta}{1 + \tan^2 \theta} \quad (6.42)$$

$$\varepsilon_x = \frac{\varepsilon_2 + \varepsilon_1 \tan^2 \theta}{1 + \tan^2 \theta} \quad (6.43)$$

Step 12: Calculate the stress in the transverse reinforcement:

$$f_{sy} = E_{sy} \varepsilon_y \leq f_{y \text{ yield}} \quad (6.44)$$

Check the f_{sy} calculated can be agreed with f_{sy} estimated in Step 4. If not, revise estimate and return to Step 5.

Step 13: Calculate

$$f_{sx} = E_{sx} \varepsilon_x \leq f_{x \text{ yield}} \quad (6.45)$$

Step 14: Calculate the axial force on the concrete member (it is derived from Eq. (6.16) – axial force out of the web):

$$N = A_{sx} f_{sx} - V \cot \theta + f_1 b_w z - f_c (A_c - b_w z) \quad (6.46)$$

where f_c is the axial compression stress, it acts on the concrete areas outside the web. If ε_x is tensile then $f_c = 0$, otherwise:

$$f_c = f_c' \left(2 \left(\frac{\varepsilon_x}{\varepsilon_c} \right) - \left(\frac{\varepsilon_x}{\varepsilon_c} \right)^2 \right) \quad (6.47)$$

Step15: Check if the axial load equals to the desired value (usually zero). If not, a new estimate value for θ should be assumed and return to Step 2.

Step16: Check longitudinal reinforcement can satisfy Eq. (6.23). If not, return to Step 1.

The flowchart of this model is presented in Annex B.

6.4.4 MCFT vs. Truss Model

In the truss model concrete contribution of a beam with shear reinforcement is considered equal to the concrete contribution of a similar beam without shear reinforcement, and it is also assumed that concrete contribution does not vary with the amount of transverse reinforcement. However, in the MCFT concrete contribution depends on the crack width. The more shear reinforcement decreases the crack width, hence, increases the concrete contribution.

6.5 Simplified Modified Compression Field Theory

Solving the equations of the MCFT is complicated if done by hand (Bentz and Collins 2001). A simplified approach was suggested by Bentz et al. (2006). There are some assumptions in this model: i) crushing of the concrete is approximately to 0.002, and ii) yield strain of the stirrups at failure is greater than 0.002. If ε_x is also equal to 0.002 at failure, Eq. (6.26), (6.29), (6.30), (6.36), and Eq. (6.37) in Figure 6-11 predict that the maximum shear stress is approximately $0.28f'_c$. For very low values of ε_x the shear stress at failure is approximately $0.32f'_c$ (Annex C).

1. As a conservative simplification the shear stress (v) before yielding of transverse reinforcement is $0.25f'_c$.
2. If failure occurs at a shear stress level below $0.25f'_c$, then it is assumed that at failure the stresses in transverse reinforcement in between cracks (f_{sy}) and stresses at cracks (f_{sver}) equal the yield stress of the transverse reinforcement (Bentz et al. 2006).

The shear strength of a section is a function of two parameters β and θ . β is a factor for the tensile stresses in the cracked concrete and θ is the inclination of the diagonal compressive stresses in the web of the section.

In Simplified MCFT the shear strength of an element is modeled in the flexural region of the beam and it is assumed that the clamping stress, f_y , is negligible small. The clamping stresses, f_y , are regions with high vertical compressive stresses near the point loads and supports, and they cause stirrup strains in these locations to be close to zero. Eq. (6.28) given

in Figure 6-11 can be derived by summing the forces in y-direction for the free force body diagram as shown in Figure 6-13 and assuming $f_y = 0$ and stresses in transverse reinforcement between cracks and at the cracks will be equal to yield stresses ($f_{sycr} = f_{y\text{yield}}$ and $f_{sy} = f_{y\text{yield}}$).

$$v = f_1 \cot \theta + \rho_y f_{y\text{yield}} \cot \theta \quad (6.48)$$

$$v = v_{ci} + \rho_y f_{y\text{yield}} \cot \theta \quad (6.49)$$

Both of the above equation can be expressed as:

$$v = v_c + v_s = \beta \sqrt{f'_c} + \rho_y f_{y\text{yield}} \cot \theta \quad (6.50)$$

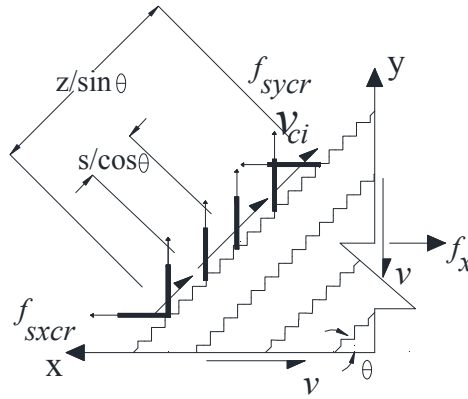


Figure 6-13: Transmission of forces across cracks

From the Eq. (6.36) in Figure 6-11 and Eq. (6.48) and Eq. (6.50) and assuming $f_{cr} = 0.33\sqrt{f'_c}$ the value of β can be determined as:

$$f_1 = \frac{f_{cr}}{1 + \sqrt{500\varepsilon_1}} = \frac{0.33\sqrt{f'_c}}{1 + \sqrt{500\varepsilon_1}} \Rightarrow f_1 \times \cot \theta = \left(\frac{0.33}{1 + \sqrt{500\varepsilon_1}} \sqrt{f'_c} \right) \times \cot \theta$$

$$\beta = \frac{0.33 \cot \theta}{1 + \sqrt{500\varepsilon_1}} \quad (6.51)$$

Similarly, from Eq. (6.38) in Figure 6-11, Eq. (6.49) and Eq. (6.50) the value of β must satisfy:

$$\beta \leq \frac{0.18}{0.31 + \frac{24w}{a_g + 16}} \quad (6.52)$$

The crack width, w , is calculated as multiple of crack spacing, s_θ , to principal tensile strain, ε_1 (Eq. (6.21)). The crack spacing depends on the crack control characteristics of the

x-direction reinforcement, and crack control characteristics of the y-direction reinforcement. As a simplification, crack spacing of longitudinal bars (s_{mx}) can be taken as the vertical distance between bars in the x-direction (s_x), and s_{my} can be taken as the horizontal distance between bars in the vertical direction (s) (Figure 6-12). For elements with no transverse reinforcement ($s_{my} = \infty$) s_θ will equal to $\frac{s_x}{\sin \theta}$ and:

$$w = \varepsilon_1 s_\theta = \varepsilon_1 \frac{s_x}{\sin \theta}$$

$$\beta \leq \frac{0.18}{0.31 + \frac{24 \left(\varepsilon_1 \frac{s_x}{\sin \theta} \right)}{a_g + 16}}$$

$$\beta \leq \frac{0.18}{0.31 + 0.686 s_{xe} \varepsilon_1 / \sin \theta} \quad (6.53)$$

where

$$s_{xe} = \frac{35 s_x}{a_g + 16} \geq 0.85 s_x \quad (6.54)$$

For concrete member containing only longitudinal reinforcement s_x can be assumed max $[0.9d, 0.72h_w]$ (Kuchma et al. 2008), where d is the effective depth of the concrete member and h_w is height of the concrete member.

For member without transverse reinforcement, the highest values of β , hence, maximum post-cracking shear capacity occurs when Eq. (6.53) and Eq. (6.51) are equal:

$$\tan \theta = \frac{0.5686 + 1.258 s_{xe} \varepsilon_1 / \sin \theta}{1 + \sqrt{500 \varepsilon_1}} \quad (6.55)$$

The relation between θ and ε_1 for different crack spacing is shown in Figure 6-14.

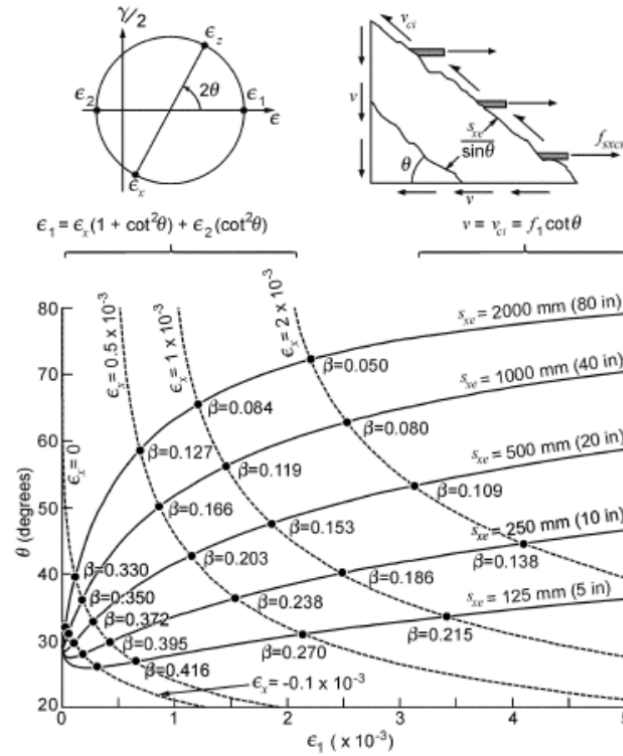


Figure 6-14: Determination of β and θ values for element without transverse reinforcement (Bentz et al. 2006)

To relate longitudinal strain ϵ_x to ϵ_1 , Eq. (6.29) and Eq. (6.30) can be rearranged:

$$\epsilon_1 = \epsilon_x(1 + \cot^2 \theta) + \epsilon_2 \cot^2 \theta \quad (6.56)$$

The principal compressive strain, ϵ_2 , depends on compressive stress. For a member without transverse reinforcement Eq. (6.25) and Eq. (6.26) can be rearranged:

$$f_2 = f_1 \cot^2 \theta \quad (6.57)$$

The principal compressive strain equals f_2 / E_c , where $E_c = 4950\sqrt{f'_c}$. Then Eq. (6.56) becomes:

$$\epsilon_1 = \epsilon_x(1 + \cot^2 \theta) + \frac{\cot^4 \theta}{15000(1 + \sqrt{500\epsilon_1})} \quad (6.58)$$

The relation between ϵ_1 and θ for different values of ϵ_x is shown in Figure 6-14. The intersection points of the lines ϵ_x and s_{xe} define the values of θ and ϵ_1 , which solve both Eq. (6.55) and Eq. (6.58). The corresponding values of β are shown also in Figure 6-14. It can be seen from this figure, as the crack spacing increases the values of β and, hence, shear strengths, decrease.

Based on these results the β value in MCFT for elements without transverse reinforcement depends on ϵ_x and s_{xe} , longitudinal strain and crack spacing parameter, respectively. Bentz et al. (2006) suggested that these two factors affect the shear strength β and crack inclination θ as “strain effect factor” and “size effect factor” and these parameters can be multiplied by each other.

$$\beta = \text{“strain effect factor”} \times \text{“size effect factor”}$$

$$\theta = \text{“strain effect factor”} \times \text{“size effect factor”}$$

These two factors are not really independent, but for the simplified calculation of the MCFT this interdependence is ignored.

Bentz et al. (2006) suggested Eq. (6.59) to calculate the inclination of diagonal compressive stress of the beam with and without transverse reinforcement. As shown in Figure 6-15 the suggested equation for diagonal compressive stress gives a conservative value than MCFT.

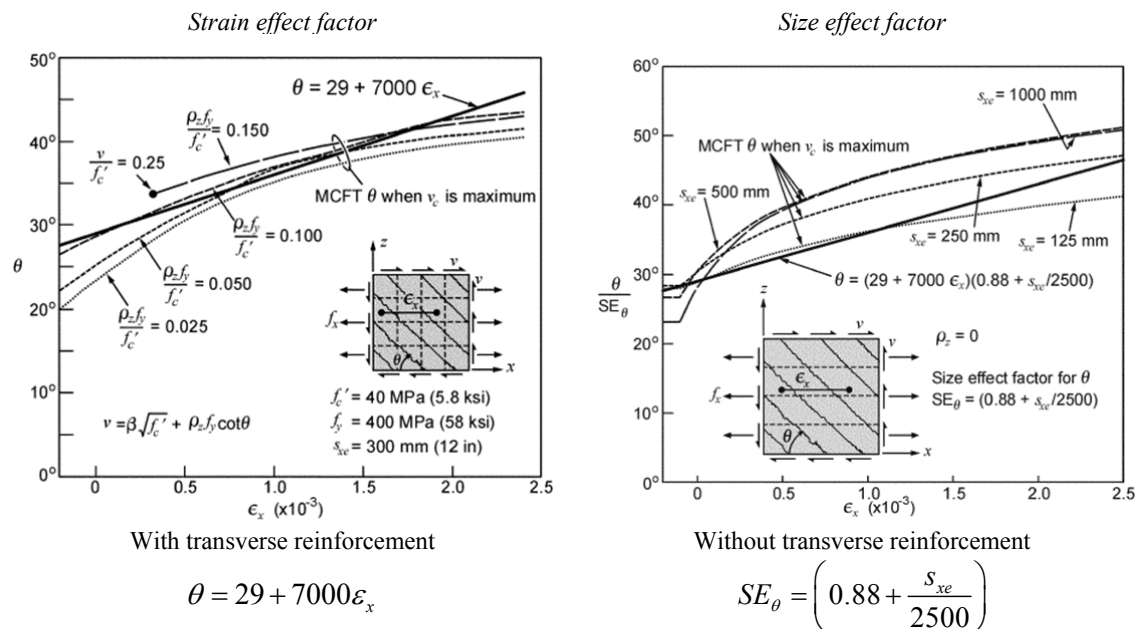


Figure 6-15: Comparison of values for θ given by simple equations with values determined from MCFT for elements with and without transverse reinforcement (Bentz et al. 2006)

$$\theta = (29 + 7000\epsilon_x) \cdot \left(0.88 + \frac{s_{xe}}{2500} \right) \leq 75^{\circ} \tag{6.59}$$

To calculate β , Eq. (6.60) is suggested for concrete members with and without transverse reinforcement. The β values given by this equation are compared to the β values from MCFT in Figure 6-16.

$$\beta = \frac{0.4}{1 + 1500\epsilon_x} \cdot \frac{1300}{1000 + s_{xe}} \quad (6.60)$$

If the longitudinal reinforcement is not yield Eq. (6.61) can be used to calculate the ϵ_x .

$$\epsilon_x = \frac{f_{sx}}{E_s} = \frac{v_c \cot \theta - v_c / \cot \theta}{E_s \rho_{sx}} \quad (6.61)$$

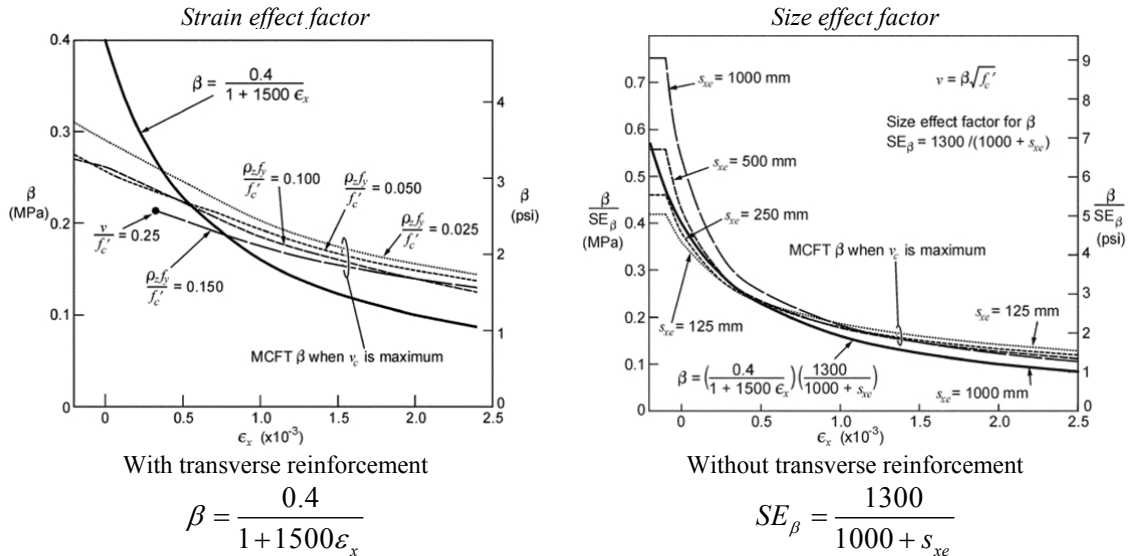


Figure 6-16: Comparison of values for β given by simple equations with values determined from MCFT for elements with and without transverse reinforcement (Bentz et al. 2006)

6.5.1 Solution technique for simplified MCFT

Step 1: Estimate a value for ϵ_x .

Step 2: Calculate the crack spacing, using Eq. (6.54).

Step 3: Calculate θ and β using Eq. (6.59) and Eq. (6.60), respectively.

Step 4: Calculate the shear stress based on Eq. (6.50).

Step 5: Calculate the longitudinal strain, ϵ_x , according to Eq. (6.61) and compare to ϵ_x that was estimated in step 1. Return to Step 2 with ϵ_x that was calculated in Step 5 until convergence is obtained.

6.6 ACI Building Code

ACI Committee (2011) design code for reinforced concrete beams in shear is based on 45° truss model. The shear strength is an average shear stress on the full effective cross section

$b_w d$. In a member without steel stirrups, shear is assumed to be carried by concrete web, while in the beams with shear reinforcement the shear strength is assured by concrete web (V_c) and steel stirrups (V_s) as follows:

$$V = V_c + V_s \quad (6.62)$$

where:

$$V_c = 0.17\sqrt{f'_c} b_w d \quad (6.63)$$

is actually the sum of the three separated components: a) concrete in compression, b) aggregate interlock, and c) dowel resistance provided by the longitudinal reinforcement.

The 45° truss model is used to calculate contribution of steel stirrups:

$$V_s = \frac{A_{sy} f_{sy}}{s} d \quad (6.64)$$

To avoid diagonal crushing of the compression chords and limit diagonal cracking at service loads the steel contribution is limited to:

$$V_s \leq 0.66\sqrt{f'_c} b_w d \quad (6.65)$$

6.7 Eurocode

6.7.1 Concrete members without shear reinforcement

The shear force that can be carried without shear reinforcement is calculated from:

$$V_{Rd,c} = \left[C_{Rd,c} k (100 \rho_l f_{ck})^{1/3} + k_1 \sigma_{cp} \right] b_w d \geq (v_{min} + k_1 \sigma_{cp}) b_w d \quad (6.66)$$

where

$$k = 1 + \sqrt{\frac{200}{d}} \leq 2.0, \quad d \text{ in mm}$$

$$\rho_x = \frac{A_{sx}}{b_w d} \leq 0.02$$

σ_{cp} is the compressive stress due to pre-stress force applied to the member:

$$\sigma_{cp} = N_{Ed} / A_c < 0.2 f_{cd}, \quad \text{in MPa}$$

The factor $k_1 = 0.15$ and values of $C_{Rd,c}$ and v_{min} are determined as:

$$C_{Rd,c} = \frac{0.18}{\gamma_c}$$

$$v_{min} = 0.035 k^{3/2} f_{ck}^{1/2}$$

Even if no transverse reinforcement is necessary, a minimum percentage is required:

$$\frac{A_{sw}}{s} = \rho_w \cdot b_w \cdot \sin \alpha \quad (6.67)$$

$$\rho_{w,min} = \frac{0.08\sqrt{f_{ck}}}{f_{yk}} \quad (6.68)$$

6.7.2 Concrete members with shear reinforcement

Eurocode (2001) is based on truss model, where the inclined compression struts are aligned at an angle θ . The inclination of the compression chords should be limited:

$$1 \leq \cot \theta \leq 2.5$$

The design shear resistance provided by stirrups is the smallest of:

$$V_{Rd,s} = \frac{A_{sw}}{s} \cdot z \cdot f_{ywd} \cdot \cot \theta \leq V_{Rd,max} \quad (6.69)$$

$$V_{Rd,max} = \alpha_{cw} b_w z v_1 f_{cd} / (\cot \theta + \tan \theta) \quad (6.70)$$

where z is internal arm (Figure 6-8a). α_{cw} is 1 for non-pre-stress member. v_1 is a reduction factor for concrete cracked in shear:

$$v_1 = \begin{cases} 0.6 & f_{ck} \leq 60 \text{ MPa} \\ 0.9 - f_{ck}/200 > 0.5 & f_{ck} \geq 60 \text{ MPa} \end{cases}$$

6.8 Formulation of NSM Technique

6.8.1 Nanni approach

The approach used to calculate nominal shear capacity of a concrete member strengthened with NSM technique is similar to that used in ACI Committee 440 (2000) for the case of externally bonded FRP laminates. The total transverse force V can be calculated as follows:

$$V = V_c + V_s + V_f \quad (6.71)$$

where V_f is the shear resistance of the FRP laminates.

Shear resistance of the FRP laminates based on Nanni et al. approach is computed using the following assumption (De Lorenzis and Nanni 2001):

1. The inclination angle of the shear crack is constant and equal to 45°;

2. The bond stresses are uniformly distributed along the effective length of the FRP laminates at ultimate state conditions;
3. The average bond strength is reached in all the laminates intersected by the crack at ultimate state conditions;

The contribution for the shear resistance provided by the FRP laminates is determined from the following equation:

$$V_f = [4(a_f + b_f)\tau_b L_{totmin}] \sin \theta_f \quad (6.72)$$

where a_f and b_f represent the cross section of rectangular FRP laminate, τ_b is the average bond stress developed at laminate-concrete substrate interface, θ_f is inclination of FRP laminates, and L_{totmin} can be obtained as follows:

$$L_{totmin} = \sum_i L_i \quad (6.73)$$

where L_i represents the effective bond length of each single NSM laminate intercepted by the critical shear crack. L_{totmin} corresponds to the minimum possible value assumed by the sum of the effective bond length of each laminate:

$$L_i = \begin{cases} \min\left(\frac{s_f}{\cos \theta_f + \sin \theta_f} i; l_{max}\right) & i = 1 \cdots N/2 \\ \min\left(l_{net} - \frac{s_f}{\cos \theta_f + \sin \theta_f} i; l_{max}\right) & i = N/2 + 1 \cdots N \end{cases} \quad (6.74)$$

where s_f is the horizontal spacing between laminates and l_{net} can be determined from (Figure 6-17):

$$l_{net} = l_b - \frac{2c}{\sin \theta_f} \quad (6.75)$$

which represents the net length of FRP laminates to account for cracking of the concrete cover and installation tolerances. l_b is the actual length of the FRP laminate while c is the concrete clear cover. In Eq. (6.74) N is the number of the FRP laminates crossing the shear crack that can be determined as follows:

$$N = \frac{l_{eff} (1 + \cot \theta_f)}{s_f} \quad (6.76)$$

by rounding off N to the lowest integer, and l_{eff} represents the length of the vertical projection of l_{net} :

$$l_{eff} = l_b \sin \theta_f - 2c \quad (6.77)$$

In Eq. (6.74) L_i is limited to l_{max} that is obtained from the force equilibrium condition, taking an upper bound value for the effective strain, ε_{fe} , (refer to Figure 6-18):

$$l_{max} = \frac{\varepsilon_{fe}}{2} \frac{a_f b_f}{a_f + b_f} \frac{E_f}{\tau_b} \quad (6.78)$$

where E_f is the modulus of elasticity of FRP. Bond is a mechanism through which stresses are transferred to the surrounding concrete. Barros and Dias (2006) suggested $\tau_b = 16.1$ MPa and $\varepsilon_{fe} = 0.59\%$ for rectangular cross section laminates, while Nanni et al. (2004) recommended $\tau_b = 6.9$ MPa and $\varepsilon_{fe} = 0.4\%$ for the CFRP rods.

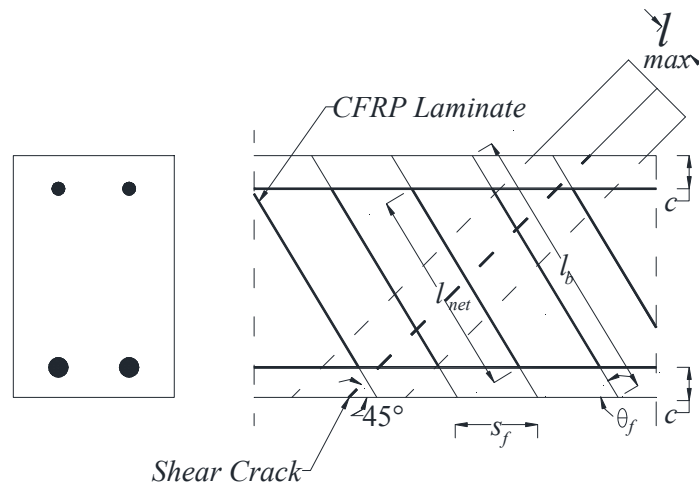


Figure 6-17: Definition of l_{net} , l_b , l_{max} (Nanni et al. 2004)

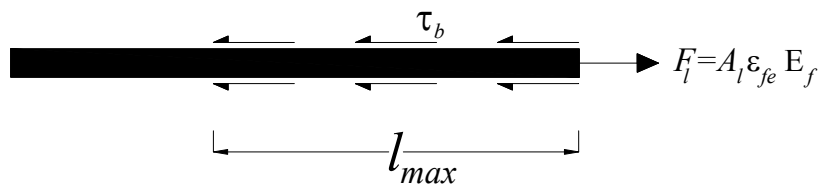


Figure 6-18: Representation of l_{max} (Nanni et al. 2004)

6.8.2 Bianco approach

Bianco et al. (2011) proposed a 3D mechanical model to predict the shear strength contribution of NSM CFRP laminates. Recently the same authors proposed a simplified

version of this model (Bianco et al. 2014) by introducing the following simplifications (Figure 6-19):

1. The local bond stress-slip relationship $\tau(\delta)$ can be modeled by a bi-linear curve instead of a multi linear curve.
2. Concrete fracture surface is assumed a semi-pyramid instead of a semi-cone.
3. The mode of failure of an NSM FRP laminate subjected to an imposed end slip can be categorized into four groups: debonding, tensile rupture of laminate, concrete semi-pyramid tensile fracture, and a mixed shallow semi-pyramid plus debonding failure mode. These modes of failure are dependent on the relative mechanical and geometrical properties of the materials involved.
4. Determining the constitutive law of the average available bond length of the NSM FRP laminates.

During the loading process of a RC beam, when the concrete average tensile strength is overcome at the web intrados, some shear cracks originate, and successively progress towards the web of the beam. These cracks can generate a single crack, Critical Diagonal Crack (CDC), with inclination of θ with respect to the beam longitudinal axis (Figure 6-19a). At load step t_1 , the two web parts become separated by the CDC and they start moving apart by rotating around the crack tip (point E in Figure 6-19a). From that step, by increasing the applied load, the CDC opening angle $\gamma(t_n)$ progressively widens. The laminates that bridge the CDC offer resistance to its widening. The load imposed to the laminate, in consequence of the loaded end slip (δ_{Li}) evolution, is transferred by bond to the concrete surrounding the laminate along its effective bond length, L_{fi} which is the shorter length between the two parts into which the crack divides its actual length L_f .

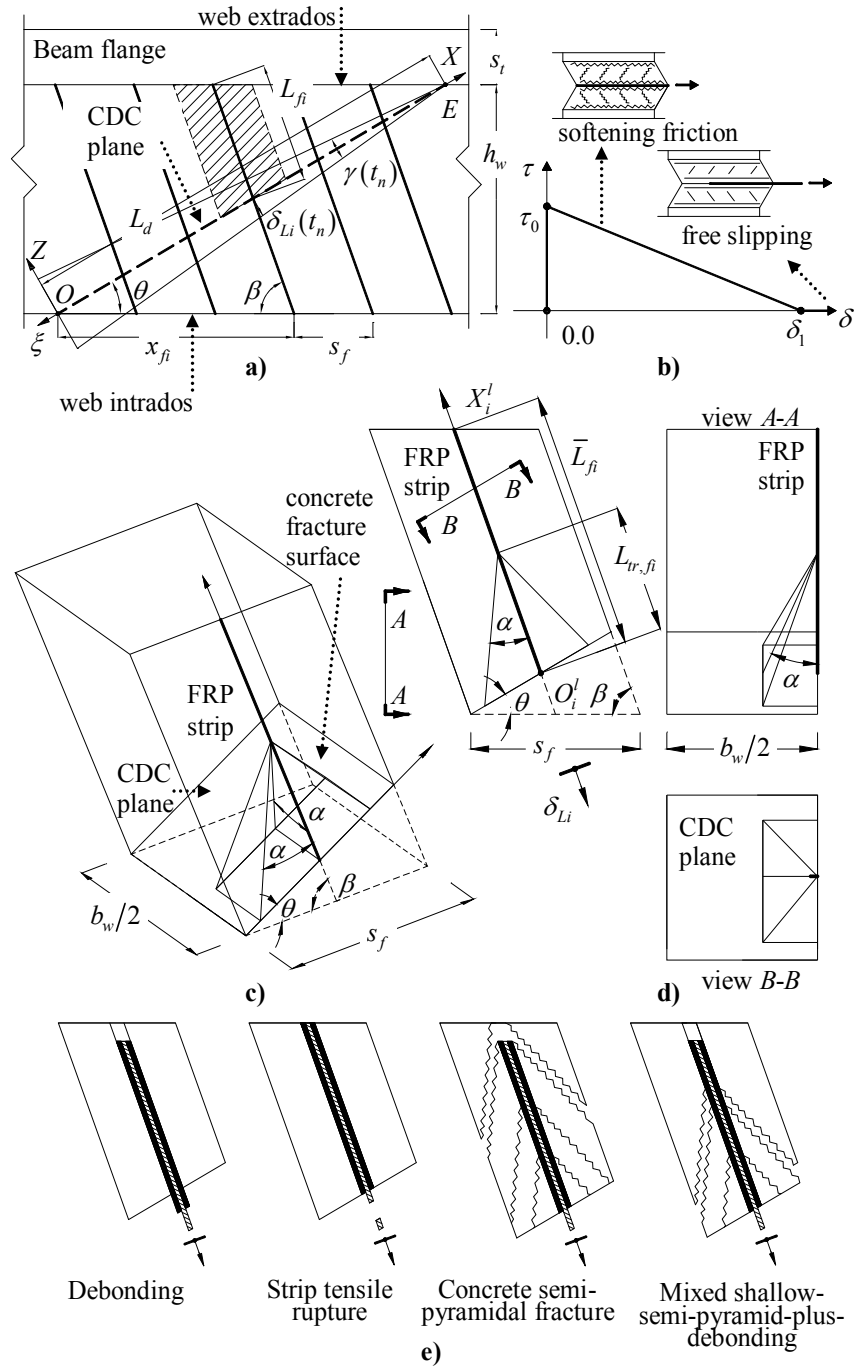


Figure 6-19: Schematic representation of the Bianco et al. (2014) model

There are two other assumptions that simplify the original formulation proposed by Bianco et al. (2011) and Bianco et al. (2014):

- 1) The concrete fracture can be accounted to determine the equivalent value of the average resisting bond length \bar{L}_{Rfi}^{eq} . The equivalent value of the average resisting bond length is the portion of the available average resisting bond length, $\bar{L}_{Rfi}^{eq} = \eta \bar{L}_{Rfi}$.
- 2) The post peak behavior of the bond based constitutive law $V_{fi}^{bd}(\bar{L}_{Rfi}^{eq}; \delta_{Li})$ of the equivalent value of the average resisting bond length can be ignored.

The following paragraphs resume the formulation of this approach:

Step 1: Input parameters data includes: beam cross section (h_w, b_w) , Inclination of CDC and NSM FRP laminates (θ, θ_f) , Horizontal spacing of NSM FRP laminates s_f , angle α between axis and principal generatrices of the semi-pyramidal fracture surface (this angle is assumed equal to 28.5° for all the experimental programs (Bianco et al. 2011)), Young's modulus and tensile strength of FRP (E_f, f_{fu}) , concrete average compressive strength (f'_c) , thickness and width of the NSM FRP laminates (a_f, b_f) , the value of the bond stress and slip (τ_0, δ_1) (these values are assumed 20.1MPa and 7.12mm, respectively (Bianco et al. 2011)).

Step 2: Determining the average available resisting bond length and the minimum integer number of FRP strips that crossing the CDC:

$$\bar{L}_{Rfi} = \frac{h_w \cdot \sin \theta \cdot (\cot \theta + \cot \theta_f)}{4 \cdot \sin(\theta + \theta_f)} \quad (6.79)$$

$$N_{f,int}^l = \text{round} \left[h_w \cdot \frac{\cot \theta + \cot \theta_f}{s_f} \right] \quad (6.80)$$

Step 3: Evaluation of various constants:

There are three types of constants:

- 1) Geometrical constants:

Perimeter of CFRP cross section, cross sectional area of the relevant prism surrounding concrete, and CDC length:

$$L_p = 2b_f + a_f; A_c = s_f \frac{b_w}{2}; L_d = \frac{h_w}{\sin \theta} \quad (6.81)$$

- 2) Mechanical constants:

The laminate tensile strength, concrete tensile strength, and concrete Young's modulus:

$$V_f^{tr} = a_f \cdot b_f \cdot f_{fu} \quad (6.82a)$$

$$f_{ctm} = 1.4 \left(\frac{f'_c - 8}{10} \right)^{2/3} \quad (6.82b)$$

$$E_c = 2.15 \times 10^4 \left(\frac{f'_c}{10} \right)^{1/3} \quad (6.82c)$$

3) Bond-Modeling constants encompass:

Bond modeling constant (J_1), integration constant for the softening friction phase (C_3), constant entering the governing differential equation for elastic phase (λ), effective resisting bond length (L_{Rfe}), and maximum value of force transferable through bond by the given CFRP NSM system (V_{f1}^{bd}):

$$J_1 = \frac{L_p}{A_f} \left[\frac{1}{E_f} + \frac{A_f}{A_c E_c} \right]; C_3 = \frac{V_f^{tr} \cdot J_1}{L_p \cdot \lambda}; \frac{1}{\lambda^2} = \frac{\delta_1}{\tau_b J_1}; L_{Rfe} = \frac{\pi}{2\lambda}; V_{f1}^{bd} = \frac{L_p \lambda \delta_1}{J_1} \quad (6.83)$$

Step 4: Reduction factor of the initial average available resisting bond length (η), and equivalent value of the average resisting bond length (\bar{L}_{Rfi}^{eq}):

The average resistance bond length is determined from:

$$\bar{L}_{Rfi}^{eq} = \eta \cdot \bar{L}_{Rfi} \quad (6.84)$$

where:

$$\eta = \begin{cases} \frac{f_{ctm}}{f_{ctm}^*} & \text{if } f_{ctm} < f_{ctm}^* \\ 1 & \text{if } f_{ctm} \geq f_{ctm}^* \end{cases} \quad (6.85)$$

with:

$$f_{ctm}^* = \frac{L_p \lambda \delta_1 \sin(\lambda L_{Rfi})}{J_1 \cdot \min(L_{Rfi} \cdot \tan \alpha, b_w / 2) \cdot \min(s_f \cdot \sin \theta_f, 2L_{Rfi} \cdot \tan \alpha)} \quad (6.86)$$

representing the concrete average tensile strength for values larger than which concrete fracture does not occur, where:

$$L_{Rfi} = \begin{cases} \bar{L}_{Rfi} & \text{if } \bar{L}_{Rfi} \leq L_{Rfe} \\ L_{Rfe} & \text{if } \bar{L}_{Rfi} > L_{Rfe} \end{cases} \quad (6.87)$$

Step 5: Determine the value of imposed slip in correspondence of which the comprehensive peak force transmissible by \bar{L}_{Rfi}^{eq} is attained ($V_{fi}(\bar{L}_{Rfi}^{eq}; \delta_{Li})$):

$$\delta_{Lu} = \begin{cases} \delta_{L1}(\bar{L}_{Rfi}^{eq}) & \text{if } V_{f1}^{db} < V_f^{tr} \\ \min[\delta_{L1}(\bar{L}_{Rfi}^{eq}); \delta_{Li}(V_f^{tr})] & \text{if } V_{f1}^{db} \geq V_f^{tr} \end{cases} \quad (6.88)$$

where $\delta_{Li}(\bar{L}_{Rfi}^{eq})$ is the value of imposed end slip in correspondence of which the bond-based constitutive law $V_{fi}^{bd}(\bar{L}_{Rfi}^{eq}; \delta_{Li})$ attains the peak value:

$$\delta_{Li}(\bar{L}_{Rfi}^{eq}) = \begin{cases} \delta_1 [1 - \cos(\lambda \bar{L}_{Rfi}^{eq})] & \text{if } \bar{L}_{Rfi}^{eq} \leq L_{Rfe} \\ \delta_1 & \text{if } \bar{L}_{Rfi}^{eq} > L_{Rfe} \end{cases} \quad (6.89)$$

and $\delta_{Li}(V_f^{tr})$ is the imposed end slip in correspondence of which the strip tensile strength is attained ($V_f^{tr} = a_f \cdot b_f \cdot f_{fu}$):

$$\delta_{Li}(V_f^{tr}) = \delta_1 \left\{ 1 - \cos \left[-\arcsin \frac{C_3}{\delta_1} \right] \right\} \quad (6.90)$$

Step 6: Maximum effective capacity $V_{fi,eff}^{max}$ of the NSM CFRP laminate with equivalent average resisting bond length \bar{L}_{Rfi}^{eq} :

The $V_{fi,eff}^{max}$ is evaluated by neglecting the post behavior of the constitutive law:

$$V_{fi,eff}^{max} = \frac{\delta_1 A_2}{2L_d A_3 \gamma_{max}} \left[\frac{\pi}{2} - \arcsin \varphi - \psi \sqrt{1 - \psi^2} \right] \quad (6.91)$$

where:

$$A_2 = \frac{L_p \lambda}{J_1} \quad ; \quad A_3 = \frac{\sin(\theta_f + \theta)}{2\delta_1} \quad ; \quad \gamma_{max} = \frac{2\delta_{Lu}}{L_d \sin(\theta_f + \theta)} \quad ; \quad (6.92)$$

$$\psi = 1 - A_3 \cdot \gamma_{max} \cdot L_d$$

Step 7: Shear strength contribution provided by a system of NSM CFRP laminates:

$$V_{fd} = 2 \cdot N_{f,int}^l \cdot V_{fi,eff}^{max} \cdot \sin \theta_f \quad (6.93)$$

6.9 New Approach to Determine Shear Capacity of RC Beams Strengthened with NSM Technique

As previously mentioned, based on ACI 440, shear strength of concrete member strengthened with CFRP can be determined by Eq. (6.71). In the present work, two new shear design approaches are presented based on simplified MCFT adapted to NSM technique. The results of 80 beams with and without shear reinforcement and with and without CFRP laminates are summarized, and the new design proposal approaches are compared to other design approaches, namely, ACI Committee (2011) and Eurocode (2001). Nanni et al. approach and

Bianco et al. approach combined with ACI and Eurocode to predict shear capacity of RC beams strengthened with NSM technique.

6.9.1 Nanni simplified MCFT (NSMCFT)

Adapting the simplified MCFT to the NSM technique is performed by adding formulation of NSM technique, suggested by Nanni et al. (2004) to SMCFT.

The simplified MCFT is a linear analysis and the FRP materials behavior is linear elastic up to the failure too. Thus, the values describing the tensile behavior of concrete (β), inclination of the diagonal compressive stress (θ), and effective crack spacing (s_{xe}) are assumed do not change when a linear elastic material such as FRP is adopted for the shear strengthening of a RC element (Blanksvärd 2009).

Therefore, the shear stress of a concrete member strengthened with NSM technique can be expressed as:

$$v = \text{Eq. (6.50)} + \text{Eq. (6.72)} / b_w d$$

$$v = v_c + v_s + v_f = \beta \sqrt{f'_c} + \rho_y f_{yield} \cot \theta + \left[4(a_f + b_f) \tau_b L_{totmin} \right] \cdot \frac{\sin \theta_f}{b_w d} \quad (6.94)$$

where the expressions for θ and β are provided by Eq. (6.59) and Eq. (6.60), respectively, while the longitudinal strain is calculated from (Eq. (6.61)):

$$\varepsilon_x = \frac{v \cot \theta - v_c / \cot \theta}{E_s \rho_{sx}} \quad (6.95)$$

6.9.2 Bianco simplified MCFT (BSMCFT)

One of the parameters in Bianco approach is inclination estimation of the CDC respect to the longitudinal axial of the beam. This problem can be solved by combining the Bianco and SMCFT approaches. Inclination of the CDC can be predicted by Eq. (6.59).

The new formulation for shear stress based on SMCFT combined with Bianco approach can be expressed as:

$$v = \text{Eq. (6.50)} + \text{Eq. (6.93)} / b_w d$$

$$v = v_c + v_s + v_{fd} = \beta \sqrt{f'_c} + \rho_y f_{yield} \cot \theta + 2 \cdot N_{f,int}^l \cdot V_{fi,eff}^{\max} \cdot \frac{\sin \theta_f}{b_w d} \quad (6.96)$$

The solution procedure to calculate the shear strength of concrete beams according to the simplified MCFT adapted to NSM technique is obtained applying the following procedures:

Step 1: Estimate a value for ε_x .

Step 2: Calculate the crack spacing using Eq. (6.54).

Step 3: Calculate θ and β using Eq. (6.59) and Eq. (6.60), respectively.

Step 4: Calculate the shear stress based on Eq. (6.94) for NSMCFT and Eq. (6.96) for BSMCFT.

Step 5: Calculate the longitudinal strain, ε_x , according to Eq. (6.95) and compare to ε_x that was estimated in step 1. Return to Step 2 with ε_x that was calculated in Step 5 until convergence is obtained.

The solution procedures based on NSMCFT and BSMCFT are available in Annex D.

6.10 Estimate of Shear Capacity of Concrete Beams

Table 6-1 summarizes the available experimental results for the NSM shear strengthening of RC beams (De Lorenzis and Nanni 2001, Dias et al. 2007, Dias 2008, Dias and Barros 2008, Islam 2009, Rizzo and De Lorenzis 2009, Dias and Barros 2010, Chaallal et al. 2011, Dias and Barros 2013). These experimental programs include beams of different size, with different amount of longitudinal and transverse reinforcement, and different NSM CFRP type and strengthening ratio.

The beams tested by (Dias et al. 2007, Dias and Barros 2008, 2010, 2013) were of type T cross section with the same ratio between shear span and effective depth (2.5), CFRP laminates and epoxy, and they differed on the amount of existing still stirrups ($\rho_{sw} = 0.1\%$ and 0.17%), percentage of longitudinal reinforcement ($\rho_{sx} = 2.8\%$ and 3.2%), and concrete compressive strength ($f'_c = 39.7, 18.6, \text{ and } 31.1 \text{ MPa}$). These series presented different configurations of NSM strips, in term of both inclination θ_f and spacing s_f . However, the series V and VI of these authors (Dias 2008) are formed by beams of a higher shear aspect ratio (3.3) and concrete average compressive strength ($f'_c = 59.4 \text{ MPa}$).

Those beams are characterized by the following common geometrical and mechanical parameters: $b_w = 180 \text{ mm}$; $h_w = 300 \text{ mm}$; $f_{fu} = 2952 \text{ MPa}$ (for the series I, II, III, IV) and $f_{fu} = 2848 \text{ MPa}$ (for the series V and VI); $E_f = 166.6 \text{ GPa}$ (for the series IV), $E_f = 174.3 \text{ GPa}$ (for the series III, V, and VI), and $E_f = 170.9 \text{ GPa}$ (for series I and II); $a_f = 1.4 \text{ mm}$; $b_f = 9.5 \text{ mm}$ (for the series I, II, III, V and IV) and $a_f = 1.4 \text{ mm}$; $b_f = 10 \text{ mm}$ (for series IV).

The beams tested by Chaallal et al. (2011) are of T cross section type, and were strengthened in shear by CFRP rods and tested under three point bending. These beams were characterized by cross-section dimensions of $b_w = 152$ mm and $h_w = 304$ mm. Concrete had average compressive strength of 25 MPa and 35 MPa. CFRP rods of 9.5 mm diameter, with tensile strength of $f_{fu} = 1270$ MPa and modulus of elasticity of $E_f = 148$ GPa were used.

The beams tested by De Lorenzis and Nanni (2001) were T cross section type and were shear strengthened with CFRP rods, and tested under four point bending. These beams were characterized by cross-section dimensions of $b_w = 150$ mm and $h_w = 305$ mm. The concrete had an average compressive strength of 31 MPa. CFRP rods of nominal diameter around 9.5 mm, with tensile strength $f_{fu} = 1875$ MPa and modulus of elasticity $E_f = 104.8$ GPa were adopted. Two different percentages of steel stirrups were used ($\rho_{sw} = 0.0\%$ and 0.26%).

The beams tested by Rizzo and De Lorenzis (2009) were of rectangular cross-section type, strengthened in shear by either bars (NB) or strips (NS), and tested under four point bending. These beams were characterized by cross-section dimensions of $b_w = 200$ mm and $h_w = 210$ mm. The concrete had an average compressive strength of 29.3 MPa. Round CFRP bars of 8 mm diameter, with tensile strength $f_{fu} = 2210$ MPa and modulus of elasticity $E_f = 145.7$ GPa were used. The strips have cross-section dimensions $a_f = 2.0$ mm and $b_f = 16.0$ mm, and mechanical properties of $f_{fu} = 2070$ MPa and $E_f = 121.5$ GPa.

The beams tested by Islam (2009) were of rectangular cross-section type, strengthened in shear with CFRP round bars and tested under four point bending. These beams were characterized by cross-section dimensions of $b_w = 254$ mm and $h_w = 305$ mm. The concrete had an average compressive strength of 49.75 MPa. Round CFRP bars of 9 mm diameter, with tensile strength $f_{fu} = 2070$ MPa and modulus of elasticity $E_f = 124$ GPa were used.

The angle α for BSMCFT was assumed equal to 28.5° for all the experimental programs (Bianco et al. 2014). The average bond stress and effective tensile strain of CFRP laminate and rods (Figure 6-18) are assumed $\tau_b = 16.1$ and 6.9 MPa and $\varepsilon_{fe} = 0.59\%$ and 0.4% , respectively. The parameters characterizing the adopted local bond stress-slip relationship (Figure 6-19a) are assumed $\tau_0 = 20.1$ MPa and $\delta_1 = 7.12$ mm (Bianco et al. 2014).

When CFRP rods are employed instead of laminates, the equivalent square cross-section is employed in the calculations. The same values of the equivalent square cross section dimensions are adopted to evaluate the effective perimeter $L_p = 2 \cdot b_f + a_f$.

The size aggregates (a_g) were assumed 20 mm for all the experimental programs.

Table 6-1: Summary of experimental and analytical results

Beam Label	f'_c (MPa)	Reinforcement				F_{exp} (kN)	$F_{exp} / F_{prediction}$				
		ρ_{sx}	θ_f	$\frac{\rho_y f_{y yield}}{f'_c}$	$\frac{\rho_f f_{yf}}{f'_c}$		NSMCFT	BSMCFT	Eurocode $\theta = 45^\circ$	Eurocode $\theta = 21.8^\circ$	ACI
<i>Dias and Barros (2010, 2013)</i>											
C-R	39.7	0.028	-	0	0	207	1.11	1.11	1.90	1.90	1.78
2S-R-I	39.7	0.028	-	0.0143	0	303.8	1.18	1.18	1.83	0.98	1.78
7S-R	39.7	0.028	-	0.038	0	467.5	1.25	1.25	1.85	1.23	1.78
2S-4LV-I	39.7	0.028	90°	0.0143	0.056	337.4	1.14	1.09	1.72	1.03	1.66
2S-7LV-I	39.7	0.028	90°	0.0143	0.09	374.1	1.17	0.99	1.70	0.97	1.65
2S-10LV-I	39.7	0.028	90°	0.0143	0.12	397.5	1.14	1.03	1.64	0.90	1.60
2S-4LI45-I	39.7	0.028	45°	0.0143	0.055	392.8	1.3	1.18	1.87	1.21	2.02
2S-7LI45-I	39.7	0.028	45°	0.0143	0.9	421.7	1.11	1.05	1.45	0.90	1.80
2S-10LI45-I	39.7	0.028	45°	0.0143	0.13	446.5	1.03	1.09	1.29	0.79	1.70
2S-4LI60-I	39.7	0.028	60°	0.0143	0.49	386.4	1.28	1.22	1.86	1.16	1.94
2S-6LI60-I	39.7	0.028	60°	0.0143	0.076	394.4	1.14	1.13	1.57	0.94	1.74
2S-9LI60-I	39.7	0.028	60°	0.0143	0.11	412.7	1.06	1.01	1.39	0.82	1.62
4S-4LV-II	39.7	0.028	90°	0.0237	0.055	424.5	1.24	1.19	1.82	1.01	1.77
4S-7LV-II	39.7	0.028	90°	0.0237	0.09	427.4	1.16	1.12	1.66	0.89	1.62
4S-4LI45-II	39.7	0.028	45°	0.0237	0.055	442.5	1.27	1.17	1.79	1.06	1.92
4S-7LI45-II	39.7	0.028	45°	0.0237	0.09	478.1	1.12	1.07	1.46	0.86	1.76
4S-4LI60-II	39.7	0.028	60°	0.0237	0.048	443.9	1.27	1.22	1.81	1.04	1.88
4S-6LI60-II	39.7	0.028	60°	0.0237	0.076	457.6	1.16	1.16	1.58	0.90	1.73
<i>Dias et al. (2007)</i>											
C-R-III	18.6	0.028	-	0	0	147	1.08	1.08	1.75	1.75	1.86
2S-R-III	18.6	0.028	-	0.0304	0	226.5	1.08	1.08	1.63	1.02	1.69
4S-R-III	18.6	0.028	-	0.0508	0	303.8	1.17	1.17	1.73	0.97	1.78
2S-7LV-III	18.6	0.028	90°	0.0304	0.199	273.7	0.98	1.04	1.39	0.75	1.46

Table 6-1: (Continued.)

Beam Label	f'_c (MPa)	Reinforcement				F_{exp} (kN)	$F_{exp} / F_{prediction}$				
		ρ_{sx}	θ_f	$\frac{\rho_y f_y yield}{f'_c}$	$\frac{\rho_f f_{yf}}{f'_c}$		NSMCFT	BSMCFT	Eurocode $\theta = 45^\circ$	Eurocode $\theta = 21.8^\circ$	ACI
2S-4LI45-III	18.6	0.028	45°	0.0304	0.122	283	1.11	1.14	1.51	0.93	1.85
2S-7LI45-III	18.6	0.028	45°	0.0304	0.199	306.5	0.91	1.08	1.14	0.69	1.58
2S-4LI60-III	18.6	0.028	60°	0.0304	0.107	281.6	1.09	1.17	1.52	0.91	1.74
2S-6LI60-III	18.6	0.028	60°	0.0304	0.168	297.7	0.98	1.16	1.29	0.75	1.56
4S-7LV-III	18.6	0.028	90°	0.0508	0.199	315.2	0.96	1.05	1.35	0.69	1.38
4S-4LI45-III	18.6	0.028	45°	0.0508	0.122	347.2	1.13	1.17	1.55	0.87	1.79
4S-7LI45-III	18.6	0.028	45°	0.0508	0.199	356.4	0.92	1.07	1.17	0.66	1.52
4S-4LI60-III	18.6	0.028	60°	0.0508	0.107	345.6	1.13	1.19	1.56	0.86	1.73
4S-6LI60-III	18.6	0.028	60°	0.0508	0.168	362.3	1.02	1.19	1.36	0.74	1.59
<i>Dias and Barros (2008)</i>											
C-R-IV	31.1	0.032	-	0	0	243	1.47	1.47	2.41	2.41	2.41
2S-R-IV	31.1	0.032	-	0.0182	0	315	1.35	1.35	2.05	1.34	2.03
6S-R-IV	31.1	0.032	-	0.0303	0	410	1.27	1.27	1.82	1.00	1.82
2S-3LV-IV	31.1	0.032	90°	0.0182	0.057	316	1.33	1.24	2.03	1.32	2.01
2S-5LV-IV	31.1	0.032	90°	0.0182	0.095	357	1.29	1.29	1.89	1.11	1.88
2S-8LV-IV	31.1	0.032	90°	0.0182	0.152	396	1.25	1.25	1.78	0.98	1.78
2S-3LI45-IV	31.1	0.032	45°	0.0182	0.057	328	1.16	1.11	1.62	1.02	1.82
2S-5LI45-IV	31.1	0.032	45°	0.0182	0.095	384	1.16	1.18	1.54	0.95	1.88
2S-8LI45-IV	31.1	0.032	45°	0.0182	0.152	382	1.01	1.05	1.29	0.79	1.68
2S-3LI60-IV	31.1	0.032	60°	0.0182	0.057	374	1.32	1.45	1.89	1.14	2.01
2S-5LI60-IV	31.1	0.032	60°	0.0182	0.085	392	1.32	1.28	1.84	1.12	2.03
2S-7LI60-IV	31.1	0.032	60°	0.0182	0.123	406	1.22	1.22	1.64	0.98	1.90
<i>Dias (2008)</i>											
C-R-V	59.4	0.031	-	0	0	207	0.79	0.79	1.34	1.34	1.22

Table 6-1: (Continued.)

Beam Label	f'_c (MPa)	Reinforcement				F_{exp} (kN)	$F_{exp} / F_{prediction}$				
		ρ_{sx}	θ_f	$\frac{\rho_y f_y yield}{f'_c}$	$\frac{\rho_f f_{yf}}{f'_c}$		NSMCFT	BSMCFT	Eurocode $\theta = 45^\circ$	Eurocode $\theta = 21.8^\circ$	ACI
3S-R-V	59.4	0.031	-	0.0095	0	359.9	1.05	1.05	1.64	1.14	1.53
3S-6LV-V	59.4	0.031	90°	0.0095	0.025	387	0.97	0.91	1.49	0.92	1.40
3S-10LV-V	59.4	0.031	90°	0.0095	0.041	491.7	1.14	0.91	1.71	1.00	1.62
3S-5LI45-V	59.4	0.031	45°	0.0095	0.025	492.1	1.21	1.07	2.73	1.18	1.86
<i>Chaallal et al. (2011)</i>											
3S-9LI45-V	59.4	0.031	45°	0.0095	0.041	563.6	1.12	0.99	1.51	0.96	1.80
3S-5LI60-V	59.4	0.031	60°	0.0095	0.022	497.9	1.22	1.14	1.82	1.17	1.84
3S-8LI60-V	59.4	0.031	60°	0.0095	0.035	584.5	1.27	1.20	1.78	1.10	1.92
5S-R-VI	59.4	0.031	-	0.0143	0	409.7	1.05	1.05	1.63	1.03	1.53
5S-5LI45-VI	59.4	0.031	45°	0.0143	0.025	559.5	1.25	1.12	1.79	1.12	1.88
5S-9LI45-VI	59.4	0.031	45°	0.0143	0.041	627.5	1.16	1.03	1.55	0.94	1.82
5S-5LI60-VI	59.4	0.031	60°	0.0143	0.022	556.4	1.23	1.16	1.81	1.10	1.84
5S-8LI60-VI	59.4	0.031	60°	0.0143	0.035	654.6	1.3	1.24	1.81	1.07	1.94
<i>Chaallal et al. (2011)</i>											
S0-CON	25	0.038	-	0	0	180.6	0.99	0.99	1.59	1.59	1.80
S1-CON	25	0.038	-	0.0812	0	230.4	1.07	1.07	1.57	0.79	1.63
S3-CON	35	0.038	-	0.0386	0	255.3	0.98	0.98	1.44	0.77	1.48
S0-NSM	25	0.038	90°	0	0.54	331	1.01	1.13	1.47	0.89	1.57
S1-NSM	25	0.038	90°	0.0812	0.54	355.9	0.92	0.98	1.29	0.62	1.34
S3-NSM	35	0.038	90°	0.0386	0.39	306.5	1.02	1.04	1.45	0.72	1.48
<i>De Lorenzis and Nanni (2001)</i>											
BV	31	0.024	-	0	0	180.6	1.09	1.09	1.90	1.90	1.77
B90-7	31	0.024	90°	0	0.31	230.4	1.04	1.08	1.60	1.05	1.53
B90-5	31	0.024	90°	0	0.44	255.3	1	1.07	1.46	0.87	1.40

Table 6-1: (Continued.)

Beam Label	f'_c (MPa)	Reinforcement				F_{exp} (kN)	$F_{exp} / F_{prediction}$				
		ρ_{sx}	θ_f	$\frac{\rho_y f_{y yield}}{f'_c}$	$\frac{\rho_f f_{yf}}{f'_c}$		NSMCFT	BSMCFT	Eurocode $\theta = 45^\circ$	Eurocode $\theta = 21.8^\circ$	ACI
B45-7	31	0.024	45°	0	0.45	331	0.92	1.07	1.11	0.73	1.62
B45-5	31	0.024	45°	0	0.63	355.9	0.81	1.02	0.93	0.59	1.45
BSV	31	0.024	-	0.029	0	306.5	1.11	1.12	1.67	0.97	1.61
BS90-7A	31	0.024	90°	0.029	0.31	413.7	1.24	1.27	1.78	0.92	1.73
<i>Rizzo and De Lorenzis (2009)</i>											
C	29.3	0.044	-	0.0401	0	244.3	1.04	1.04	1.56	0.91	1.78
NB90-73-b	29.3	0.044	90°	0.0401	0.5191	297	1	1.04	1.44	0.77	1.61
NB90-45-b	29.3	0.044	90°	0.0401	0.8421	301.5	0.89	0.99	1.27	0.65	1.39
NB45-146-a	29.3	0.044	45°	0.0401	0.3671	322.6	0.96	1.11	1.67	0.98	2.08
NB45-73-a	29.3	0.044	45°	0.0401	0.7341	300.3	0.68	0.94	1.03	0.76	1.74
NS90-73-a	29.3	0.044	90°	0.0401	0.3097	345.3	0.93	1.20	1.31	0.65	1.42
NS45-146-a	29.3	0.044	45°	0.0401	0.219	309.7	0.74	1.06	1.23	0.72	1.68
<i>Islam (2009)</i>											
Beam1	49.75	0.017	-	0.0338	0	365	0.86	0.86	1.17	0.62	1.07
Beam2	49.75	0.017	90°	0.0338	0.1404	454	0.94	0.93	1.22	0.62	1.14
Beam3	49.75	0.017	90°	0.0169	0.1404	427	1.12	1.09	1.53	0.85	1.39
Beam4	49.75	0.017	90°	0.0008	0.1404	436	1.32	1.28	1.86	1.12	1.66

Figure 6-20 shows the results of different design approaches. This figure shows the ratio between experimental and analytical approach for NSMCFT, BSMCFT, ACI, Eurocode $\theta = 45^\circ$ and Eurocode $\theta = 21.8^\circ$. As shown in Table 6-2 and Figure 6-20, the ACI approach predicts the highest $F_{exp} / F_{prediction}$ values, with an average of 1.70 and with a Standard Deviation (SD) of 0.22.

Table 6-2: Average and Standard Deviation of $F_{exp} / F_{prediction}$ for different approaches

	<i>NSMCFT</i>	<i>BSMCFT</i>	<i>Eurocode</i> $\theta = 45^\circ$	<i>Eurocode</i> $\theta = 21.8^\circ$	<i>ACI</i>
<i>Average</i>	1.10	1.12	1.60	0.99	1.70
<i>SD</i>	0.15	0.10	0.29	0.30	0.22
<i>COV</i>	13.6%	8.9%	18%	30%	13%

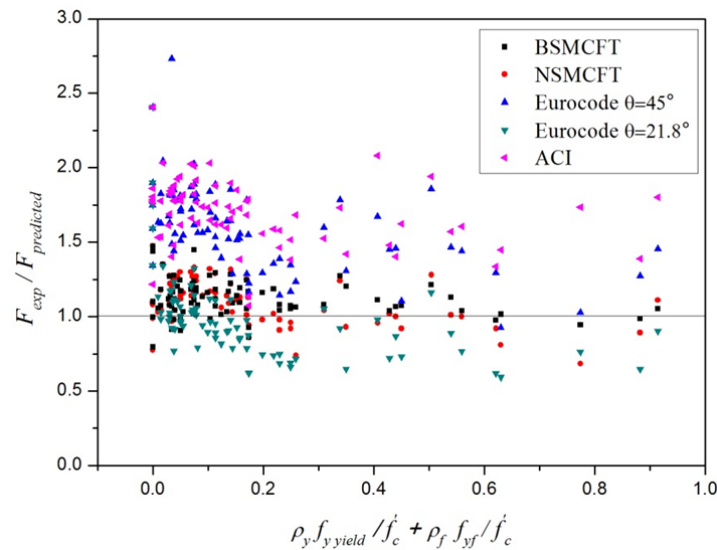


Figure 6-20: Ratio between experimental and predicted shear resistance

As already indicated, for the inclination of compression strut Eurocode (2001) recommends to be in the interval $1 \leq \cot \theta \leq 2.5$. Choosing the lower limit of θ overestimates the shear resistance observed experimentally. In fact, for $\theta = 21.8^\circ$ the average ratio between experiments and predictions is 0.99, with the highest SD (0.30). By choosing the upper limit for θ the average $F_{exp} / F_{prediction}$ was relatively high (1.60), as well as the SD (29%).

The NSMCFT gives fairly safe estimations with a few overestimations (refer to Figure 6-20 and Table 6-2). For this approach the average ratio between experiments and predictions is 1.10 with SD of 15%.

A systematic trend in the error can be highlighted if the results are plotted in non-dimensional form, as is shown in Figure 6-21, where the shear resistance is normalized by the force dimensional parameter $b_w d f_c'$. It is verified that the scatter of the predicted values *versus* the experimental ones increases linearly with the non-dimensional shear. In the figure, two lines limiting to $\pm 20\%$ the deviation of the predicted values from the experimental values are also represented, and it is verified that almost all of the results of BSMCFT and NBSCMFT are inside of these bounds.

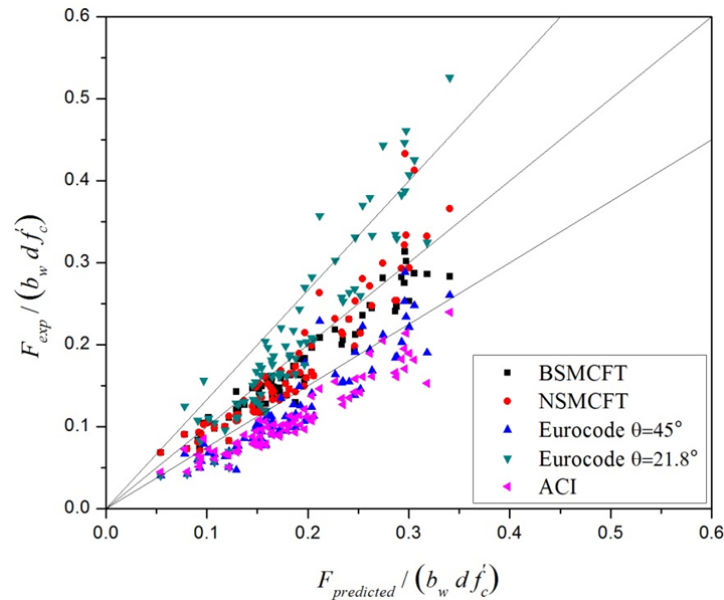


Figure 6-21: Predicted non-dimensional failure shear force of the beams, in compression with experimental values

The BSMCFT estimates average value for the $F_{exp} / F_{prediction}$ similar (1.12) to NSMCFT, but with smaller SD and COV (0.10 and 8.9%). While in the Nanni approach a constant $\theta = 45^\circ$ is assumed, in the Bianco formulation the inclination of CDC can vary.

Based on the data presented in Table 6-2 and Figure 6-20 it can be concluded that the two new approaches predict with good accuracy the experimental results.

6.11 Assessment of the Applicability of Analytical Formulations for Predicting the Shear Capacity of RC Beams Strengthened with Hybrid Composite Plate

The analytical formulations described in previous section are adopted to predict the shear capacity of the RC beams strengthened with HCPs described in Chapter 3.

6.11.1 Shear resistance of the SHCC plate

In a rectangular non-cracked section the maximum shear stress in the cross section is:

$$\tau_{\max} = \frac{VQ}{It} = \frac{3V}{2A} \quad (6.97)$$

where V is the total shear force, Q and I are the first and second moment of area, respectively, and t is total thickness. Blanksvärd (2007) has suggested a member does not need shear reinforcement if the principal stress is less than $0.5f_{ct}$, hence, shear resistance of the SHCC plate by assuming perfect bond between SHCC plate and concrete substrate can be expressed as:

$$V_{SHCC} = 2\left(\frac{1}{3}t_{SHCC}h_{SHCC}f_{ct}\right) \quad (6.98)$$

Note that the factor 2 originates from that the SHCC plates are applied on both sides of the beam. The shear stress of a strengthened concrete beam with HCP can be expressed as:

$$v = v_c + v_s + v_f + v_{SHCC} \quad (6.99)$$

6.11.2 Assessment of the predictive performance of the considered formulations

In RC beams strengthened with NSM CFRP laminates, NSM-4L90-I and NSM-4L45-II beams, the width of the base of the concrete semi-pyramidal tensile fracture (b_w^*) is limited by the half width of the beams' cross section ($b_w^* = b_w / 2$). Due to the detachment of HCPs that included a concrete cover of a thickness that varied between 5 mm and 10 mm (Figure 3-12a and Figure 3-13b), the dimension of this limit should vary between $b_w^* = t_{HCP} + 5$ mm and $b_w^* = t_{HCP} + 10$ mm, where t_{HCP} is the thickness of the HCP (20 mm). In the present work an average value of 27.5 mm was considered for b_w^* in the beams shear strengthened with HCPs and bonded with epoxy adhesive without mechanical anchors. Therefore, in the formulation herein presented b_w should be regarded the cross section width, and $b_w = 2 \times b_w^* = 55$ mm in the case of the beams strengthened with HCPs without mechanical anchors.

The Eq. (6.82c) was proposed by CEB-FIP Model Code (1993) for conventional concretes, was used in the present formulation because parametric studies carried out demonstrated that the Young's modulus has small influence on the shear contribution of CFRP laminates (Bianco et al. 2012).

In the NSMCFT formulation the values $\tau_b = 16.1$ MPa and $\varepsilon_{fe} = 0.59\%$ suggested in Barros and Dias (2006) were adopted since in the present research program rectangular laminates similar to the ones used in that work were applied. Since in the beams shear strengthened with HCPs the final failure has mainly progressed through the concrete substrate, for the α , τ_0 and δ_1 the values of 28.5° , 20.1 MPa and 7.12 mm were adopted, following the recommendations of Bianco et al. (2011 and 2014).

Table 6-3 summarized all the results of the tested beams, whose experimental programs are described in Chapter 3. These programs are composed of control beams, beams reinforced with steel stirrups, and beams strengthened with NSM technique, SHCC plates, and HCPs. A previously damaged beam, shear strengthened with HCPs is also considered in this analysis.

Table 6-3: Analytical vs. experimental results of the strengthened and repaired beams with HCPs

Beam Label	f'_c (MPa)	Reinforcement				F_{exp} (kN)	$F_{exp} / F_{prediction}$	
		ρ_{sx}	θ_f	$\frac{\rho_y f_{y yield}}{f'_c}$	$\frac{\rho_f f_{yf}}{f'_c}$		NSMCFT	BSMCFT
<i>Rectangular cross section (Series I)</i>								
0S-R-I	32.7	0.016	-	-	-	81	0.90	0.90
NSM-4L90-I	32.7	0.016	90°	-	0.08	143	1.17	1.11
SP-I	32.7	0.016	-	-	-	130	1.15	1.15
SP-4L90-I	32.7	0.016	90°	-	0.08	151	1.03	1.07
SP-3L45-I	32.7	0.016	45°	-	0.08	166	1.00	0.97
7S-R-I	32.7	0.016	-	0.11	-	182	0.62	0.62
<i>T cross section beam (Series II)</i>								
C-R-II	32.7	0.029	-	-	-	214	1.15	1.15
NSM-3L45-II	32.7	0.029	45°	-	0.064	291	1.27	1.16
SP-II	32.7	0.029	-	-	-	255	1.20	1.20
SP-3L45-II	32.7	0.029	45°	-	0.064	367	1.43	1.50
SP-3L45-B-II	32.7	0.029	45°	-	0.064	363	1.42	1.29
SP-5L45-II	32.7	0.029	45°	-	0.11	306	0.89	1.02
SP-5L45-B-II	32.7	0.029	45°	-	0.11	364	1.06	1.07
7S-R-II	32.7	0.029	-	0.056	-	530	1.34	1.34
<i>Repaired beams (Series III)</i>								
R-SP-3L45-III	32.7	0.016	45°	-	0.14	161	0.70	0.98
4S-SP-5L45-III	32.7	0.029	45°	-	0.11	552	1.03	1.04
R-SP-5L45-III	32.7	0.029	45°	-	0.11	530	0.99	1.00

Table 6-4: Average, Standard Deviation, and coefficient of variation of all the tested beams

	NSMCFT	BSMCFT
Average	1.11	1.12
SD	0.20	0.15
COV	18%	13%

Table 6-5: Average, Standard Deviation, and coefficient of variation of the strengthened beams with HCPs

	<i>NSMCFT</i>	<i>BSMCFT</i>
<i>Average</i>	1.08	1.11
<i>SD</i>	22%	16%
<i>COV</i>	20%	14%

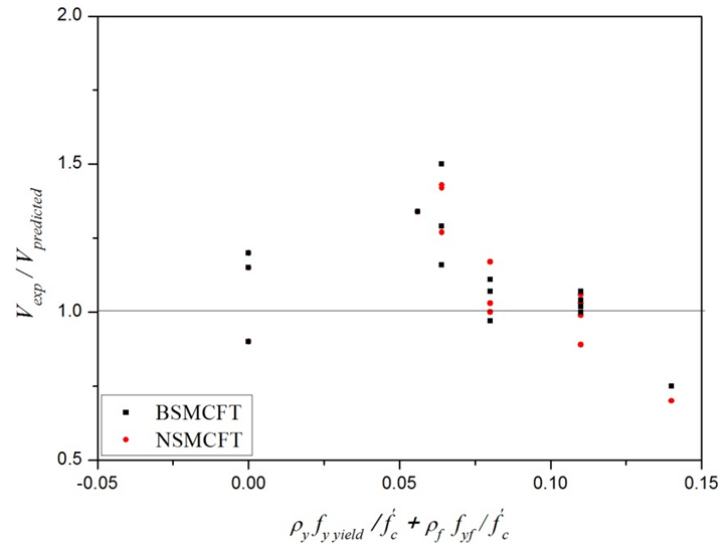


Figure 6-22: Ratio between experimental and predicted results of the beams strengthened with HCPs

The results in Figure 6-22, Table 6-4, and Table 6-5 show the capability of BSMCFT and NSMCFT formulation to predict with good accuracy the ultimate shear capacity of RC beams strengthened or repaired with HCPs. The average ratio between experimental to predicted shear resistance for the strengthened beams with HCPs and SHCC plates are 1.11 and 1.12 for NSMCFT and BSMCFT techniques, respectively, while the corresponding COV was smaller for BSMCFT. This might be justified on the capability of BSMCFT capturing the detachment of the HCPs by changing the width of the base of the concrete semi-pyramidal tensile fracture ($b_w=55$ mm for the beams without mechanical anchors with detachment failure, and b_w = width of the beams for those with mechanical anchors).

Furthermore, specific investigation in this domain needs to be executed in order to obtain these values for the SHCC for attending the situations where fracture propagates through this material. Future improvements in the model should also be implemented in order to contemplate the possibility of the semi-pyramid be formed by planes crossing different types of materials (SHCC and concrete substrate).

6.12 Conclusion

Understanding the shear behavior of concrete beam is a complicated approach, due to several parameters that are involved in shear mechanism. There are two prominent models that are used to predict the shear capacity of concrete beams: truss model and modified compression field theory. In Truss model is assumed the contribution of the tensile stress of concrete is neglected, therefore conservative values are estimated.

The results of the experimental tests indicated the diagonal compressive stress is not only a function of the diagonal compressive strain but also of the coexisting principal tensile strain too. The modified compression field theory takes into account the resisting contribution of cracked concrete in tension. However, this model is tedious if done by hand due to huge amount of parameters and assumptions.

Simplified MCFT (SMCFT) takes into account the tensile stress in cracked concrete (β), and inclination of diagonal compressive stress (θ), while smaller number of parameters and assumptions are considered in its formulation.

A new model was proposed by combining of SMCFT with Nanni et al. and Bianco et al. formulation (NSMCFT and BSMCFT, respectively) to predict shear capacity of reinforced concrete beams strengthened with CFRP laminates/rods. The experimental results of 80 beams with different strengthening configurations and percentage of CFRP laminates/rods were used to access the predictive performance of these new approaches. The results provided satisfactory estimates of the experimental recordings. An average value of 1.10 and 1.12 for the $F_{exp} / F_{prediction}$, with standard deviation of 15% and 10% were obtained by using the NSMCFT and BSMCFT, respectively.

By applying the models of NSMCFT and BSMCFT to the beams strengthened with HCPs it was verified that the last one has predicted with more accuracy the shear capacity of the strengthened beams due to its capability of capturing the detachment of the HCPs by changing the width of the base of the concrete semi-pyramidal tensile fracture.

Chapter 7

Conclusions and Recommendations for Future Research

7.1 Experimental research

Due to the demand for strengthening intervention on relatively large stock of existing reinforced concrete (RC) structures, in order to carry higher ultimate loads, satisfy certain new functionalities, or to restore the load carrying capacity affected by materials damage, accidents or extreme events, new retrofitting and strengthening materials and techniques are being proposed. Fiber reinforced polymer (FRP) materials has been proposed for this purpose, and have been extensively studied during the last two decades. However, surface preparation, premature debonding of the FRP and lack of protection against vandalism and fire are some disadvantages of the techniques based on the FRP, such is the case of externally bonded reinforcement (EBR) and Near Surface Mounted (NSM).

This PhD thesis was dedicated to the assessment of the effectiveness of a new technique for the shear strengthening of RC beams. This technique is based on the application of Hybrid Composite Plates (HCPs) on the lateral faces of the RC beams to be strengthened, and its effectiveness was investigated by carrying out three experimental programs. HCP is a thin plate of Strain Hardening Cementitious Composite (SHCC) reinforced with CFRP laminates. The SHCC surrounding the CFRP laminates in the HCP has offered effective resistance to the degeneration of micro-cracks on macro-cracks, which has avoided the occurrence of mixed shallow fracture-plus-debonding failure modes registered when used the NSM-CFRP technique.

These experimental programs have also investigated the influence that the following parameters have on effectiveness of HCPs for the shear strengthening of RC beams:

- Orientation of the CFRP laminates that reinforce the SHCC plate;
- CFRP shear strengthening ratio;
- Using mechanical anchors to install the HCPs;

The effectiveness of this technique was also explored for the repairing RC beams that have previously failed in shear.

From the experimental programs it was observed that the effectiveness level of the HCP technique was limited by the tensile strength of the concrete substrate of the RC beams, since

at failure, a concrete cover layer of an average thickness that varied between 5 to 10 mm was attached to the HCPs. The detachment of HCPs has avoided the mobilization of the shear strengthening potentialities of the CFRP laminates. However, when the HCPs were bonded with epoxy and fixed with mechanical anchors, the tensile capacity of the CFRP laminates of the HCPs was effectively mobilized, since maximum tensile strains in the CFRP closely to its ultimate tensile strain were measured. Furthermore, by controlling the torque to apply the mechanical anchors, a certain post-tension is introduced, which installs a favorable confinement into the concrete of the beam to be strengthened, with high shear strengthening effectiveness of the HCPs.

The results of the tested beams have also shown that for deflections higher than the one corresponding to the formation of the first shear crack in the beam strengthened with NSM technique, the technique based on the application of HCPs have assured higher load carrying capacity and deflection performance than the NSM technique. It was also observed that when HCPs are applied with epoxy adhesive and mechanical bolts, the load carrying capacity of RC beams failed in shear can be fully restored.

The shear behavior of the SHCC was investigated by Iosipescu shear test method. The shear stress-sliding curves obtained in these tests were characterized by three phases: 1) a first phase where the SHCC developed linear behavior, that ends at an average shear stress of 0.07 MPa and sliding of 0.08 mm; second phase corresponding to the development of micro cracks with a continuous decrease of shear stiffness up to peak load (at an average shear strength of 3.9 MPa and sliding of 0.5 mm); the third phase corresponds to the shear softening stage where micro cracks start degenerating in a macro-crack in the shear critical region, but for an average slip 2 times the average slip at peak load the SHCC was still capable of supporting 50% of the average shear strength, which denotes the ductility of this composite material when subjected to shear deformations. By calculating the area under the curve of average shear stress versus sliding, the fracture energy mode II of SHCC material was estimated about 1.4 N/mm, which corresponds to 40% of its mode I fracture energy.

7.2 Numerical research

Advanced material nonlinear numerical simulations based on the finite element method (FEM) were carried for contributing for a better understanding of the shear strengthening mechanisms provided by the developed technique, as well as to explore its potentialities by executing parametric numerical studies. In this regard, the capability of a FEM-based

computer program to predict with high accuracy the behavior of the beams strengthened in shear with hybrid composite plates (HCPs) up to its collapse was demonstrated. The shear crack softening diagram of the multi-directional fixed smeared crack model available in the FEMIX computer program allowed to a good prediction of the load carrying capacity, crack patterns and failure modes of the tested beams. Due to the lack of specific experimental tests, the data to define the shear crack softening diagram for plain concrete was obtained by inverse analysis, while the data for SHCC was determined from Iosipescu shear tests.

In the perspective of providing valuable information for the optimization of the proposed shear strengthening technique, and by using the aforementioned FEM-based constitutive model, a parametric study was carried out to investigating the influence of: the arrangement of CFRP laminates and its shear strengthening ratio; the use of mechanical anchors for fixing the HCP to the RC beam; the post-tension level applied to the mechanical anchors for installing different favorable level of concrete confinement in the beam to be shear strengthened; the advantages of using SHCC instead of mortar.

When SHCC was used instead of mortar, a higher ultimate load is predicted, since the strain hardening character of the SHCC assured a much more diffuse crack pattern in the HCP, with a consequent better mobilization of the high tensile capacity of the CFRP laminates. It was also demonstrated that the load carrying capacity and deformability performance of beams strengthened with HCPs increase with the torque level applied to the mechanical bolts due to the higher confinement introduced in the concrete of the beam to strengthen.

A parametric numerical study was also carried out for Iosipescu shear test to analyze the influence of the shear retention factor (β) that defines the crack shear stiffness of the first branch of crack shear softening diagram. It was verified that by increasing the β value the specimen fails at a lower average shear strength due to the higher crack shear stress transfer.

It was observed that by using the concept of shear retention factor for modeling the crack shear stress transfer, an abnormal high load carrying capacity is estimated with an incorrect failure mode and crack pattern. However, by adopting a crack shear softening diagram, the smeared crack approach has correctly predicted the response and failure mode of the specimens.

7.3 Analytical work

For predicting the contribution of the HCPs for the shear resistance of RC beams, two analytical approaches were developed, and their predictive performance was assessed by

considering the results obtained on the experimental programs and those available in the specialized bibliography.

Both approaches are based on simplified modified compression field theory (SMCFT), which takes into account the tensile resistance of the cracked concrete (β), and inclination of diagonal compressive strut (θ). For estimating the contribution of the CFRP laminates that reinforce an HCP, two formulations were selected, one proposed by Nanni et al. and the other by Bianco et al. The designations of NSMCFT and BSMCFT were attributed to the approaches that combine SMCFT with, respectively, the Nanni et al. and the Bianco et al. formulation. The experimental results of 80 beams with different configurations and percentage of CFRP laminates/rods were used to appraise the predictive performance of the developed approaches. By evaluating the ratio between the experimental results and the analytical predictions, an average value of 1.10 and 1.12 was obtained for the NSMCFT and BSMCFT approaches, respectively, with a standard deviation of 0.15 and 0.10.

By applying the models of NSMCFT and BSMCFT to the beams strengthened with HCPs it was verified that the last one has better predicted the shear capacity of the strengthened beams due to its capability of capturing the detachment of the HCPs.

7.4 Suggestions for Future Research

In the following, some recommendations are proposed for future research:

- Evaluate the effectiveness of other kinds of SHCC materials with higher tensile strength and deformability;
- Evaluate the effectiveness of HCPs for shear strengthening of continuous RC beams by experimental and numerical research;
- Evaluate the influence of concrete confinement provided by mechanical anchors used to install HCPs, when this strengthening technique is applied in real scale RC beams;
- Evaluate the influence of the percentage of existing steel stirrups on the effectiveness of the proposed strengthening technique;
- Apply the digital image correlation technique in the Iosipescu shear test to better determine the shear behavior of SHCC, with the final aim of determining the crack shear stress versus sliding, as well as the strain field in the critical shear region. This information can be of paramount relevance in the development of more reliable crack

constitutive mode in the framework of FEM material nonlinear analysis of fiber reinforced cement composites;

- Explore the applicability of HCPs for the shear strengthening of deep RC beams and walls, mainly for those walls pertaining to buildings that need to be strengthened against to lateral loads like those typical of seismic events;
- Evaluate experimentally the cyclic behavior of SHCC in tension and compression, and implementation of the obtained laws in a FEM-based constitutive model in order to be possible the simulation of the behavior of RC structures strengthened with HCPs when submitted to cyclic loadings.
- Extend the use of the proposed technique for the increase of the load carrying capacity and ductility performance of masonry type structures.

References:

- Abdel-Jaber, M. S., Walker, P.R., and Hutchinson, A.R. (2003). "Shear strengthening of reinforced concrete beams using different configurations of externally bonded carbon fiber reinforced plates." *Materials and Structures* 36: 291-301.
- ACI-ASCE Committee 445 (1999). *Recent Approaches to Shear Design of Structural Concrete ACI 445R-99*, American Concrete Institute.
- ACI Committee 440 (2000). *Guide for the design and construction of externally bonded FRP systems for strengthening concrete structures*, American Concrete Institute.
- ACI Committee & International Organization for Standardization (2011). *Building code requirements for structural concrete (ACI 318-08) and commentary*, American Concrete Institute.
- Alnatit, N. M. E. (2011). *Computational study on shear strengthening of RC continuous beams using CFRP sheet*. Master Thesis, University Tun Hussein Onn Malaysia (UTHM).
- Alzoubi, F., Qi, Z., and Zheng-ling, L. (2007). "Shear strengthening of pre-damaged reinforced concrete beams with carbon fiber reinforced polymer sheet strips." *Journal of Chongqing University: English Edition* 6: 305-310.
- ASSHTO, L. R. F. D. (1998). *Bridge Design Specifications.*, American Association of State Highway and Transportation Officials.
- ASTM, A. S. f. T. a. M., 1993, "ASTM D 5379, Standard Test Method for Shear Properties of Composite Materials by the V-Notched Beam Method."
- Ballatore, E., Carpinteri, A., Ferrara, G., and Melchiorri, G., 1990, "Mixed Mode Fracture Energy of Concrete," *Engineering Fracture Mechanics*, 35, pp. 145-157.
- Banks-Sills, L., and Arcan, M., 1983, "An Edge Crack Mode II Fracture Specimen," *Experimental Mechanics*, pp. 257-261.
- Barr, B., and Derradj, M., 1990, "Numerical Study of a Shear (Mode II) Type Test Specimen Geometry," *Engineering Fracture Mechanics*, 335, pp. 171-180.
- Barros, J. A. O., and Dias, S.J.E. (2003). *Shear strengthening of reinforced concrete beams with laminate strips of CFRP*. International Conference Composites in Constructions (CCC2003), Cosenza.
- Barros, J. A. O., and Dias, S.J.E. (2006). "Near surface mounted CFRP laminates for shear strengthening of concrete beams." *Cement and Concrete Composites* 3: 276-292.
- Barros, J.A.O., Costa, I. G., Ventura Gouveia, A. (2011) "CFRP flexural and shear strengthening technique for RC beams: experimental and numerical research." *Advances in Structural Engineering Journal*, 14(3): 559-581.
- Barros, J. A. O., Baghi, H., Dias, S.J.E., and Ventura-Gouveia, A. (2013). "A FEM-based model to predict the behaviour of RC beams shear strengthened according to the NSM technique." *Engineering Structures* 56: 1192–1206.
- Barros, J. A. O., and Dalfre, G.M. (2013). "Assessment of the Effectiveness of the Embedded Through-Section Technique for the Shear Strengthening of Reinforced Concrete Beams." *Strain* 49: 75-93.
- Barros, J. A. O., and Dias, S.J.E. (2013). *Assessment of the effectiveness of the NSM shear strengthening technique for deep T cross section RC beams*.FRPRCS11. UM, Guimarães.
- BBK 94 (1994). *Bestämmelser för betongkonstruktioner, Band 1: Konstruktion*, Svensk Byggtjänst, Solna, Sweden.

References

- Bentz, E. C. (2000). Sectional Analysis of Reinforced Concrete Members. Doctoral university of Toronto.
- Bentz, E. C., and Collins, M.P. (2001). Response-2000 Shell-2000 Triax-2000 Membrane-2000 User Manual, University of Toronto.
- Bentz, E. C., Vecchio, F.J., and Collins, M.P. (2006). "Simplified Modified Compression Field Theory for Calculating Shear Strength of Reinforced Concrete Elements." *ACI STRUCTURAL JOURNAL* 103: 614-624.
- Bianco, V., Barros, J.A.O., and Monti, G. (2010). "New approach for modeling the contribution of NSM FRP strips for shear strengthening of RC beams." *ASCE Composites for Construction Journal* 14(1): 36-48.
- Bianco, V., Monti, G., and Barros, J.A.O. (2011). "Theoretical model and computational procedure to evaluate the NSM FRP strips shear strength contribution to a RC beam." *ASCE Journal of Structural Engineering* 137(11): 1359-1372.
- Bianco, V., Barros, J.A.O., and Monti, G. (2012). "Three dimensional mechanical model to simulate the NSM FRP strips shear strength contribution to a RC beam: parametric studies." *Engineering Structures* 37: 50-62.
- Bianco, V., Monti, G., and Barros, J.A.O. (2014). "Design formula to evaluate the NSM FRP strips shear strength contribution to a RC beam." *Composites Part B: Engineering* 56: 960-971.
- Blanksvärd, T. (2007). Strengthening of concrete structures by the use of mineral based composites. Licentiate Thesis, Luleå University of Technology.
- Blanksvärd, T. (2009). Strengthening of concrete structures by the use of mineralbased composites. PhD Thesis, Luleå University of Technology.
- Breveglieri, M., Aprile, A., and Barros, J.A.O. (2014). "Shear strengthening of reinforced concrete beams strengthened using embedded through section steel bars." *Engineering Structures* 81: 76-87.
- British Standards Institution (2001). Eurocode 2: Design of Concrete Structures: Part 1-1: General Rules and Rules for Buildings, British Standards Institution.
- Brown, M. D., Sankovich, C. L., Bayrak, O., Jirsa, J.O., Breen, J.E., and Wood, S.L. (2005). Design for Shear in Reinforced Concrete Using Strutand Tie Models. University of Texas.
- Boulifa, R., Laid-Samami, M., and benhassine, M. T., 2013, "A New Technique for Studying the Behaviour of Concrete in Shear," *Journal of King Saud University*, 25(2), pp. 149-159.
- Carolin, A., and Täljsten, B. (2005). "Theoretical Study of Strengthening for Increased Shear Bearing Capacity." *Composites for Construction* 9: 497-506.
- Chaallal, O., Mofidi, A., Benmokrane, B., and Neale, K. (2011). "Embedded Through-Section FRP Rod Method for Shear Strengthening of RC Beams: Performance and Comparison with Existing Techniques." *Composites for Construction* 19: 374-383.
- Coelho, M., Fernandes, P., Sena-Cruz, J.M., and Barros, J.A.O. (2012). "Bond behavior between concrete and multi-directional CFRP laminates using the MF-EBR strengthening technique." *Advanced Materials Research*: 1110-1115.
- Collins, M. P., and Mitchell, D. (1991). Prestressed concrete structures, New Jersey:Prentice-Hall.
- Collins, M. P., Mitchell, D., Adebar, P., J. and Vecchio F. (1996). "A General Shear Design Method." *ACI STRUCTURAL JOURNAL* 93: 36-60.
- Costa, I. G., and Barros, J.A.O. (2010). "Flexural and shear strengthening of RC beams with composite materials – The influence of cutting steel stirrups to install CFRP strips." *Cement and Concrete Composites* 32(7): 544-553.

- De Lorenzis, L., Nanni, A. (2001). "Shear Strengthening of Reinforced Concrete Beams with Near-Surface Mounted Fiber-Reinforced Polymer Rods." *ACI Structural Journal* 98: 60-68.
- de Normalisation, C. E. (2000). "Concrete - Part 1: Specification, performance, production and conformity." EN206-1, CEN. , 69.
- Derradj, M. K., S. , 2008, "Numerical Study of Compact Shear (Mode II) Type Test Specimen Geometry," *Materials and Structures*, 41, pp. 1203-1210.
- Dias, S. J. E., Bianco, V., Barros, J.A.O., and Monti, G. (2007). Low strength concrete T cross section RC beams strengthened in shear by NSM technique. Workshop *Materiali ed Approcci Innovativi per il Progetto in Zona Sismica e la Mitigazione della Vulnerabilità delle Strutture*. University of Salerno, Italy.
- Dias, S. J. E. (2008). Experimental and analytical research in the shear strengthening of reinforced concrete beams using the near surface mounted technique with CFRP strips. PhD Thesis, University of Minho, Guimarães-Portugal, in Portuguese.
- Dias, S. J. E., and Barros, J.A.O. (2008). "Shear Strengthening of T Cross Section Reinforced Concrete Beams by Near Surface Mounted Technique." *Journal of Composites for Construction*, ASCE 12(No.3): 300-311.
- Dias, S. J. E., and Barros, J.A.O. (2010). "Performance of reinforced concrete T beams strengthened in shear with NSM CFRP laminates." *Engineering Structures* 32: 373-384.
- Dias, S. J. E., and Barros, J.A.O. (2013). "Shear strengthening of RC beams with NSM CFRP laminates: Experimental research and analytical formulation." *Composite Structures* 99: 477-490.
- Dogan, E., and Krstulovic-Opara, N. (2003). "Seismic retrofit with continuous slurry-infiltrated mat concrete jackets." *ACI Structural Journal* 100(6): 713-722.
- Duthinh, D., and Carino, N.J. (1996). *Shear Design of High-Strength Concrete Beams: A review of the State-of-the-Art*. Building and Fire research Laboratory National Institute of Standards and Technology Gaithersburg, MD 20899.
- Esmaeeli, E., Barros, J., and Mastali, M. (2012). Effects of curing conditions on crack bridging response of PVA reinforced cementitious matrix. 8th RILEM international symposium on fibre reinforced concrete: challenges and opportunities (BEFIB2012). Guimaraes, Portugal.
- Esmaeeli, E., Barros, J.A.O., and Baghi, H. (2013a). Hybrid Composite Plates (HCP) for Shear Strengthening of RC Beams. FRPRCS11. UM, Guimarães.
- Esmaeeli, E., Manning, E., and Barros, J.A.O. (2013b). "Strain hardening fibre reinforced cement composites for the flexural strengthening of masonry elements of ancient structures." *Construction and Building Materials* 38: 1010-1021.
- Esmaeeli, E., Barros, J.A.O., and Baghi, H., Sena-Cruz, J. (2014). Development of Hybrid Composite Plate (HCP) for the Repair and Strengthening of RC Elements. 3rd International RILEM Conference on Strain Hardening Cementitious Composites (SHCC3-Delft). Delft University.
- Esmaeeli, E., Barros, J.A.O., Sena-Cruz, J., Varum, H., and Melo, J. (2015). "Assessment of the efficiency of prefabricated hybrid composite plates (HCPs) for retrofitting of damaged interior RC beam-column joints." *Composite Structures*(119): 24-37.
- European Standard (1996). *Plastics - Determination of tensile properties - Part 2: Test conditions for moulding and extrusion plastics*. ISO 527-2, London South Bank University.
- European Standard (1997). *Plastics - Determination of tensile properties Part 5: Test conditions for unidirectional fibre-reinforced plastic composites*. ISO 527-5, Geneva (Switzerland): International Organization for Standardization (ISO).

References

- Farhat, F. A., Nicolaidis, D., Kanellopoulos, A., and Karihaloo, B.L. (2007). "High performance fibre-reinforced cementitious composite (CARDIFRC) – Performance and application to retrofitting." *Engineering Fracture Mechanics* 74: 151-167.
- Halim, H. A., Rasheed, A.H., and Esmaily, A. (2011). *Software for AASHTO LRFD Combined Shear and Torsion Computations Using Modified Compression Field Theory and 3d Truss Analogy*. Kansas State University.
- Harajli, M. H., and Rteil, A.A. (2004). "Effect of confinement using fiber-reinforced polymer or fiber reinforced concrete on seismic performance of gravity load-designed columns." *ACI Structural Journal* 101(1): 47-56.
- Ho, H., Tsai, M.Y., Morton, J., Farley, G.L., 1993, "Numerical analysis of the Iosipescu specimen for composite materials," *Composites Science and Technology*, 46(2), pp. 115-128.
- Iosipescu, N., 1967, "New accurate method for single shear testing of metals," *Journal of Materials*, 3, pp. 537-566.
- Islam, A. A. (2009). "Effective methods of using CFRP bars in shear strengthening of concrete girders." *Engineering Structures* 31: 709-714.
- ISO, E. (1990). "Metallic materials Tensile testing-Part 1: Method of test (at ambient temperature)." Brussels: European committee for standardization (cen).
- Khalifa, A., Gold, W.J., Nanni, A., and Aziz, A. (1998). "Contribution of externally bonded FRP to shear capacity of RC flexural members." *Composites for Construction* 2(4): 195-203.
- Khalifa, A., and Nanni, A. (2000). "Improving shear capacity of existing RC T-section beams using CFRP composites." *Cement & Concrete Composites* 22: 165-174.
- Khalifa, A., Tumialan, G., Nanni, A., and Belarbi, A. (1999). *Shear Strengthening of Continuous RC Beams Using Externally Bonded CFRP Sheets*. 4th International Symposium on FRP for Reinforcement of Concrete Structures (FRPRCS4). Baltimore: 995-1008.
- Krishnan, A., Roy Xu, L., "Stress Distribution on the Interfacial Shear Strength Measurements," *Proc. SEM Annual Conference*.
- Kuchma, D. A., M. Hawkins, N., Kim, S., Sun, S., and Su Kim, K. (2008). "Simplified shear provisions of the AASHTO LRFD Bridge Design Specifications." *PCI Journal*: 53-73.
- Kwak, Y., Eberhard, O.M., Kim, W., and Kim, J. (2002). "Shear Strength of Steel Fiber-Reinforced Concrete Beams without Stirrups." *ACI Structural Journal* 99: 530-538.
- Li, V. C. (1998). "Engineered Cementitious Composites for Structural Applications." *Materials in Civil Engineering* 10: 66-69.
- Maheri, M. R., Karihaloo, B.L., and Alaei, F.J. (2004). "Seismic performance parameters of RC beams retrofitted by CARDIFRC." *Engineering Structures* 26: 2069-2079.
- CEB-FIP Model Code 90, (1993) *Bulletin d'Information N° 213/214*, Final version printed by Th. Telford, London, (1993; ISBN 0-7277-1696-4; 460 pages).
- Mofidi, A., and Chaallal, O. (2011). "Shear Strengthening of RC Beams with EB FRP: Influencing Factors and Conceptual Debonding Model." *Journal of Composites for Construction* 15: 62-74.
- Morton, J., Ho, H., Tsai, M.Y., Farley, G.L., , *An evaluation of the Iosipescu specimen for composite materials shear property measurement*. *Journal of Composite materials*, 1992. 26(5): p. 708-750.
- Mostosi, S., Meda, A., Paolo, R., and Maringoni, S. (2011). *Shear strengthening of RC beams with high performance jacket*. Concrete Engineering for Excellence and Efficiency. fib Symposium PRAGUE.

- Nanni, A., Di Ludovico, M., and Parretti, R. (2004). "Shear Strengthening of a PC Bridge Girder with NSM CFRP Rectangular Bars." *Advances in Structural Engineering* 7: 97-109.
- Ohno, K., 1957, "Shear Tests of Reinforced Concrete Beam by Special Type of Loading," *Transactions of the Architectural institute of Japan* pp. 581-584.
- Orosz, K., Blanksvärd, T., Täljsten, B., and Fischer, G. (2013). "Crack development and deformation behaviour of CFRP-reinforced mortars." *Nordic Concrete Research* 48: 49-69.
- Parra-Montesinos, G., and Wight, J.K. (2000). "Seismic response of exterior RC column-to steel beam connections." *Structural Engineering* 126: 1113-1121.
- Reinhardt, H. W., Ozbolt, J., Xu, S., and Dinku, A., 1997, "Shear of Structural Concrete Members and Pure Mode II Testing," *Advanced Cement Based Materials* 5, pp. 75-85.
- Rezazadeh, M., Costa, I., and Barros, J. (2014). "Influence of prestress level on NSM CFRP laminates for the flexural strengthening of RC beams." *Composite Structures* 116: 489-500.
- Rizzo, A., and De Lorenzis, L. (2009). "Behaviour and capacity of RC beams strengthened in shear with NSM FRP reinforcement." *Construction and Building Materials* 3(No.4): 1555-1567.
- Rots, J. G. (1988). Computational modeling of concrete fracture. PhD Thesis, Delft University of Technology.
- Ruano, G., Isla, F., Pedraza, R.I., Sfer, D., and Luccioni, B. (2014). "Shear retrofitting of reinforced concrete beams with steel fiber reinforced concrete." *Construction and Building Materials* 54: 646-658.
- Saafan, M. A. A. (2006). "Shear Strengthening of Reinforced Concrete Beams Using GFRP Wraps." *Acta Polytechnica* 46: 24-32.
- Sang-Yeol, P. (1999). "Prediction of Shear Strength of R/C beams using Modified Compression Field Theory and ACI Code." *KCI Concrete Journal* 3: 5-17.
- Sena-Cruz, J. M. (2004). Strengthening of concrete structures with near-surface mounted CFRP laminate strips. PhD Thesis, University of Minho.
- Shang, Q., and Zijl, G.V. (2007). "Characterising the Shear Behaviour of Strain-Hardening Fiber-Reinforced Cement-Based Composites." *Journal of the South African Institution of Civil Engineering* 49: 16-23.
- Shannag, M. J., Barakat, S., and Jaber, F. (2001). "Structural repair of shear-deficient reinforced concrete beams using SIFCON." *Magazine of Concrete Research* 53(6): 391-403.
- Slater, E., Moni, M., and Alam, S. (2012). "Predicting the shear strength of steel fiber reinforced concrete beams." *Construction and Building Materials* 26: 423-436.
- Swartz, S. E., Lu, L.W. Tang, L.D. Refai, T.M.E., 1987, "Mode II Fracture-Parameter Estimates for Concrete from Beam Specimens," *Experimental Mechanics* pp. 146-153.
- Vecchio, F. J., and Collins, M.P. (1986). "The Modified Compression-Field Theory for Reinforced Concrete Elements Subjected to Shear." *ACI Journal*: 219-231.
- Ventura-Gouveia, A., Barros, J., Azevedo, A., and Sena-Cruz, J. (2008). Multi-fixed smeared 3d crack model to simulate the behavior of fiber reinforced concrete structures. CCC2008 - Challenges for Civil Construction. Porto, Portugal.
- Ventura-Gouveia, A. (2011). "Constitutive models for the material nonlinear analysis of concrete structures including time-dependent effects." PhD Thesis, University of Minho.

References

Xavier, J. C., Garrido, N.M., Oliveira, M., Morais, J.L., Camanho, P.P., and Pierron, F., 2004, "A comparison between the Iosipescu and off-axis shear test methods for the characterization of Pinus Pinaster Ait," *Composites part A: applied science and manufacturing*, 35, pp. 827-840.

List of Symbols:

a_f	=	CFRP width
a_g	=	Aggregate size
A_c	=	Area of concrete cross section
A_f	=	Area of the strip's cross section
A_{sx}	=	Area of longitudinal steel reinforcement
A_{sz}	=	Area of transverse steel reinforcement
A_2	=	Integration constant entering the expressions to evaluate the $V_{f_i,eff}^{\max}$
A_3	=	Integration constant entering the expressions to evaluate the $V_{f_i,eff}^{\max}$
b_f	=	CFRP thickness
b_w	=	beam web width
c	=	Clear concrete cover
c_x	=	Maximum distance from the longitudinal reinforcement
c_z	=	Maximum distance from the transverse reinforcement
C_3	=	Integration constant for the softening friction phase
d	=	effective depth of the longitudinal steel bars
d_x	=	Longitudinal bar diameter
d_y	=	Transverse bar diameter
D_{fi}^{cr}	=	opening fracture mode stiffness modulus of the i^{th} branch of the stress-strain diagram to simulate the fracture mode I crack propagation
$D_{I,i}^{cr}$	=	crack constitutive matrix component relative to the i^{th} crack normal opening mode (mode I)
$D_{I,k}^{cr}$	=	crack constitutive matrix component relative to the crack normal opening mode (mode I) for the k iteration
$D_{II,i}^{cr}$	=	crack constitutive matrix component relative to the i^{th} crack sliding mode (mode II)
$D_{II,k}^{cr}$	=	crack constitutive matrix component relative to the crack sliding mode (mode II) for the k iteration
\underline{D}^{co}	=	elastic constitutive matrix
\underline{D}^{cr}	=	crack constitutive matrix
\underline{D}^{crco}	=	constitutive matrix for the cracked concrete
\underline{D}^{cr}	=	constitutive matrix that takes into account the assembly of several (m) cracks with distinct directions
\underline{D}_i^{cr}	=	crack constitutive matrix of the i^{th} crack
E_c	=	concrete elasticity modulus
E_f	=	modulus of elasticity of CFRP laminates and strips
E_s	=	Young's modulus of the longitudinal tensile steel bars
E_{sm}	=	modulus of elasticity of steel
f_1	=	Principal tensile stress
f_2	=	Diagonal Compressive stress
$f_{2\max}$	=	Maximum diagonal Compressive stress
f_c'	=	Cylinder compressive strength of concrete

Symbols

f_c	=	Axial compressive stress outside the web
f_{cr}	=	Compressive strength for concrete at cracking
f_{ctm}^*	=	Value of concrete average tensile strength for values larger than which concrete fracture does not occur
f_{ctm}	=	Concrete average tensile strength
f_{cm}	=	average compressive strength
f_{ct}	=	tensile strength
f_{fu}	=	tensile strength of the FRP
f_{sum}	=	steel tensile strength
f_{sx}	=	Longitudinal stress in steel
f_{sy}	=	Transverse stress in steel
f_x	=	Longitudinal stress
$f_{x\text{yield}}$	=	Yield stress in longitudinal steel reinforcement
f_{yield}	=	Yield stress in reinforcement
f_{sym}	=	steel yield strength
$f_{y\text{yield}}$	=	Yield stress in transverse steel reinforcement
f_y	=	Transverse stress
F_{\max}	=	maximum experimental load
G_C	=	concrete elastic shear modulus
G_f^I	=	mode I fracture energy
IP	=	integration point
J_1	=	Bond modeling constant
l_b	=	crack band width
l_{eff}	=	Vertical length of FRP NSM bar used as shear reinforcement
L_d	=	CDC length
L_i	=	Length of each FRP bar crossed by a 45 degrees shear crack
l_{\max}	=	Length of FRP bar to maintain shear integrity of concrete
l_{net}	=	Net length of a FRP NSM bar used as shear reinforcement
L_p	=	Effective perimeter of the strip cross section
L_{Rfe}	=	Effective resisting bond length
L_{Rfi}	=	i^{th} strip resisting bond length
\bar{L}_{Rfi}^{eq}	=	Equivalent average resisting bond length
\bar{L}_{Rfi}	=	Average available resisting bond length
L_{tot}	=	Sum of effective lengths of rods crossed by crack
L_{totmin}	=	Minimum value of L_{tot}
L_i	=	span length i
M	=	Moment
NSM	=	near surface mounted
$N_{cr,\max}$	=	Maximum number of cracks per each integration point

$N_{f,int}^l$	=	Equivalent average resisting bond length
N_V	=	Tensile force due to shear
p	=	parameter that defines the shape of the last branch of the steel stress-strain curve
p_1	=	shear degradation factor
p_2	=	parameter defining the fracture energy available to the new crack
S	=	Stirrup distance
S_{mx}	=	Average spacing of cracks perpendicular to the x-reinforcement
S_{my}	=	Average spacing of cracks perpendicular to the y-reinforcement
S_f	=	distance between CFRP laminates
S_x	=	Distance between longitudinal reinforcement
S_{xe}	=	Effective longitudinal crack spacing
S_θ	=	Distance between diagonal cracks
t_f	=	thickness of FRP
\underline{T}^{cr}	=	transformation matrix that takes into account the assembly of several (m) cracks with distinct directions
\underline{T}_k^{cr}	=	transformation matrix that takes into account the assembly of several (m) cracks with distinct directions for the k iteration
\underline{T}_i^{cr}	=	transformation matrix of the i^{th} crack
v	=	Shear stress
V	=	Shear force
V_a	=	Internal friction
v_c	=	Shear stress in concrete
V_c	=	Shear force in Concrete
v_{ci}	=	Shear stress at crack
V_d	=	Dowel force in longitudinal bars
V_f	=	Shear resistance contribution of fibers
V_f^{tr}	=	Strip tensile rupture capacity
V_{fd}	=	Design value of the NSM shear strengthening contribution
$V_{\beta,eff}^{max}$	=	Maximum effective capacity
V_{f1}^{bd}	=	Maximum value of force transferable through bond by the given FRP NSM system
V_s	=	Shear resistance contribution of steel reinforcement
v_y	=	Shear stress in transverse reinforcement
w	=	Crack width
α	=	Angle defining the concrete fracture surface
α_1	=	Factor accounting for the bond characteristics of reinforcement
α_2	=	Factor accounting for the sustained or repeated loading
α_i	=	fracture parameters used to define the trilinear stress-strain softening diagram
β	=	shear retention factor and
β	=	Factor accounting for the tensile stress in the cracked concrete
γ_{nt}^{cr}	=	crack shear strain
$\Delta\gamma_{nt,i}^{cr}$	=	incremental crack shear strain of the i^{th} crack
$\Delta\epsilon_{n,i}^{cr}$	=	incremental crack normal strain of the i^{th} crack

Symbols

$\underline{\Delta \varepsilon}$	=	vector containing the strain incremental components
$\underline{\Delta \varepsilon}^{co}$	=	vector containing the incremental strain of the uncracked concrete between the cracks
$\underline{\Delta \varepsilon}^{cr}$	=	vector containing the incremental strain of the crack
$\underline{\Delta \varepsilon}_{\ell}^{cr}$	=	vector of the incremental crack strain components in the crack coordinate system
$\Delta \sigma_{n,i}^{cr}$	=	incremental crack normal stress of the i^{th} crack
$\underline{\Delta \sigma}$	=	vector containing the stress incremental components
$\Delta \tau_{nt}^{cr}$	=	incremental crack shear stress
$\Delta \tau_{nt,i}^{cr}$	=	incremental crack shear stress of the i^{th} crack
δ_1	=	Slip corresponding to the end of softening friction
δ_{Li}	=	Imposed slip at the loaded extremity of the i^{th} strip
δ_{Lu}	=	Imposed slip in correspondence of which the comprehensive peak force transmissible by \bar{L}_{Rfi}^{eq} is attained
δ_{L1}	=	Value of δ_{Li} defining the end of the first phase of the bond-based constitutive law
ε_1	=	Principal tensile strain
ε_2	=	Principal compressive strain
ε_c'	=	Strain at the peak compressive strength
ε_{cr}	=	Tensile cracking strain for concrete
ε_f	=	Effective tensile strain in FRP reinforcement
ε_n^{cr}	=	crack normal strain
$\varepsilon_{n,i}^{cr}$	=	crack normal strain used to define point i in the trilinear stress-strain softening diagram
$\varepsilon_{n,u}^{cr}$	=	ultimate crack normal strain
ε_{sh}	=	strain corresponding to point 2 (PT2) of the steel stress-strain relationship
ε_{su}	=	strain corresponding to point 3 (PT3) of the steel stress-strain relationship
ε_x	=	Longitudinal strain
ε_y	=	Transverse strain
ε_{sy}	=	strain corresponding to point 1 (PT1) of the steel stress-strain relationship
γ_{max}	=	CDC opening angle for which the maximum effective capacity is attained
γ_{xy}	=	Shear strain
θ	=	Direction of the principal stress/strain
θ_i	=	angle between the x_i axis and the vector orthogonal to the plane of the i^{th} crack
θ_{new}^{cr}	=	orientation between the new crack and the already existing cracks
θ_{th}	=	threshold angle
θ_f	=	inclination of CFRP
ν_c	=	poisson's ratio
ξ_i	=	fracture parameters used to define the trilinear stress-strain softening diagram
ρ_x	=	Longitudinal steel reinforcement ratio
ρ_y	=	Transverse steel reinforcement ratio

ρ_f	=	strengthening ratio of the NSM laminates
$\rho_{l,eq}$	=	equivalent flexural reinforcement ratio
ρ_{sl}	=	reinforcement ratio of the bottom longitudinal steel bars
σ_I	=	maximum principal tensile stress
σ_{k-1}	=	normal stress for the $k-1$ iteration
σ_n^{cr}	=	crack normal stress
$\sigma_{n,i}^{cr}$	=	crack normal stress used to define point i in the trilinear stress-strain softening diagram
σ_{sh}	=	stress corresponding to point 2 (PT2) of the steel stress-strain relationship
σ_{su}	=	stress corresponding to point 3 (PT3) of the steel stress-strain relationship
σ_{sy}	=	stress corresponding to point 1 (PT1) of the steel stress-strain relationship
τ_0	=	adhesive-cohesive initial bond strength
τ_b	=	Average bond stress of laminates crossed by a shear crack
τ_{nt}^{cr}	=	crack shear stress
η	=	Reduction factor of the initial average available resisting bond length
λ	=	Constant entering the governing differential equation for elastic phase
ψ	=	Constant necessary to evaluate the maximum effective capacity provided by the equivalent average resisting bond length

Annex A

Iosipescu shear test fixture:

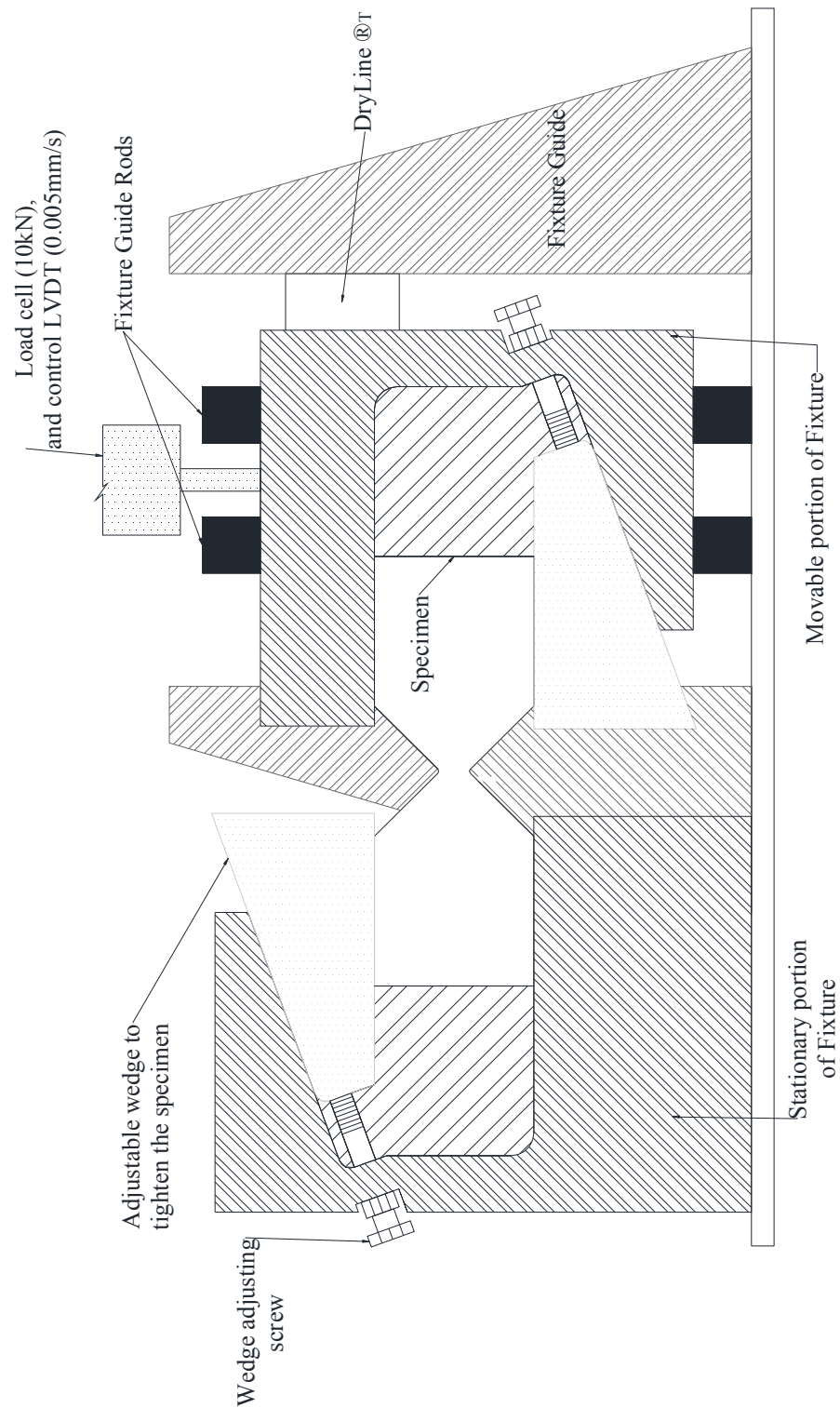


Figure 1A: Iosipescu shear test device (Front view)

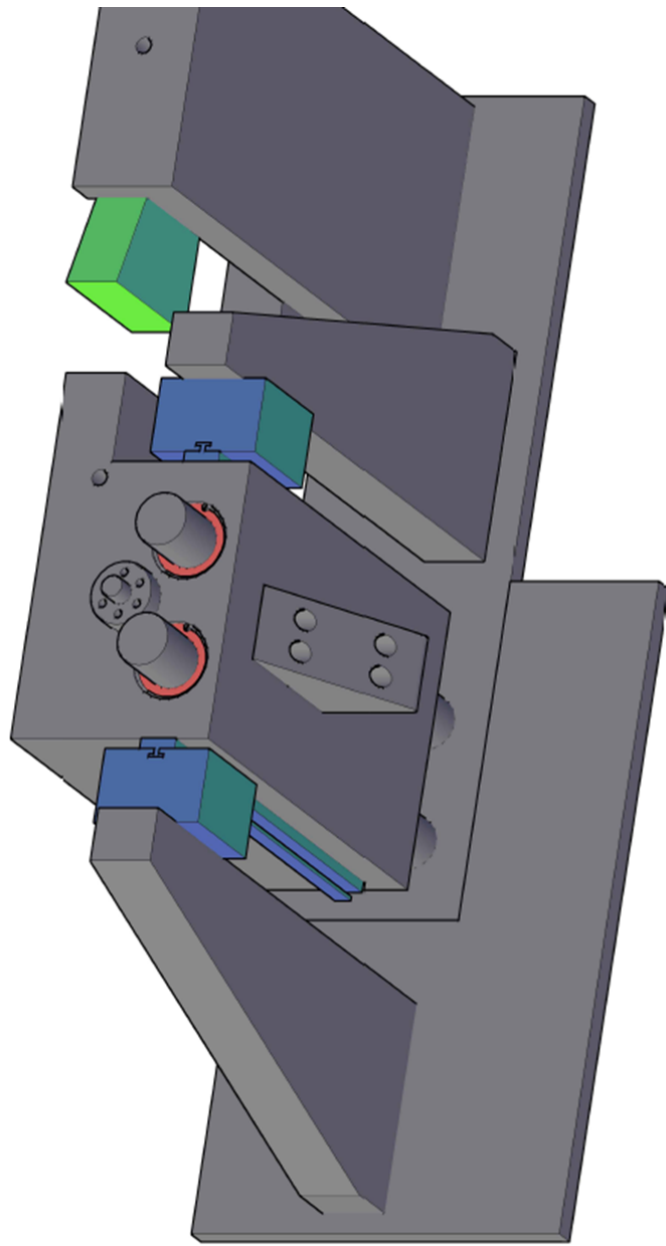


Figure 2A: Iosipescu shear test (rear view)

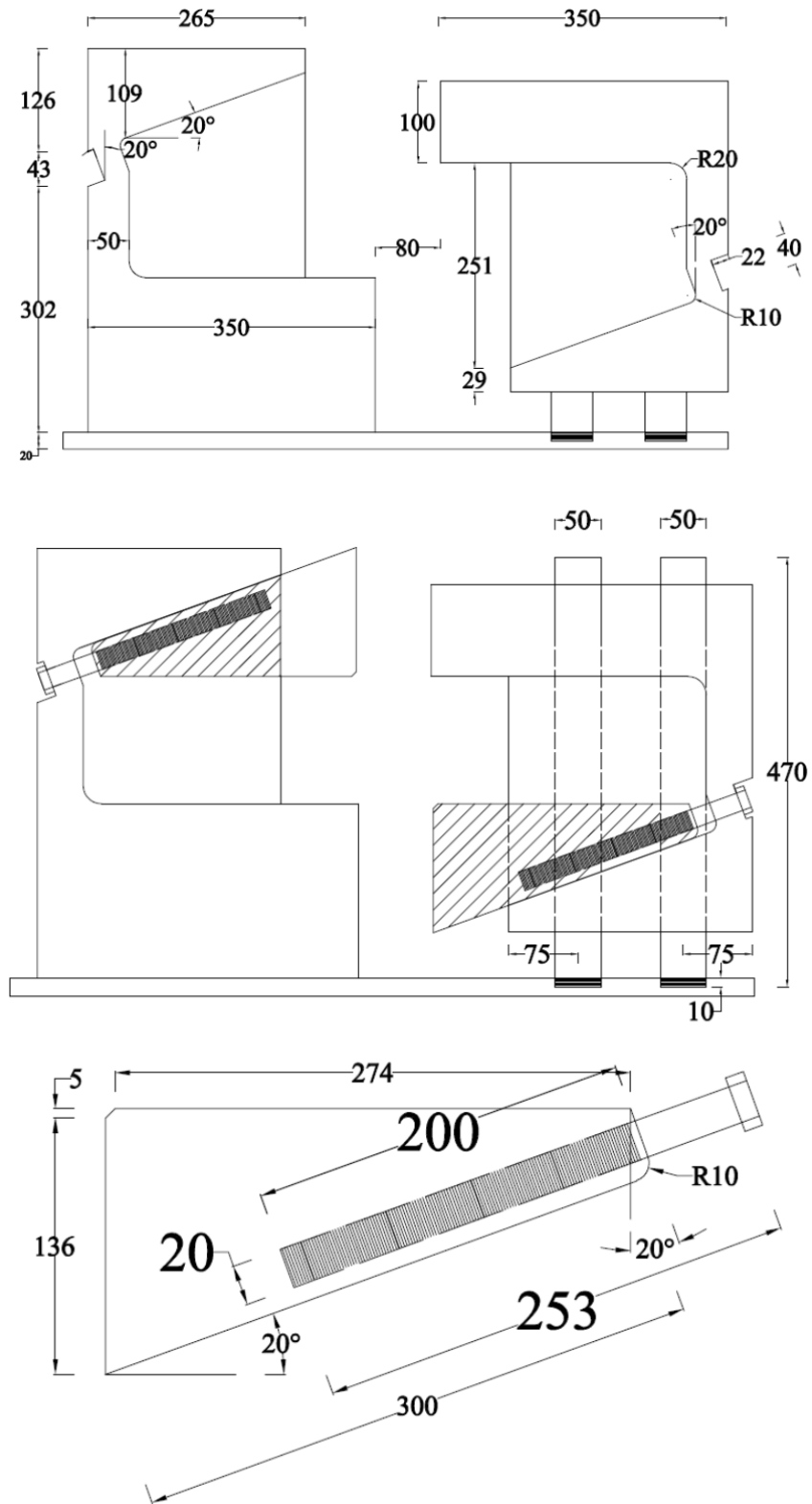


Figure 3A: Details of Iosipescu Fixture (dimensions in mm)

Annex B

Modified Compression Field Theory:

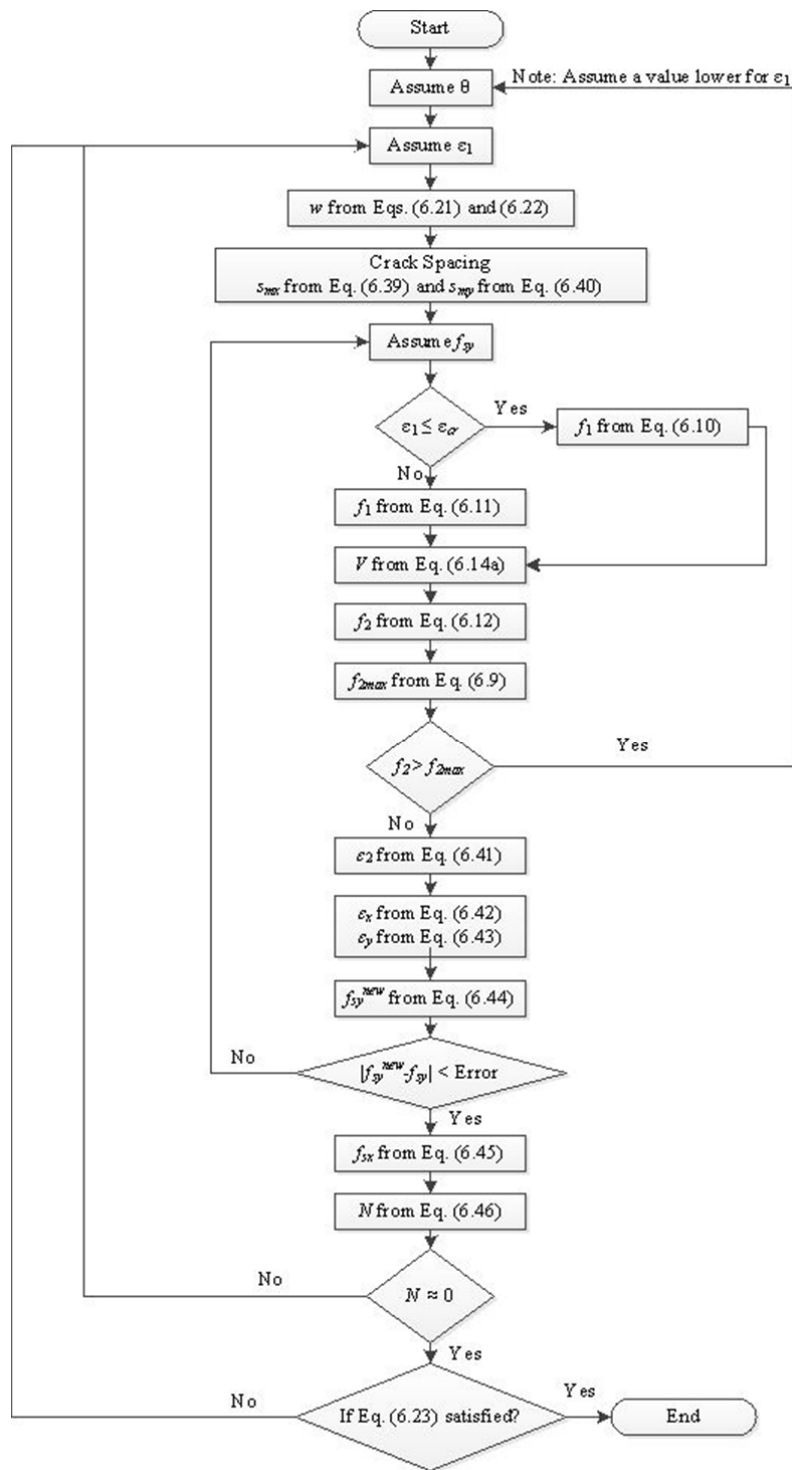


Figure 1B: Flowchart of MCFT

Annex C

Simplified Modified Compression Field Theory:

Assumptions:

Crushing of the concrete (ε_c') is limited to 0.002, yield strain of the stirrup (ε_y) is greater than 0.002.

When ε_x is equal to 0.002 at failure:

$$\varepsilon_1 + \varepsilon_2 = \varepsilon_x + \varepsilon_y \Rightarrow \varepsilon_1 = 0.006 \quad \text{Eq. (6.30)}$$

$$\tan^2 \theta = \frac{\varepsilon_x - \varepsilon_2}{\varepsilon_y - \varepsilon_2} = 1 \Rightarrow \theta = 45^\circ \quad \text{Eq. (6.29)}$$

$$f_1 = \frac{f_{cr}}{1 + \sqrt{500\varepsilon_1}} = \frac{0.33\sqrt{f_c'}}{2.73} \quad \text{Eq. (6.36)}$$

$$f_2 = \frac{f_c'}{0.8 + 170\varepsilon_1} \times \left[2 \left(\frac{\varepsilon_2}{\varepsilon_c'} \right) - \left(\frac{\varepsilon_2}{\varepsilon_c'} \right)^2 \right] = \frac{f_c'}{0.8 + 170 \times 0.006} = \frac{f_c'}{1.82} \quad \text{Eq. (6.37)}$$

$$v = \frac{f_1 + f_2}{\tan \theta + \cot \theta} = \frac{\frac{0.33\sqrt{f_c'}}{2.73} + \frac{f_c'}{1.82}}{2} \quad \text{Eq. (6.26)}$$

Table 1C

f_c'	$v = \frac{\frac{0.33\sqrt{f_c'}}{2.73} + \frac{f_c'}{1.82}}{2}$	$v = 0.28f_c'$
20 MPa	5.6 MPa	5.7 MPa
30 MPa	8.5 MPa	8.4 MPa
40 MPa	11.3 MPa	11.2 MPa
50 MPa	14 MPa	14 MPa
60 MPa	17 MPa	16.8 MPa
70 MPa	19.7 MPa	19.6 MPa
80 MPa	22.5 MPa	22.4 MPa

When ε_x is equal to 0.00001 at failure:

$$\varepsilon_1 + \varepsilon_2 = \varepsilon_x + \varepsilon_y \Rightarrow \varepsilon_1 = 0.00401 \quad \text{Eq. (6.30)}$$

$$\tan^2 \theta = \frac{\varepsilon_x - \varepsilon_2}{\varepsilon_y - \varepsilon_2} = 0.5025 \Rightarrow \theta = 35^\circ \quad \text{Eq. (6.29)}$$

$$f_1 = \frac{f_{cr}}{1 + \sqrt{500\varepsilon_1}} = \frac{0.33\sqrt{f'_c}}{2.4} \quad \text{Eq. (6.36)}$$

$$f_2 = \frac{f'_c}{0.8 + 170\varepsilon_1} \times \left[2 \left(\frac{\varepsilon_2}{\varepsilon'_c} \right) - \left(\frac{\varepsilon_2}{\varepsilon'_c} \right)^2 \right] = \frac{f'_c}{0.8 + 170 \times 0.00401} = \frac{f'_c}{1.48} \quad \text{Eq. (6.37)}$$

$$v = \frac{f_1 + f_2}{\tan \theta + \cot \theta} = \frac{\frac{0.33\sqrt{f'_c}}{2.4} + \frac{f'_c}{1.48}}{2.18} \quad \text{Eq. (6.26)}$$

Table 2C

f'_c	$v = \frac{\frac{0.33\sqrt{f'_c}}{2.4} + \frac{f'_c}{1.48}}{2.18}$	$v = 0.32f'_c$
20 MPa	6.4 MPa	6.4 MPa
30 MPa	9.6 MPa	9.6 MPa
40 MPa	12.8 MPa	12.8 MPa
50 MPa	16 MPa	16 MPa
60 MPa	19.1 MPa	19.2 MPa
70 MPa	22.2 MPa	22.4 MPa
80 MPa	25.4 MPa	25.6 MPa

Annex D

Example of NSMCFT and BSMCFT

The procedure solution for one beam strengthened with NSM CFRP laminate (2S-4LI45 (Dias and Barros 2010)) is herein explained. The geometry and material properties of the beam are presented in Figure D1 and Table D1, respectively.

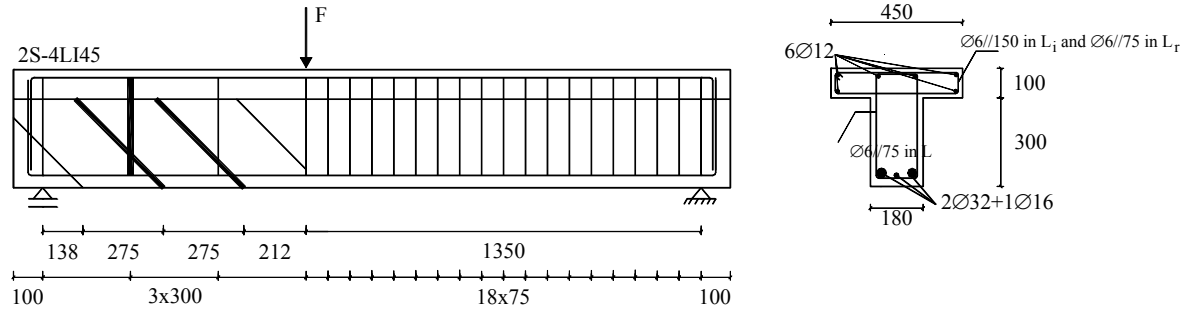


Figure 1D: geometry of the beam 2S-4LI45 (Dias and Barros 2010)

Table 1D: Material properties

Concrete	Concrete strength at age of beam test				
	39.7 (MPa)				
Steel	Tensile strength	Ø6	Ø12	Ø16	Ø32
	Yield strength	500 (MPa)	490 (MPa)	470 (MPa)	625 (MPa)
CFRP laminates	Maximum tensile strength	2741.7 MPa		Young's Modulus	170.9 GPa
				Maximum strain	$\epsilon_{fu} = 1.60\%$

Step 1: Estimate a value for ϵ_x .

Step 2: Calculate the crack spacing:

$$S_{xe} = \frac{35s_{mx}}{a_g + 16} \geq 0.85s_x$$

Step 3: Calculate β and θ :

$$\theta = (29 + 7000\epsilon_x) \cdot \left(0.88 + \frac{S_{xe}}{2500} \right) \leq 75^\circ$$

$$\beta = \frac{0.4}{1 + 1500\epsilon_x} \cdot \frac{1300}{1000 + S_{xe}}$$

Step 4: Calculate the shear stress:

NSMCFT:

$$v = v_c + v_s + v_f = \beta \sqrt{f'_c} + \rho_y f_{yield} \cot \theta + \left[4(a_f + b_f) \tau_b L_{totmin} \right] \cdot \frac{\sin \theta_f}{b_w d}$$

BSMCFT:

$$v = v_c + v_s + v_{fd} = \beta \sqrt{f'_c} + \rho_y f_{yield} \cot \theta + 2 \cdot N_{f,int}^l \cdot V_{fi,eff}^{\max} \cdot \frac{\sin \theta_f}{b_w d}$$

Step 5: Calculate the longitudinal strain, ε_x , and compare to ε_x that was estimated in step1.

Return to Step1 until convergence is obtained:

$$\varepsilon_x = \frac{v \cdot \cot \theta - v_c / \cot \theta}{E_s \rho_{sx}}$$

Table 2D: Nanni SMCFT approach

Iteration	$A = \varepsilon_x$ Estimated	S_{xe}	β	θ	v_c	v_s	v_f	v	$B = \varepsilon_x$ Eq.	$A-B$
1	0.001	276.58	0.1629	35.66	1.03	0.79	0.50	2.32	4.31e-4	5.67e-4
2	4.31e-4	276.58	0.2475	31.72	1.56	0.92	0.55	3.03	6.79e-4	-2.48e-4
3	6.79e-4	276.58	0.2018	33.43	1.27	0.86	0.53	2.66	5.50e-4	1.29e-4
4	5.50e-4	276.58	0.2232	32.54	1.41	0.89	0.54	2.84	6.11e-4	-6.1e-5
5	6.11e-4	276.58	0.2125	32.97	1.34	0.87	0.54	2.75	5.81e-4	3e-5
6	5.81e-4	276.58	0.2177	32.75	1.37	0.88	0.54	2.79	5.95e-4	-1.4e-5
7	5.95e-4	276.58	0.2151	32.86	1.36	0.88	0.54	2.78	5.88e-4	7e-6
8	5.88e-4	276.58	0.2164	32.81	1.36	0.88	0.54	2.74	5.88e-4	0

Table 3D: Bianco SMCFT approach

Iteration	$A = \varepsilon_x$ Estimated	S_{xe}	β	θ	v_c	v_s	v_f	v	$B = \varepsilon_x$ Eq.	$A-B$
1	0.001	276.58	0.1629	35.66	1.03	0.79	0.84	2.66	4.55e-4	5.45e-4
2	5.11e-4	276.58	0.2307	32.27	1.45	0.90	0.95	3.30	7.43e-4	-2.32e-4
3	7.43e-4	276.58	0.1926	33.88	1.21	0.84	0.90	2.95	6.17e-4	1.26e-4
4	6.17e-4	276.58	0.2115	33.01	1.33	0.87	0.93	3.13	6.81e-4	-6.40e-5
5	6.81e-4	276.58	0.2015	33.45	1.27	0.86	0.91	3.04	6.48e-4	3.30e-5
6	6.48e-4	276.58	0.2066	33.22	1.30	0.87	0.92	3.09	6.65e-4	-1.70e-5
7	6.65e-4	276.58	0.2039	33.34	1.28	0.86	0.91	3.06	6.55e-4	1.00e-5
8	6.55e-4	276.58	0.2053	33.28	1.29	0.86	0.92	3.07	6.61e-4	-6.00e-6
9	6.61e-4	276.58	0.2046	33.31	1.29	0.86	0.92	3.07	6.61e-4	0